UC Santa Barbara

UC Santa Barbara Electronic Theses and Dissertations

Title

High Temperature Mechanical Behavior of Copper-Niobium Multilayer Composites

Permalink

https://escholarship.org/uc/item/1cg1w1zj

Author

Avallone, Jaclyn Taylor

Publication Date

2018

Peer reviewed|Thesis/dissertation

eScholarship.org Powered by the California Digital Library
University of California

University of California
Santa Barbara

High Temperature Mechanical Behavior of Copper–Niobium Multilayer Composites

A dissertation submitted in partial satisfaction
of the requirements for the degree

Doctor of Philosophy
in
Materials

by

Jaclyn Taylor Avallone

Committee in charge:

Professor Tresa M. Pollock, Chair
Professor Carlos G. Levi
Professor Matthew R. Begley
Professor Micheal R. Gordon

September 2018

The dissertation of Jaclyn Taylor Avallone is approved.

Carlos G. Levi

Matthew R. Begley

Micheal R. Gordon

Tresa M. Pollock, Committee Chair

August 2018

This thesis is dedicated to the Begley family for simultaneously providing the motivation and distractions that I needed to get this done. Thank you for being some of the most loving and patient humans on the planet.

Acknowledgements

Funding and Support

This material is based upon work supported by the UC Lab Fees program 12-LR-238091, as well as the Department of Energy, National Nuclear Security Administration under Award No. DE-NA0003857, for the Center for Research Excellence on Dynamically Deformed Solids (CREDDS).

Committee

Tresa, thank you for providing me with guidance and advice for 6 long years! Being a part of your group was the best part of grad school because you facilitate such a wonderful and supportive environment for all of us. Thank you for encouraging me to get involved with various department events/workshops and TMS committees, and for the opportunity to have amazing internship experiences - those things took a large part in shaping my professional persona.
Finally, thank you (and Bill) for the deck parties and other social gatherings that you have hosted and facilitated throughout the years. I hope to reciprocate the hospitality some day!

Carlos, thank you for adding thoughtful discussion and sincerity into everything that you do. I hope you know that your passion for materials science and for this department is inspiring and motivating to all of us students. Thank you for your honest criticism and for promoting excellence in us all.

Mike, thank you for your genuine interest in me and my research. I have enjoyed getting to know you in both social and professional capacities. Thank you for making me think about broader impacts of my work, and for supporting my path to post-graduate life!

Matt, thank you for everything. I only hope that I can put all of your wisdom and advice into regular practice. Thank you (and Kyle) for facilitating such an amazing community for the structural materials folks with BTS - the late night discussions of science and life are of my most fond memories in all of graduate school. I am so glad that I had the opportunity to insert myself into your family.

Collaborators

This work would not have been possible without the help of Tom Nizolek. Thank you for making my material. Thank you for including me in your work and for being such an integral part of mine. Thank you for teaching me how to prep Cu-Nb to your standards, make a bubbler system, roll-bond material, navigate my experiments, and so much more. Thank you for getting into the weeds about everything from kinking to epoxy mounting to making wine bottle openers. Thanks for supporting me when I was not supporting myself. You were a better project-mate than I could have dreamed up in my wildest dreams.

Ben, thank you for teaching me about statistics, making me laugh when my data was depressing, and for investing so much time into Cu-Nb creep analysis. You are a wonderful collaborator and friend.

The hardness testing was performed by Xiaoxi (Brooke) Liu. Thank you for your patience and excitement to learn and improve yourself.

Thank you to the staff at the Physics and Mech E machine shops for doing precision work and ensure successful experiments. Thank you to the UCSB glassblower, Richard, for your assistance making and repairing my creep set-up.

Irene and Nate, thank you for supporting me during my time at LANL.
It was a wonderful learning experience.

Thank you to Siamak Shishvan and Vikram Desphande for your interest in Cu-Nb creep and for contributing time and effort to understanding the discrete dislocation dynamics necessary to model this system.

Technical Mentors

Thank you to Chris Torbet for showing me the ropes of experimental design, teaching me how to electroplate, and use an EDM. Without you, I might still be working on my creep set-up. Your wisdom, patience, and advice was essential to my growth as an experimentalist. I cannot thank you enough.

A significant portion of this work was performed in lab spaces or using equipment that were amazingly kept and run by Deryck Stave and Kirk Fields. Thank you for facilitating collaboration and sharing your wealth of practical knowledge!

All microscopy presented in this dissertation would not have been possible without Stephan Kraemer and Mark Cornish. Thank you to Mark for much needed chats to break up the monotony of TEM sample prep and for sharing his expertise. Special thank you to Stephan Kraemer for his ENDLESS patience, knowledge, and support in TEM and FIB operation. I cannot express my gratitude enough for the hours he spent teaching me about these instruments, fixing my mistakes, and convincing me that my frustrations were not the end of the world.

Thank you to Tori for your patiences in teaching me about PIPS and sample prep for EBSD. Thanks to both Tori and Marissa for sharing your knowledge about EBSD and scan parameters in the many times that I was ready to throw in the towel. Thank you Chandra and Katie for helping me navigating the struggles of FIB and TITAN.

Professional Development

Thank you to all of the professional development and outreach staff who facilitated amazing opportunities to learn and give back to our community. (Specifically, Dotti, Maria, Wendy, Frank, Arica and Lana). Attending non-technical seminars and panels reminds us that we can and should be well rounded human beings. Volunteering with young students was one of the most rewarding things that I did for myself in graduate school - and I am very grateful to all of you who shared your experiences and opportunities with me.

Thank you Dan, Suveen, and Rod for being wonderful professional role models. Your active lives (personally and professionally) inspire me to be collaborative and open minded in the general science community. Dan, thank you for talking with me and connecting me with my future job! Suveen, thank you for forcing me to try new things and network my brains out at TMS - I have really enjoyed the experience. Rod, thank you for such a wonderful welcome into toastmasters at LANL - I have really benefited from it, professionally.

Personal Development

I would not have had this opportunity without the love and support of my parents - thank you for being my rocks. I love you so much!

Begley family, I cannot express my gratitude enough for your love and support. Thanks for being amazing people and role models. Some specific thanks are necessary. Matt and Kyle, thank you for spending so much time convincing me that I deserve to have a PhD. I aspire to be as accomplished as you both know I can be (professionally and/or personally). Sara and Griff, reading with you, learning about animals, and making up games together was the best part of my entire year! I love you guys.

Thank you to all who sent me encouraging memes and pictures of cute babies and animals to get me through the rough days: Steve, Avallone cousins, Tachel, Tori, Minal, Derek, and Kalie - you are all wonderful humans.

Thank you to Brent, Rob, and Will for being the best intro-to-grad-school bunch I could have asked for from trivia nights to weekly dinners and office political debates: I learned so much from all of you.

Thank you to all who have helped me keep my sanity when classes and experiments got my spirits down. You are the best. Specifically, my groupmates, my cohort, residents of the Shepot, residents of Coolbrook, residents of the Mill house, and the Dream Team.

Thank you to Brent and Megan for the nights of endless HW and studying at the beginning.

Thanks to Tom, Tori and Brent for making late night office life a good time.

Brent, Marissa, and Chris for babysitting me in the final hours of PhD life - I would not have made it without you.

David, thank you for being my orchestra buddy and navigating work-life-solitaire balance with me.

Dream team, thank you for forcing me into physical activity; but mostly thank you for the friendship and continued support of healthy living and socializing.

Curriculum Vitæ

Jaclyn Taylor Avallone

Education

U.C., Santa Barbara, Materials Department CA
PH.D. IN MATERIALS, POLLOCK GROUP 2012-2018

Arizona State University, Ira A. Fulton School of Engineering AZ
B.S.E. IN MATERIALS SCIENCE AND ENGINEERING 2008-2012

Publications

1. **J.T. Avallone**, X. Liu, T.J. Nizolek, N.A. Mara, I.J. Beyerlein, T.M. Pollock. "Thermal Stability and Structural Evolution of Cu-Nb Multilayers made via Accumulative Roll-Bonding," *In preparation for Met. Trans. A*. (2018).
2. **J.T. Avallone**, T.J. Nizolek, B.B. Bales, M.R. Begley, T.M. Pollock. "A Model for High Temperature Deformation of Nanolaminate Cu-Nb Composites," *In preparation for Materials Science and Engineering A*. (2018).
3. **J.T. Avallone**, T.J. Nizolek, B.B. Bales, T.M. Pollock. "Creep Resistance of Bulk Copper-Niobium Composites: an Inverse Effect of Multilayer Length Scale," *In preparation for Acta Materialia*. (2018).
4. T.J. Nizolek, N.A. Mara, I.J.Beyerlein, **J.T. Avallone**, T.M. Pollock. "Tensile Behavior and Flow Stress Anisotropy of Accumulative Roll Bonded Cu-Nb Nanolaminates," *Applied Physics Letters*. 108(5) 051903 (2016).
5. T.J. Nizolek, N.A. Mara, I.J.Beyerlein, **J.T. Avallone**, T.M. Pollock. "Enhanced Plasticity via Kinking in Cubic Metallic Nanolaminates," *Advanced Engineering Materials*. 17(6) 781-785 (2015).
6. T.J. Nizolek, N.A. Mara, I.J.Beyerlein, **J.T. Avallone**, J.E. Scott, T.M. Pollock. "High Strength Bulk Metallic Nanolaminates," *Advanced Materials and Processes*. 173(2), 18-21 (2015).
7. T.J. Nizolek, N.A. Mara, I.J.Beyerlein, **J.T. Avallone**, T.M. Pollock. "Processing and Deformation Behavior of Bulk Cu-Nb Nanolaminates," *Metallography, Microstructure, and Analysis*. 3(6), 470-476 (2014).
8. A. Makas, **J.T. Avallone**, R. MacKinnon, I. Atodaria and P.D. Peralta "Variability on Nucleation and Growth of Short Fatigue Cracks Due to Material Anisotropy in Al 2024-T351 and its Implications for Damage Modeling," *Journal of Intelligent Material Systems and Structures*. 24(17) 2148-2167 (2013).

Awards and Recognition

2017 Oustanding K-12 Volunteer Award *by Materials Research Laboratory, UCSB*
2017 Best Speaker: Student Travel Grant *by C.S.S.S. Committee, UCSB*
2016 TMS Young Scientist Competition Gold Certificate *by Symposium Organizers*
2012 Fulton Undergraduate Travel Grant *by Arizona State University*
2011 Fulton Undergraduate Research Initiative Grant *by Arizona State University*
2008-2012 Sun Devil Academic Scholarship *by Arizona State University*

Research Experience

UNIVERSITY OF CALIFORNIA, SANTA BARBARA S.B., CA
Graduate Researcher, Pollock Group 2012-2018

Characterization

- Operate TEMs (including STEM, BF, and HAADF), regularly.
- Prepare samples via traditional metallography, PIPS, and Focused Ion Beam.
- Collect and analyze orientation and composition using SEM (BSE, EBSD, EDX).
- Expand microscopy techniques (EELS, PED, HRTEM, HAADF, FIB) by attending hands-on workshops, by *NanoMEGAS and LeRoy Eyring Center at ASU.*

Experimentation and Design

- Design creep setup for bulk sheet materials in inert environment, including novel automated image processing and strain analysis coded in Java and Matlab.
- Model and quantify creep rates with length scale, temperature history, and stress.
- Establish FEA simulation with ABAQUS to observe strain distributions.

ATI SPECIALTY ALLOYS & COMPONENTS Albany, OR
Technology Student Intern Summer 2017

- Performed thermomechanical tests on established and novel refractory alloys.
- Analyzed and characterized alloy structures w. microscopy and image processing.
- Modeled temperature, strain and stress variations in processing using DEFORM.
- Presented regular project updates for employees of various backgrounds.

LOS ALAMOS NATIONAL LABORATORY Los Alamos, NM
Visiting Scholar Summer 2014

- Prepared FIB foils for in-situ TEM tensile testing of HCP-BCC thin films.
- Characterized microstructural evolution in Cu-Nb multilayers by performing heat treatments, and using SEM (EBSD) and aberration corrected TEM.

ARIZONA STATE UNIVERSITY Tempe, AZ
Undergraduate Researcher, Peralta Group 2009-2012

Characterization

- Performed interrupted fatigue tests and evaluated crack propagation using optical and electron microscopy.
- Prepared Al alloys for SEM (EBSD); analyzed fatigue failure w.r.t. processing.

Experimentation and Design

- Proposed experiments studying the effects of precipitate alignment on anisotropy of rolled Al alloy; developed heat treatment procedures to influence microstructure evolution; programmed PID furnaces for various material geometries. *Funding awarded by the Fulton Undergraduate Research Initiative.*
- Designed grips to accommodate unique woven fiber composite geometries for tensile testing; performed Digital Image Correlation to analyze strain localization.
- Collaborated with a start-up to systematically measure mechanical properties of fiber composites under a variety of environmental conditions *Nuovo Wind LLC. & ASU Materials Senior Design.*

Poster Presentations

1. J.T. Avallone, T.J. Nizolek, B.B.Bales, T.M. Pollock. "Creep Behavior of Accumulatively Roll Bonded Copper-Niobium Multilayers," Winter Study Group on High Performance Materials, UCSB (2018)

2. J.T. Avallone, T.J. Nizolek, T.M. Pollock. "Length Scale Dependence of Creep Behavior of Copper-Niobium Multilayer Composites," Winter Study Group on High Temperature Materials, UCSB (2016)

3. J. Avallone, A. Makas, R. MacKinnon, I. Atodaria, P. Peralta, "Anisotropic Fatigue Behavior Rolled Aluminum 2024," Arizona State University Fulton Undergraduate Research Initiative Spring Symposium, Tempe, AZ, (2012)

4. J.T. Avallone, A. Makas, P.D. Peralta "Effects of Heat Treatment on the Anisotropic Fatigue Behavior of Rolled Aluminum 2024," TMS Annual Meeting, Orlando, FL (2012)

Oral Presentations

1. J.T. Avallone, T.M. Pollock. "Microstructural Evolution and Thermal Stability of Accumulatively Roll-bonded Cu-Nb Nanolaminates," *Ultra Fine Grain Materials X: Early Career Scientist*, TMS Annual Meeting, Phoenix, AZ (2018)

2. J.T. Avallone, T.M. Pollock. "Creep Behavior of Cu-Nb Multilayer Composites," *Invited Seminar at Intel Corporation*, Chandler, AZ (2018)

3. J.T. Avallone, T.M. Pollock. "Creep Behavior of Cu-Nb Multilayer Composites," *Invited Seminar at HRL Laboratories, LLC.*, Malibu, CA (2018)

4. J.T. Avallone, T.J. Nizolek, N.A. Mara, I.J.Beyerlein, T.M. Pollock. "Structure Dependent Creep Behavior of CuNb Nanolaminates," *Mechanical Behavior of Nanostructured Materials: Mechanical Properties of Low Dimensional Material*, TMS Annual Meeting, San Diego, CA (2017)

5. J.T. Avallone, T.M. Pollock,T.J. Nizolek, N.A. Mara, I.J.Beyerlein. "Effects of Length Scale on Creep Behavior of Bulk CuNb Nanolaminates," *Ultra Fine Grain Materials IX: Young Scientists*, TMS Annual Meeting, Nashville, TN (2016)

6. J.T. Avallone, T.M. Pollock. "Thermal Stability of Copper-Niobium Multilayer Composites," *Structural Materials Seminar*, UC Santa Barbara (2015)

7. J.T. Avallone, T.M. Pollock. "Microstructure Analysis on the Nanoscale: STEM techniques," *Structural Materials Seminar*, UC Santa Barbara (2014)

8. J.T. Avallone, T.J. Nizolek, T.M. Pollock, N.A. Mara, I.J.Beyerlein. "Electron Microscopy of Copper-Niobium Accumulative Roll Bonded Metallic Nanolaminates," *Nuclear Technology and Materials Science Symposium*, Annual Academy for Co-creative Edu. of Environment and Energy Science, Huntington Beach, CA (2013)

Outreach Experience

Beyond Academia Conference, *UCSB* 2017
Programming committee member

Our Material World Event, *by the Materials Research Laboratory, UCSB* 2016
Speaker programming and communication

Ask a Scientist, *UCSB* 2015-2018
Media Relations Co-chair

Family Ultimate Science Experience, 2014-2018
Center for Science and Engineering Partnership, UCSB
Volunteer instructor

It's a Material World, *Materials Research Lab, UCSB* 2013-2018
Volunteer instructor and demonstrator

Science Detectives, *ASU* 2010-2012
Volunteer instructor, demonstrator, and lesson planner

Mentor Experience

Problem-based Initiatives for Powerful Engagement Summer 2016
and Learning In Naval Engineering and Science (PIPELINES) program,
Center for Science and Engineering Partnership, UCSB
Mentor to a 1^{st} place team of four undergraduate students

Materials Department, University of California, Santa Barbara Winter 2014
MATRL 100B: Structure and Properties of Materials II
Teaching Assistant

Professional Activities

The Minerals, Metals, and Materials Society

Young Professionals Committee member	2018-Current
Education Committee member	2017-Current
Diversity Committee member	2017-Current
Nanomechanical Materials Behavior Committee member	2016-Current
Mechanical Behavior Committee member	2016-Current
Conference Attendee	2012-Current

Tau Beta Pi, Engineering Honor Society

Community Service Coordinator	2011-2012

Omega Phi Alpha, Community Service Sorority

Active member	2009-2011
Chapter Treasurer	2010-2011

Special Events

Diversity Summit by TMS, UCSB, Santa Barbara, CA	2018
Study Group on High Performance Materials, UCSB, Santa Barbara, CA	2018
ICMR Workshop on ... design for additive... UCSB, Santa Barbara, CA	2016
Materials Advantage Congressional Visit Days, Washington, D.C.	2016
Study Group on High Temperature Materials, UCSB, Santa Barbara, CA	2016
School on High Res. Microscopy, LeRoy Eyring Center at ASU, Tempe, AZ	2014
NanoMEGAS workshop on Precession Electron Diffraction, UCLA, L.A., CA	2013

Abstract

High Temperature Mechanical Behavior of Copper−Niobium Multilayer Composites

by

Jaclyn Taylor Avallone

Metallic multilayers are composites comprised of alternating layers of two or more metal components. Laminates with micro and nanoscale layer thicknesses have extraordinary properties when compared to the single phase metals; these advantages are due to the presence of and structural constraints imposed by bi-metal interface boundaries. High densities of bi-metal interfaces provide enhanced resistance to structural damage under irradiative and high impact shock conditions. While single phase nanocrystalline materials easily recrystallize and coarsen, metallic multilayers can maintain nanoscale microstructures at elevated temperatures. Constraints of the laminate structure and bi-metal interfaces cause this system to outperform its metallic components. Thermal instabilities can degrade this structure over time at temperature to different degrees depending on layer thicknesses.

This dissertation presents theory, experiments and modeling of high temperature behavior of copper-niobium multilayer composites made by accumulative roll bonding (ARB). Composites with different nominal layer thicknesses were assessed to characterize the influence of bi-metal interface densities and microstructure on mechanisms of deformation and structural evolution.

The creep behavior of bulk, ARB Cu-Nb multilayers was assessed at 400 °C as a function of layer thickness, ranging from 2 μm to 65 nm. Similar to single phase metallic systems, three regimes were observed during creep: transient, steady-state

and tertiary. The mechanism controlling minimum creep rate for all conditions tested has a strong dependence on stress, consistent with dislocation-dominated creep. Unlike the conventional effect of grain size on creep resistance, the unique result of this study reveals that *decreasing* length scale *increases* creep resistance.

The deformation response of ARB copper-niobium multilayers was modeled as a composite system, accounting for the behavior of Nb and Cu phases individually. The model assumes a continuous laminate structure of 50 % Cu and 50 % Nb in which deformation is controlled by stage II creep for the copper ($\dot{\epsilon}_{cr} = A\sigma^n$) and plasticity in Nb. The results identify regimes in which composite steady-state creep at constant stress can be achieved, and illustrates that strain-hardening in the niobium plays a critical role in the transient response of the multilayer, which can dominate the creep lifetime. The combination of experiments and models strongly suggest that dislocation climb mechanisms in the copper control the time-response at 400 °C for all layer thicknesses tested.

Heat treatments were performed at high temperatures for copper (0.50-0.57 T_m), but at which niobium diffusivity is limited (0.25-0.28T_m). Annealing times range from 30 minutes to 30 days at temperature. Structural evolution and hardness measurements were assessed for laminates with layer thicknesses ranging from 8 μm to 30 nm. After 30 days, 65 nm laminates remain nanostructured with no significant coarsening. Voids at bi-metal interfaces grow larger and more frequent with time; interfacial void formation is a phenomena that has not been previously reported in these systems. Analysis of structural evolution mechanisms and system stability will be discussed in relation to microstructure, thermal property mismatch, and the driving force for copper recrystallization.

Contents

Title Page **i**

Curriculum Vitae **xi**

Abstract **xvii**

Contents **xix**

List of Figures **xxiv**

List of Tables **xxx**

1 Introduction **1**

1.1 Metallic Multilayer Composites 1

1.1.1 Structural Applications in Extreme Environments 2

1.1.2 Cu-Nb Model System 5

1.2 Accumulative Roll Bonded Cu-Nb 7

1.2.1 Need for ARB 8

1.2.2 Multi-stack Clad ARB Process Method 9

1.2.3 Structure Characterization 11

1.2.4 Cu-Nb Interfaces 22

1.3 Mechanical Behavior 27

1.3.1 Variations with Length Scale . . . 27
1.3.2 Insight from PVD Mechanical Tests . . . 28
1.3.3 Anisotropy . . . 30
1.4 Thermal Behavior . . . 34
1.4.1 Structural stability . . . 34
1.4.2 Texture Evolution . . . 35
1.4.3 Driving Forces For Microstructure Degradation . . . 36
1.4.4 Layer Instability Mechanisms . . . 38
1.4.5 Groove Theory . . . 40
1.5 Objectives and Approach . . . 45

2 Experimental Procedures **46**
2.1 Sample Preparation . . . 46
2.1.1 Metallographic preparation . . . 46
2.1.2 TEM sample preparation . . . 48
2.2 Microscopy Procedure . . . 57
2.2.1 Scanning Electron Microscopy . . . 57
2.2.2 Scanning Transmission Electron Microscopy . . . 58
2.3 Heat Treatment Procedure . . . 63
2.4 Creep Testing Procedure . . . 64
2.4.1 Design of Experiment . . . 64
2.4.2 Set-Up and Procedure . . . 67
2.4.3 Optical Strain Tracking . . . 72
2.4.4 Creep Rate Fitting . . . 74
2.5 Hardness Procedure . . . 74
2.6 High Temperature Tensile Procedure . . . 76

3 Cu-Nb Creep **78**

3.1 Background . . . 79

3.2 Relevant Experimental Details . . . 79

3.2.1 Creep Behavior . . . 80

3.2.2 Structure Evolution During Creep . . . 84

3.2.3 Composite Failure . . . 86

3.3 Discussion . . . 89

3.4 Conclusions . . . 94

4 Model for Creep Deformation **95**

4.1 Relevant Experimental Details . . . 96

4.2 Tension and Creep Behavior at 400 °C . . . 98

4.3 The Laminate Creep Model . . . 100

4.3.1 Basis and Assumptions . . . 100

4.3.2 Details . . . 105

4.4 Comparison of Modeling and Experiments . . . 107

4.5 Discussion . . . 111

4.5.1 Creep Mechanism . . . 111

4.5.2 Impact of Inhomogeneity . . . 115

4.6 Summary and Conclusions . . . 118

5 Structural Evolution **120**

5.1 Background . . . 121

5.2 Relevant Experimental Details . . . 122

5.2.1 Recovery Anneal . . . 123

5.2.2 2 Day Anneal: Varied Length Scales . . . 124

5.2.3 30 Day Anneal: 65 nm laminates over time . . . 132

5.3 Discussion . . . 139
5.3.1 Texture and recrystallization . . . 139
5.3.2 Layer morphology . . . 141
5.3.3 Temperature effects and thermal stresses . . . 143
5.4 Summary and Conclusions . . . 145

6 Conclusions and Outstanding Questions **147**

6.1 Summary and Conclusions . . . 147
6.1.1 Creep . . . 148
6.1.2 Structural evolution . . . 150
6.2 Outstanding Questions . . . 153
6.2.1 Structure Evolution . . . 153
6.2.2 Creep . . . 154
6.2.3 Pre-existing Conditions . . . 155
6.2.4 Dislocations . . . 155

Experimental Procedures: Appendix **156**

2.A FIB Daily Procedure . . . 156
2.B TITAN Daily Alignment . . . 162
2.C Creep Procedure Code . . . 165
2.C.1 AutoHotKey Image capture with DigiCamControl . . . 165
2.C.2 Image J Processing . . . 166
2.C.3 Matlab Strain Tracking . . . 167
2.C.4 Matlab Creep Spline Fitting . . . 171

Cu-Nb Creep: Appendix **176**

3.A As Rolled Cu-Nb creep 177
3.A.1 Micrographs of 65 nm Cu-Nb Interrupted Creep 178
3.A.2 Post-failure Micrographs of 65 nm Cu-Nb 185
3.A.3 Micrographs of 200 nm Cu-Nb Interrupted Creep 192
3.A.4 Post-failure Micrographs of 200 nm Cu-Nb 200
3.B "Heat treated" Cu-Nb creep at 400 °C 205
3.B.1 Post-failure Micrographs of 65HT 205
3.B.2 Creep Curves 211
3.C "As rolled" Cu-Nb creep at 500 °C 213
3.C.1 Post-failure Micrographs of 200 nm Cu-Nb 214
3.C.2 Creep Curves 221

Structural Evolution: Appendix **223**

5.A 65 nm Anneal Micrographs 223
5.A.1 2 Days at 400 °C 223
5.A.2 5 Days at 400 °C 225
5.A.3 15 Days at 400 °C 231
5.A.4 15 Days at 500 °C 235
5.A.5 30 Days at 400 °C 241
5.A.6 30 Days at 500 °C 248
5.B Single Crystal Anneal: 2 h at 800 °C 249
5.C 8 μm EBSD 257
5.D 28 nm Anneal: 2 Days at 400 °C 259

Bibliography **261**

List of Figures

1.1 ARB Cu-Nb Multilayers 2

1.2 Cu-Nb multilayer structure in extreme environments 3

1.3 Nuclear reactor environments 4

1.4 Phase diagram for Cu and Nb 6

1.5 ARB Process Schematic 9

1.6 As rolled texture variation with length scale 12

1.7 As rolled grain structure variation with length scale 14

1.8 Transitions in ARB grain structure 15

1.9 Cu-Nb ARB grain size distributions 16

1.10 As rolled layer structure 17

1.11 Table of layer thickness distributions 19

1.12 Finite element simulation of rolling a Cu-Nb bilayer 20

1.13 Process induced structures: deformation twins and shear bands . . 21

1.14 Comparison of PVD and ARB 23

1.15 Typical ARB interface structures 24

1.16 Interface variation due to cross-rolling 25

1.17 Deformation mechanism transitions with layer thickness 26

1.18 Tensile behavior anisotropy 31

1.19 Kink Band Micrographs 33

1.20 ARB Cu-Nb texture evolution with temperature 35

1.21 Instability Mechanisms 37
1.22 Pinch-off Mechanism 40
1.23 Groove Depth Over Time 41

2.1 Challenges of SEM sample preparation 47
2.2 Equipment for TEM sample preparation 49
2.3 Challenges of PIPS sample preparation 50
2.4 Steps of FIB sample preparation 55
2.5 Challenges of FIB sample preparation 56
2.6 (S)TEM camera length schematic 59
2.7 Comparison of TEM and (S)TEM 60
2.8 LAADF contrast change with tilt angle 61
2.9 Custom grips for sheet geometry 65
2.10 Creep frame set-up 66
2.11 Cu and Nb creep mechanism maps 68
2.12 Dogbone sample geometry 69
2.13 Image processing of sample gauge section 73
2.14 Vicker's hardness schematic 75
2.15 High temperature tensile test conditions 77

3.1 Creep results: strain over time for standard and jump tests 81
3.2 Experimental minimum creep rates 82
3.3 Normalized strain rates with stress and length scale dependence . . 83
3.4 Creep structure evolution 85
3.5 2 μm laminate layer structure before and after creep 87
3.6 Creep failure overview 88
3.7 Cu and Nb creep mechanism maps 90

4.1 Laminate structure, 400 °C tensile tests, and strain hardening fit . . 97
4.2 Creep curves with varied stress and length scale 99
4.3 Map of conditions necessary for steady-state behavior 100
4.4 Creep curves with transient fits 109
4.5 Experimental minimum creep rates with predictions 110
4.6 Experimental minimum creep rate as a function of Cu stress 113
4.7 Voids in crept 65 nm laminates 116

5.1 As rolled and recovery annealed results: tensile and hardness data . 123
5.2 Hardness for 2 day anneals at 400 °C and 500 °C 125
5.3 Layer structures after 2 day anneal at 500 °C 126
5.4 8 μm layer structure AR and annealed at 400 and 500 °C for 2 days 127
5.5 8 μm grains AR and annealed at 400 and 500 °C for 2 days 128
5.6 2 μm Cu grains AR and annealed at 400 and 500 °C for 2 days . . 129
5.7 30nm Laminate: As rolled v. 2 Days at 400°C 130
5.8 Hardness for 65 nm layer thickness laminates over time 131
5.9 65 nm laminate evolution: variation over time 133
5.10 65 nm laminate evolution: variation with temperature 134
5.11 65 nm laminate grain structure evolution 136
5.12 65 nm laminate layer structure evolution 137
5.13 Voids in 65 nm laminate 138
5.14 Stability Map for 400 °C and 500 °C 142

3.A.1 i 65 nm Interrupted Overview 179
3.A.1 ii 1: 65 nm Interrupted Large Area 180
3.A.1 iii 2: 65 nm Interrupted Large Area 181
3.A.1 iv 3: 65 nm Interrupted Large Area 182

3.A.1 v 4: 65 nm Interrupted Large Area 183
3.A.1 vi 65 nm Interrupted Close-up 184
3.A.2 i 1: 65 nm Post Failure Large Area 186
3.A.2 ii 2: 65 nm Post Failure Large Area 187
3.A.2 iii 3: 65 nm Post Failure Large Areas 188
3.A.2 iv 1: Crept 65 nm Close-up 189
3.A.2 v 2: Crept 65 nm Close-up 190
3.A.2 vi Crept 65 nm Voids 191
3.A.3 i Large Area: Interrupted 200 nm 193
3.A.3 ii 1: Interrupted 200 nm Tilt Series 194
3.A.3 iii 2: Interrupted 200 nm Tilt Series 195
3.A.3 iv 3: Interrupted 200 nm Tilt Series 196
3.A.3 v Pinch off in Interrupted 200 nm 197
3.A.3 vi Interrupted 200 nm Voids 198
3.A.3 vii 200 nm Interrupted Close-up 199
3.A.4 i 1: 200 nm Post Failure Overview 201
3.A.4 ii 2: 200 nm Post Failure Overview 202
3.A.4 iii Crept 200 nm Tilt series 203
3.A.4 iv Crept 200 nm Interface Voids 204
3.B.1 i Overview of HT 65 nm Post Failure 206
3.B.1 ii Crept HT 65 nm Local Kink 207
3.B.1 iii 1: Crept HT 65 nm Tilt Series 208
3.B.1 iv 2: Crept HT 65 nm Tilt Series 209
3.B.1 v 3: Crept HT 65 nm Tilt Series 210
3.B.2 i Creep Curves of Heat Treated Cu-Nb 211
3.B.2 ii Minimum Creep Rates Heat Treated v As Rolled 212

3.C.1 i 1: 200 nm Post Failure (500 °C) Large Area 215
3.C.1 ii 2: 200 nm Post Failure (500 °C) Large Area 216
3.C.1 iii 3: 200 nm Post Failure (500 °C) Large Area 217
3.C.1 iv 1: Crept 200 nm (500 °C) Pinch off 218
3.C.1 v Crept 200 nm (500 °C) Evolution 219
3.C.1 vi Crept 200 nm (500 °C) Shear Band 220
3.C.2 i Creep Curves at 500 °C 221
3.C.2 ii Minimum Creep Rates 500 °C v 400 °C 222

5.A.1 i 65 *nm* Annealed 2 days at 400 °C 224
5.A.2 i 1: 65 *nm* Annealed 5 days at 400 °C 226
5.A.2 ii 2: 65 *nm* Annealed 5 days at 400 °C 227
5.A.2 iii 3: 65 *nm* Annealed 5 days at 400 °C 228
5.A.2 iv Overview of 65 *nm* Annealed 5 days at 400 °C 229
5.A.2 v Zoom: 65 *nm* Annealed 5 days at 400 °C 230
5.A.3 i 1: 65 *nm* Annealed 15 days at 400 °C 232
5.A.3 ii 2: 65 *nm* Annealed 15 days at 400 °C 233
5.A.3 iii 3: 65 *nm* Annealed 15 days at 400 °C 234
5.A.4 i 1: 65 *nm* Annealed 15 days at 500 °C 236
5.A.4 ii 2: 65 *nm* Annealed 15 days at 500 °C 237
5.A.4 iii 3: 65 *nm* Annealed 15 days at 500 °C 238
5.A.4 iv Zoom: 65 *nm* Annealed 15 days at 500 °C 239
5.A.4 v Zoom: 65 *nm* Annealed 15 days at 500 °C 240
5.A.5 i 1: 65 *nm* Annealed 30 days at 400 °C 242
5.A.5 ii 2: 65 *nm* Annealed 30 days at 400 °C 243
5.A.5 iii 3: 65 *nm* Annealed 30 days at 400 °C 244

5.A.5 iv Tilt Series 1: 65 nm Annealed 30 days at 400 °C 245
5.A.5 v Tilt Series 2: 65 nm Annealed 30 days at 400 °C 246
5.A.5 vi Zoom: 65 nm Annealed 30 days at 400 °C 247
5.A.6 i Overview of 65 nm Annealed 30 days at 500 °C 250
5.A.6 ii 1: 65 nm Annealed 30 days at 500 °C 251
5.A.6 iii 2: 65 nm Annealed 30 days at 500 °C 252
5.A.6 iv 3: 65 nm Annealed 30 days at 500 °C 253
5.A.6 v Tilt Series 1: 65 nm Annealed 30 days at 500 °C 254
5.A.6 vi Tilt Series 2: 65 nm Annealed 30 days at 500 °C 255
5.B.i Single Crystal Anneal 256
5.C.i EBSD of 8 μm Grain Evolution with Anneal 258
5.D.i 28 nm Annealed 2 days at 400 °C 260

List of Tables

1.1 Cu and Nb constant values used in calculations 7

4.1 Strain hardening parameters for Cu-Nb at 400 °C 103

4.2 Fit Cu creep parameters: ($\dot{\epsilon_o}$,n) 111

4.3 Dislocation climb calculations 114

5.1 Hardness for laminates: as rolled and annealed 30 min at 400 °C . . 123

5.2 Hardness for 2 day anneals at 400 °C and 500 °C 125

5.3 Hardness for 65 nm layer thickness laminates over time 131

5.4 Thermal Expansion Stresses 144

3.i Summary of All Creep Tests 176

3.A.i As Rolled Creep Tests at 400 °C 177

3.B.i Heat Treated Creep Tests at 400 °C 205

3.C.i As Rolled Creep Tests at 500 °C 213

Chapter 1

Introduction

1.1 Metallic Multilayer Composites

Metallic multilayers, often called laminates, are composites comprised of at least two metallic components stacked in alternating layers. The structure of metallic laminates can be tailored for specific applications by varying metallic components, volume fractions of components, layer thicknesses, textures, and processing methods.

Decreasing the layer thickness increases the area of bi-metal interfaces, and eventually, interface area exceeds the area of single-phase grain boundaries. Many advantageous properties of metallic multilayers (when compared to single phase materials) are due to the presence of and structural constraints imposed by bi-metal interface boundaries. Particularly, small length scale multilayers (micro- and nanolaminates) can be dominated by interfacial behaviors [1–4].

Optical micrographs of the copper−niobium (Cu−Nb) system of interest in this dissertation are shown in Figure 1.1. This bi-metallic system has a 50 %

volume fraction of each phase, and the layer thickness was systematically varied in processing. The nominal layer thicknesses of laminates investigated in this work range from 8 μm down to 28 nm : 480 bi-metal interfaces down to over 150,000 interfaces through thickness of a 4 mm sheet.

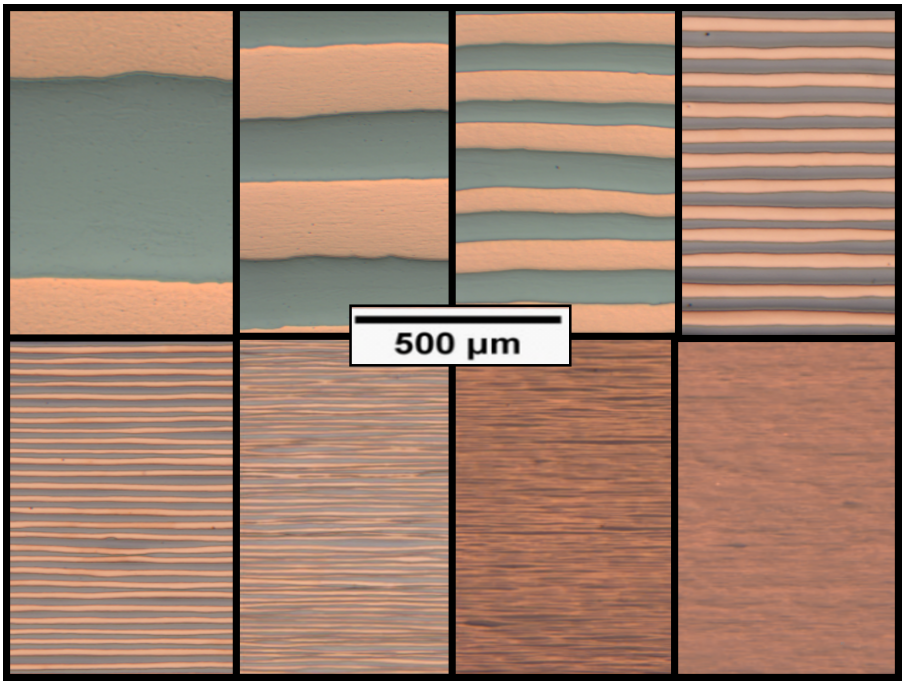


Figure 1.1: ARB Cu-Nb multilayers are shown with decreasing layer thicknesses. These optical micrographs were taken by Thomas Nizolek.

1.1.1 Structural Applications in Extreme Environments

Metallic multilayer composites have remarkable microstructural stability in severe environments. Point defects created by irradiation combine and annihilate at bi-metal interfaces, rather than coalescing to form voids as they would in single phase materials [5–9]. Similarly, defects created by high impact shock waves are absorbed at bi-metal interfaces, leaving negligible structural damage to the composite [10, 11]. In stark contrast to single phase nanocrystalline metals, nanoscale

multilayers maintain morphological stability at elevated temperatures (even up to $0.8T_m^{Cu}$) [12–16]. Structures are shown before and after exposure to these extreme environments in Figure 1.2. The strength of these laminates can greatly exceed that of the individual metallic components at room temperature: yield and flow stresses increase with decreasing laminate length scale according to a Hall-Petch relationship, discussed further in section 1.3 [17, 18].

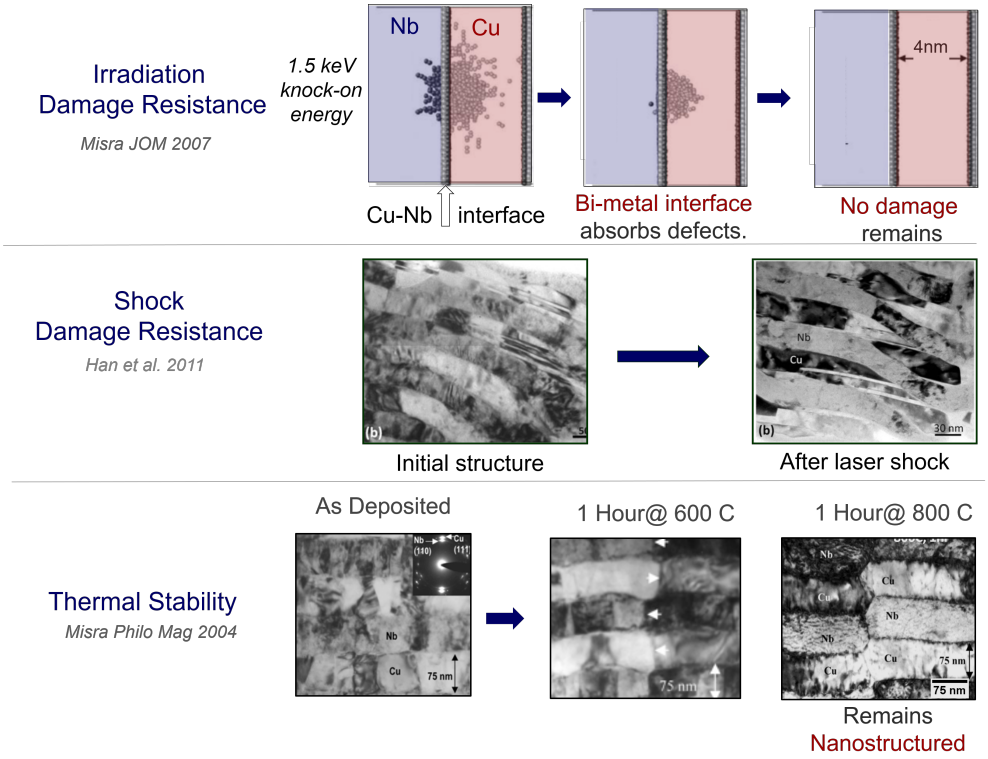


Figure 1.2: Cu-Nb multilayer structure in extreme environments: irradiation, laser shock, and elevated temperatures. (Top [19], Middle [20], Bottom [5])

This combination of properties makes metallic laminate promising candidate material for structural components exposed to extreme conditions. For example, future nuclear reactor designs require materials that can withstand irradiation and temperature extremes far in excess of the structural materials currently used for these applications. Figure 1.3 is a comparison of various nuclear reactor designs

with respect to irradiation dosage and operating temperature. Clearly, material improvements are needed to accommodate the advancement in nuclear technologies.

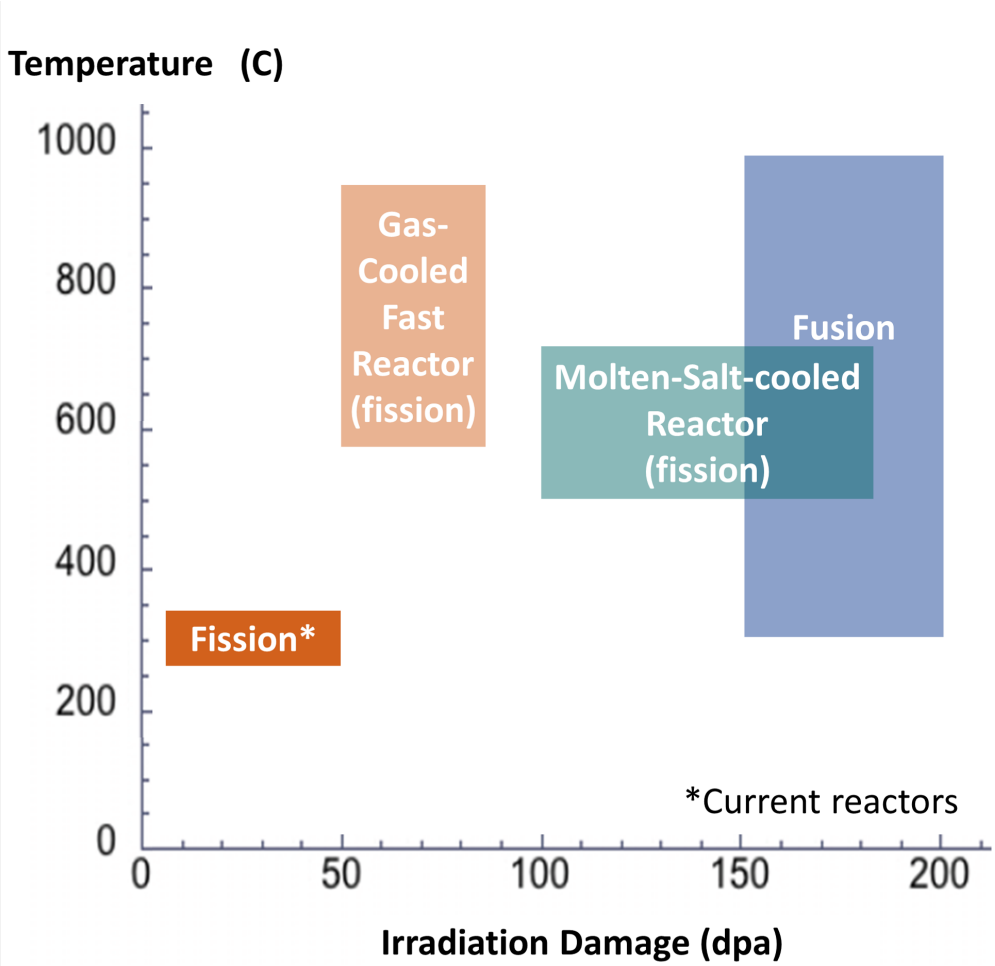


Figure 1.3: The schematic shows operating conditions for various nuclear reactor model types. The Fission* region represent current models, where as the other reactors (in more extreme environments) are future models. This Figure was reproduced from Reference [21]

Enhanced structural stability in such severe environments is associated with the high density of sharp bi-metallic interfaces, particularly those which form preferential low energy boundaries [22–24]. Bi-metal interfaces are imperfect sinks, or that the flux of vacancies and atoms is approximately equal [25]. They can initiate, terminate, and store dislocations [1,26–28]. The relative area of single phase bound-

aries decreases and that of phase interfaces increases with decreasing laminate layer thickness. This creates interesting opportunities to tailor properties by balancing behavior of metal constituents with interface-dominated behavior [1, 22, 29].

The motivation for investigating thermal stability and high temperature mechanical behavior of multilayer systems stems from their potential use as structural components in nuclear reactors which operate at elevated temperature. The copper-niobium (Cu-Nb) system is a model laminate to understand the role of low energy interfaces on creep properties and thermal stability of structure.

1.1.2 Cu-Nb Model System

Cu and Nb are immiscible metals, therefore bi-metal interfaces are atomically sharp. The phase diagram for this system, Figure 1.4, shows that there is no solubility up to 900 °C, and even then solubility is very limited up to the melting point of copper. It is important to note the variation in melting temperatures between the two phases, and similarly the thermal properties. The coefficients of thermal expansion of Cu and Nb are $16.5 \times 10^{-6}\ K^{-1}$ and $7.3 \times 10^{-6}\ K^{-1}$, respectively [30, 31].

The Cu-Nb system is a good model system to explore experimentally because of the preferential low-energy interfaces created by face-centered-cubic (FCC) and body-centered-cubic (BCC) metals. Interface character, energies, and defect interaction behavior are reported in literature for several orientation relationships which are commonly found in the ARB Cu-Nb system: notably Kurdjumov-Sachs (K-S) and Nishiyama-Wassermann (N-W), $\{112\}\langle 110\rangle$Cu//$\{112\}\langle 111\rangle$Nb and $\{110\}\langle 111\rangle$Cu//$\{001\}\langle 110\rangle$Nb, respectively [29, 33]. Dislocation motion [2, 27, 28, 34–39], as well as resistance to irradiation [6, 7, 9, 40, 41] and high impact shock

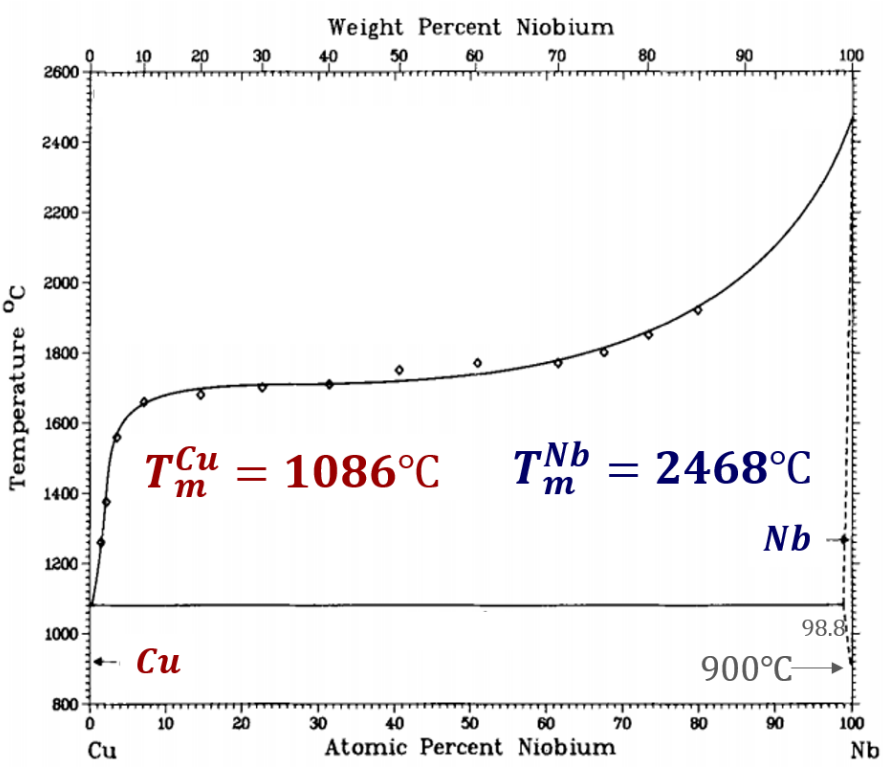


Figure 1.4: This is the phase diagram for Cu and Nb. [32]

[20, 42] has been studied and modeled extensively for these interface orientation relationships. Major insights are that low energies interfaces act as sinks allowing defects to annihilate, leaving little to no damage to the laminate structure, and therefore higher interface densities improve damage resistance of multilayers.

Cu and Nb have similar Young's moduli (120 GPa and 105 GPa, respectively) and flow stresses at room temperature[1]. For this reason, processing by accumulative roll bonding (ARB) can yield a 50-50 composite with well-bonded bi-metal interfaces [24, 43, 44]. All constant material values used for calculations in this document are tabulated below:

[1]Initial sheet material, with rolled texture and coarse polycrystalline structure, for Cu and Nb have flow stress of 150 MPa and 190 MPa, respectively [3]

Property	Copper (Cu)	Niobium (Nb)
Young's Modulus E (GPa)	120	105
Shear Modulus G (GPa)	48	38
Poisson's Ratio ν	.34	.40
Burgers Vector b (nm)	.255	.286
Atomic Volume Ω (m^3)	1.1×10^{-29}	4.2×10^{-29}
Melting Temperature T_m (K)	1359 [32]	2741 [32]
Coeff. of Thermal Expansion α (K^{-1})	16.5×10^{-6} [30]	7.3×10^{-6} [31]
Lattice Diffusion Coeff. D_l (m^2/s)	$(7 \pm 30 \times 10^{-5})\, e^{-\frac{Q_l}{RT}}$ [45]	$(6.1 \pm 4 \times 10^{-5})\, e^{-\frac{Q_l}{RT}}$ [46]
Activation Energy Q_l (kJ/mol)	~ 200	397-478 [13, 46–48]
Grain Boundary Diffusion Coeff. D_{gb} (m^2/s)	$(3 \times 10^{-19})\, e^{-\frac{Q_{gb}}{RT}}$ [49]	$(1.1 \times 10^{-11})\, e^{-\frac{Q_{gb}}{RT}}$ [13, 47]
Activation Energy Q_{gb} (kJ/mol)	$61.7 - 92.3$ [49, 50]	263 [47]

Table 1.1: Cu and Nb constant values used in all calculations. Unlabeled values are from reference [51]. Multiple references may have been used to calculate values.

1.2 Accumulative Roll Bonded Cu-Nb

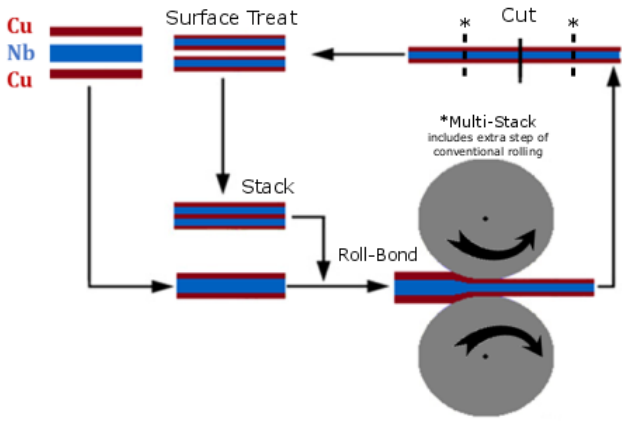
The process of roll bonding is not trivial and cannot successfully produce laminates with all metallic systems. In addition to rolling reduction and surface preparation, the inherent material characteristics influence the difficulty of roll bonding metals. Many dissimilar metals with face-centered-cubic crystal structures have been successfully roll bonded [52]. However, few combinations of metals with differing crystal structures have similar enough deformation behavior to create a successful bond.

The laminates investigated in this dissertation were created at Los Alamos National Laboratory (LANL) by Nizolek and Scott in 2012 [53]. This section will discuss the need for this bulk processing method, details of processing for the material used, characterization of ARB microstructure, and a comparison of other processing methods to that outlined here.

1.2.1 Need for ARB

Mechanical properties of bi-metallic laminates have been characterized for a variety of vapor deposited thin-film systems [8, 50, 54]. Authors have explored the effects of interfacial density and temperature on thin film laminate hardness and strength [13,26,55,56]. The structural performance of bulk material cannot be predicted accurately by micromechanical testing of thin films because they are highly dependent on surface effects and have geometric limitations in design of mechanical testing experiments. As previously mentioned, the application of interest for these metallic multilayers is structural. Ideally, materials should consist of high temperature metallic phases with high densities of low energy bi-metallic interfaces, processed in bulk by conventional wrought processing methods. For this reason, accumulative roll bonding (ARB), an industrially scalable method to produce bulk material [53], was selected for laminate production. The ARB process affords control over three orders of magnitude variation in the microstructural scale of the laminate and grain structures: initially 2 mm thick sheets, and processed down to 9 nm thick layers [43, 53]. ARB laminates will be referenced with respect to the orthogonal directions associated with the geometry of rolling: normal to the sheet (ND), in the rolling direction (RD), and transverse to the rolling direction (TD).

1.2.2 Multi-stack Clad ARB Process Method



Number of Bi-metallic Interfaces	480	1,920	19,200	38,400	64,512	153,600
Layer Thickness (nm)	8,000	2,000	200	100	65	28
General Grain Structure	Multiple grains through thickness		All grains touch bi-metal interface		Single Crystal layers	

Figure 1.5: Schematic shows the "copper-clad" accumulative roll bonding process used to produce the materials in this table. As shown, all Cu-Nb interfaces were created in the first processing step, with subsequent steps bond copper to copper. Multi-stack processing involves an additional conventional rolling step, and additional cuts to maintain 4 mm sheet thickness. Six layer thicknesses, the number of interfaces associated with these laminates, and the transition in grain structures are shown in this table. Note: all laminates have a sheet thickness of approximately 4 mm. [43]

Accumulative roll bonding is a severe plastic deformation process in which bulk sheets of metal are joined by co-deformation. Cu and Nb are roll-bonded together at about $50-60$ % reduction per pass. Deformation is equal in both phases because these metals have similar room temperature flow behavior. The ARB process has gone through several development iterations to fine-tune details and produce the most uniform structures to date. The notable innovations by the ARB team at LANL are Cu-clad sheet geometries, multi-stack roll bonding, lower roughness sur-

face treatments, and guides for alignment [57]. The schematic in Figure 1.5 shows the full processing procedure as a loop.

The Cu-clad method creates all Cu-Nb bonds during the first roll-pass by sandwiching the Nb layer (2 mm) between two Cu half-layers (1 mm). All bi-metal interfaces experience the same total strain as a result of this process. Cu-Cu interface bonds therefore see variable amounts of strain, but continuous recrystallization during rolling heals the majority of those Cu layers [58]; the most recently bonded interface are at the most risk of unsuccessful bonding.

The bonded laminates are cut, stacked, and subsequently roll-bonded several times, until the desired layer thicknesses are achieved. To decrease processing time, the multi-stack method was implemented. After initial roll bonding, subsequent conventional rolling steps are added, and the thin, rolled sheet is cut at multiple points to create 3, 4 ,or 5 sheets. With the goal of keeping final sheet thickness to about 4 mm for laminates of all length scales, this procedure varied depending on the desired final layer thickness.

Before each roll bonding step, metallic surfaces are cleaned thoroughly[2], and wire brushed to increase surface roughness and facilitate roll bonding. Previous iterations of the ARB process at LANL used a coarse wire brush that resulted in an aggressive surface roughness and significant flaws associated with burrs and by product particulates (note: these flaws will be discussed further in Section 1.2.3). Introducing a finer wire brush greatly reduced these flaws and increased the uniformity of the multilayers macroscopically.

The rolling mills at LANL are larger than laboratory scale, but not of the capacity required for industry. High loads (necessary for large reductions) can cause roll deflection and non-uniform distributions of load on the rolled sheets. Non-

[2]Acetone is used to remove any grease accumulated by the rolling mill

uniform rolling of sheets can increase the tendency for bending, splitting, buckling, and edge cracking of bulk sheets. By adding fixed plates to the rolling mill as a guide for material prior to bonding, the LANL team increased yield and consistency of ARB materials.

1.2.3 Structure Characterization

Initial (as rolled, or AR) microstructures influence thermal and mechanical properties significantly. The grain and layered structures of ARB laminates are less "ideal" than deposited multilayers in both grain and layer structures. The ARB process results in non-uniformities within a given layer thickness laminate, texture anisotropy associated with rolling and co-deformation, as well as a variations with laminate length scale (i.e. more processing steps). The bulk processing approach can result in the presence of rolling defects, shear localization, a distribution of layer thickness, and elongated grains within individual layers [3, 24, 59].

A very important aspect of ARB is that laminates of smaller final length scales have experienced more processing steps and thus larger amounts of strain. With every roll pass: texture evolves, grain structure evolves, and processing flaws exaggerate non-uniformities in the layer structure.

Texture

The strong texture components found in Cu-Nb multilayer systems increase with decreasing layer thickness [17, 33]. Orientations of Cu and Nb crystals associated with stable interfaces correspond to some of the traditional FCC and BCC rolling textures as well as some recrystallization textures [60,61]. Therefore, texture evolution in rolling strengthens these textures and increases the area of stable interface

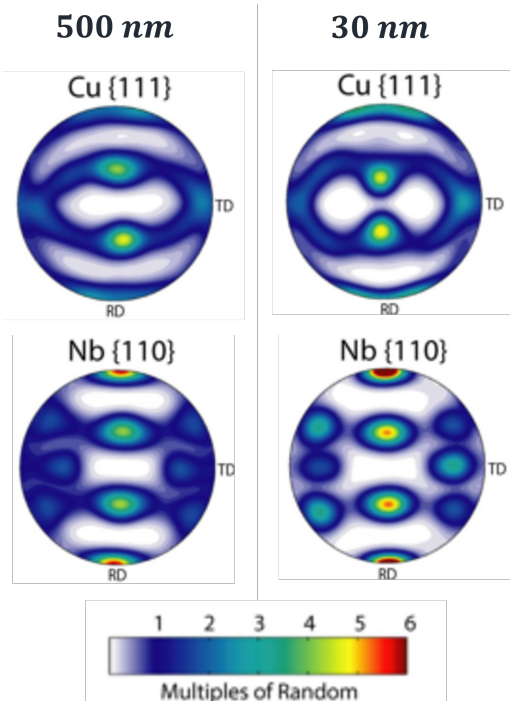


Figure 1.6: Pole Figures showing as rolled textures of Cu and Nb in 500 nm and 30 nm ARB Cu-Nb. [17]

boundaries. Figure 1.6 shows pole Figures of {111} Cu and {110} Nb for laminates with nominally 500 nm and 30 nm layer thicknesses for comparison. These directions are strongly correlated with each other in the rolling plane, which is the relationship associated with the low energy, Kurdjamov-sacs interface described earlier. Both larger and smaller laminates have this texture, and the it evolves as grains rotate to accommodate the 50% reduction during rolling. Therefore, as you can see from the increased PF intensity, the area of favorable interfaces increases with every processing step, and smaller length scales have stronger texture.

Continuous recrystallization occurs dynamically during rolling [33]. The ARB process introduces extremely high dislocation densities ($\sim 10^{15}\ m^{-2}$) which drive recrystallization, particularly in the Cu phase [58]. This grain structure evolution is eventually limited by the critical radius for nucleation of new grains and there

is a drop in dislocation density: Lim and Rollett measured dislocation densities in 19 μm and 200 nm laminates via transmission electron microscopy and found 1.2×10^{15} and 0.5×10^{15} $(dislocations/m^2)$ in Cu, respectively [58]. That noted, these dislocation densities are far in excess of those observed for single phase Cu.

Grain structure

Figure 1.7 shows inverse pole Figure (IPF) maps of multilayers with nominal layer thicknesses of 2000 nm, 500 nm, and 30 nm. Grain elongation occurred during rolling reduction and is notable in Nb at all layer thicknesses shown. Continuous recrystallization of the Cu phase during rolling decreases this effect in largely polycrystalline layers. At low layer thicknesses, however, all grains were constrained by Cu-Nb interfaces and grain elongation was inevitable.

Grain aspect ratios increased and the number of grains through the layer thickness decreased as the laminate length scale was decreased through processing. Below 1.5 μm layer thickness, the majority of layers are of the order of 2 grains through thickness (all confined by a bi-metal interface), and below 135 nm the majority of layers are single crystalline through thickness and deformation twinning occurs [3]. These transitions in grain structure (and subsequently interface stability) were identified by Bronkhorst *et al.* and are labeled in Figure 1.8 [3]. It is evident, however, that thin, single crystalline layers exist in "large" length scale laminates and that polycrystalline layers exist in "small" length scale laminates due to the large distribution of layer thicknesses in ARB material [24].

An interesting point about the grain structure is that the in-plane grain size, or the distance between grain boundaries transverse to the rolling direction, is very similar between varying laminate length scales. The rolling process greatly increases the aspect ratio of grains, as the grain size normal to the rolling direction

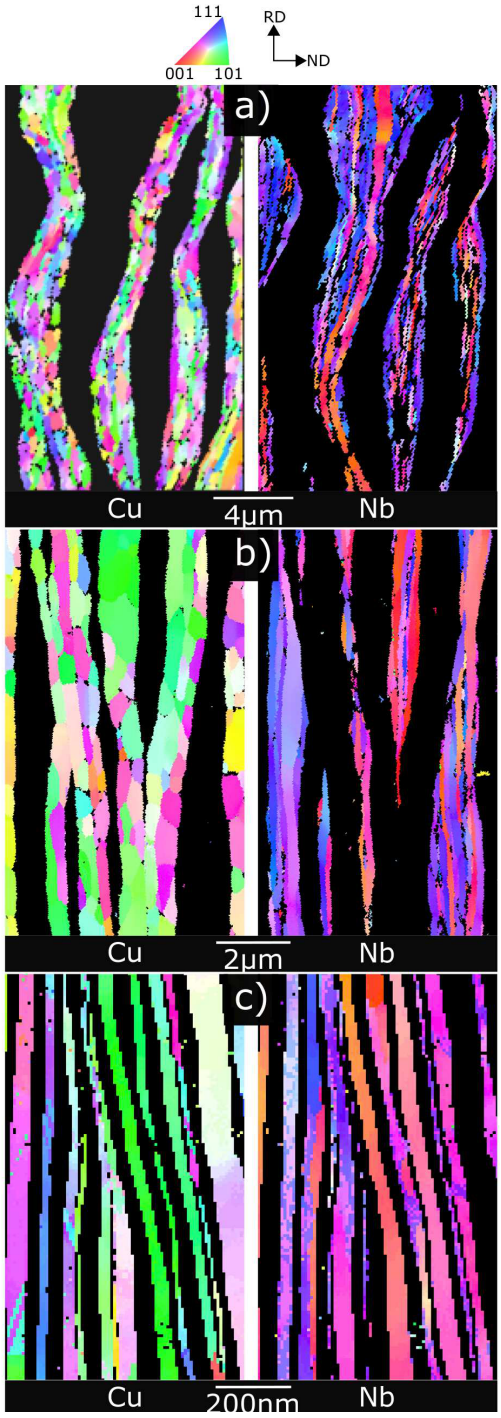


Figure 1.7: Inverse pole Figure (IPF) maps showing initial grain structures of Cu (left) and Nb (right) in (a) 2000 nm,(b) 500 nm, and (c) 30 nm ARB Cu-Nb.

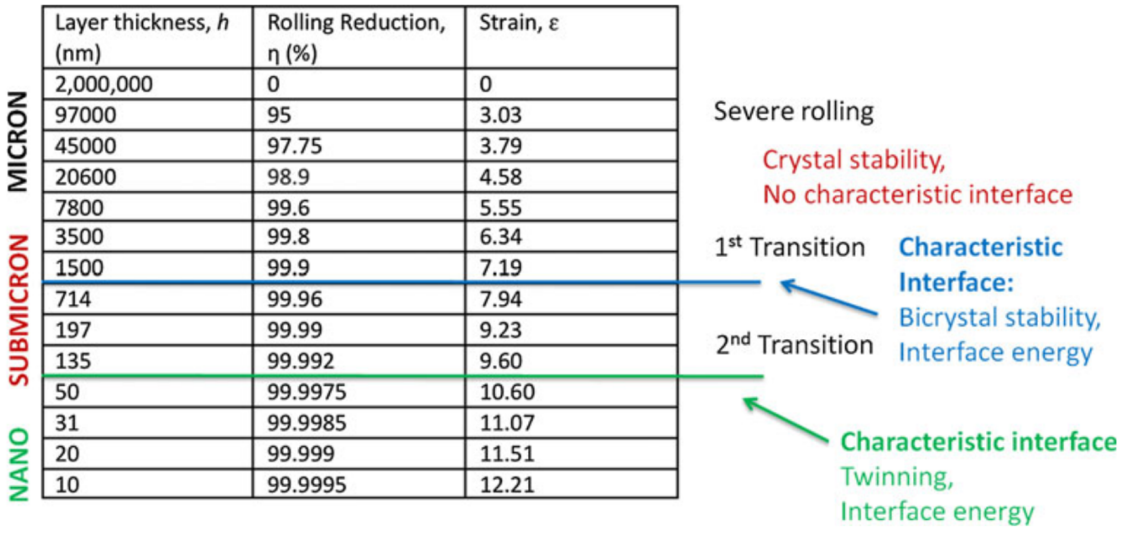


Figure 1.8: Transitions in grain structure are identified with different nominal layer thickness laminates [3].

is continuously refined. Zheng *et al.* reported that in-plane grain sizes for 58 nm and 30 nm ARB laminates were on average 2 μm for Cu grains [29]. Statistics on ARB Cu-Nb laminates or varying length scales is shown in Figure 1.9. While the grain size normal to the sheet (the direction associated with the layer thickness) decreases with processing, the grain size in-plane of the rolling direction has a Gaussian distribution for all length scales shown.

Layer structure

As rolled material contained highly continuous layers at all length scales. Variation of layer thickness was drastic, and often layers were beyond the resolution of imaging techniques (particularly EBSD). Figure 1.10 shows multilayers of nominally 8000 nm, 2000 nm, 200 nm, and 65 nm layer thicknesses with atomic contrast to discern phases: Cu is dark, Nb is light. Some notable macroscopic and local shear regions are highlighted in Figure 1.10 with arrows.

Layer thickness variation occurred at all length scales, and below 770 nm the

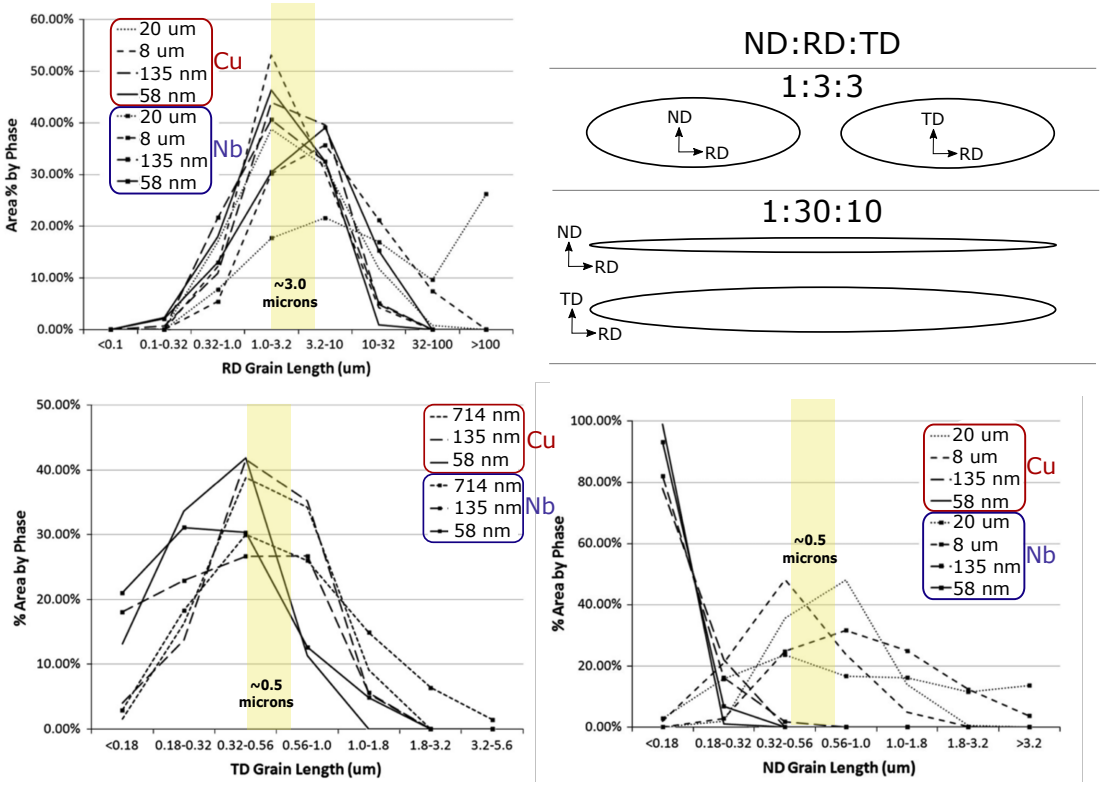


Figure 1.9: Cu and Nb grain size statistics, taken from EBSD data, is shown for various length scale laminates in the RD, TD, and ND. Schematic shows grain shapes similar to those observed in large and small layer thicknesses, $1:3:3$ and $1:30:10$, respectively [62].

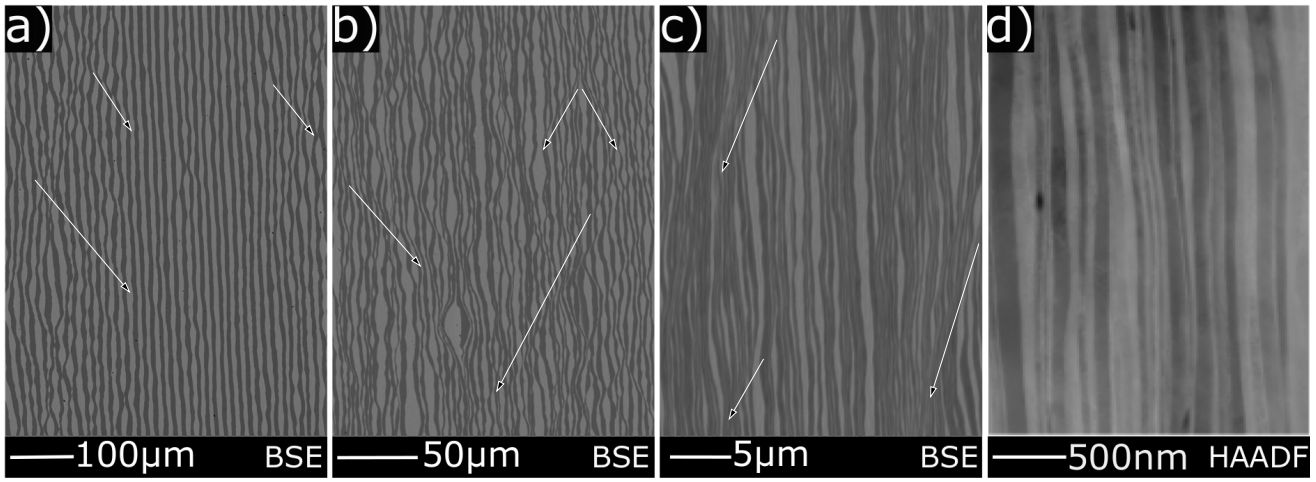


Figure 1.10: Atomic contrast micrographs showing (a) 8000 nm, (b) 2000 nm, (c) 200 nm, and (d) 65 nm laminate structures as rolled. Cu is the dark phase, Nb is the light phase. (a-c) are SEM images taken using a BSE detector. (d) is a (S)TEM image taken with a HAADF detector.

distribution changes from Gaussian to lognormal. Beyerlein *et al.* produced the table in Figure 1.11 showing the details of the statistical study determining these distributions [24]. Transition in thickness distributions are similar to the grain structure transition identifying bi-crystal stability in Figure 1.8 [3].

Variation in layer thickness in these materials is due to macroscopic shear induced by the rolling process as well as variation in deformation at the grain level. Bronkhorst *et al.* used finite element analysis to model deformation of a Cu-Nb bi-layer with grain structures and textures, matching that of ARB Cu-Nb, from 24 μm layer thicknesses reduced 50 %. Figure 1.12 shows that the local orientation variation within the polycrystalline layers produces a tortuous interface morphology as grains elongate and deform to different degrees [3].

The grain structure is dependent on the layer layer thickness, as mentioned previously. An important note, however, is that within the same nominal length scale laminate, the grain structure varies between thinner and thicker layer thickness regions, often even within the same layer.

	Average measured layer thickness (μm)		Variance (μm)			
Nominal layer thickness	Cu	Nb	Cu	Nb	Number of layers sampled	Distribution type
45.0 micrometers	47.179	42.405	37.127	54.723	99	Gaussian
20.6 micrometers	20.898	19.652	8.842	18.527	613	Gaussian
7.8 micrometers	7.875	7.704	4.937	14.288	1447	Gaussian
2.0 micrometers	2.029	1.999	0.718	2.560	975	Gaussian
1.5 micrometers	1.472	1.469	0.892	0.900	1693	Gaussian
770 nm	0.755	0.724	0.117	0.291	1400	Gaussian
200 nm	0.198	0.172	0.0173	0.0419	932	Lognormal
197 nm	0.249	0.219	0.0247	0.0822	609	Lognormal
135 nm	0.122	0.136	0.00715	0.0343	1317	Lognormal
86 nm	0.086	0.075	0.00412	0.00566	366	Lognormal
56 nm	0.052	0.038	0.00141	0.00140	800	Lognormal
30 nm	0.032	0.026	0.000353	0.000781	800	Lognormal
20 nm	0.025	0.021	0.000203	0.000396	800	Lognormal
10 nm	0.015	0.013	0.0000791	0.000135	640	Lognormal

Figure 1.11: This is a table of layer thickness statistics for various Cu-Nb multilayers produced by ARB [24].

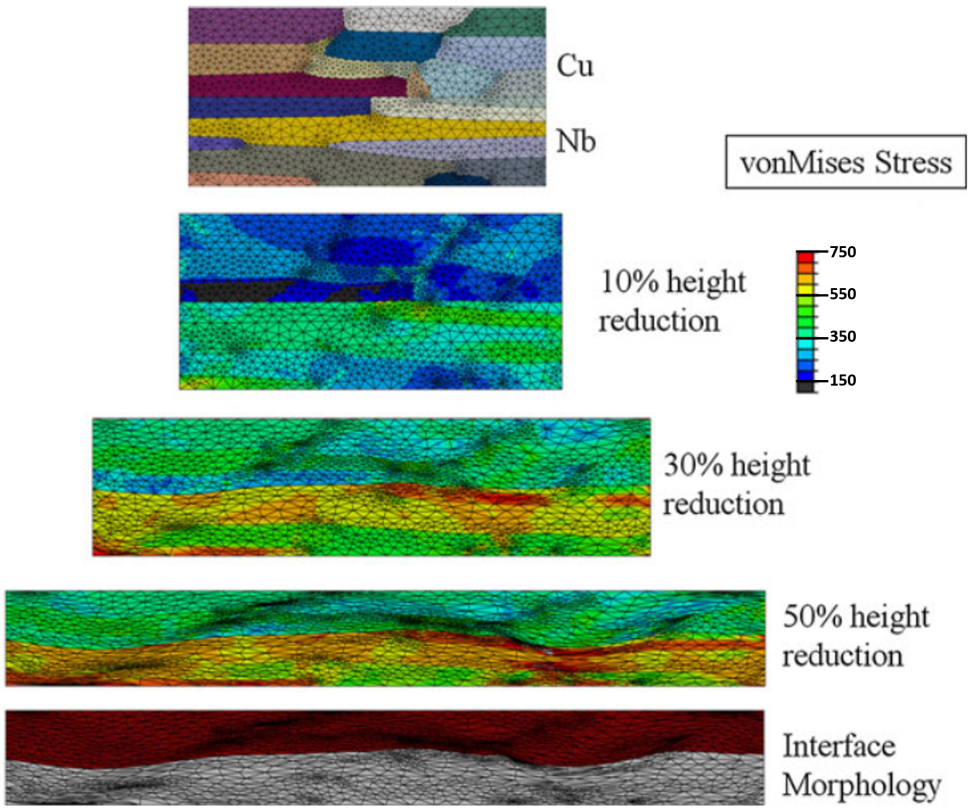


Figure 1.12: Finite element analysis simulated 50 % reduction in rolling of a Cu-Nb bilayer. Grain structures and textures are consistent with ARB Cu-Nb at 24 μm nominal layer thickness. The von Mises stress with height reduction are shown incrementally [3].

Processing Effects

Shear bands and twins are observed in rolled Cu-Nb multilayers and account for significant changes in texture at the smaller length scales [43, 58, 65]. Although macroscopic shear bands typically accompany strain softening, the shear banding observed in ARB Cu-Nb is uniformly distributed throughout the microstructure and accounts for significant strain before failure [22,24]. Both shear bands and twins are a result of the severe deformation processing path used to create the laminates for this research and exist in the AR microstructure of these materials. These aspects

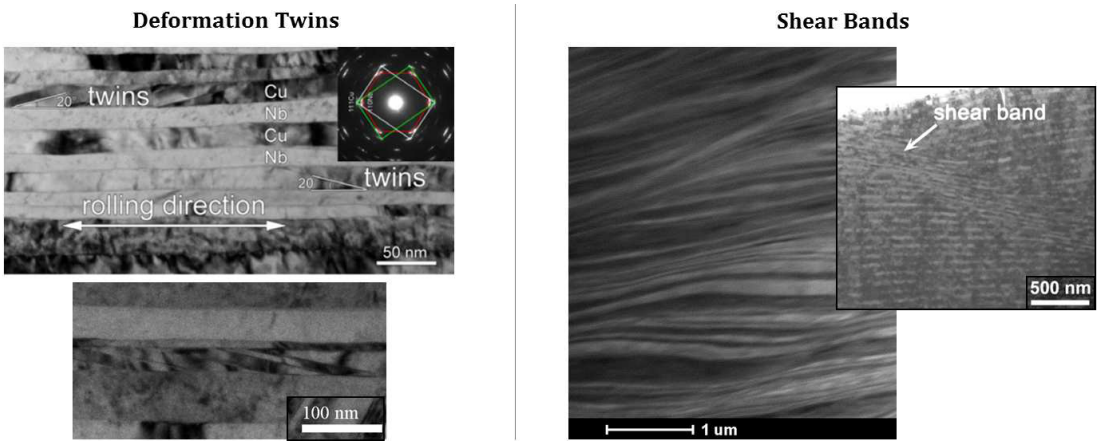


Figure 1.13: Deformation twinning occurs in copper layers during extreme strain conditions in rolling. A bright field TEM image (top) and diffraction pattern [63] indicate twins in rolled material. A STEM micrograph (bottom) shows deformation twinning in material used in this research. Twinning occurs in the Cu phase below 100 nm layer thickness. Shear bands are observed in bright field TEM (right) [64] as well as atomic contrast STEM (left). Shear bands occur at all length scales, effecting micro and macro laminate structure.

of ARB microstructure may be controlled better by future innovations to the rolling process.

Processing flaws which *must* be improved for consistent material performance are poorly bonded interfaces and rolling "inclusions". Metal particulates (by products of wirebrushing) are roll bonded into the material in error. They contribute to unsuccessful bonding of sheets in rolling and serve as stress concentrations that exacerbate shear localizations. Poorly bonded regions can result in cracks and failure initiation sites. As the roll-bond interfaces are Cu-Cu, the continued rolling of laminates and subsequent continuous recrystallization [33] of Cu greatly aids the bonding process. Most recently bonded interfaces have not co-deformed to the same strains as surrounding material, therefore the bond at that interface is not as cohesive.

1.2.4 Cu-Nb Interfaces

The production of multilayers by vapor deposition methods only yields small volumes of material and thus necessitates small sample geometries. Mechanical testing of first generation physical vapor deposited (PVD) multilayers was limited to thin film tests. Recently, mechanical testing of ARB laminate sheets [17,68] has proven that bulk ARB composites perform similar to PVD thin films [14,22,26,69], in that multilayer structures outperform the rule of mixtures for the metallic constituents and conform to a modified Hall-Petch relationship. The grain and layer structures are compared for these two methods in Figure 1.14. PVD multilayers have parallel layers throughout and columnar grains with aspect ratios close to unity; while ARB composites contain elongated grains and non-uniform layer morphologies.

Both methods produce continuous layers with sharp, low-energy interfaces with predominantly Kurdjumov–Sachs (K-S) orientation relationships [43,60]. The K-S interface character of Cu-Nb varies with processing; PVD interfaces are atomically flat, while ARB interfaces are faceted [63]. A comparison of these interfaces at the atomic level is shown in Figure 1.14.

Figure 1.15 shows additional interface orientations typically seen in ARB Cu-Nb produced by the clad multi-stack method. At small length scales, low energy orientations are maintained even when deformation twins form in Cu [70]. Another ARB method used to produce Cu-Nb in bulk is "cross rolling". This process is very similar to that described in the previous section, however between each roll-bonding step, the laminate is rotated 90 °. Rather than perpetuating rolling textures, alternate deformation paths change grain deformation and result in a different macroscopic texture and different low energy interfaces. Figure 1.16 shows

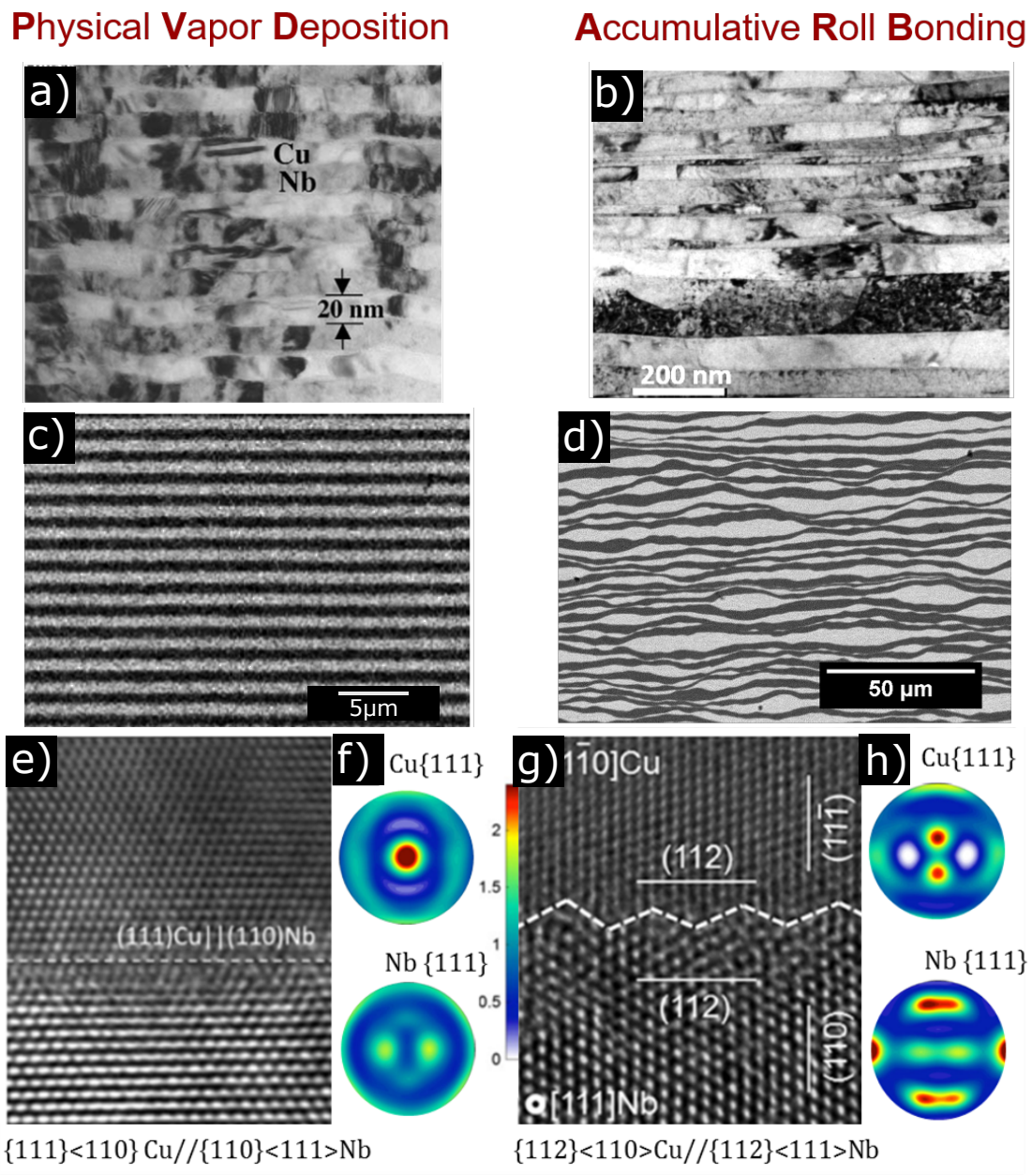


Figure 1.14: This is a comparison of PVD and ARB laminate structures. a) and b) are layered structures [66]. c) and d) are bright field TEM images of microstructures in 20 *nm* AD PVD laminates [19] and 28 *nm* AR ARB laminates, respectively. e) and g) are high resolution TEM images of the preferred K-S Cu-Nb interfaces found in PVD [67] and ARB [29] materials, respectively. f) and h) are {111} pole Figures (PF) which show the texture (bulk orientation) of 20 *nm* PVD and 18 *nm* ARB, respectively [67]. Note that inverse pole Figures in both cases have strong texture.

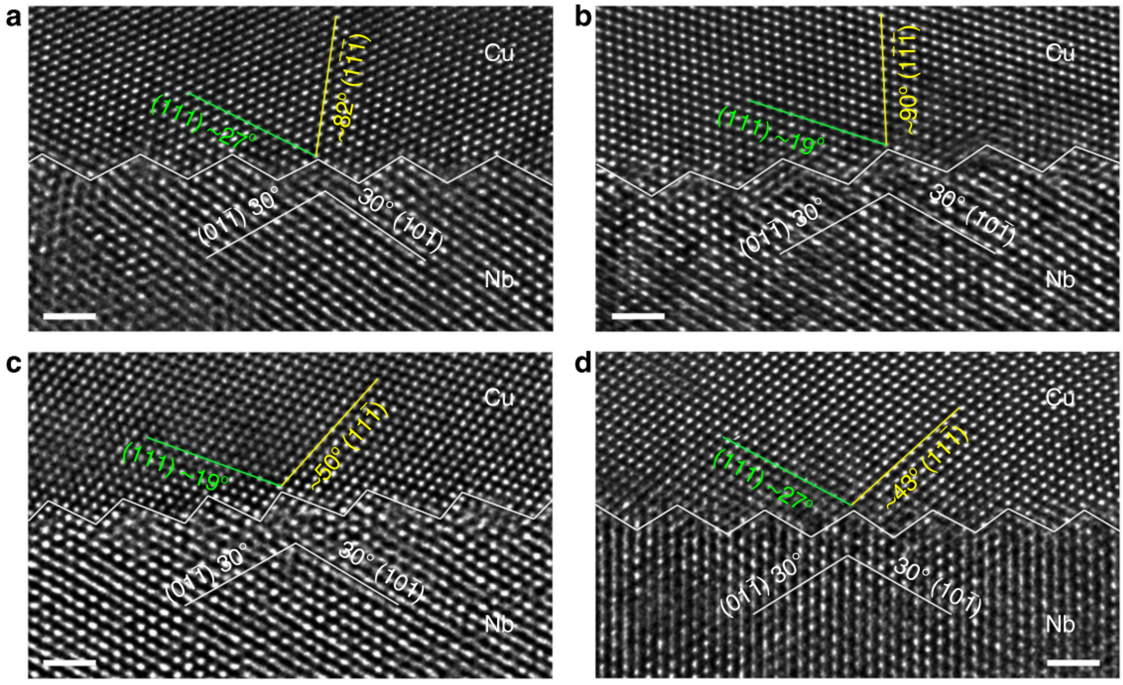


Figure 1.15: Typical interface structures and their energies. (a–d) HRTEM images showing the typical interfaces with the beam direction along $< 110 >$Cu$||<$ $111 >$Nb, before twinning (a) (4411)Cu$||$ (11$\bar{2}$) Nb and (b) (112)Cu$||$(11$\bar{2}$)Nb, and after twinning (c) (552)Cu$||$ (112)Cu$||$ (11$\bar{2}$) Nb, and (d) (551)Cu$||$ (112)Cu$||$(11$\bar{2}$) Nb. The favored fcc/bcc slip system pair for interface transmission is marked in green lines in Cu. Scale bars are 1 nm [70]

a comparison of interfaces produced by the two different methods: CR referring to laminates rotated between steps, and LR referring to laminates with a constant rolling direction.

Figure 1.14 shows how the microstructures of as-rolled (AR) laminates differ from as-deposited (AD) thin films. The most significant differences between these structures are grain shape, grain orientation, dislocation density, and uniformity of layer thickness. PVD laminates contain relatively defect free, columnar grains that span entire layers, regardless of the layer thickness. Microstructural analysis shows that ARB grain shape changes with the amount of processing and thus, the

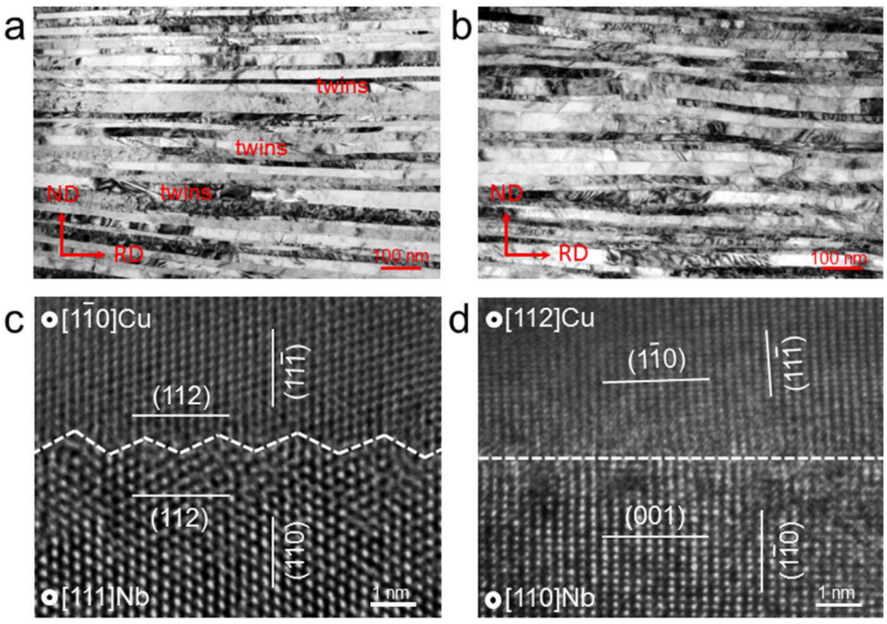


Figure 1.16: Schematic allows for comparison of Cu-Nb interface geometry of ARB laminates produced with the methods described in Section 1.2.2 (labeled LR) and laminates which were rotated 90 ° between steps, or "cross-rolled", labeled (CR). Typical bright field TEM images showing nanolamellar morphologies of the (a) 20 nm ARB-LR sample and (b) 20 nm ARB-CR sample. A large number of twins are present in the Cu phase of 20 *nm* ARB-LR material, but not in the 20 *nm* ARB-CR material. Representative HRTEM images of the predominant interface in the (c) 20 *nm* ARB-LR material, which is noticeably faceted and (d) 20 *nm* ARB-CR material, which is atomically flat [29].

length scale [43, 65]. Initial microstructures for large and small layer thicknesses Cu-Nb ARB material are shown in Figure 1.7. As layer thickness is refined, via roll bonding, layer morphology changes from containing multiple grains through thickness, to single crystal through thickness where every grain is bound by a bi-metal interface to the layers above and below [43].

Transitions in ARB Cu-Nb polycrystalline structure are accompanied by changes in grain aspect ratio and a strengthening of the texture associated with the {112}⟨110⟩Cu//{112}⟨111⟩Nb Kurdjumov-Sacs (K-S) interface orientation relationship, which is similar to the {111}⟨110⟩Cu//{110}⟨111⟩Nb K-S interfaces characteristic of depostied laminates, see Figure 1.14 [29,67]. This interface orientation relationship is relatively low energy, compared to other orientation of Cu-Nb interfaces, and is the most mechanically stable in rolling [3, 14, 43]. The measurement of strong texture in Cu-Nb metallic laminates (PVD and ARB) after large deformation, annealing, or other extreme environments is often thought to prove the abundance of stable interfaces and thus stability of laminate system [3,12,43,65,67].

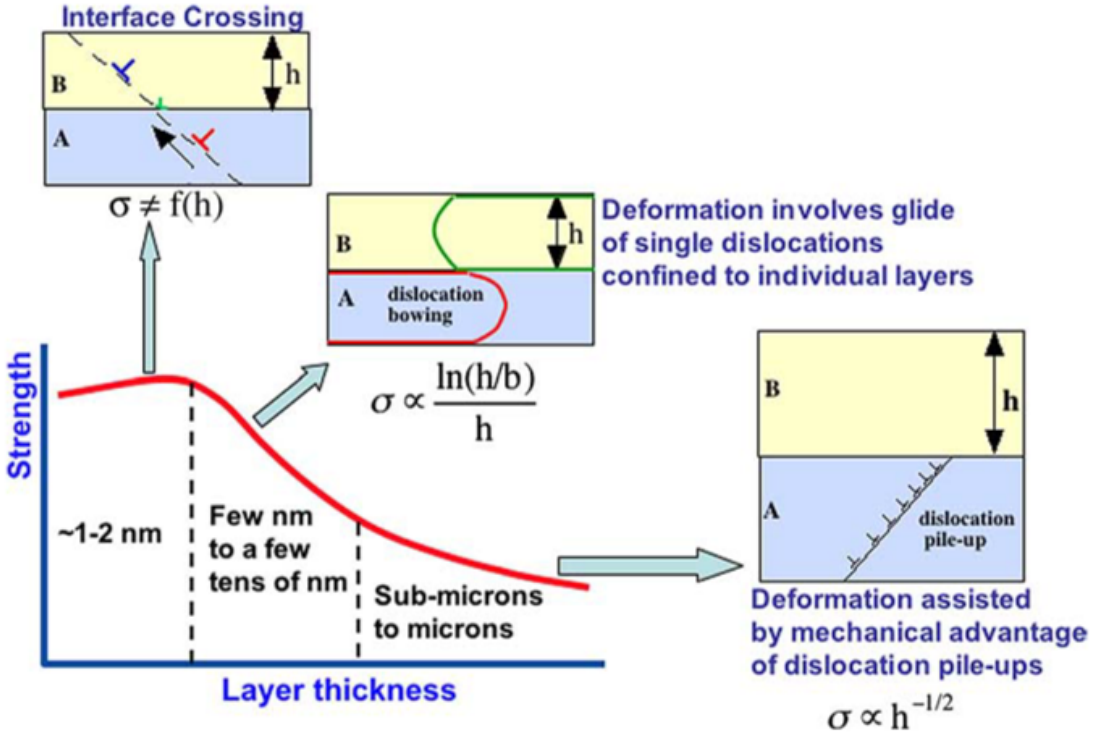


Figure 1.17: At small length scales, Hall-Petch cannot describe deformation behavior in multilayers due to confined geometries. This map shows deformation mechanism transitions proposed by Misra et al. [26]).

1.3 Mechanical Behavior

1.3.1 Variations with Length Scale

Dominant deformation mechanisms, involving dislocation glide and pile-up, bowing, and dislocation transmission, have been proposed over a range of length scales for laminates at room temperature [26, 69]. At elevated temperatures, however, the relative dominance of these mechanisms change as thermally activated processes and evolution of the laminate microstructure significantly impact the overall behavior. Therefore it is important that the mechanical behavior of metallic laminate systems be considered as a function of both interfacial density and temperature.

Dislocation content and motion affects the strength of materials, and is expected to contribute significantly to the stability of ARB Cu-Nb laminates [26, 58, 65]. In 2005, Misra *et al.* proposed strengthening mechanisms for metallic multilayers based on dislocation models and experimental hardness data for Cu-Nb thin films [26]. Figure 1.17 shows the proposed length scale dependence of room temperature deformation mechanisms in the Cu-Nb multilayer system.

Dislocation mechanism transitions due to the confined nature of the multilayer structure below 100 nm, and again below 5 nm. At larger length scales, the strengthening fits to Hall-Petch (H-P) type strengthening which is assumes that grain size is related to the length of a dislocation pile-up. In this deformation regime, the strength is proportional to the inverse square root of layer thickness: $\sigma \propto h^{\frac{-1}{2}}$. Models and observations in PVD materials suggest that below 100 nm, the primary strengthening mechanism transitions to dislocation bowing in confined layer slip (CLS) [26,37]. This mechanism is difficult to experimentally differentiate

from pile-up because the macroscopic behavior has a similar relationship to length scale: $\sigma \propto h^{-1} * ln[h/b]$.

Deformation by dislocation crossing at bi-metal interfaces occurs in layer thicknesses of $\sim 1-2\ nm$, as the stress required for interface crossing is less than that necessary to bow a dislocation with such a small radius of curvature. At this length scale, strength is no longer dependent on layer thickness; using molecular dynamics simulations, this strength is estimated at $\sim 4-5\ GPa$ [26].

It is important to note that the strength of laminates should vary significantly from ARB to PVD laminates due to the variation in layer thickness for a given ARB composite. In any ARB laminate, there is a combination of these deformation mechanisms active because microscale and nanoscale layers are co-deforming within the multilayer.

1.3.2 Insight from PVD Mechanical Tests

Recently, Monclus *et al.* compared the stability of PVD and ARB Cu-Nb with high temperature nanoindentation, finding an increase in hardness with decreasing temperature and layer thickness [71]. This is expected because tests were performed at elevated temperatures which increased dislocation mobility. Addition of thermal energy to a deforming system can activate dislocation climb and cross-slip of dislocations [72], ultimately changing the strengthening mechanism and the material behavior. One notable result from this study is that there is a critical layer thickness below which the hardness actually begins to decrease. This critical length (5 nm for PVD and 18 nm for ARB) is thought to correspond to a transition from deformation by CLS, to interface crossing of dislocations since the mechanisms are effected differently by the addition of thermal energy into the system [71]. Although

no micrographs were published for length scales below this "critical length", an alternative explanation for this behavior could be a discontinuity in layered structure due to a shorter time to pinch off of smaller layer thicknesses.

Mara *et al.* tested the effects of temperature and layer thickness on the tensile behavior of PVD Cu-Nb [55, 56, 73]. Predictably, increased ductility and lower strength are associated with an increasing temperature at a given strain rate due to dislocation mobility [56]. Thermally activated climb and cross-slip may contribute to this apparent softening at temperature [56, 73]. Similar to room temperature deformation of both PVD and ARB material, the trend of increased strength and decreased strain to failure with decreasing layer thickness at elevated temperature (500 °C, 600 °C, and 700 °C) [28, 56, 74]. Deformation by grain boundary sliding is supported by the strain rate exponents calculated from jump tests as well as the observed grain pull out in the fracture surfaces [55, 56]. This high temperature mechanism requires substantial movement of dislocations at grain boundaries (and interface boundaries) and is common in fine grained materials [48, 55, 56, 75–78].

The high grain aspect ratio of ARB Cu-Nb laminates may suppress this mechanism due to a lack of grain boundaries transverse to the loading direction in comparison to the PVD microstructure. The application of stress to a system introduces spatial dependence of defect mobility, which is important at elevated temperatures [76, 78, 79]. The multilayers in the above experiments were oriented with the loading direction parallel to the bi-metal interface, thus diffusion along transverse boundaries is higher [55, 56, 76, 79]. Engineering design of laminate systems for these applications may include various processing paths to decrease the amount of in-plane boundaries and potentially increase the material resistance high temperature deformation [29].

1.3.3 Anisotropy

ARB Cu-Nb laminates are anisotropic in nature due to the elongated microstructure and strong crystallographic textures; this property, therefore, also varies with length scale. Figure 1.18 shows results for samples oriented parallel to the rolling direction (RD) and transverse to the rolling direction (TD) tested in tension. It is clear for all layer thicknesses that TD samples have higher layer parallel yield strength, σ_y, than RD. The Hall-Petch relation was characterized for both orientations, such that:

$$\sigma_y^{RD} = 438 + 0.078h^{\frac{-1}{2}} \tag{1.1}$$

$$\sigma_y^{TD} = 434 + 0.080h^{\frac{-1}{2}} \tag{1.2}$$

where units are in MPa and m and h is the nominal layer thickness [17]. It is notable that the reference stress is about twice that of the pure metals, and the Hall-Petch parameter is between the values reported for Cu and Nb [51]. This is in part due to the strong texture within the ARB laminates compared to randomly oriented polycrystals reported in literature. Mechanical anisotropy in hardening behavior is even more notable in this system when comparing the ultimate tensile strength (UTS)[3] of RD and TD orientations, rather than yield strengths.

$$\sigma_p^{RD} = 475 + 0.092h^{\frac{-1}{2}} \tag{1.3}$$

$$\sigma_p^{TD} = 501 + 0.114h^{\frac{-1}{2}} \tag{1.4}$$

The Hall-Petch parameter is a metric for hardening associated with a change in

[3]In this document, the UTS is taken as equal to the composite plateau stress, σ_p.

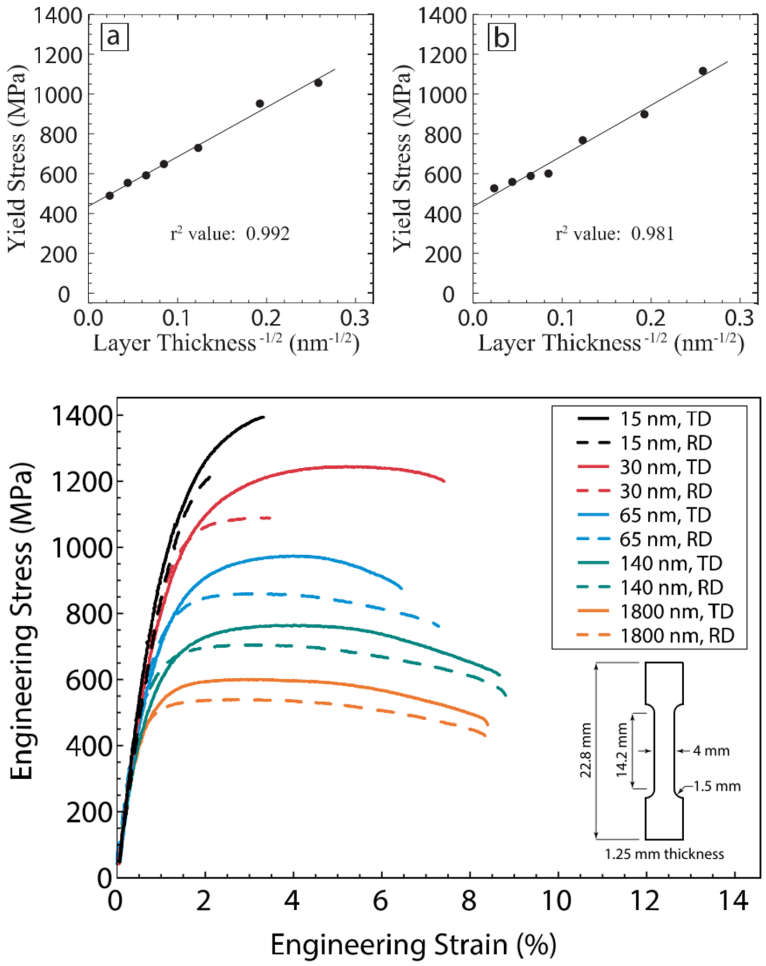


Figure 1.18: Hall-Petch relationships can be used to describe Cu-Nb strength as a function of layer thickness. Tensile behavior varies according to sample orientation; tension parallel to the rolling direction (RD), or transverse to the rolling direction (TD) [17]).

laminate length scale. Clearly, the plateau stress has a high dependence on length scale, and the variation in anisotropy is amplified. Analysis of this tensile behavior using visco-plastic self-consistent modeling determined that the variation in plateau strength between RD and TD is due to the difference in crystallographic texture between the two orientations [17]. This effect may also be convoluted with the fact that grain sizes are smaller in-plane of a layer when oriented with the TD parallel

to loading.

The grain structure of small length scale laminates contributes to anisotropic deformation behavior in compression. Laminates with nominal length scales of below 500 nm form kink bands in layer parallel compression [44, 68, 80]. Above this layer thickness, compression results in specimen barreling. The transition in behavior aligns with that identified in Fig. 1.8 and 1.17.

Compressive Kinking

Kink bands are regions of locally deformed material which is misorientated from the rest of the material (microstructurally, or crystallographically). Formation of kink bands a phenomenon observed in highly anisotropic materials. Specifically, local misorientations in a microstructure with low shear strength parallel to loading in an orientation with high compressive strength can initiate this mechanism [57]. Not only do ARB Cu-Nb laminates have tortuous layer morphologies, but at the transition from polycrystalline grain structure to bi-crystalline (below 500 nm) the layer parallel shear strength deviates from a Hall-Petch relationship. Shear strengths are effectively unchanging at the lower length scales [57]. Kinking does not occur in Cu-Nb produced by PVD, likely due to the very different grain structure and tendency for interface sliding in layer parallel shear.

Macroscopically, kink bands display the relationship $\phi = 2\beta$, where ϕ is the angle of misorientation and β is the angle between the deformed and undeformed material. The geometry of this relationship, as well as a complex network of kink bands (maintaining this relationship) is shown in Figure 1.19. High resolution scanning transmission electron microscopy revealed that, unlike most kinking composite materials, the two phases remain bonded and continuous throughout the kink bands in ARB Cu-Nb [80].

Kinking in Cu-Nb multilayers is *not* a failure mechanism[4], but instead an effective energy dissipation mechanism during compressive deformation [44,80]. After a kink band is formed, it propagates and thickens at a constant load without initiating voids or cracks [44, 74, 80].

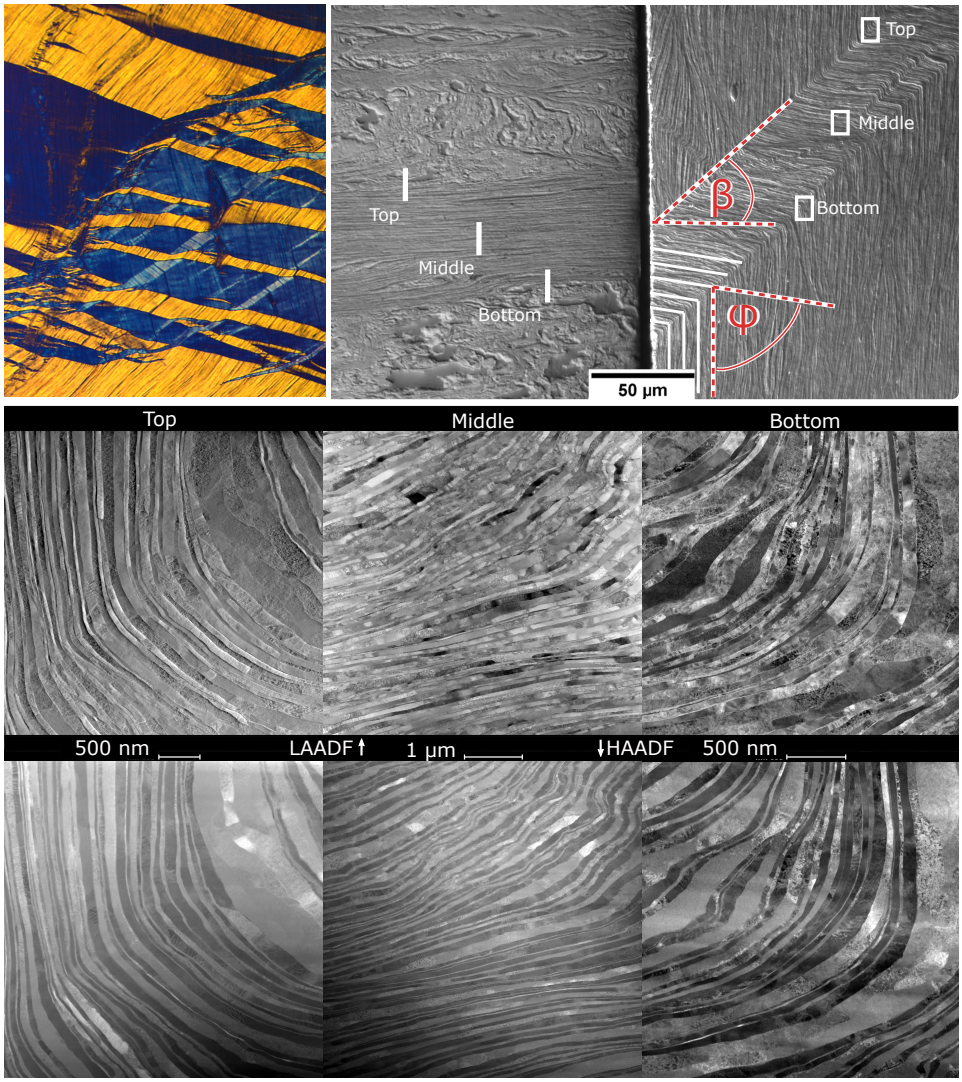


Figure 1.19: Light optical microscopy (LOM) highlights networks of kink bands in Cu–Nb. SEM of a single kink band viewed from ND (center) and TD (right), labeled with FIB samples shown below. Representative (S)TEM images of the three regions are shown in LAADF and HAADF contrast. LOM courtesy of Thomas Nizolek.

[4]Cracks can develop around kink bands after 25 % strain.

The formation of kink bands within Cu-Nb is associated with stress fields similar to mode II cracks [68]. Analytical modeling of kink band formation, corroborated with digital image correlation measurements, confirm experimental kinking geometries observed in the ARB Cu-Nb system [68].

1.4 Thermal Behavior

1.4.1 Structural stability

Microstructural stability can be defined as the laminate system's ability to maintain a continuous layered structure [19, 50, 66, 81–86], a sharp interface [77, 87–89], a crystallographic texture [12], a defining microstructural length scale [12, 90, 91], or a combination of these criteria. These conditions are codependent. For example, changes in texture, due to grain growth, locally change interface morphology, which can lead to layer discontinuity. Ultimately the microstructure can coarsen because of these instability mechanisms, decreasing strength benefits of small structures and high interface densities. The most important criterion for thermal stability of multilayer structures is therefore the continuity of layers.

Current literature on multilayer stability primarily describe material that was processed by physical vapor deposition. Analysis of PVD material cannot sufficiently describe structural evolution in ARB materials because the difference grain structures, dislocation densities and energies driving boundary motion. There is a notable lack of information about microstructural evolution for Cu-Nb exposed to elevated temperatures for long periods of time [5]. This is the motivation for experiments in Chapter 5.

[5]Most studies conclude stability after $1 - 2$ h at temperature [12, 19, 29, 66, 71, 86, 92]. One study reports stability after 60 h with very little detail about structure evolution [13].

1.4.2 Texture Evolution

Thermal evolution in ARB Cu-Nb is largely related to the evolution within each phase effecting the grain structure and interface character. High energy interfaces decrease at high temperatures, sharpening the texture peaks associated with low energy interface orientations [59]. Additionally, the sharpness of the texture tends to increase with increasing temperature, as shown in Figure 1.20 [12]. As previously mentioned, the recrystallization texture of Cu reinforces the strong rolling texture [33, 58]. Diffusion allowing for texture evolution also enables the Cu and Nb layer structure to evolve.

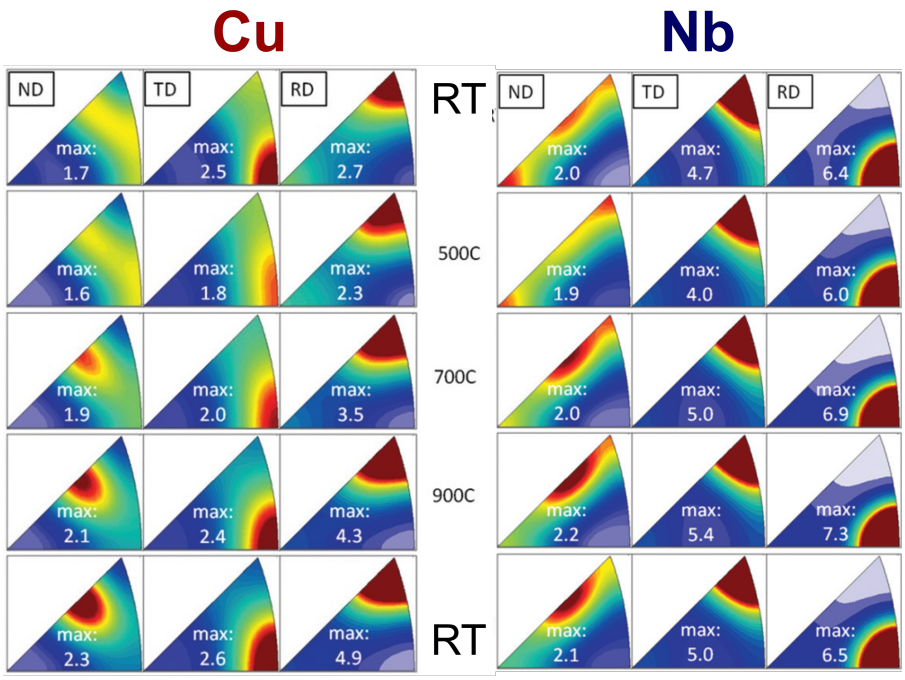


Figure 1.20: Inverse pole Figures show preferred orientations that are associated with the ARB Cu-Nb K-S interface. Textures strengthen as temperature increases. [12].

1.4.3 Driving Forces For Microstructure Degradation

Thermal stability in a microlaminate orientation relationships between grains of individual phases and bi-metal interface orientations. Stability is achieved by a balance of these energies and the associated shape of a triple point between grains [93–95]. The commonly used Young's equilibrium equation for a single triple point junction between three phases [94–96] has been modified for a multilayer system as:

$$\gamma_B = 2\gamma_{int} cos\phi \tag{1.5}$$

where 2ϕ is the angle formed by the interface, or surface. Away from triple points, the shape of a boundary contributes considerably to the drive for structural evolution. The Gibbs-Thompson relation describes the change in system free energy ($\Delta\mu$) with the ratio of boundary energy (γ) to the radius of curvature of that boundary (r) [89, 95, 96].

$$\Delta\mu \propto \frac{\gamma}{r} \tag{1.6}$$

Boundary curvature in this equation must be minimized to achieve the lowest potential, locally flattening structures. Considering equations 1.5 and 1.6, the most stable multilayer configuration should have alternating non-reactive phases with perfectly flat grain boundaries and interfaces with all triple point angles satisfying equilibrium conditions of the interfacial energies. This configuration is not physically realistic, particularly when considering material processed by large scale methods; therefore, structural evolution is inevitable.

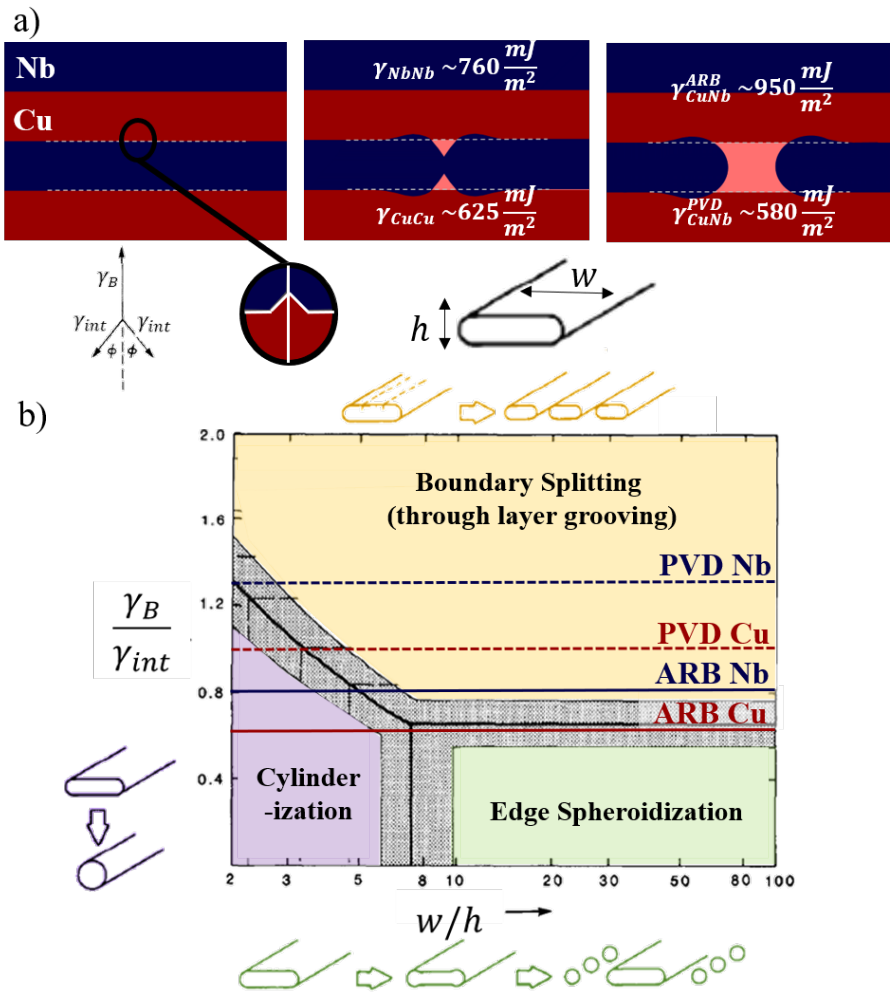


Figure 1.21: a) is a schematic of grain boundary grooving. The left image shows an initially perfect structure with one grain boundary that terminates at triple points with bi-metal interfaces. Infinitely close to the triple point eqn. 1.5 is satisfied. Over time boundary diffusion changes the interface shape to accommodate the triple point angle (middle), and eventually the groove depth will surpass the layer thickness causing pinch-off (right). [94,97,98] b) is a map of instability mechanisms which relates boundary energy ratios to aspect ratios of plate-like structures (or grains within multilayers) [99]. Schematics of the mechanisms are shown: boundary splitting (top), cylinderization (left) and edge spheroidization (bottom). Average boundary energies for Cu-Nb are shown [13, 28]

1.4.4 Layer Instability Mechanisms

On a macroscale, the multilayer structure is a vertical series of finite plates separated by interface boundaries. High temperatures activate mass transport mechanisms to reduce the system free energy by altering the curvatures of the initial structures. Although a truly stable morphology is one with the lowest possible free energy, there are shapes that form preferentially in the process of reducing boundary energy. Malzahn et al. explain the degradation of plate-like structures via three processes: cylinderization, edge spheroidization, and boundary splitting [83,99]. These processes, shown in Figure 1.21, have been applied to the loss of layer continuity in multilayer structures [13,19,100], as the combination of macro and microstructures are plate-like. If plate-like grains traverse a layer of laminate, boundary splitting, also referred to as boundary grooving, results in pinch-off of that layer. Similarly, if grains at a bi-metal interface experience cylinderization or spheroidization layers will become discontinuous at those locations. The likelihood of any one of these instabilities occurring depends on the plate aspect ratio and perturbations within the structure. Morphology change is achieved through mass transport therefore the rates of these processes are controlled by diffusion. Courtney et al. have analyzed the kinetics behind these three types of instabilities for both volume and surface diffusion controlled transport. The most probable morphology progression, based on the aspect ratio and boundary energies of a system, is expressed by an instability map (Fig.1.21b), normalized for any system. The amount of mass transport required for each process changes with the aspect ratio of the initial plate-like structure, thus the instability process can be predicted for a system of known boundary energy [99].

The three processes to lower free energy detailed by Malzahn *et al.* involve either

edge recession to decrease boundary area or boundary splitting to replace high energy boundaries with lower energy boundaries. The process of recession forms a ridge at a plate edge; if this ridge is not created uniformly, as is most likely to happen over a long period of time, periodic perturbations may form and grow into spheres. This process, edge spheroidization, is more likely to occur in high aspect ratio plates due to the amount of initial recession needed. Spheroidization lowers the aspect ratio of the plate-like structure. Low aspect ratio plates preferentially recede into cylinders because the decrease in interfacial energy outweighs the increase in radius of curvature in that dimension. Contrary to edge recession, boundary splitting increases boundary area.

The free energy of a system is lowered by increasing the phase interfacial area while decreasing grain boundary area, pinching off the plate through the boundary. The theory behind the pinch-off process was termed thermal grooving by Mullins in 1957 [94]. This mechanism is often observed in multilayer systems and has been detailed as the primary reason for multilayer degradation [19,50,59,81–86,90,91,93]. ARB laminates experience layer pinch-off due to instabilities from rolling defects, boundary grooving [12, 13, 66, 82, 86], and even Rayleigh effects [101, 102]. Interface and grain boundary energies dictate that Nb layers are subject to pinch-off to a greater degree [19, 86, 92]. Smaller layer thicknesses have a higher driving force to pinch-off and a shorter time before layers become discontinuous at elevated temperature. Layer discontinuity fundamentally changes the multilayer structure, decreasing the interface density and allowing the microstructure to coarsen. The improvement in strength achieved through layer size refinement can be negated by significant coarsening at elevated temperatures [70].Figure 1.22 shows various multilayer structures that have experienced pinch off after exposure to elevated temperatures.

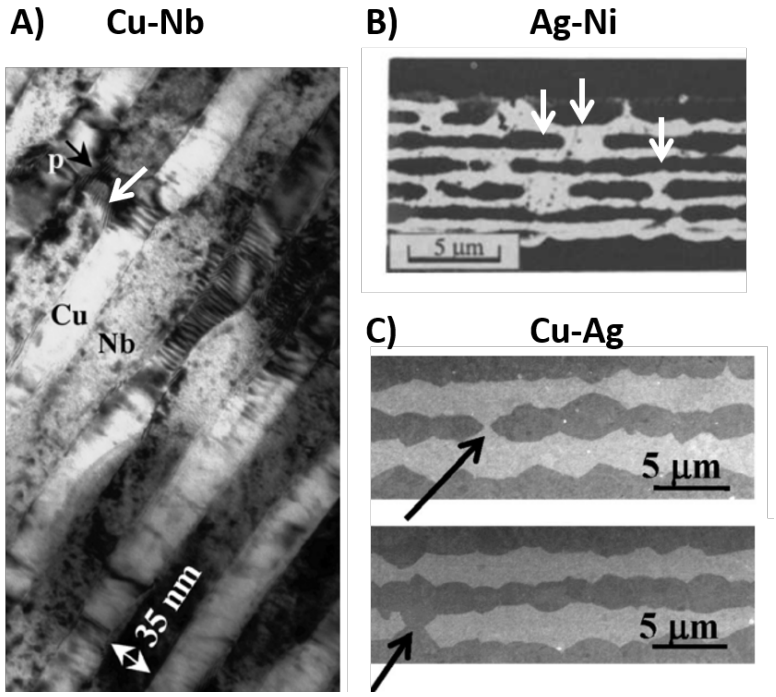


Figure 1.22: A) Nb layers pinch-off in 35 *nm* Cu-Nb after 30 *min* at 700 °C [13]. B) Ni layers pinch off in Cu-Ni laminate after creep at 700 °C, lasting about 3 days [103]. C) Both phases pinch off in the Cu-Ag system (reproduced from Reference [50]).

1.4.5 Groove Theory

Microstructural evolution is thermodynamically driven by non-equilibrium grain boundary and interface geometries, and is achieved through kinetic processes such as interfacial diffusion and dislocation motion. The activation energy required to rearrange a crystal either by dislocation movement, boundary diffusion, interface diffusion, or lattice diffusion is intrinsic to that material. The velocity of dislocations ($\bar{v}$) and mobility of atoms (D), however, are dependent on the ratio of activation energy to the amount of thermal energy in the system. [72]

$$\bar{v} \propto e^{\frac{-\Delta G}{kT}} D \propto e^{\frac{-E}{kT}} \tag{1.7}$$

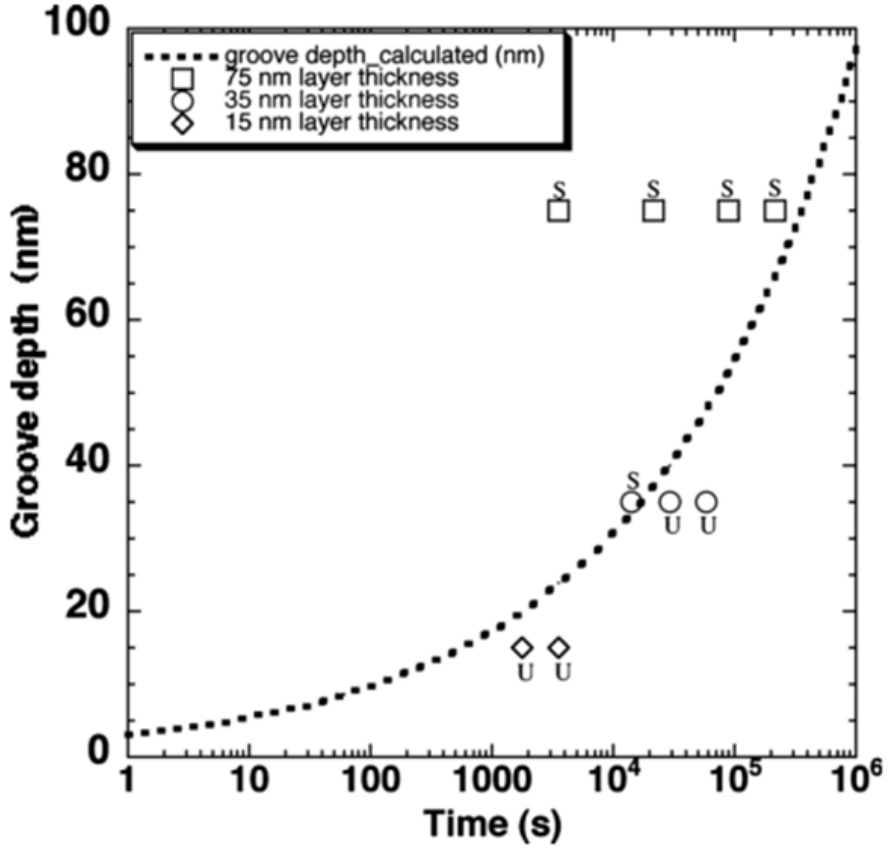


Figure 1.23: Calculated groove depth using the Josell-–Spaepen model [82], as a function of annealing time at 700 °C in Cu–Nb. Assuming that layer splitting occurs when groove depth is on the order of layer thickness, data points from experiments on multilayers with layer thickness of 15, 35, and 75 *nm* with the corresponding annealing times are superimposed. Samples where the layered structure was maintained are marked S, and those that showed unstable behavior are marked U. The Figure can be regarded as a thermal stability map that provides a guide for the layer pinch-off time at a given temperature. [13]

Thermal energy is defined as the product of Boltzmann's constant (k) and temperature (T). Clearly at elevated temperatures, mobility of atoms and dislocations increases and mechanisms of crystal reordering, such as microstructural evolution or deformation, can be activated and/or occur at higher rates. While this equation holds true for all crystalline materials, at a given temperature, the relative mobility of Cu and Nb vary by several orders of magnitude.

Mullins evaluated the depth of thermal grooves over time for both surface and volume diffusion, however only surface diffusion will be discussed. As previously mentioned, morphological changes are founded on the Gibbs-Thompson relation, which suggests that a gradient in chemical potential is proportional to interfacial free energy and curvature.

The structure is in thermodynamic equilibrium when the surface has a constant slope m. Considering a single, grooving triple junction at a free surface, Mullins postulated a theory founded upon the Nernst-Einstein relation [94–96],

$$V = \frac{-D_{int}\gamma_{int}\Omega}{kT}\frac{\delta\kappa}{\delta\chi} \tag{1.8}$$

The average velocity of atoms diffusing along a surface or interface,V, is proportional to the diffusion coefficient of that interface D_{int}, the energy of the interface γ_{int} , and the curvature gradient along the interface $\delta\kappa/\delta\chi$. Applying the boundary conditions inherent to the grooving process, Mullins proposed that the depth of a groove at any time and position along the surface can be described by

$$y(x,t) = m(\beta t)^{\frac{1}{4}} * Z[x/(\beta t)^{\frac{1}{4}}] \tag{1.9}$$

known as Mullins'groove theory. This groove profile describes the groove depth at a grain boundary, y, and the maximum peak-to-peak width of the groove, s, to be shown as functions of time [94]:

$$y = 0.973 * m * (\beta t)^{\frac{1}{4}} \tag{1.10}$$

$$s = 4.6 * (\beta t)^{\frac{1}{4}} \tag{1.11}$$

Both of these groove profile parameters have the same time dependence. Figure

1.23 is a plot of a groove profile showing the relationship between groove depth and width is independent of time [98], and these equations are commonly used to assess multilayers for pinch-off prediction.

Young's equation (eqn. 1.5) has also been related to grooving because as the microstructure evolves, the angle of the interface (2ϕ) will become a pronounced and measurable groove, allowing for the calculation of boundary energies [50, 81, 82, 86]. Groove angle measurements and subsequent calculations of average interfacial energy at various temperatures show that interfacial energy tends to decrease with increasing temperature [50]. Thermal grooving associated with the evolution of triple point boundaries, was analyzed with respect to diffusion kinetics, and quantified as [50, 94, 97, 98]:

$$y = 0.78m(\beta t)^{\frac{1}{4}} \tag{1.12}$$

It is clear that the depth of a surface groove (y), or a bi-metal interface groove in the case of multilayers, increases with time (t) and is dependent on the temperature and interface character dependent parameter (β). The disadvantage of smaller layer thicknesses is clear when we consider Mullin's groove theory and the schematic in Figure 1.21. Loss of layer continuity occurs when y is greater than the layer thickness. Therefore, decreasing the layer thickness by a factor of 10 is expected to decrease the time that that microstructure is stable by 4 orders of magnitude. Misra and Hoagland found that this relationship accurately predicts the stability of PVD Cu-Nb multilayers, results shown in Figure 1.23, by analyzing 15 nm, 35 nm , and 75 nm layer thickness films after annealing at 700 °C for various times. Thermal grooving is the primary mechanism of thermal instability in many PVD systems [50, 66, 77, 81, 90] and is expected to play a large role in the microstructural

evolution of ARB Cu-Nb as well.

Another instability mechanism of multilayer structures is the growth of boundary perturbations resulting in spheroidization [83, 92, 99]. PVD microstructures often have a periodic undulation due to imperfections in the deposition source [20, 26, 28]. Kinetic limitations prevent the structure from achieving the perfectly flat interfaces needed to satisfy the Gibb's relation (eqn. 1.6). Therefore, a more locally defined radius of curvature is optimized, ultimately necking and pinching off the layered structure like grooving. This mechanism has been observed in 20 nm layer thickness ARB Cu-Nb [101] after one hour at 500 °C. Zheng *et al.* suggest that smaller layer thicknesses of ARB materials are particularly susceptible to this type of pinch-off because there is a relative lack of grain boundaries (compared to interface boundaries) and the diffusion away from "necked regions is promoted by potential gradients caused by facets in high energy interfaces (see Figure 1.14) [101].

Misra et al. performed a more direct analysis of groove theory with respect to layer thickness and recorded various breakdown temperatures in the same experiment [13]; however, the temperature results were not correlated to thickness and time results in analysis. Pinch-off causes discontinuity in the layers of a laminate when the groove depth is equal to the layer thickness [13, 82] (or half of the thickness if there are grooves on both sides [50, 85, 86]). In Figure 1.23, groove depth is plotted against time with data presenting the condition of the multilayers overlaid indicating a stable or unstable condition. This plot effectively maps the thermal stability for multilayers at a given temperature [13].

Several other terms in the thermodynamic and kinetic equations described above are also temperature dependent, including boundary energy and diffusion coefficient. In line with the dependence of groove depth on temperature, Ludtke Knoedler et al. noted that the diffusion coefficient increases with increasing temperature [50].

In the same study, groove angle measurements and subsequent calculations of average interfacial energy at various temperatures showed that interfacial energy tends to decrease with increasing temperature [50]. This decrease in energy and increase in the diffusion coefficient may also be related as both boundary diffusion and energy are dependent on the orientation relationship of surrounding grains. Diffusion occurs preferentially in the direction of dislocation cores at a boundary; interfacial energy is also tied to these dislocation cores by the prevalence and extent of strain energy in these areas [95].

1.5 Objectives and Approach

Understanding the high temperature mechanical behavior of ARB Cu-Nb multilayers is critical to designing structural components for extreme environments. The unique microstructures that result from the ARB process pose significant variation from PVD materials in both mechanical and thermal stability behavior. It was the objective of this work to quantify and explain the creep behavior of ARB Cu-Nb for laminates of length scales varying from nominally 8 μm down to 65 nm.

The experimental approach involved characterization of initial, heat treated, and crept microstructures via microscopy techniques. Additionally, it required development of a set-up and strain tracking method for creep and high temperature testing. Analysis of creep behavior involved image processing, quantification of traditional strain rate dependences, as well as the development of a composite model.

Chapter 2

Experimental Procedures

2.1 Sample Preparation

2.1.1 Metallographic preparation

A slow-speed saw[1] was used to cut samples from sheet materials and/or to section a specimen. The majority of samples were cold-mounted in vacuum with two-part epoxy resin.[2] Unmounted samples were glued to flat Bakelite pucks, distributed evenly to avoid beveling.

Challenges of Cu-Nb laminate metallography include variable polishing rates as well as material hardnesses. Composite and individual phase hardness varies with layer thickness. The hardness between phases is also variable, particularly after annealing. Figure 2.1 highlights these challenges by showing polished surfaces with (a) particles embedded in softer pure metals and (b) significant surface relief after

[1]Either a diamond blade, or thin SiC blade was used, depending on the precision needed for the cut.

[2]At risk of changing the structure, high temperature Bakelite mounting was avoided.

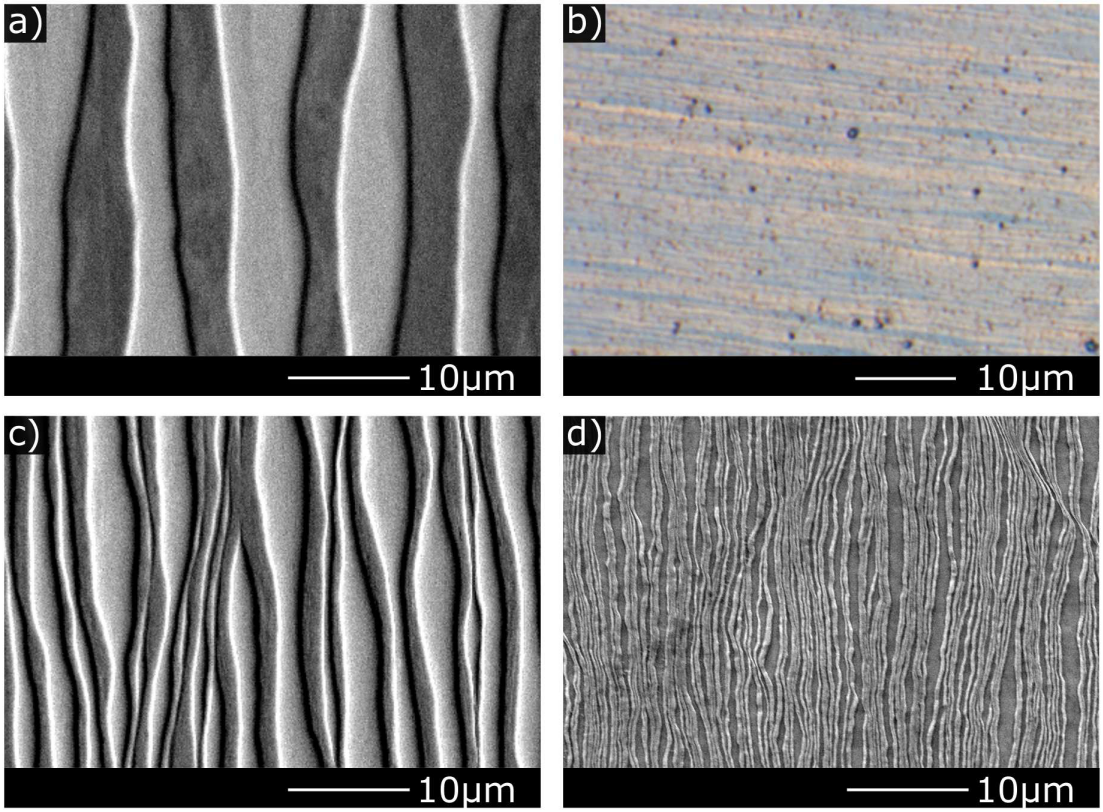


Figure 2.1: a,c,d) BSE images of 8000 nm, 2000 nm, and 200 nm Cu-Nb chemically etched by colloidal silica. This relief is inevitable if left on the vibratory polisher for longer than one hour. b) Optical micrograph featuring hard alumina particles embedded within 245 nm Cu-Nb were not removed despite ultrasonic cleaning and polishing at smaller particle sizes.

chemo-mechanical polishing for too long.

Machining damage was removed from samples with 400 grit SiC paper. Samples were ground using SiC paper of 600, 800, and 1200 grit, sequentially, and water lubricated. Polishing steps include 9 μm, 6 μm, 3 μm, and 1 μm polycrystalline diamond suspensions, lubricated with Allied "BlueLube", on Buehler "TextMet" and "MicroCloth" pads. All polishing was performed using polishing wheels; step changes occurred after grit lines visually changed orientation twice. Diamond grits were visually inspected using optical microscopy. Between every step, samples were cleaned in alcohol using an ultrasonic cleaner to remove any embedded grit particles.

A Vibromet automatic polishing machine was used for the final polishing steps: 4 hours of 0.05 μm alumina suspension on a "MicroCloth" pad, and 30 minutes of 0.05 μm colloidal silica on a "ChemoMet" pad. Times for the chemo-mechanical silica step varied because the polishing and etching rates of Cu and Nb vary from one another as well as with defect content. Highly deformed material is removed more quickly and scatters electrons more poorly than undeformed of recrystallized material.

For analysis using backscattered electron detection (BSE) or focused ion beam (FIB) machining, carbon paint was sufficient to prevent image drift. EBSD analysis required more robust grounding, and samples were coated with a layer, $1 - 3$ μm thick, of sputtered carbon or gold-palladium alloy.

2.1.2 TEM sample preparation

PIPS

Preparing TEM samples by ion milling is an arduous, time consuming process with a low success yield. Steps involve grinding, polishing, disk cutting, dimpling,

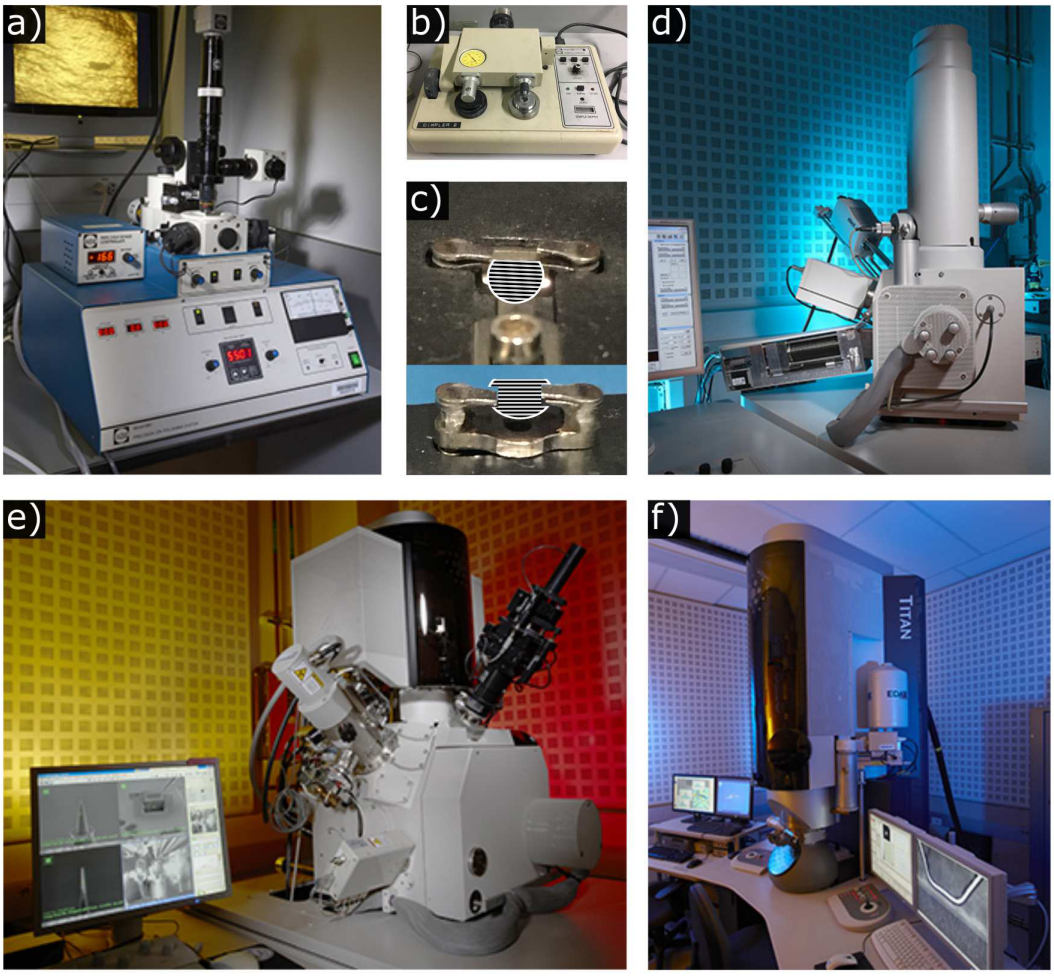


Figure 2.2: a)Gatan PIPS b) Dimpler c) PIPS clamp mount showing sample orientation d) FIB e) FEI XL-30 f) FEI TITAN

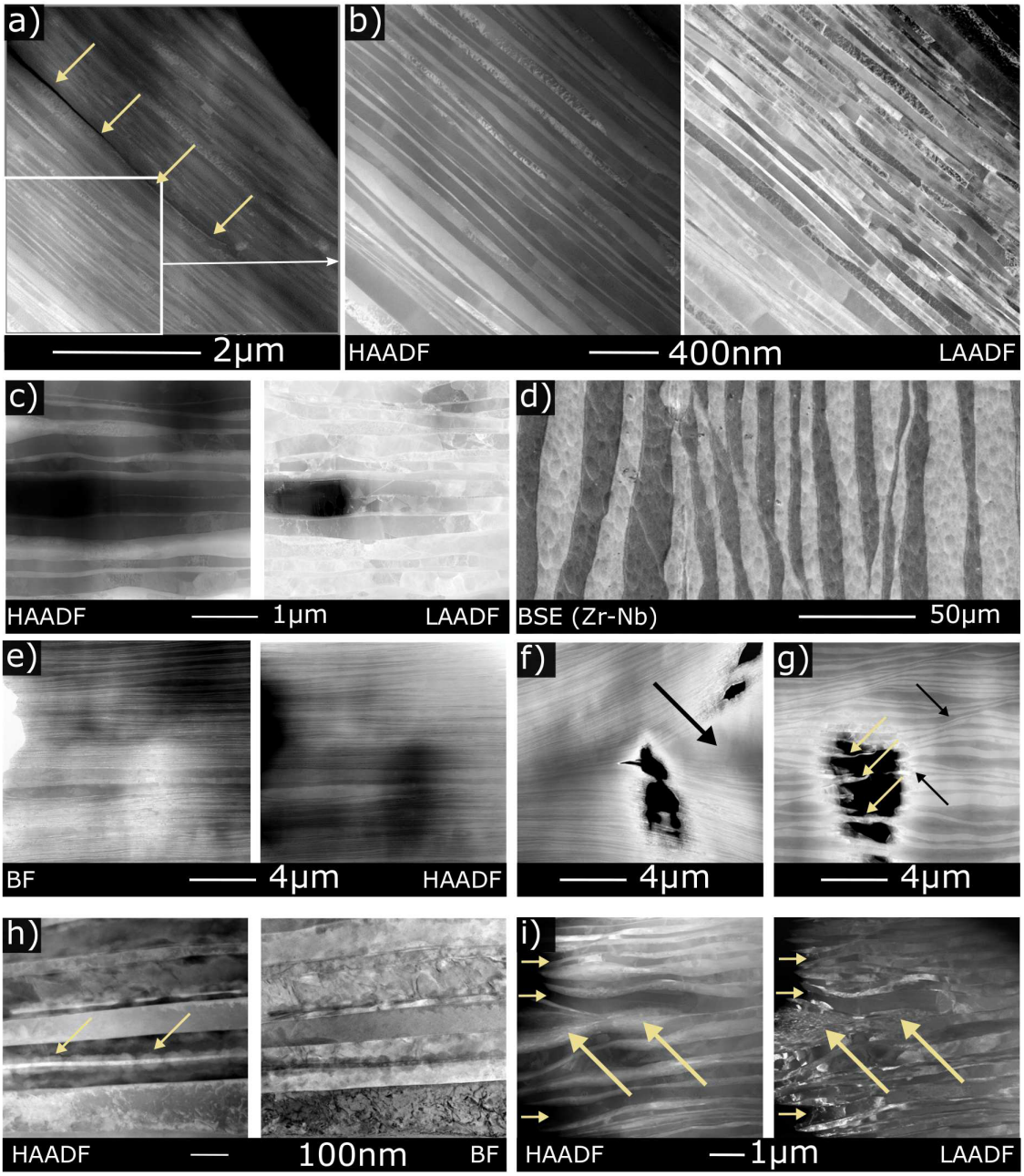


Figure 2.3: Challenges of samples prepared by PIPS. a) Cracking along interfaces. b) A "good" region, despite obvious contrast issues due to thickness variation. c,e) Extreme thickness variations d) Dimpled PIPS surface. f,g,i) Preferential milling of defect areas. h) Re-deposition of material. g,i) Nb fingers protruding.

and precision ion polishing. The entire process takes, on average, 30 h per sample using parameters which were found most successful for Cu-Nb multilayer samples. Details of the optimal Cu-Nb PIPS process follow.

Metallagraphic preparation was similar to that described previously, however, with the addition of specific desired thicknesses at given polishing steps. Bulk sheets are sectioned using a slow speed diamond saw. Several samples could be prepared at once during the next step. One side of the samples was polished to 1200 grit SiC paper immediately and glued to a flat polishing mount. Next, samples were ground down to about 800 μm using 400 grit SiC paper. 600, 800, and 1200 grit SiC paper was used, sequentially, to reduce sample thicknesses down to about 200 μm. Finally, diamond lapping films (particle sizes 9 μm, 6 μm, 3 μm, and 1 μm) were used, sequentially, to reduce the thickness to about 90μm. [3] At this thickness, a GATAN punch was used to punch 3mm disks from the sheets (3.5 mm to 4 mm wide due to initial sheet thickness). In order to keep note of the sheet orientation, disks were cut out to off center to include a flat edge parallel to the rolling direction.

Next, a single disk is glued to a glass cylinder and aligned in the "Dimpler 2". Moderate rotation speeds were used to dimple one side of the disk and achieve a minimum thickness of about 20 μm. First a 9 μm diamond paste is applied to a lubricated brass wheel[4] in order to remove material down to an 70 μm minimum. Felt wheels[5] are used for the final dimple steps: minimum thickness progresses to 50 μm, 18 μm, and finally 9 μm using 5 μm boron nitride[6], 1 μm boron nitride, and 0.25 μm diamond pastes, respectively. Isopropanol soaked cotton swabs are

[3]GATAN standard is 150 μm. Thinner disks result in a less drastic dimple angle and higher likelihood for the process to yield a larger thin region at hole edges.

[4]Allied brand "BlueLube", an isopropyl alcohol based lubricant is used for all dimpling.

[5]Soft wheels take more time to remove material, however they are more forgiving of alignment and particles do not embed as often as with brass wheels.

[6]Boron nitride paste is used because it does not embed in the Cu as badly as diamond pastes

used to clean the dimpled sample between every polishing step. The sample is removed from the glass cylinder and cleaned, with acetone and isopropyl alcohol, respectively.

Next, the PIPS is used to remove material at the center of the dimple and create a hole, the edges of which are electron transparent. Argon flow is adjusted and both ion guns are aligned using a phosphorus disk at 5 keV and $+10°$. The PIPS is cooled with liquid nitrogen to prevent local heating of Cu-Nb.

The sample is positioned dimple up, with the RD aligned parallel to the long axis of a two-sided clamp mount and placed into the PIPS (axis parallel to front of the machine). Using the toggle option, the ion beam only mills at certain angles which do not interfere with the clamp mount; this alignment ensures that the beam is primarily milling perpendicular to the laminate layers. [7]

One ion gun is positioned into the dimple, $+6°$, and one below the sample, $-4°$, both at 5 keV. [8] After 10 hours, the sample would be flipped (dimple down), and the gun angles would be adjusted, $+4°$ and $-6°$. [9] The sample is checked every few hours until a hole is made by milling (usually 10 more hours). Once a very small hole is made, the angles are made more shallow by $2°$ and the voltage is brought down to 2 keV for one hour.

The advantage of this technique is that samples have a larger area of electron transparent material. Challenges of this technique with the ARB Cu-Nb system include a variation in Cu and Nb milling behavior, and a higher milling rate of defect regions. As seen in figure 2.3, uneven milling results in extreme thickness

[7]Nb does not mill away as easily as Cu, therefore milling at all angles results in complete removal of Cu layers with Nb fingers sticking out. At very small laminate thicknesses, this is less of a problem because the beam spot size encompasses many layers and Cu is more protected.

[8]For this particular PIPS and metallic system, currents would reach a maximum around 55 mA for 5 keV , or 15 mA for 2 keV.

[9]More redeposition occurs if milling is only done with the dimple up, as well as if milling is done from only top or bottom angles.

variations, and debonding. Even though there is a larger area of material, it is often not the most representative or of the best quality because of the composite milling behavior.

FIB

Focused ion beam (FIB) foil preparation takes $5 - 6\ h$ per foil and involves four main tasks: trenching, lift-out, attachment, and cleaning. The details (ie: dimensions, beam voltages and currents) are outlined in the FIB procedure Appendix. Figure 2.4 shows various steps as captured during the process of making Cu-Nb samples for TEM analysis. Challenges of this procedure are shown in figure 2.5, including: initial surface preparation, layer orientation, curtaining effects, and bending.

Samples should be polished with finer grit that 1200 SiC papers because surface damage (while less than 2 μm deep) is a significant area of FIB samples. Lamella oriented with Cu-Nb layers parallel to the sample surface reduce curtaining effects because Cu and Nb mill at different rates and defect-filled interfaces mill more easily than bulk crystals.

Samples must be loaded into the chamber with precision because FIB lamella must be horizontal in the view of the ion beam[10]. Platinum is deposited in the region of interest in order to protect the underlying material and limit curtaining effects during milling. Angled trenches are machined away on either side of the platinum, creating the shape of the FIB foil [11]. Lower currents are used to clean up the sides of a foil and thin it to about 800 nm. A "U-cut" is used to remove the sample from the bulk, leaving a small section uncut.

[10]Cutting out the sample requires trenches along the tilt axis.
[11]The depth of the trench ultimately determines the height of a foil.

Next, the sample must be lifted out of the bulk using an OmniProbe manipulator. The probe is brought to the platinum foil top and "glued" to the sample by depositing a small amount of platinum. The uncut region is then milled away, freeing the sample completely from the bulk. The probe is removed from the chamber center with the sample attached. At this point the bulk sample is removed from the chamber and replaced with a TEM grid [12]

Molybdenum grids were used so that the Cu-Nb analysis was not complicated by extra redeposition of copper. These grids required some preliminary FIB machining to create a flat surface for foil attachment. The probe is brought back into the chamber and lowered to the prepared grid area. The sample is attached to the grid, again with Pt deposition, and removed from the probe. The best method to secure the sample and avoid bending during thinning was to attach the sample at both bottom corners from both sides [13].

The FIB foil at this time is about 800 nm and the goal thickness of a final specimen is $90 - 150$ nm. The foil is thinned from above to avoid ion implantation and damage. At different thicknesses, lower ion beam currents are used, also to avoid damage. The outer edges are kept thick for stability, with dimensions of about $(10 - 15)$ $\mu m \times (4 - 7)$ μm the final electron transparent region. Challenges of this step include curtaining due to milling rate variation across the sample, and sample bending due to internal stresses (and stress relief) in the material, Fig. 2.5d-g .

[12]Molybdenum OmniProbe lift-out grids were primarily used. Mo PELCO grids were used, but found to be too thick near the sample and shadowing was significant without > 1 h extra prep time.

[13]Physical rotation of 180° is required to attach from both sides.

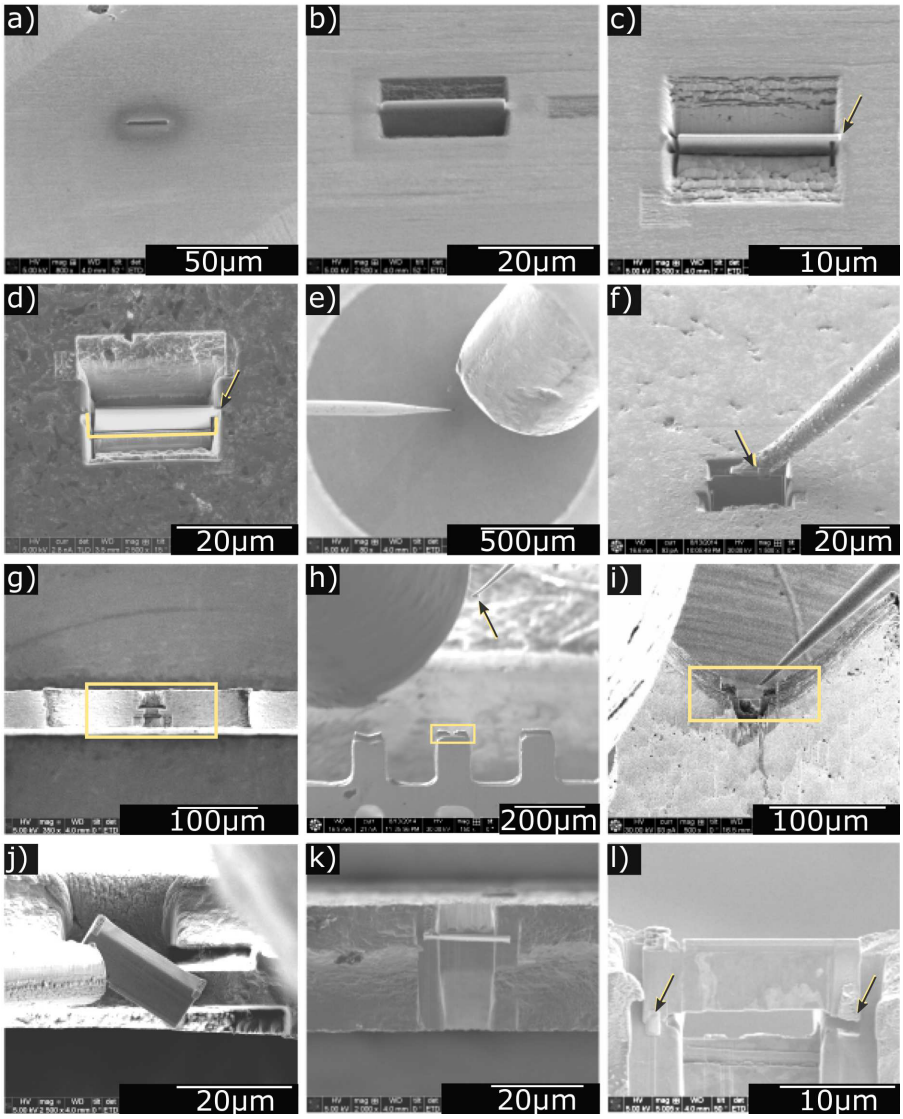


Figure 2.4: a) Deposited Pt. b) Angled side view of foil, Pt top with roughly trenched sides. c) Top view of foil, final thickness with U-cut. Arrow indicates the small section by which it is still attached to the bulk. d) Angled side view of U-cut foil. e) Pt needle (right) and Omniprobe manipulator (left) before lift-out. f) Omniprobe attached to foil by Pt deposited square (shown with arrow). g) PELCO Mo grid pre-cut to accomodate FIB foil with minimal shadowing. h) Side view of Omniprobe Mo grid pre-cut, with Pt needle and foil (on manipulator). i) Foil in place on Mo grid to be attache dwith Pt. j) Static forces stick foil to manipulator (in the wrong orientation) when Pt attachment between foil and manipulator was broken. k) Top view of foil, properly attached to Mo grid. l) Side view of foil, properly attached to Mo grid.

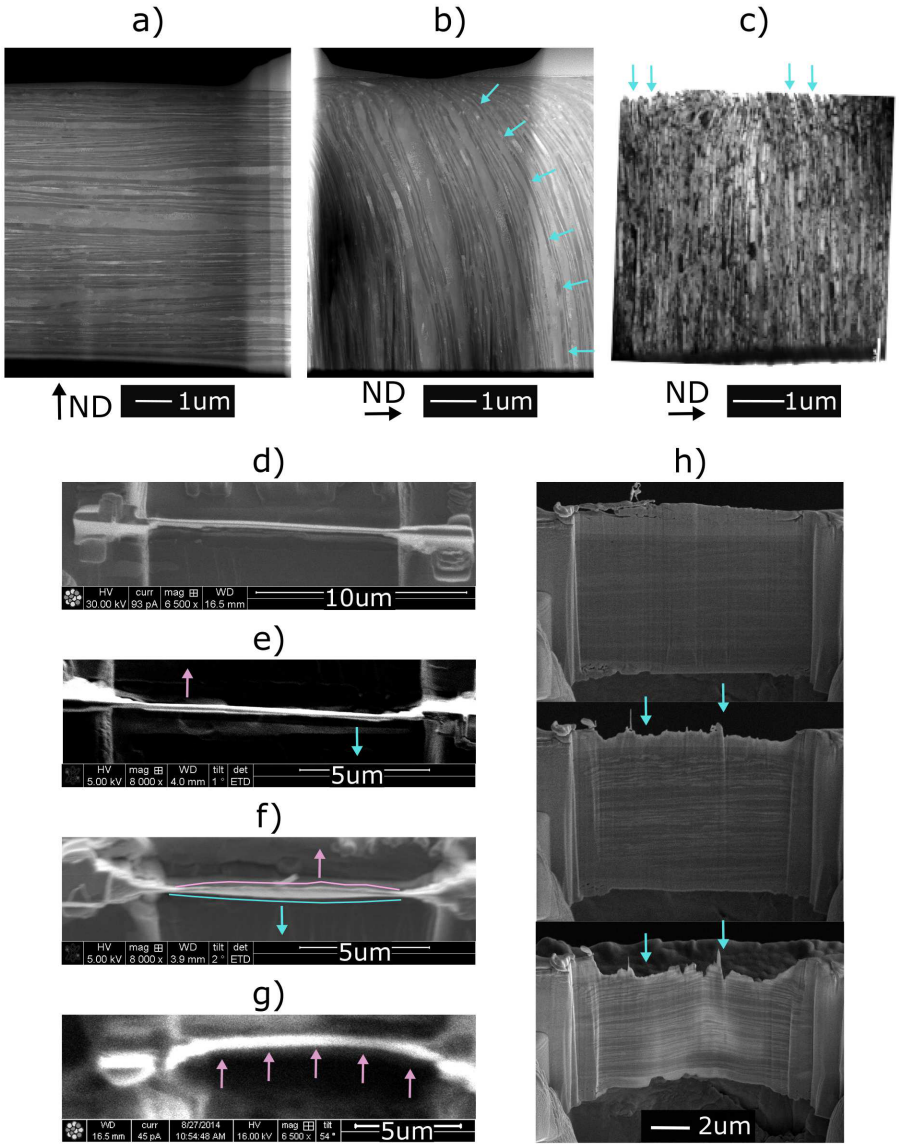


Figure 2.5: Challenges associated with FIB foil preparation. a) Correctly prepared Cu-Nb FIB foil. b) Foil taken from an unpolished bulk sample shows surface damage. c) Foil taken parallel to layer direction mills unevenly. d) Shows a good FIB foil, without bending. e-g) Show foil bending do to stress relief and ion implantation during final thinning. e) left and right bow to opposite sides. f) top and bottom bow to opposite sides. g) entire foil bows to one side. h) Shows a progression of thinning which results in bad curtaining effects at indicated regions.

2.2 Microscopy Procedure

Figure 2.2e-f features the FEI X-L30 SEM and TITAN TEM instruments at UCSB used for characterization of this Cu-Nb material. Both scanning and transmission electron microscopy (SEM and TEM) are necessary to characterize Cu-Nb in the range of length scales interrogated for this study. For larger layer thickness laminates, SEM backscatter electron detection and diffraction techniques (BSE and EBSD) were used to evaluate layer morphologies, and grain size and orientations, respectively. Smaller length scale laminates were analyzed via TEM with scanning (S)TEM capabilities and a high angle annular dark field (HAADF) detector.

2.2.1 Scanning Electron Microscopy

Microscopy was performed on an FEI XL-30 with an EDAX detector for electron backscatter diffraction (EBSD) analysis, and a backscatter electron (BSE) detector. Sample stubs were chosen based on imaging techniques: BSE samples were mounted on flat stubs and imaged at 0°, EBSD samples were mounted on 45° stubs and imaged at 70°.

An accelerating voltage of 20 kV and a spot size of $4 - 6$ was used for standard operation and alignment. Atomic contrast using BSE detection allows for identification of copper, atomic number 29, and niobium, atomic number 41, layers as dark and light phases. Optimal contrast was achieved at lower accelerating voltage (15 keV).

EBSD was used to collect orientation, phase, as well as grain size and shape information. Accelerating voltage, spot size, and step size were varied depending on the laminates interrogated. No one step size fully captures annealed grain structures

in Cu-Nb because of the difference between Cu and Nb grains. Smaller length scale laminates experienced significant drift due to charge build-up at small step-sizes and long dwell times.

Aligning the layers of a sample perpendicular to the scanning direction (vertical in the image) was optimal for minimizing effects of drift and shadowing effects of surface relief.

2.2.2 Scanning Transmission Electron Microscopy

The ARB Cu-Nb system is quite difficult to analyze via TEM because it is two phase and nanocrystalline. The primary challenges are discerning between Cu and Nb phases, and imaging representative defect structures in multiple grains. The best way to analyze these materials is by imaging the same region of a sample with a variety of contrasts. An FEI TITAN with scanning transmission electron microscopy, (S)TEM, capabilities was used for the majority of TEM images. This microscope does not have a full (S)TEM detector, which would collect both direct electrons and a large range of scattered electrons; this set-up detects the outter most scattered electrons with a High Angle Annular Dark Field (HAADF) detector. Contrast variation between images can still be achieved with this detector with various realignments of the beam and focal planes. The (conventional) HAADF contrast (S)TEM images were created using low camera lengths (between 48mm and 100mm). Low Angle Annular Dark Field (LAADF) contrast (S)TEM images were created using high camera lengths (between 480mm and 600mm). Bright Field (BF) contrast (S)TEM images were created by shifting the direct beam onto the HAADF detector; at high camera lengths (600mm) this does not change the beam alignment or affect image quality significantly. Figure 2.6 is a schematic showing

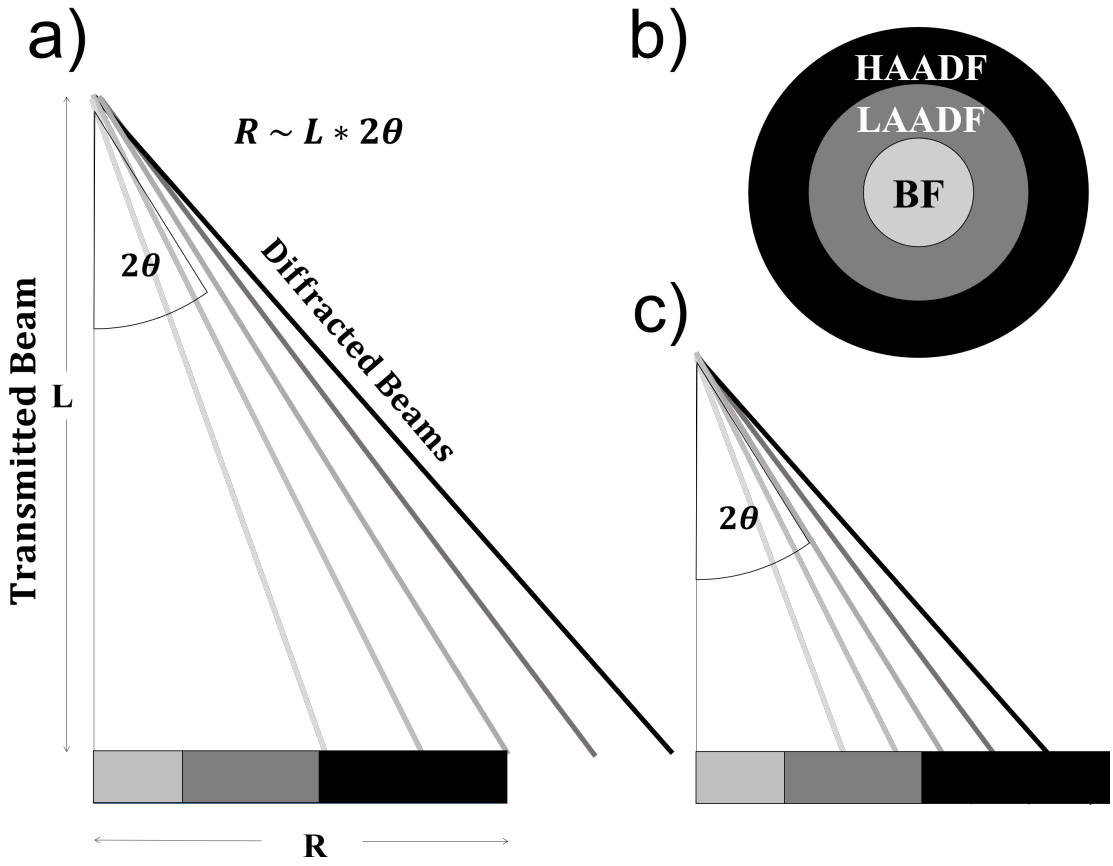


Figure 2.6: Schematic of (S)TEM detectors and the effect of changing camera length. a) High camera lengths place diffracted beams with low scatter on the HAADF detector. b) shows the top-view of (S)TEM detectors which are cross-sectioned for the other schematic views. c) Lower camera lengths place diffracted beams with higher scatter on the HAADF detector.

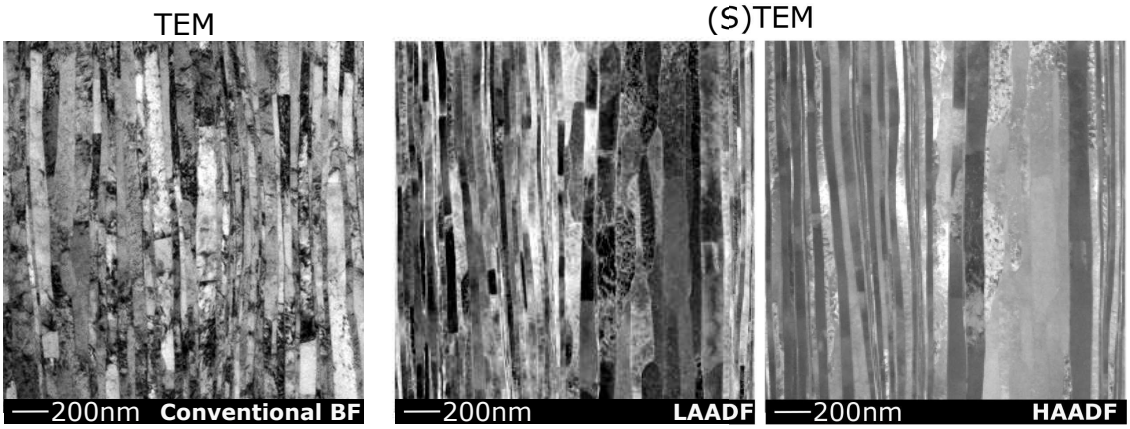


Figure 2.7: Compares contrast in TEM and (S)TEM images for 30 nm Cu-Nb laminates. TEM , left, shows boundaries and defects very clearly, with no way to discern phase other than performing diffraction pattern analysis within individual grains. (S)TEM images show the same region highlighting boundaries and defects with LAADF contrast (center) and atomic contrast with HAADF (right).

the sections of a full (S)TEM detector and the effect of changing camera length on HAADF detection.

The daily procedure for TITAN alignment can be found in the Appendices. Additional custom alignments were saved for each imaging condition. This sped up accuracy of capturing the same region with different contrasts, opposed to the the alternative of imaging many with one contrast and trying to find those same regions after switching alignment.

(S)TEM imaging with HAADF contrast addresses the concern about phase identification. This type of image is created by electrons scattered from the direct beam at high angles, most notably Rutherford scattering related to the atomic number of the elements. Copper, atomic number 29, scatters less than niobium, atomic number 41, therefore HAADF contrast images clearly indicate the phase of different layers. The detector collects more electrons scattered at the higher angles, therefore in all HAADF images niobium is the lighter phase and copper is the darker phase.

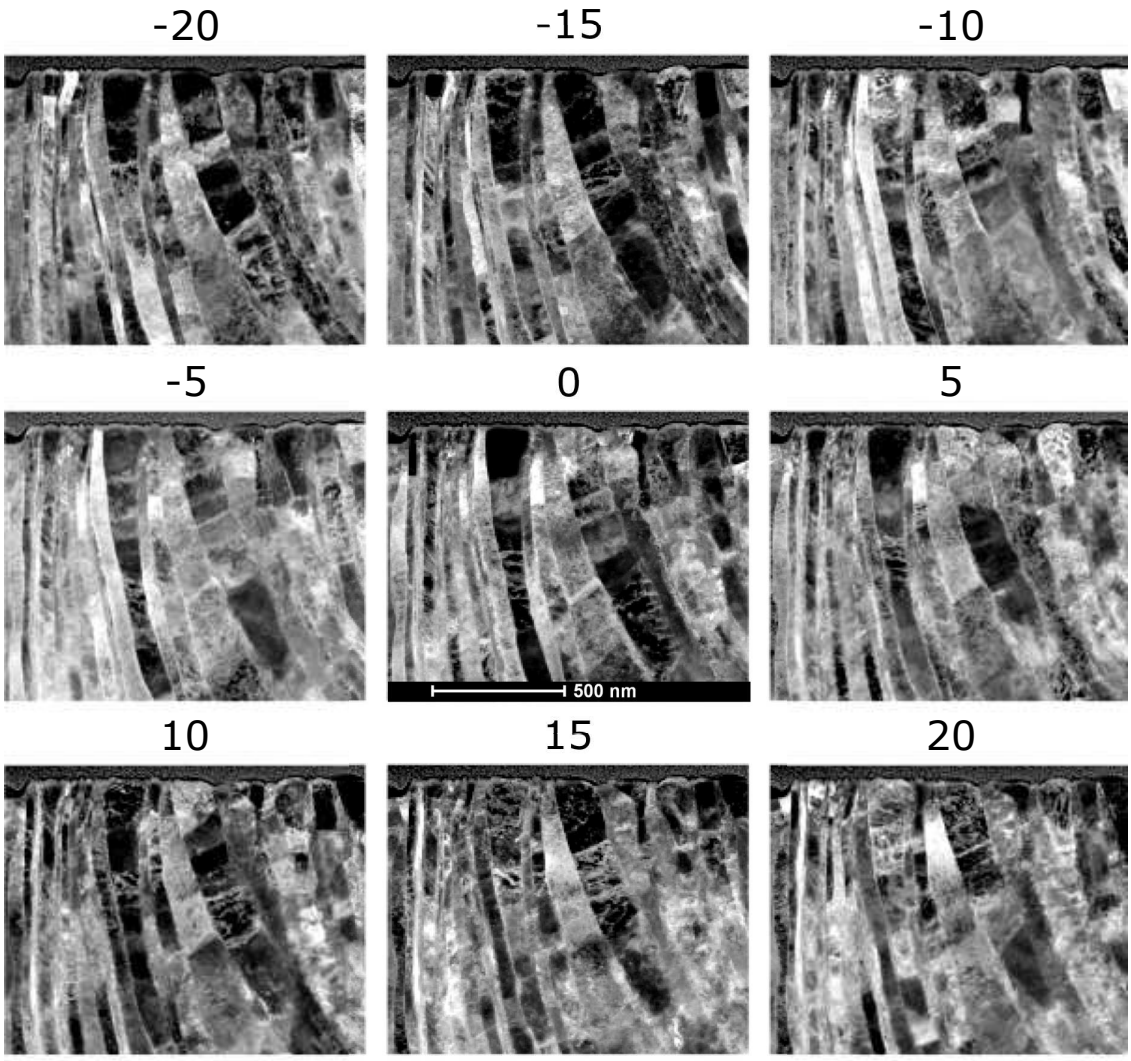


Figure 2.8: This kinked region of Cu-Nb was captured with LAADF contrast at angles from $-20°$ to $+20°$.

(S)TEM imaging with BF is very useful for finding voids. In both DF contrasts, voids are black (the absence of scattered electrons), which is often difficult to discern from boundaries. In BF contrast, voids are white (direct electrons), which is rare in the rest of the image, as there is significant defect and boundary content within these materials.

(S)TEM imaging with LAADF contrast highlight defects, grain and phase boundaries. TEM DF imaging is most useful when all grains investigated have the same crystal orientation for a given diffraction condition. Although the phases in ARB Cu-Nb are highly textured in the laminate overall, there is not a single diffraction condition that is conducive to analyzing defect structures locally for all grains. LAADF shows defect contrast for all diffraction conditions that lie within the area of the annular detector, rather than a particular diffracted beam condition. A comparison of images taken in HAADF and LAADF contrast is shown in figure 2.7.

Changing the contrast of defects and crystals can be achieved by tilting the sample, which shifts the diffraction pattern and changes the diffraction conditions in the detector area. Although the defect contrast is not as stark as traditional DF, LAADF requires less tilting in order to confidently identify defect concentrations and patterns because of this range of conditions illuminated. Single crystal regions of Cu and Nb phases must be analyzed at several tile angles to fully assess the extent of dislocation content in all regions. Figure 2.8 shows the same area at a range of tilt angles in LAADF contrast, demonstrating this principle.

2.3 Heat Treatment Procedure

Heat treatments were performed with varying procedures. All annealing was performed in inert environments to prevent oxidation. Some contrast change was observed, likely due to burn-off of hydrocarbons and other contaminants adhered to sample surfaces. All surface layers were removed prior to analysis.

At U.C. Santa Barbara, materials were vacuum encapsulated in quartz. Cu-Nb was ultrasonic cleaned in acetone to remove any oils before encapsulation. This procedure was performed on 65 nm material annealed for extended times (400 °C and 500 °C for 5, 15, and 30 days) including the annealed creep specimen. Furnaces were heated to temperature, then samples were placed into the chamber from room temperature, and removed to cooled in air. The furnace was opened briefly to incrementally remove 65 nm Cu-Nb samples over the 30 day period (at each temperature). Recovery annealed samples (400 °C for 30 min) were annealed in a quartz tube furnace in an argon atmosphere with 10 °C heating and cooling ramp.

At Los Alamos National Laboratory, materials were heat treated in large quartz tube with a controlled environment. Oils and marker were wiped away with acetone-soaked cotton swabs. This procedure was performed on material annealed for 2 days (400 °C and 500 °C) and material annealed to produce large single-crystalline layers (600 °C for 30 min , then 800 °C for 2 hr). In this system, samples were loaded outside of the hot-zone. The tube was back-filled with argon, then evacuated to vacuum. Vacuum was sustained during heating. Samples were placed in the hot-zone for the duration of annealing and removed, with a manually controlled manipulator, to cool in vacuum.

2.4 Creep Testing Procedure

Designing a creep set-up and procedure for Cu-Nb ARB multilayers was not a trivial task, as no analogous systems have ever been investigated in this way. The majority of existing creep test set-ups available at this University are in open air, and standardized for round specimen geometries. A customized set-up was required for creep testing of oxidation-prone, bulk sheet material.

2.4.1 Design of Experiment

Custom Bulk Sheet Gripping

Grips were designed to accommodate the approximately 3.6 mm thick samples and provide ease of sample alignment. The design was based a previous version, shown in figure 2.9 of a sheet-gripping which cannot accommodate high temperatures or smaller sample geometries. Steel pins fit through Cu-Nb samples and into both sides of a clamp which slides up and down to tighten or loosen grip.

Rotation about the pin can occur during loading to vertically align the sample with respect to the loading axis. Screws were added to grips to fix the location of grips centrally in line with the grip axis (ie: prevent sliding left and right of the grips themselves). Molybdenum disulfide powder was used to lubricate the sliding grips.

Protective Atmosphere Chamber

A non-oxidizing environment was designed to fit on an Instron 5882 frame, shown in Figure 2.10. A quartz tube diameter and length were chosen based on grip fixture diameter and clam-shell furnace dimensions. Steel end caps were designed

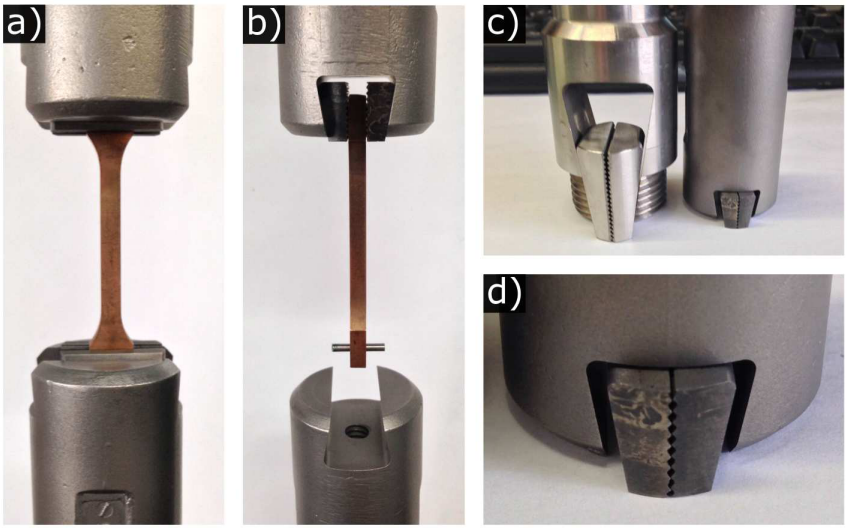


Figure 2.9: Custom grips made from inconel 718. a) front view of a dummy sample in grips, aligned to center. b) side view of sample in grips with steel pin exposed. One can also see the alignment screw in the bottom grip. c) show both the custom grip, and the previous design on which the custom grips were based. d) is a close-up of the grip area.

and machined to fit this quartz tube and frame extension bar, with ports to flow argon and directly measure sample temperature with a thermocouple. Cooling channels were also machined to flow water and prevent expansion of end caps which are very near to the furnace. The quartz tube was sealed by end caps with vacuum grease and rubber O-rings.

A continuous flow of pre-purified Argon gas flowed through steel lines[14], through a titanium getter[15], and filled the quartz tube from the bottom. Purified Ar was flowed through the system for an hour to ensure that the environment was inert prior to sample heating. Outgoing argon flowed through an oil bubbler, to prevent back flow of air, and further through a water pressurized bubbler which provided overpressure to the system and counteracted any potential leaks.

[14]Plastic lines can introduce contamination.

[15]Ti getter was heated above 850 °C and Ar was flowed through the system prior to heating for 10 *min*.

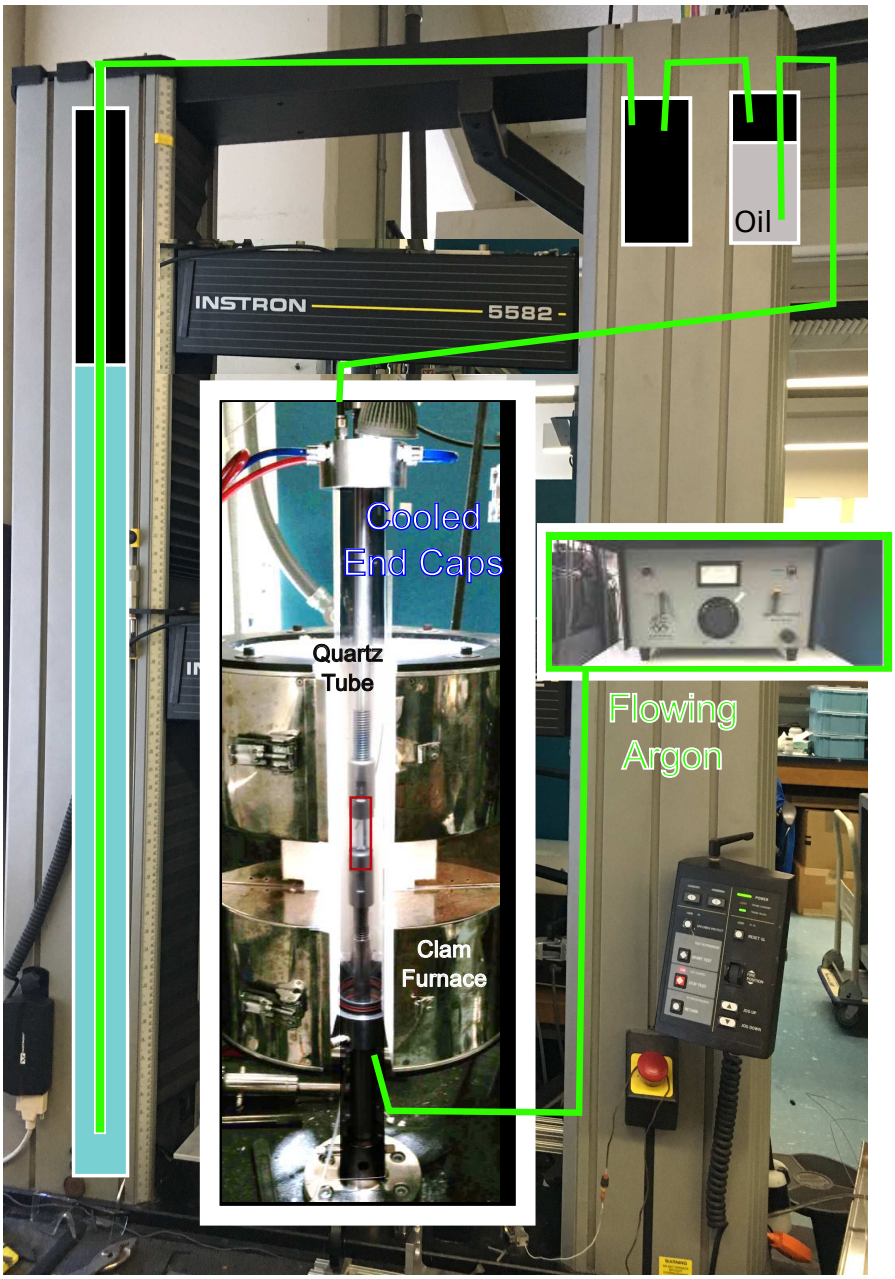


Figure 2.10: This photograph of the Instron 5582 frame was embellished and labeled to highlight the argon pathway through the set-up. The Ti gettering gas purifier connected to the enclosed quartz tube which connected to an oil bubbler. This system was pressurized by a water bubbler, and gas ultimately escaped. The clam shell furnace surrounding the quartz tube was aligned for visual analysis of the sample through a view port.

Testing Conditions

In order to compare the competing effects of enhancing initial strength and reducing thermal stability at low length scales, creep experiments were performed on ARB Cu-Nb laminates with layer thicknesses of 65 nm, 200 nm, 500 nm, 2000 nm, and 8000 nm.

Appropriate testing conditions to get measurable creep rates without immediately yielding the material ($10^{-9} < \dot{\epsilon} < 10^{-5}$ s^{-1} were determined based on knowledge of room temperature composite yield strengths and a trial and error testing. Initially performing creep tests to failure, comparing creep rate measurements to previous work, and adjusting the loads.

All tests were performed at 400 °C. The homologous temperatures of Cu and Nb are significantly different at this temperature, $0.5T_m^{Cu}$, and $0.25T_m^{Nb}$, respectively. Creep mechanism maps were approximated for very small grain sizes, shown in Figure 2.11. The creep testing conditions are plotted on these maps. The intent of testing under these conditions was to determine length scale degradation effects on mechanical behavior by aiming for a dislocation dominated (length scale independent) mechanism regime for both phases.

2.4.2 Set-Up and Procedure

Dogbone specimens were machined using a wire EDM. A schematic of the specimens used for all tests is shown in figure 2.12, labels in millimeters. The dogbone shaped samples had rectangular cross-sections approximately 3.6 $mm \times 3.5$ mm and gauge length 24 mm. The sample face was perpendicular to the sheet normal direction and load axis parallel to the rolling direction. Pin-holes were made using a hole EDM for alignment precision.

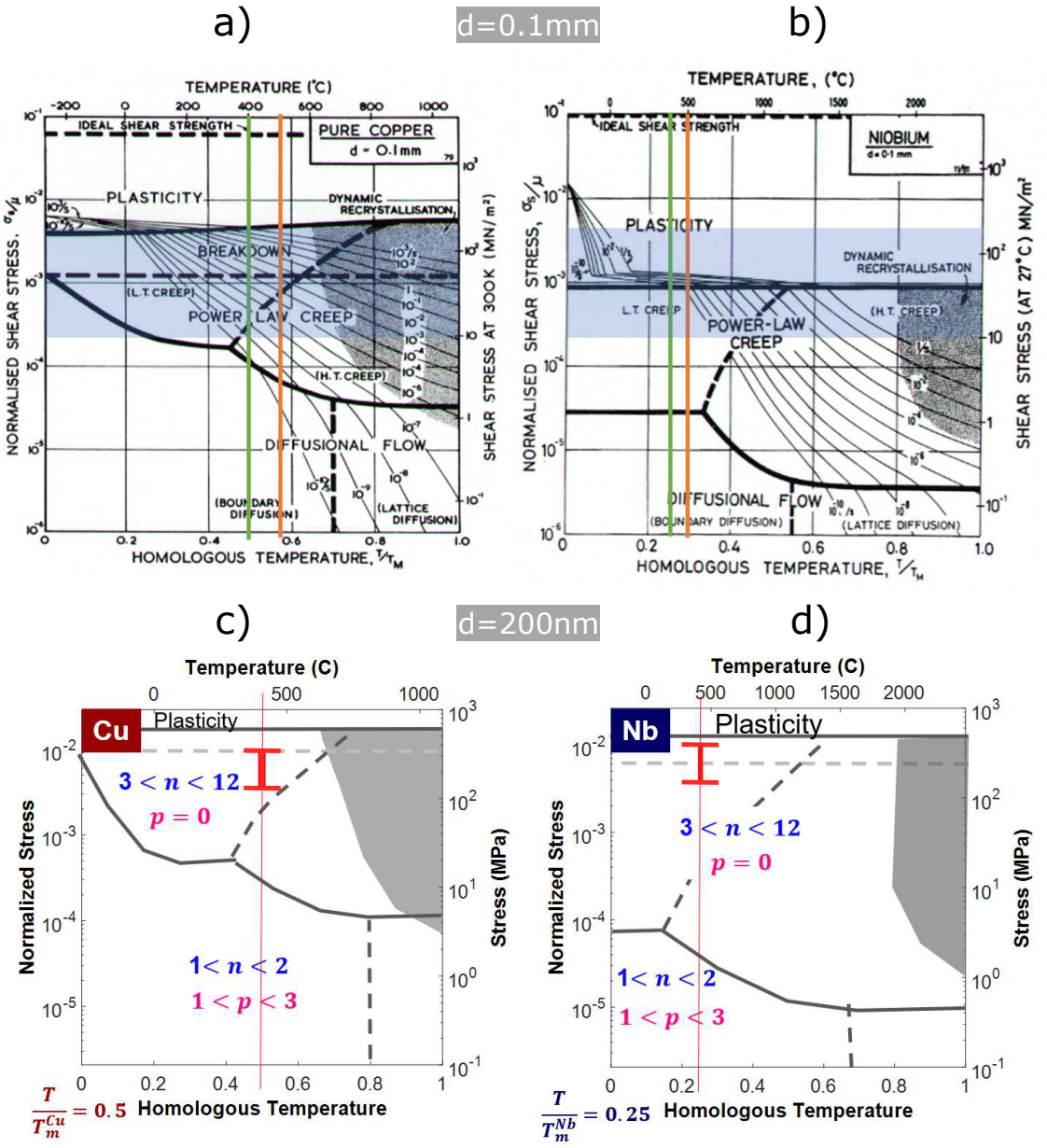


Figure 2.11: Creep mechanism maps for Cu (left) and Nb (right) are shown for small grained, pure materials both from literature, a) [104]) and b) [105]) with grain size d=100μm and approximated, c) and d) for grain sizes d=200nm . The shaded region indicates the range of stress conditions that will be covered by the experiments. The vertical lines lie at the temperatures chosen for creep, 400 °Cand 500 °C. Smaller grain size will increase the size of the boundary diffusion region and increase the value of stress achievable before plasticity.

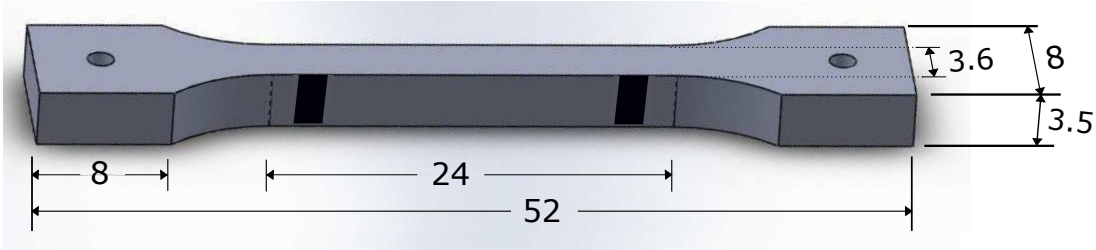


Figure 2.12: Creep and high temperature tensile test sample geometry shown here. Pin holes were 1.59 mm diameter. All dimensions are shown in millimeters.

EDM damage was removed with SiC grinding papers to 1200 grit [16]. Samples were cleaned in acetone and isopropyl alcohol. 3M fine line striping tape was used to cover the sample, and uniform sections were removed, creating a mask in the gauge section. Graphite spray paint was used to paint 2 uniform lines [17]. After paint dried for at least 4 hours, tape was carefully removed. Any excess adhesive was removed with an isopropanol soaked Q-tip.

Pins were inserted through dogbones and grip sections. The outer part of grips was lubricated with molybdenum disulfide. Grip sections and sample were slid into the outer part of grips and screwed (lightly) in place, one side at a time.

End caps were lubricated with vacuum grease. The top connecting bar for the load frame was attached above the sample, with the top end cap attached. Next, the sample (in grips) was attached to the top bar. At this point, the frame load was zeroed, to reflect only the stress applied to the sample (not including the top half of the set-up (which was about 30 N). The bottom connecting bar was then attached, with the load frame fully extended. At this point, the quartz tube was carefully placed around the sample and into the top end cap [18]. The bottom end cap

[16]Sides were polished in a circular motion to make reflection of light as uniform as possible.

[17]If paint was too thin, gauge lines were not bold enough for image processing. If paint was too thick, it chunks of it could crack and fall off during elongation.

[18]This had to be manually supported until the bottom load frame connector was attached.

was secured on the quartz tube and around the bottom connecting bar [19]. Finally, the bottom load frame connector was attached, supporting the end cap and quartz tube.

The load frame extension was manually decreased and fixed to the load frame with a large pin. At this point, all external tubes were attached to the end caps: water cooling, argon, and thermocouple. Argon was turned on and adjusted to flow through the set-up for 15 minutes before the gas purifier began to heat up. Small adjustments were made to align tubing and orient the sample for optical strain tracking. A slight tension was applied to the sample for grip alignment.

The clam-shell furnace was adjusted (up and down) to align with the sample's vertical location. The furnace was locked in place and closed. Extra (soft) furnace insulation was used at the open ends to fill gaps between the quartz tube and hard furnace insulation [20]. Next, the camera and lighting were adjusted for optimal sample visibility and contrast.

After an hour, the gas purifier would reach an appropriate temperature. Water cooling was turned on. At this point the "Pre-Creep" procedure was started using Bluehill software. This procedure adjusts load frame extension to keep a constant load (50 N) on the sample during thermal expansion. The AutoHotKey program to use DigiCam Control software for image capture (every 90 seconds) was started, and TRH central thermocouple tracking software began recording temperature. DigiCam Control software was set to record raw image files named by "SampleName"_"CreepStress"_"TIME STAMP"_ "6-Digit-Numbering", with time stamps in seconds. "Creep stress" for the pre-creep procedure was labeled "exp",

[19]This must be done VERY carefully because any movement upward of the sample takes pressure off of the grips (which align with tensile load) and can cause misalignment.

[20]This changed the variation between furnace temperature and sample temperature by $40 - 60$ degrees

for expansion. Images were saved directly to an external hard drive[21].

The furnace temperature was manually ramped to temperature over one hour. Sample and set-up expansion occurred for that hour and one full hour after set temperature was reached. The system was allowed to sit at full expansion for another hour before the application of any load.

After full extension and stabilization, Bluehill "creep" was set to the load (calculated for applied stress and sample dimensions)[22]. The AutoHotKey program was changed to capture an image every 5 seconds during loading. Load was applied at a constant rate of extension (0.4 mm/min) until the desired applied stress (between 150 MPa and 350 MPa) was achieved[23]. Creep load was sustained for a minimum of 36 hours before interruption. The AutoHotKey program was changed again (every minute for 15 hours, then every 90 seconds from there on), and DigiCam file name was changed for the following images.

At the testers discretion, images from every hour were selected and analyzed using the strain tracking procedure, explained in the following section, to "check in". During a check, approximate strains and strain rates were determined. When it was apparent that creep rates were fairly constant for over 15 hours (24 hours if creep rates were below 10^{-8} s^{-1}), the creep program was stopped, the load was increased, and the program was re-started for the new load (again, changing file names). These checks were unnecessary for non-jump tests.

The furnace controller was set to a digital input, which could be shut off with Bluehill software[24]. The test was monitored via Teamviewer for the duration of

[21]The computer storage was insufficient, and data analysis was performed on other computers.

[22]Because these tests last so many days, data capture rate must be lowered from default or the computer runs out of space and automatically stops the program.

[23]Time to creep load varies with creep stress because of this constant extension of the frame

[24]The versions of Bluehill that UCSB owns do not have the ability to shut off this input when the test ends

the test (every few hours during tertiary) so that the tester could remotely shut the furnace off once sample failure occurred. Image capture was also turned off remotely. Once the set-up returned to room temperature, water cooling, argon flow and gas purifier were shut off.

All tubes were removed from end caps and furnace was opened. Frame was manually extended to maximum height. The bottom frame and bar connections, with the bottom grip and half of the sample, were removed along with the bottom end cap, which was carefully separated from the quartz tube. The quartz tube was then carefully separated from the top end caps and cleaned thoroughly with alcohol and Kim wipes to remove any burned off hydrocarbons and vacuum grease.

2.4.3 Optical Strain Tracking

As shown in Figure 2.13, specimens were marked with a graphite paint in order to track sample elongation. Using a Nikon D5200 camera, 6000×4000 pixel images were captured every 60-90 seconds for the duration of the test, processed with Image J software, and analyzed using Matlab in order to calculate the sample strain at a given time.

Several programs were used to make this strain tracking possible. AutoHotKey was used to record a "click" action in specific programs and a loop was programmed to set this click at certain locations and time intervals. DigiCam Control was used to operate the Nikon camera. This program could control focus, contrast, and image capture. It also recorded the time of each picture in seconds. A Windows Batch File was used to create a .txt file of the numbered and time stamped file names, which would ultimately be used to calculate strain rates in matlab[25]. Nikon camera software was used to batch process all images and rename the files without

[25]Windows Batch File : $dir > original_times.01.txt$

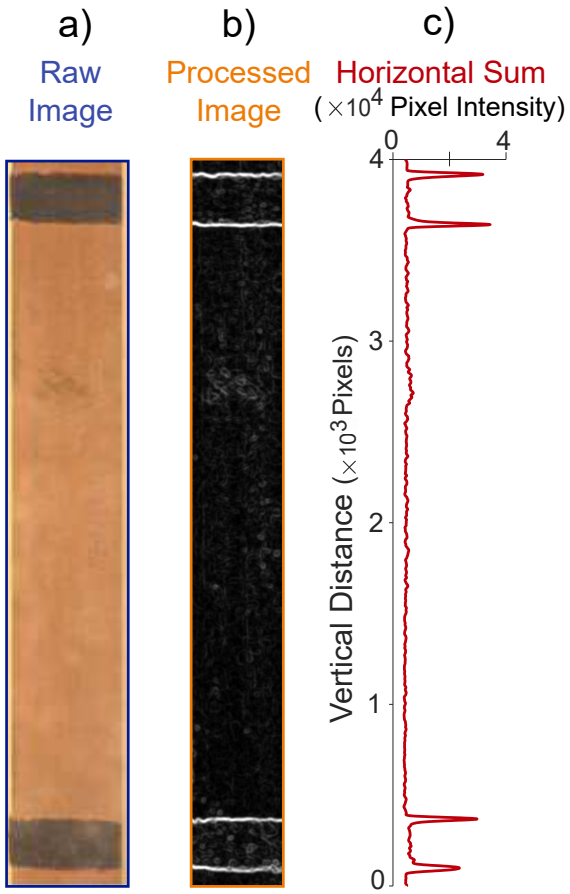


Figure 2.13: Specimen gauge section showed as captured (a), after processing image to highlight gauge line "edges" using Image J (b), and as graphed intensity of those edges as summed across pixels using matlab code (c).

time stamps.

Raw images were processed using Image J. Raw images were uploaded using the plugin "DC RawReader", cropped to an area containing only the gauge section, then processed to emphasize the edges of graphite painted regions. This procedure can be found in the Appendices. Macros changed slightly for every sample due to file naming and exact camera location[26]. Processed images were saved as .tiff files, which can be uploaded to matlab.

[26]the cropped regions vary as the sample elongates. This change was noted and adjusted for every test

Matlab code was written to loop through all processed images and sum the intensity of pixels horizontally across the image. The result was a plot of intensity as function of vertical pixel location which gives four primary peaks at the location of painted gauge edges, as shown in Figure 2.13c. The program located those peaks, calculates 2 gauge lengths and averaged them. Strain was calculated with respect to the gauge length of the sample before thermal expansion. The full matlab code can be found in the Appendices.

The result of this analysis was a list of all strains and times associated with the images captured during expansion, loading, and creep. Creep stresses were noted at creep jump intervals.

2.4.4 Creep Rate Fitting

Matlab Spline Fitting

Matlab's "smoothing spline fit" was used to smooth data, determine minimum and maximum creep rates, and identify linear regions. Details of smoothing spline code are in the Appendices.

2.5 Hardness Procedure

Hardness values were used only to assess relative effects of heat treatment on mechanical deformation response. Figure 2.14 is a schematic of the Vicker's hardness geometry. Vicker's indentation involves a pyramid shaped diamond tip with triangular faces at a 136° angle apart. Indents are square with flat edges and appear to have an "×" from the corners. The diagonals which make up that "×", labeled

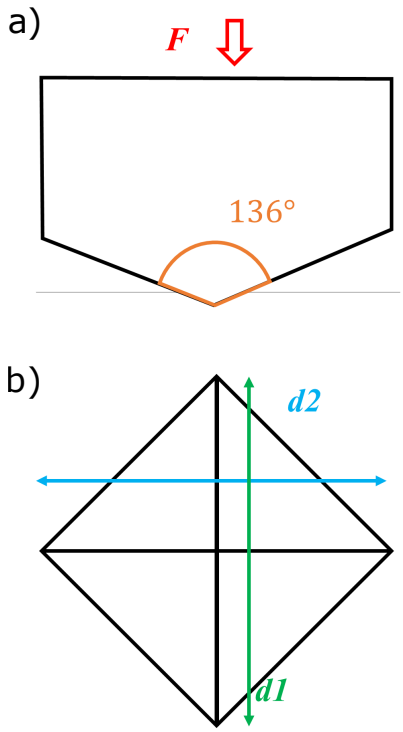


Figure 2.14: Schematic of Vicker's indent geometry. a) shows a side view of Vicker's tip indenting a sample. b) shows a top view of the indent shape.

$d1$ and $d2$ in Fig. 2.14b, are measured individually and averaged (d).

$$HV = Sin\left(\frac{136^\circ}{2}\right) \times \frac{F}{d^2} \approx 1.854 \times \frac{F}{d^2} \tag{2.1}$$

Load, F, is in kgf units and diagonal, d is in millimeters. A weight of 1000 kg was applied to the indenter (985 kgf when accounting for the set-up). This weight was determined to be optimal for the Cu-Nb system because indents span several layers [27] and good optical microscope resolution is achieved at a constant magnification.

Indents were captured with a Keyonce optical microscope and analyzed consistently using Image J software. Measurements were performed to match measurements on a steel calibration sample of known hardness.

[27] 80 $\mu m < d <$ 160 μm for all Cu-Nb tested, 15 $nm > h >$ 8 μm , regardless of heat treatment

All samples were polished to 1200 grit SiC or finer. At least 5 indents were made per sample, and at least 4 measurements were used to calculate hardness[28]. Indents were made a minimum of $3d$ away from one another, and $4d$ from sample edges.

2.6 High Temperature Tensile Procedure

The set-up and strain tracking for tensile testing at 400 °C was the same used for creep testing. The beginning of the procedure is also similar to the creep test procedure: samples were pre-loaded, temperature was ramped, and expansion in the sample and system was allowed to stabilize before loading.

All tensile tests were performed in extension control. ECAP Nb and 200 nm Cu-Nb samples were performed at a slower rate of extension.[29][30] Rates of extension and strain rates for all high temperature tensile tests is noted in figure 2.15. The fasted strain rate achieved was 2×10^{-4} strain per second.[31]

[28]Outliers were neglected. This often was associated with indents made too near to rolling defects or to beveled regions.

[29]These were the first samples tested and it was determined that such a slow rate was unnecessary.

[30]At such a slow rate, with elongations to failure over 10 %, the test took over an hour to run. Exposing the samples to temperature for longer times may make the tests less representative of the loading experienced during creep testing.

[31]Frame compliance cannot be neglected until strain is over 5 %.

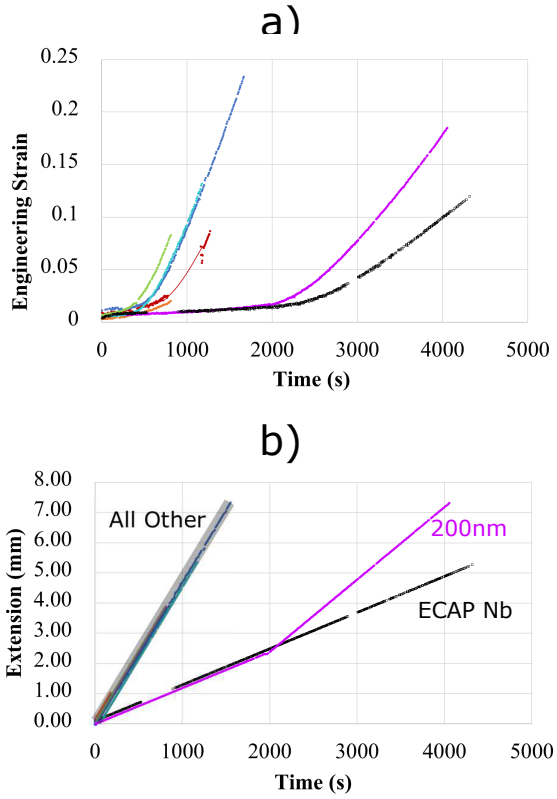


Figure 2.15: Sample strain (a) and frame extension (b) over duration of tensile tests. Strain rate varies throughout the tensile test. Maximum strain rate achieved was 2×10^{-4} $\frac{1}{s}$. Extension control varied for 2 samples.

Chapter 3

Cu-Nb Creep

This Chapter investigates the dependence of creep properties on layer thickness. Tests were performed at a moderate temperature and high stresses relative to the pure metallic constituents. Samples were characterized in detail by scanning transmission electron microscopy to evaluate creep mechanisms and structural evolution.

The creep behavior of bulk, accumulative roll bonded (ARB) Copper-Niobium (Cu-Nb) composites has been studied at 400 °C as a function of layer thickness, ranging from 2 μm to 65 nm. Similar to single phase metallic systems, three regimes are observed during creep: transient, steady-state and tertiary. The mechanism controlling minimum creep rate for all conditions tested has a strong dependence on stress, consistent with dislocation-dominated creep. Unlike the conventional effect of grain size on creep resistance, the unique result of this study reveals that *decreasing* length scale *increases* creep resistance.

3.1 Background

Creep deformation occurs at elevated temperatures and constant applied stress. Materials typically exhibit three stage creep behavior: primary, secondary, and tertiary. Primary creep is associated with structure evolution within grains, like defect generation and substructure formation. At steady-state deformation is dominated by one mechanism because the rates of defect generation and movement of atoms is constant and at a minimum. Tertiary creep occurs when enough damage accumulates to introduce voids which coalesce and ultimately cause sample failure.

Material lifetime is often measured relative to the steady-state, or minimum, creep rate. Understanding the mechanism of steady-state creep can inform design of new materials systems and longer component lifetimes. The Mukherjee-Bird-Dorn steady-state creep rate equation describes the parameters of a creep mechanism:

$$\dot{\epsilon}_{SS} = \frac{A_{cr} G b}{kT} D_0 \exp\left(\frac{-Q}{RT}\right) \left(\frac{\sigma_a}{G}\right)^n \left(\frac{b}{d}\right)^p \tag{3.1}$$

where T is temperature, k is the Boltzmann constant, σ_a is applied creep stress, d is material length scale, and the exponents n and p represent the deformation dependence on stress and length scale, respectively. When referring to single phase or homogeneous systems, A_{cr}, G, b, Q and D_0 are constant material parameters which can be found in literature or experimentally determined.

3.2 Relevant Experimental Details

In order to compare the competing effects of enhancing initial strength and reducing thermal stability at low length scales, creep experiments were performed

on ARB Cu-Nb laminates of 65 nm, 200 nm, 500 nm, and 2 μm layer thicknesses. All tests discussed in this chapter were performed at 400 °C. The homologous temperatures of Cu and Nb are significantly different at this temperature, $0.5T_m^{Cu}$, and $0.25T_m^{Nb}$, respectively.

Multilayer specimens were either tested at one creep load to failure, unloaded (interrupted) before tertiary creep began, or crept at multiple applied stresses over their lifetime. In the instances of creep load jump tests, creep was interrupted, and the load was increased after an apparent constant strain rate behavior (minimum $20hr$ at minimum rate). This procedure was repeated until tertiary failure occurred. Strain over time is graphed for all testing types in Figure 3.1. A "standard" creep test will reference all data collected from samples which have only seen one creep load. A "jump" test will refer to any data collected after a sample has experienced more than one creep load.

3.2.1 Creep Behavior

Raw data and fit curves for all creep tests, as well as a table of all Cu-Nb samples tested is included in the Appendix. Creep curves for all layer thicknesses at 400 °C (discussed in this chapter) are shown in figure 3.1. These curves show that the creep behavior of the metallic composite strongly resembles single phase metals, exhibiting transient, steady-state, and tertiary regimes. Despite process defects and the difference in homologous temperature of the copper and niobium phases, the multilayer system achieves a constant, minimum strain rate. Comparison of the creep response for selected tests in figure 3.1a shows that the smaller length scale laminate thicknesses have higher creep resistance compared to the larger laminates. Minimum creep rates have been analyzed using the Mukherjee-Bird-Dorn steady-

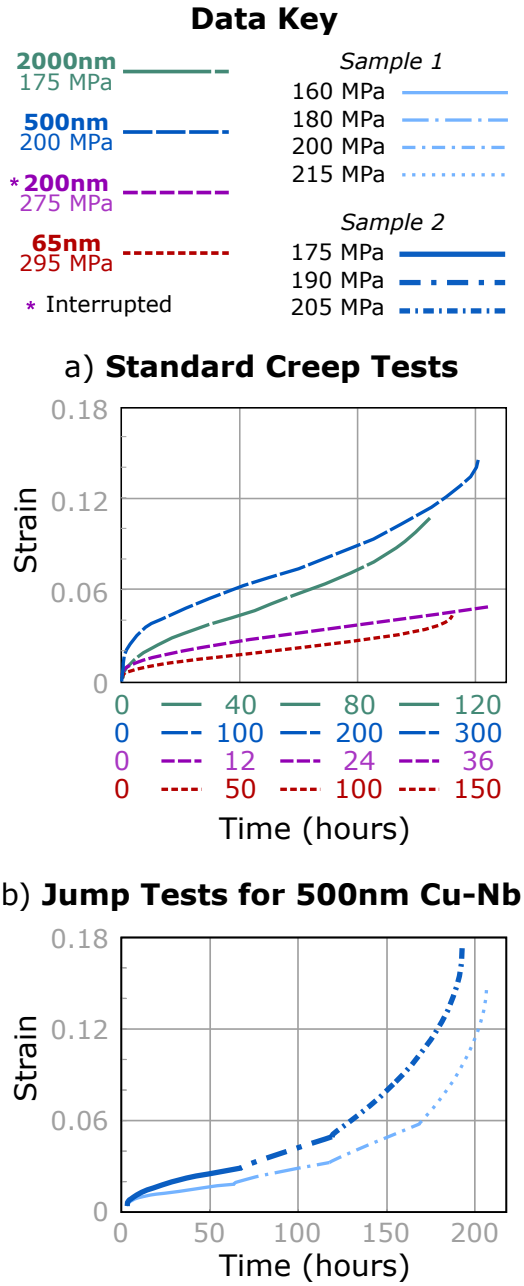


Figure 3.1: a) Standard creep tests: typical curves for all length scales showing transient and steady-state regimes. b) Jump tests for 2 samples of 500 nm laminate illustrating creep rates associated with multiple applied stresses for a given specimen. The solid lines are considered standard tests because specimen were subject to only one load for that duration. Arrows indicate load change.

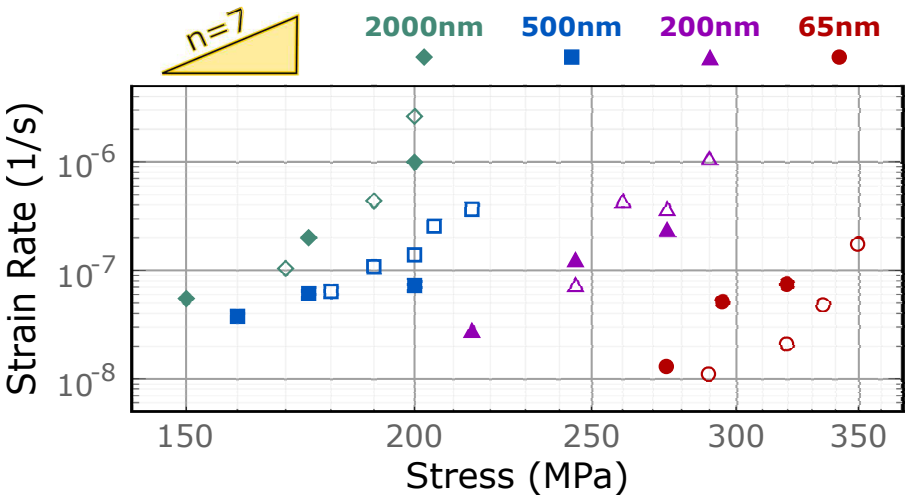


Figure 3.2: Minimum creep rate as a function of applied stress. Variation in length scale is noted with shapes. Standard tests are closed shapes. Jump tests are open shapes.

state creep rate equation, eqn. 3.1. Determining appropriate constant values of creep prefactor parameters for Cu-Nb laminates is complicated by the composite structure and presence of interfaces. The composite deformation is a complex combination of the individual phase behaviors, and it is likely that interface-controlled deformation mechanisms influence these behaviors. A reasonable assumption is that the material parameter values for the composite are also constant because steady-state behavior is observed, and they are constant within each phase.

Figure 3.2 shows minimum creep rate values as a function of the applied creep stress. The strain rates for each length scale have a high stress dependence. The creep stress exponent, at an average 7.2 with standard deviation ± 1.3, suggests that dislocation climb and glide likely controls deformation. The similar stress dependence of the creep rate across the layer thicknesses experimentally investigated suggests a constant deformation mechanism across the range of experimental conditions investigated: 400 °C, relatively high applied stresses, and relatively small length scales. With this assumption, a simplified form of eqn.3.1 allows for quan-

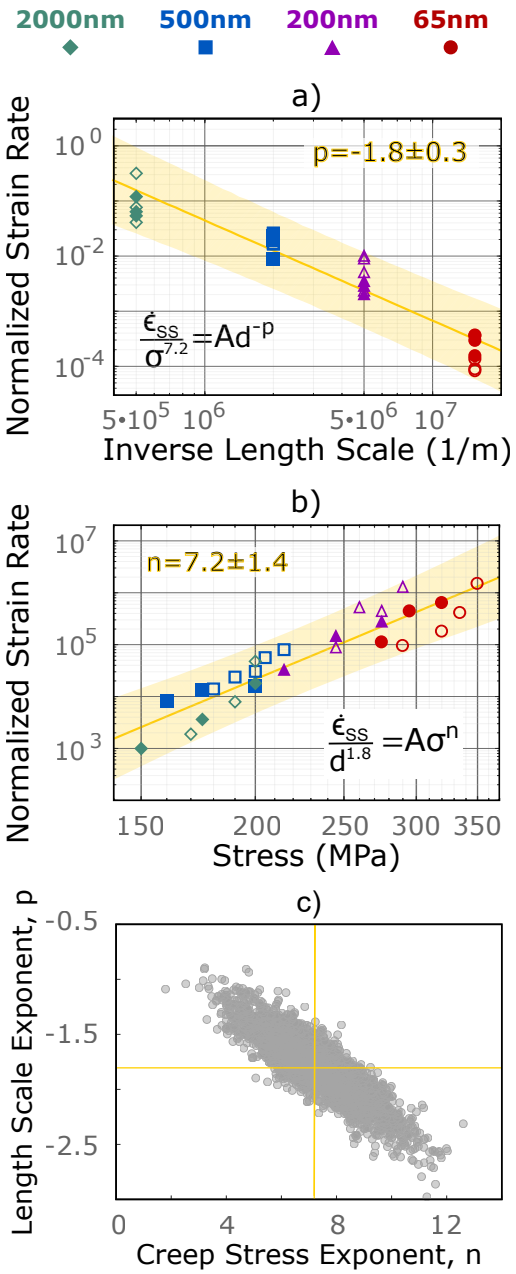


Figure 3.3: Shaded regions show 90 % confidence intervals of normalized rates predicted by fit values and experimental statistics. a) Normalizes minimum creep rates by $\sigma^{7.2}$ with units $s^{-1}GPa^{-7.2}$: slope of this plot is p. b) Normalizes minimum creep rates by $d^{1.8}$ with units $s^{-1}nm^{1.8}$: slope of this plot is n. c) Shows statistical sampling from posteriors of n and p values. Note the correlation of n and p pairs, and the average values used (marked with lines).

tification of the composite strain rate dependence on only the applied stress (σ_a) and material length scale (d), n and p, respectively.

Monte Carlo estimates were made using the statistical package Stan [106,107], assuming a lognormal distribution of minimum strain rates. Figures 3.3a and b show normalized strain rates which account for average values of the fit length scale and stress dependence, respectively. There is a correlation between the posterior predictive values of n and p , Fig. 3.3c. This is partially because of the difference in experimental stress range for each layer thickness (smaller length scales were crept at high stresses). The correlation also suggests that the stress and length scale dependences are not independent of one another, or that a length scale dependent strengthening mechanism is present. In all of the statistical samples fit to the experimental data, it is clear that p is a negative value and n is a high, positive value. Using average statistics from data sets of the tested layer thicknesses, the minimum creep rates can be predicted for Cu-Nb multilayers at any length scale and applied creep stress using the n and p values from this fit. The shaded regions of plots in Fig. 3.3 show the 90% predictive interval for minimum creep rate values given that $\dot{\epsilon}_{SS} \propto \sigma_a^{7.2} d^{1.8}$.

3.2.2 Structure Evolution During Creep

Creep induces structural evolution processes involving recrystallization, grain growth and layer pinch-off. Figure 3.4 shows TEM analyses of crept samples highlighting changes in grain and layer structure. There are several features which are key to understanding the deformation behavior of this composite: high dislocation densities, layer discontinuity, and Cu grain structure.

Both interrupted and failed specimens show similar, high dislocation densities

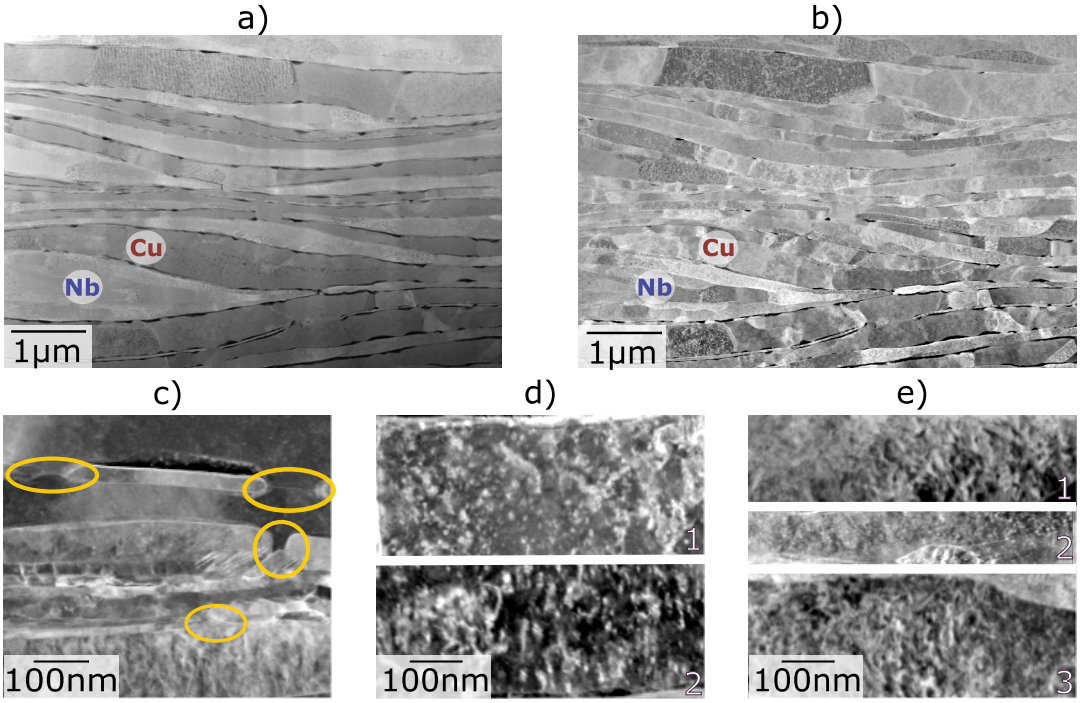


Figure 3.4: (S)TEM images feature crept Cu-Nb multilayer material with 200 nm nominal layer thickness. The same field of view is shown in a) and b). a) HAADF contrast shows Nb is the light phase, Cu is dark. b) LAADF contrast highlights grain boundaries and defects within the structure. c) is a close-up view of an area with significant pinch-off of Nb layers (circled). d) and e) show a similarly high dislocation density in Cu and Nb, respectively. Regions of different layers (2 Cu, 3 Nb) are shown on the same scale.

in both Cu and Nb layers, Figure 3.4d and e. Thus dislocations are active in both phases during deformation; however, it is difficult to assert the relative degree of dislocation activity in each phase. Nevertheless, the presence of significant densities of dislocations in both phases suggests that the creep mechanism is controlled by dislocation glide and climb.

A decrease in layer continuity after creep testing is observed for all length scales. Pinch-off areas within 200 nm thick Cu-Nb are shown in Fig. 3.4c. As predicted from boundary energies, the Nb layers are primarily subject to pinch-off [19, 66, 86], allowing Cu grains to span multiple layers. Larger layer thickness

laminates pinch off only at areas of shear localization and other regions with initially thin layers due to processing. In smaller length scale multilayers, pinch-off occurs frequently and results in regularly distributed discontinuities along all layers.

Grain evolution is much more significant in Cu than Nb, due to the higher mobility at 400 °C. The grain structure of Nb is effectively the same as the initial condition following creep testing up to 700 h. Grains within polycrystalline Cu layers experience grain growth that is confined within layers. Recall from figure 1.7 that initial grain aspect ratios are very large, and 1-2 grains span the entire thickness of a layer for 200 nm layer thicknesses and below. In these layers, the maximum diameter of the grains that can be achieved by grain growth is smaller than the highly elongated, as-rolled grains. Grain growth does not occur in this instance, and subgrain formation is observed in the Cu phase (Figure 3.4). The structure of samples subject to 400 °C annealing with no externally applied stress will be reported elsewhere [108].

Ultimately, the nominal length scales and macroscopic structure of these multilayer composites experiences negligible change over the duration of these creep experiments. Figure 3.5 shows the laminate structure of a 2 μm laminates as rolled and after creep at 200 MPa, 400 °C.

3.2.3 Composite Failure

The creep ductility of test composites varied from 3.5 % to 20 % across all layer thicknesses. In all cases, damage accumulation was influenced by the initial presence of shear bands. The 2000 nm and 500 nm laminates average 15 % strain at failure. Several shear bands contribute to final fracture, Figure 3.6. Composites with nominally 200 nm layer thickness have higher strain accumulation and fail at

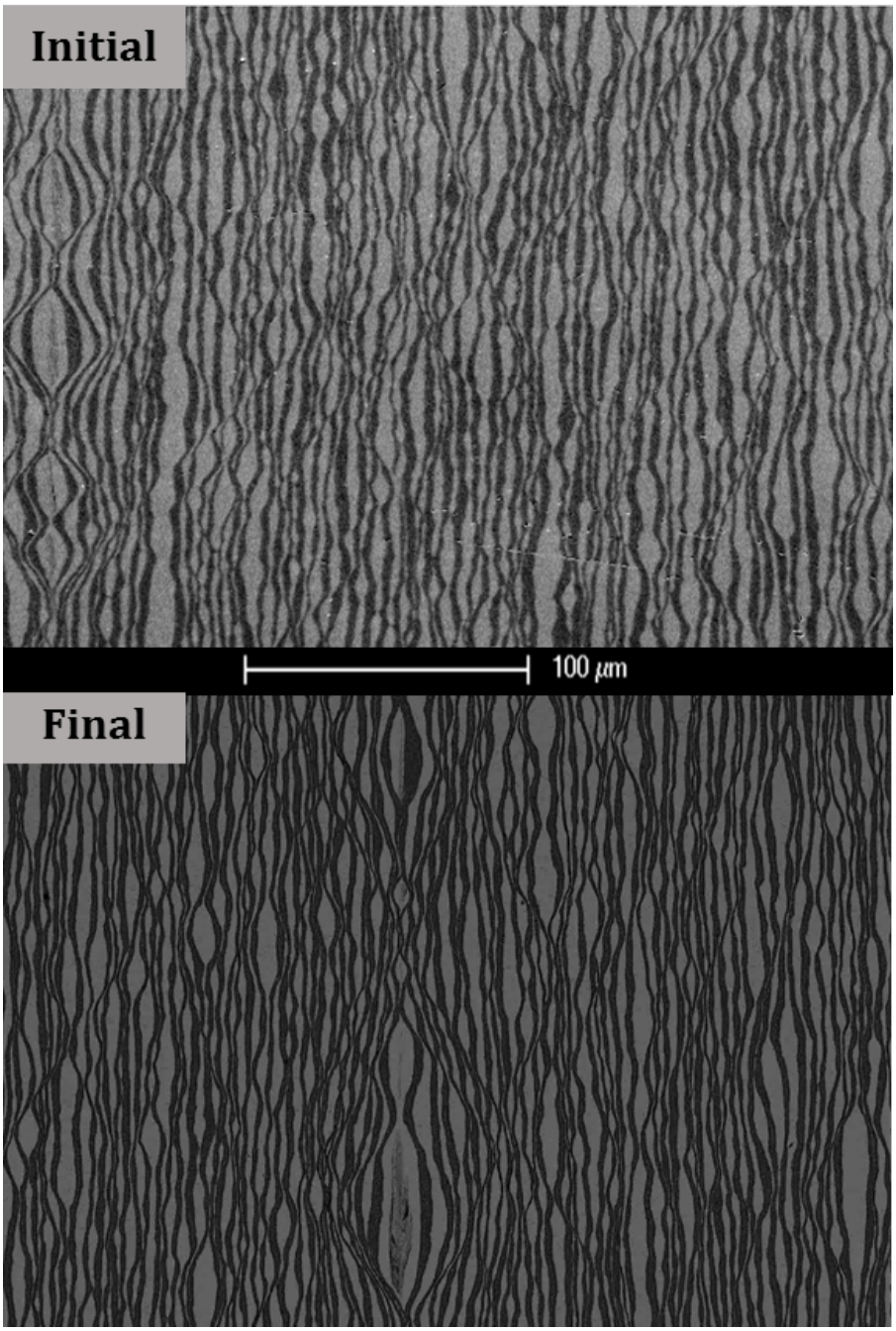


Figure 3.5: These BSE SEM micrographs indicate that the $2\mu m$ ARB Cu-Nb laminate layer morphology has not changed significantly from the initial, AR, structure (top) to the final, crept at 400°C for 26h before final failure at 26% strain, structure.

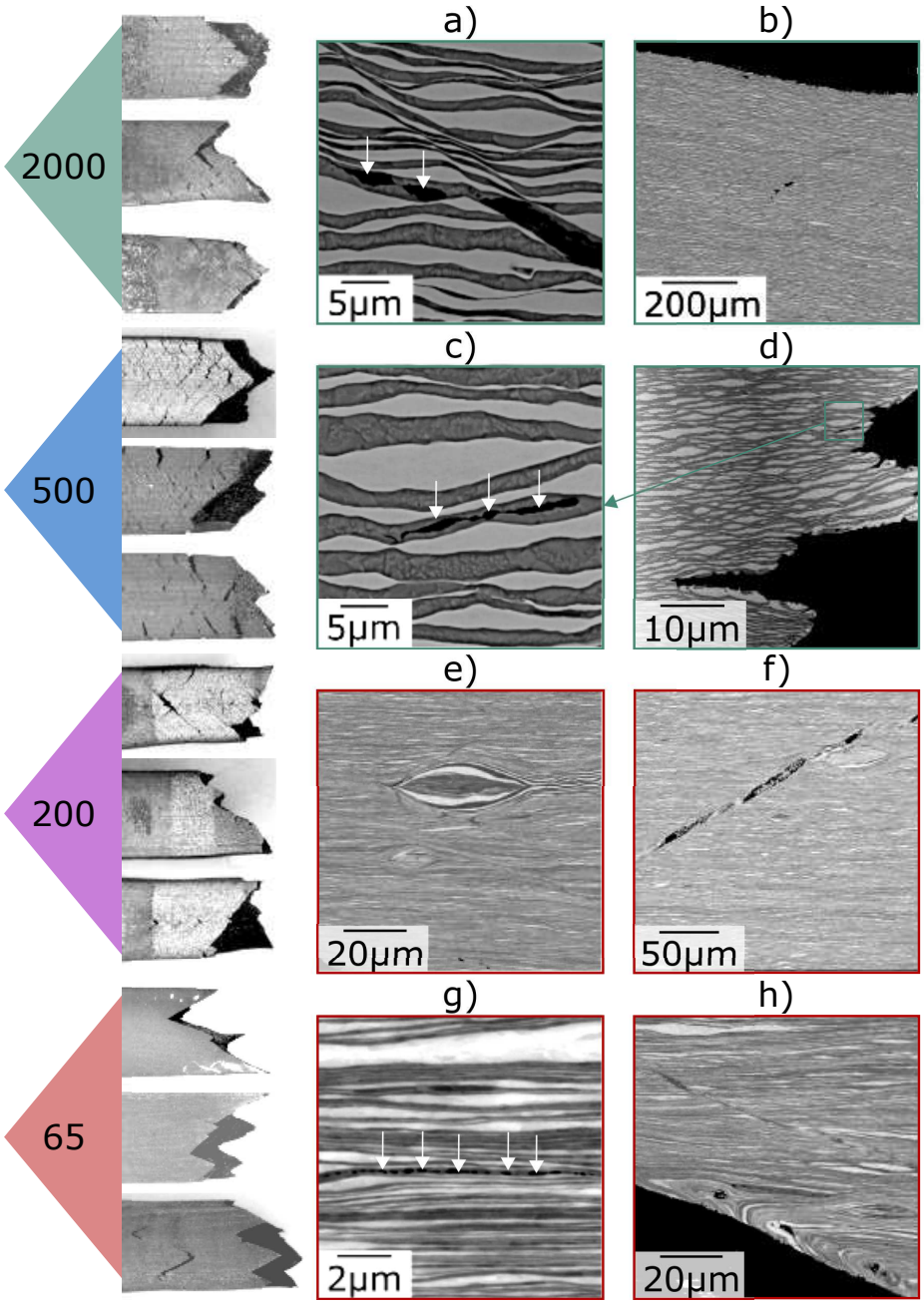


Figure 3.6: Three failed gauge sections of each length scale (left) showing macroscopic failure. a-d) and e-h) show Cu-Nb cross-sections post creep for 2000 *nm* and 65 *nm* laminates, respectively. Voids along shear bands are shown in a,b,f, and h. Voids at Cu-Cu interfaces are observed in a,c, and g. b) shows significant necking in the 2000 *nm* laminate. e and f show failure at large rolling defects. The rolling direction and creep load axis is left to right for all images. SEM micrographs show atomic contrast, where Cu is dark, and Nb is light.

coalescence of only a few shear bands. The single crystalline 65 nm multilayers, however, experience catastrophic accumulation of damage along shear banding and accommodate only 5 % strain at failure. In this instance, only one or two bands propagate to form the final fracture surface. Crack formation along shear bands occurs during tertiary creep at every length scale, and final failure is ultimately due to coalescence of these cracks. Samples with higher final elongation accrue a significant number of these cracks during tertiary creep, as seen by many of the fractured gauge sections in figure 3.6.

Analysis of fracture cross-sections show three main features that initiate void formation; all defects associated with the ARB process: poorly bonded Cu-Cu interfaces (Fig. 3.6a,c,g), inclusions of undeformed Cu and Nb (Fig. 3.6e), and shear bands (Fig. 3.6a,b,e,f,h). Shear bands and undeformed inclusion regions reorient the surrounding layers and create stress concentrations which cause macroscopic cracks (Fig. 3.6b,e,f,h). Significant shear banding along the fracture surface is observed at all tested layer thicknesses. Many voids associated with Cu-Cu interfaces were observed; these may have arisen due to incomplete bonding of the Cu-Cu interfaces in the final few ARB passes. While these are also found at all length scales, they contribute to failure more and make up a significant area of the fracture surface in larger length scale laminates (Fig. 3.6d).

3.3 Discussion

ARB Cu-Nb composites are increasingly creep resistant as the multilayer length scale decreases. At 400 °C, Cu and Nb have very different homologous temperatures (0.50 T_m^{Cu} and 0.25 T_m^{Nb}, respectively); however, steady-state behavior was observed for all layer thicknesses tested. A high dependence of the multilayer creep

rate on applied stress suggests that dislocation glide and climb control deformation.

Considering the moderate temperature and high stress conditions applied, dislocation controlled creep deformation is consistent with creep in pure copper and niobium for larger grain sizes reported in literature [104, 109]. Figure 3.7 shows creep mechanism maps with adjusted creep regimes for small grain sizes of the pure materials. The creep rates for Nb should orders of magnitude slower than Cu due to limited dislocation mobility at 400 °C. Therefore, it is likely that some load is transfered to the Nb layers from the Cu layers, potentially pushing Nb stresses into the plasticity regime, as illustrated in Figure 3.7. An analytical model that accounts for this load transfer process and predicts creep rates will be presented in Chapter 4 [110].

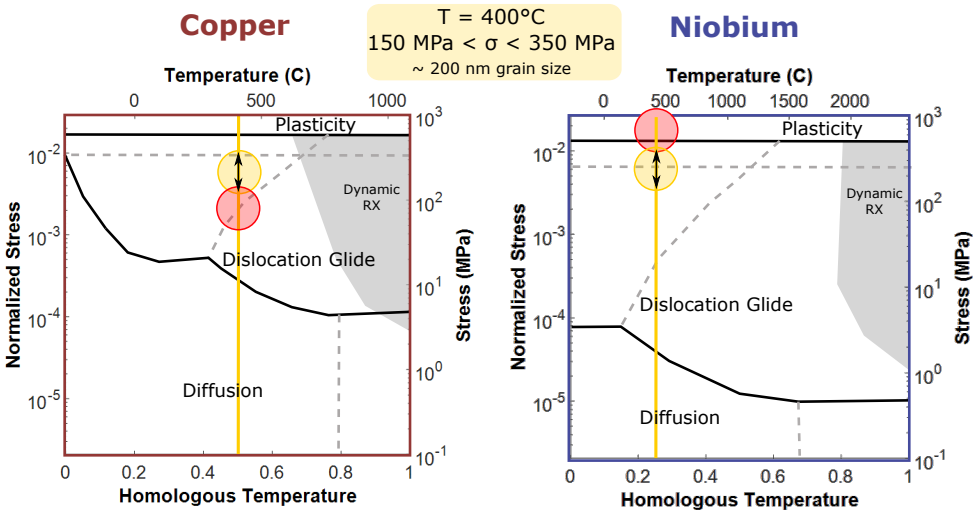


Figure 3.7: Creep mechanism maps for Cu and Nb were approximated for 200 nm grain sizes based on mechanism regimes reported for 100 μm grain sizes in literature [104, 109]. Experimental conditions are noted in yellow, lines indicating 400 °C and arrows indicating the range of applied stresses. Red regions represent a potential shift in stress condition for each phase as a result of load shed.

It is interesting to compare the ARB processed material to creep in Cu-Nb processed by alternate approaches. Lewis et al. crept 50-50, Cu-Nb PVD thin

films at 600 °C, varying length scale from 5000 nm to 500 nm. They found that at moderate to high stresses there was no length scale dependence. At lower stresses, they observed higher creep rates for smaller length scale laminates, consistent with diffusional creep mechanisms. The purpose of the aforementioned study was to determine creep behavior of "fine-grained niobium", and the contribution of copper was neglected [48]. At 0.3 T_m^{Nb} and low stresses, this assumption may be valid, in which case it is not comparable to the low temperature, high stress tests performed on ARB Cu-Nb. The stress exponent found at moderate stresses was $n \approx 3.5$ in these PVD films, also suggesting that the deformation mechanism is different than observed in this study.

Increased creep resistance with decreasing length scale was observed by Biner and Spitzig's creep of drawn Cu-20 % Nb wire at 500 °C. The wires, initially Nb dendrites in a Cu matrix, contain highly elongated Nb regions. The length scale (size and spacing) of the composite varied with processing, similarly to ARB Cu-Nb. A notable difference between the results of this investigation and their study is that below a certain dendrite (layer) spacing, further length scale refinement did not enhance creep strength. Enhanced grain boundary diffusion enabled grain boundary sliding below the spacing of 2230 nm [111]. The stress exponents, similar to this study, were $n \approx 8$. It should be noted that their reported length scale, below which grain boundary sliding dominates, is larger than the nominal layer thickness in any ARB Cu-Nb creep tested.

Biner *et al.* attributed the improved creep resistance to increasing constraint on the Cu matrix phase by the non-deforming Nb which acted as a "dispersion strengthener" [111]. They did not perform TEM analysis of the dislocation structures in the drawn composite. The high dislocation content in the ARB Nb phase suggests that Nb has a larger role than dispersion strengthening. Additionally,

despite pinch-off events, the Nb phase in the 50-50 ARB composites is highly continuous and constraints on the Cu phase are more significant than elongated islands in 20 % Nb composites.

Interestingly, in all cases, Cu-Nb composites exhibit a steady-state creep rate [48, 111]. The variation in stress and length scale dependences can be explained by differences in diffusivity caused by both creep temperature and laminate microstructure. It is not likely that grain boundary sliding occurs in ARB Cu-Nb laminates because the grain size within layers parallel to the loading axis is on the order of a few microns for all length scales tested. Raj and Ashby emphasize that elongated grains hinder deformation by diffusional creep mechanisms due to long diffusional distances [112]. Smaller length scales are associated with grain boundary sliding; as length scale decreases in an ARB system, however, the grain grain aspect ratio increases. In the ARB Cu-Nb system, which has elongated grains at all tested length scales (Chapter 1, Fig. 1.9) grain boundary sliding is not a factor.

Despite some grain shape evolution in the Cu phase of the ARB system, the final post-failure grain structure is still quite elongated. Additionally, the likely recrystallized Cu grains in the wire-drawn system have significantly more connectivity than the confined layers in ARB laminates due to the shape of reinforcing Nb and the volume fraction of phases. Even in 50-50 PVD Cu-Nb systems, however, composites would experience grain boundary sliding because the grain aspect ratios created by deposition are close to unity. The beneficial contributions of the Nb phase strengthening and constraints during creep extends to even the smallest length scales in ARB Cu-Nb. The mechanism for creep in ARB Cu-Nb is a combination of Nb plasticity and dislocation climb and glide in the Cu phase.

Grain size evolution within the Cu layers does not significantly coarsen the microstructure, even in areas with discontinuous Nb layers. Layer discontinuity

results in local stress concentrations and variation in the stress distribution between Cu and Nb layers due to changing aspect ratio of the Nb phase [113]. Despite the variation in structural evolution between length scales, the benefits of increased barriers to dislocation motion (high interface density) outweigh the negative impact of layer discontinuity in creep performance.

Structural evolution differences at different length scales was directly related to the initial grain structures of ARB Cu-Nb. Larger laminates had a higher number of polycrystalline layers compared to the smaller laminates which were largely single crystalline through the thickness. Creep stresses enhance grain evolution and layer pinch-off, however, the result is not significantly different than that of static annealing. Thin Nb layers experience pinch-off due to boundary grooving and faceted interface driven Rayleigh instabilities [85, 101]. Polycrystalline layers experience grain growth. Highly confined single crystalline layers form substructures.

It is clear that ARB processing flaws influence tertiary creep and failure. Damage accumulated along shear bands at all length scales. While pinch-off often occurred at thin layers associated with shear banded regions, pinch-off in the absence of shear bands did not contribute significantly to failure. Polycrystalline regions surrounding shear bands deform to accommodate the stress concentrations associated with the local layer misorientation. This is evident by the number of cracks along shear bands that accumulate in larger layer thickness gauge sections compared to smaller length scales in figure 3.6.

3.4 Conclusions

- Cu-Nb multilayer systems exhibit typical three stage creep behavior at all stresses and length scales investigated, despite the difference in homologous temperatures at 400 °C (0.50 T_m^{Cu} and 0.25 T_m^{Nb}).

- Quantification of the experimental steady-state creep rates yields a predictive creep equation with stress and length scale exponents of $n = 7.2$ and $p = -1.8$.

- Creep deformation is controlled by a combined plasticity mechanism involving both Cu and Nb layers. High dislocation densities and creep rate stress dependence suggest that this mechanism is mediated by dislocation glide and climb.

- Creep behavior improves with decreasing length scale, with the most creep resistant material possessing layers that are nominally 65 nm thick.

- Tertiary creep and failure ultimately occurs due to void formation and coalescence along processing defects. Shear bands and poorly bonded Cu-Cu interfaces account for a majority of post-failure void locations.

Chapter 4

Model for Creep Deformation

In this chapter, a model for the creep deformation response presented in Chapter 3 will be discussed. Results are presented for 400 °C tests of ARB Cu−Nb Composite creep conditions are discussed with respect to the boundaries of the model and material limitations. Steady-state creep parameters for Cu, assuming plasticity in Nb, are fit to the transient response of Cu−Nb at 400 °C. Predicted composite steady-state strain rates are compared to experimental minimum creep rate values. Assumptions are discussed with respect to material inhomogeneities which likely contribute to experimental deviation from the model.

The quasi-static behavior of copper-niobium laminates in both tension [17, 114–116] and compression [24, 68, 74, 80] has been studied extensively. In contrast, the time-dependent response of such multilayers at elevated temperatures has received far less attention [16], and relatively little is known regarding active deformation mechanisms. It remains an open question whether dislocation behaviors known to control quasi-static response are equally active during creep, or whether diffusional creep mechanisms are dominant. This chapter specifically targets such questions

through a combination of creep experiments and modeling.

Accumulative roll-bonding of the Cu-Nb system has proven so successful because the metallic components co-deform and develop stable interface textures. Copper and niobium have similar mechanical deformation behavior: Young's modulus, yield strength, and plateau stress. Successful ARB of this system from 2 mm sheets down to 10 nm layer thickness laminates suggests that this relationship persists at all length scales [24].

As discussed in Chapter 1, the rolling process alters grain structures with processing and maintains special interface relationships causing the smaller layer thickness laminates to have single crystalline layers with the strongest texture [33, 62] for grains. At all length scales, composites are $50 - 50$ Cu-Nb with a continuous layered structure, as shown in Figure 4.1a−d. The ARB process results in shear localization and layer thickness variation which is important in the tertiary creep and failure response of these laminates [16], but is neglected in this analysis of transient and steady-state behavior.

4.1 Relevant Experimental Details

Complete details for the testing protocol used to obtain data are outlined in Chapter 2. The model considers the transient and steady state creep response and is calibrated with high temperature tension tests at the same layer thicknesses subject to creep testing: 8 μm, 2 μm, 500 nm, 200 nm, and 65 nm. The focus of the transient creep analysis in this study was standard creep tests, wherein the applied load is increased at constant rate of extension to a fixed value and held constant. A limited number of specimen were tested due both to the limited sheet area available for each layer thickness and to the time required to prepare and

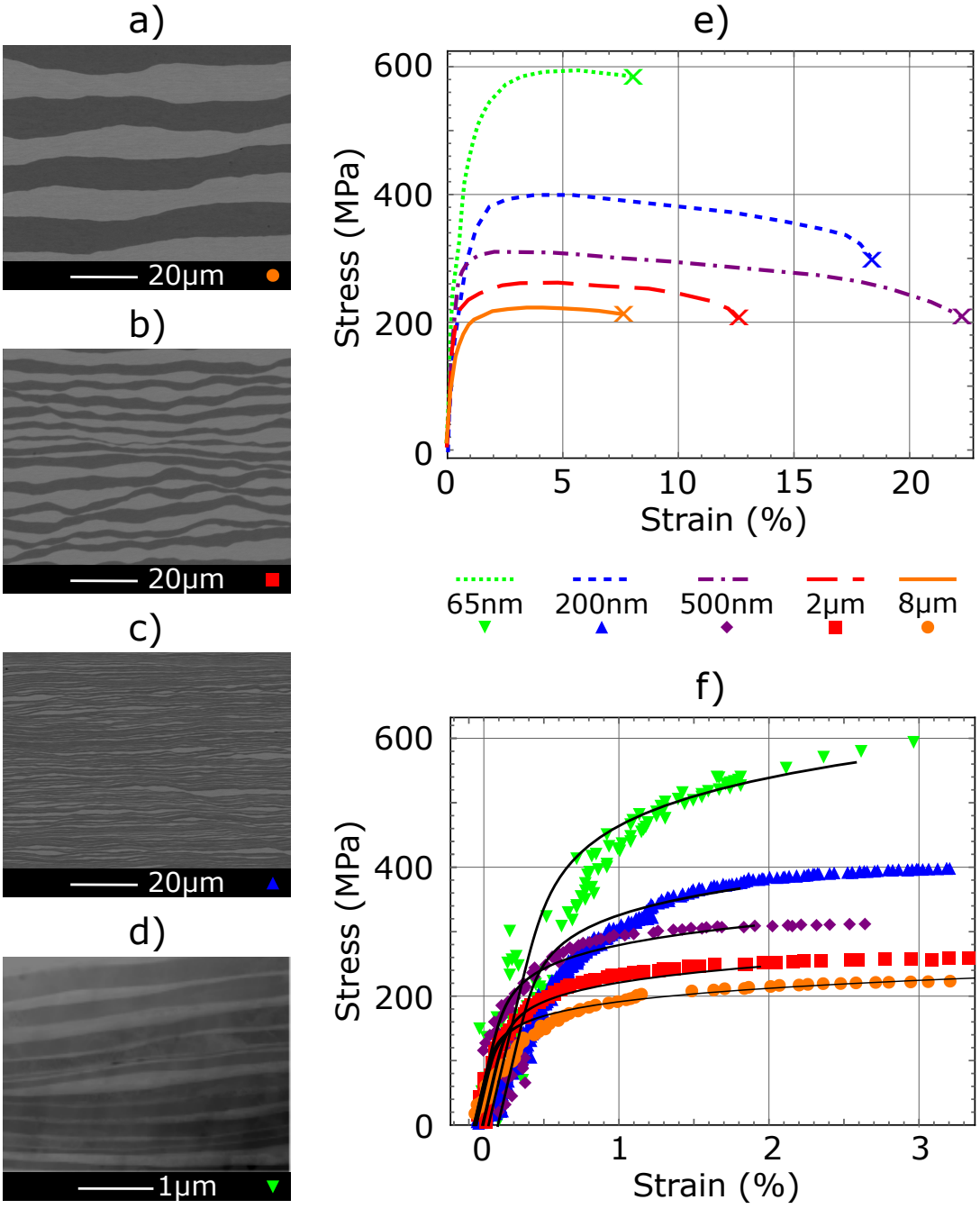


Figure 4.1: Cu-Nb composite structures are shown for laminates with nominal length scales 8 μm (a), 2 μm (b), 200 nm (c), and 65 nm (d). Full compsite stress-strain curves at 400 °C for a variety of length scales are shown in full (e), and truncated to show Ramberg-Osgood hardening curve fits (f).

test samples to failure. In addition to standard creep tests, load jump tests were performed to increase the amount of behavioral information attained per sample. After a standard test was run for 70 h, the hold load would be increased, and additional minimum creep rates were determined for a given length scale and stress. Tensile testing was performed at constant extension, with maximum strain rate $2 \times 10^{-4}\ s^{-1}$.

4.2 Tension and Creep Behavior at 400 °C

The stress-strain response of ARB Cu-Nb at 400 °C is shown in Figure 4.1e and f. While composite failure was variable and dependent on rolling defects, the strain hardening behavior was fully captured for all layer thicknesses investigated. Analysis of this response will be detailed in Section 5. The ultimate tensile stress was achieved at or below 3 % strain for all laminates, and was taken as the plateau stress for the composite.

Standard creep test strain-time histories are presented in Figure 4.2. The apparent transient and steady-state responses appear to have similar time scales, and the transition is subtle. Strain rate dependence on stress and length scale are qualitatively shown in Figure 4.2a and b, respectively.

To facilitate comparisons between the experiments and the modeling, time is measured from the end of the ramp loading step. The strains at this instant in time are the same (within experimental scatter) as that implied by the "fast loading" stress-strain curves shown in Figure 4.1; hence, creep strains during the loading stage are negligible. For comparison, additional experimental estimates for steady-state creep rates obtained from jump-tests are also included in this work, but these tests are not included in the modeling section that follows.

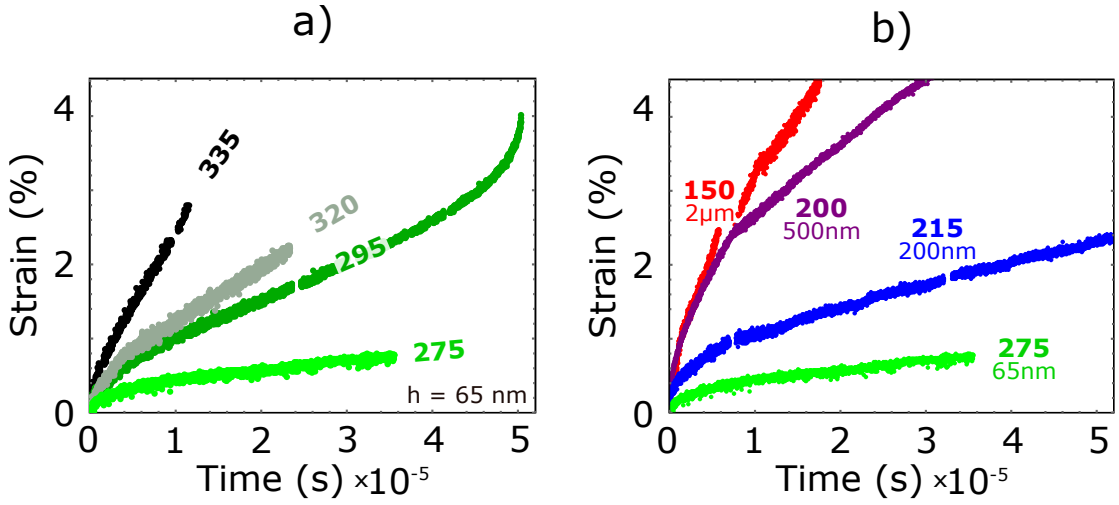


Figure 4.2: Composite creep curves are shown (a) for 65 *nm* laminate varying stress, and (b) for a variety of layer thicknesses.

Bulk tensile testing at creep temperature (400 °C), shown in Figure 4.1 illustrates the same strong length scale dependence observed previously in Cu-Nb systems [17, 18, 24]. Analysis of the variation in hardening behavior and plateau stress at the different length scales was found to be critically important to the multilayer creep response. The thermal properties of Cu and Nb are significantly different at 400 °C: 0.5 T_m^{Cu} and 0.25 T_m^{Nb}. Diffusion in Nb is negligible compared to Cu, therefore, a reasonable assumption is that Nb deforms according to the Cu-Nb multilayer 400 °C tensile response while Cu creeps, controlling the time-response of the system.

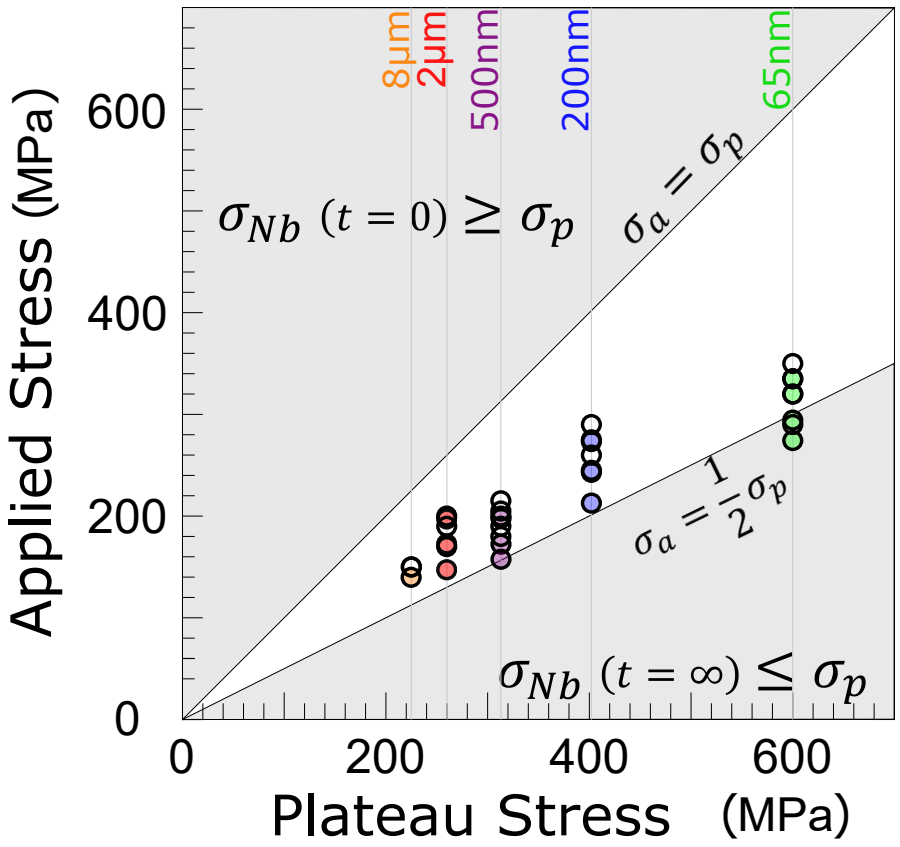


Figure 4.3: Map indicating the range of applied stresses that steady-state creep would occur for Cu-Nb multilayers: $\frac{\sigma_p}{2} < \sigma_a < \sigma_p$. Symbols indicate the loads used in this study; filled symbols represent the conditions of standard tests (with transient regimes, and minimum creep rates analyzed), while open symbols indicate jump tests (only minimum creep rate analyzed).

4.3 The Laminate Creep Model

4.3.1 Basis and Assumptions

Prediction of the time-dependent response of metal multilayers can be challenging, particularly for cases where the layers exhibit strain hardening and vastly different creep behaviors. Such is the case for copper-niobium laminates tested at

400 °C; one can can anticipate both layers are elastic-plastic at fast loading rates, while only the copper creeps at fixed load. This combination of behaviors implies that there is a narrow range of external loads that produce steady-state behavior, which limits the scope of conventional creep tests. On the one hand, low external loads may fail to produce steady-state behavior because the stress in both layers is never constant: the entire response is governed by the transient associated with shedding load from the creeping copper to the strain-hardening niobium. On the other hand, high external loads can cause failure by plastic flow at high strain rates, obfuscating the role of creep.

One can anticipate a steady-state response for applied loads between these limits, i.e. at stresses beneath those required to cause instantaneous yielding, yet above those required to reach the plateau stress of Niobium (σ_p, see Figure 4.1) after sufficient relaxation of the copper. For the present ARB multilayers, the layers are of equal volume fraction and likely exhibit similar stress-strain curves at "fast" loading rates. In this case, in order to reach constant layer stresses associated with steady-state, the applied stress must be $\sigma_p/2 < \sigma_a < \sigma_p$. The lower limit is dictated by the fact that the maximum possible stress on the niobium is twice the applied stress (after creep entirely alleviates the stress in the copper). If the stress in the niobium never reaches its plateau strength, the stress in both layers evolves continuously and steady-state creep rates for the composite are never obtained. Note in Figure 4.1 that the plateau stresses are not reached until composite strains of $2-3\%$.

This highlights the inherent challenge in using conventional creep tests (at fixed load) to characterize these materials; such tests are limited to a load range that spans only a factor of two, at most. Figure 4.3 provides a creep regime map for the laminate responses shown in Figure 4.1, with indications of the stresses used in the

present study. Beneath the bottom curve, the stresses in the layers approaches a constant state only in the asymptotic limit of infinite time; i.e. the entire response is transient. Above the top curve, the niobium yields instantly upon application of the load, such that creep response is eliminated in favor of plastic flow. In the intermediate region, an initial transient is followed by a steady-state in which the stress in both layers becomes constant at fixed load, and $\sigma_{Nb} = \sigma_p$.

Even in the intermediate stress range where constant creep rates can be anticipated, identifying portion of the response associated with steady-state can be extremely difficult. This is illustrated by the strain-time responses shown in Figure 4.2, which depict the response for a single layer at different levels of applied stress. In these curves, zero time corresponds to the end of a ramp loading; hence, the composite strain starts approximately at that corresponding to the strain in Figure 4.1 at the applied load. Clearly, the transient response can formulate a significant fraction of the measured response; indeed, examination of Figure 4.1 suggests that constant stress in the layers cannot be achieved for composite strains less than $\sim 2.5\%$ due to strain hardening that occurs to this point.

Thus, strain-hardening in the niobium layer is an important feature of the time-response of copper-niobium laminates at moderate temperatures. In Figure 4.4, the stresses in the niobium are evolving until the plateau stress is reached, implying that the majority of these curves are associated with transient composite response. Idealizations that ignore hardening fail to capture the niobium's changing resistance to elongation during creep of the copper, leading to far shorter transients that fail to capture even the qualitative shape of the measurements shown in Figure 4.4. Put another way, if one assumes a constant flow stress in the niobium, one must eliminate composite strains less than $\sim 3\%$ to invoke a steady-state model, thus eliminating a substantial fraction of the measured response.

Layer thickness	α	N	σ_p MPa
8 μm	$4.00x10^{19}$	8	225
2 μm	$1.21x10^{19}$	8	260
500 nm	$1.78x10^{18}$	8	313
200 nm	$3.52x10^{17}$	8	402
65 nm	$1.81x10^{16}$	8	600

Table 4.1: Strain hardening parameters for composite multilayers, assuming Ramberg-Osgood hardening (eqn. 3) with $E \sim 100\ GPa$.

In this work, the fully transient response of such laminates is modeled assuming stage II creep in the copper and strain-hardening in the niobium, without any invocation of constant stress in either layer. The central objective is to infer creep properties for the copper layers, which can then be used to infer active deformation mechanisms and predict composite response under varying load conditions. An important outcome of the model is an estimate of the time required to reach steady-state; this allows one to identify time ranges for which simpler steady-state creep models can be applied appropriately.

We assume that both layers exhibit linearly elastic behavior during the initial "fast" ramp loading, which is reasonable in light of the limited strain hardening that occurs during fast loading to the applied loads considered here. (This is justified upon examination of the applied stress levels shown in Figure 4.3 and the composite response shown in Figure 4.1.) After the initial loading ramp, we assume that the niobium exhibits strain hardening that is independent of strain rate, while creep in the copper (occurring at low strain rates) eliminates any strain hardening in the copper during the hold segment.

The strain hardening of the niobium is taken to be identical to that of the composite, which is reasonable considering the layers are processed simultaneously and subjected to the same deformation. Strictly speaking, given the equal volume

fractions of the layers, this also implies that the "fast response" of the copper strain hardens in the same manner as niobium. However, it is assumed that creep eliminates this effect during the creep test, such that the copper is effectively described as linearly elastic, followed by creep. Simply put, creep during the hold segment enables recovery processes in the copper but does not affect the strain hardening in the niobium, which follows the composite response.

The creep response of copper (for individual layer thickness laminates) is assumed to obey the Mukherjee-Bird-Dorn steady-state creep rate equation[1] [51],

$$\dot{\epsilon}_{cr} = \frac{A_{cr}^{''} G b}{kT} \left(\frac{b}{h}\right)^{p} \left(\frac{\sigma}{G}\right)^{n} \tag{4.1}$$

where G is shear modulus, b is burgers vector, kT is thermal energy, A_{cr} is the creep pre-factor, n and p are the stress (σ) and length scale (h) exponents, respectively. A_{cr} and kT are temperature dependent; A_{cr}, n, and p vary with deformation mechanisms. This relationship can be simplified significantly at constant temperature and length scale:

$$\dot{\epsilon}_{cr} = \dot{\epsilon}_{o} \left(\frac{\sigma_{Cu}}{E_{Cu}}\right)^{n} \tag{4.2}$$

where $\dot{\epsilon}_o$ and n are the characteristic reference strain rate and stress exponent, respectively. Presumably, any primary or stage I creep of the copper layer occurs over much smaller time scales than the creep test of the composite. Further, tertiary or stage III creep in the copper is neglected in the modeling of the transient. Finally, thermal misfit strains due to differences in coefficients of thermal expansion are neglected; the resulting composite strains are small and as such are difficult to isolate

[1]Simplified here from eqn. 3.1 so that $A_{cr}^{''} = A_{cr} * D_0 * exp[\frac{-Q}{RT}]$

in experiments from other effects. It is worth emphasizing that the plausibility of more detailed models is undermined by the narrow range of stresses that can be applied without violating the limits outlined above.

4.3.2 Details

The response of the niobium during the creep test is determined via a Ramberg-Osgood fit to the composite response, determined the results shown in Figure 4.1. The constitutive law for this layer is given by:

$$\epsilon_{Nb} = \frac{\sigma_{Nb}}{E_{Nb}} + \alpha \left(\frac{\sigma_{Nb}}{E_{Nb}} \right)^N \tag{4.3}$$

where E_{Nb} is the elastic modulus of niobium, while α and N are fitting constants that account for hardening. Values for α and N determined via fitting are provided in Table4.1. The copper layer, the creep constitutive law is given by:

$$\epsilon_{Cu}(t) = \frac{\sigma_{Cu}}{E_{Cu}} + \epsilon_{cr}(t) \tag{4.4}$$

where E_{Cu} is the elastic modulus of copper and ϵ_{cr} is the creep strain that accrues in the copper. Strain in the copper is time dependent, in accordance with eqn. 4.2. Assuming no macroscopic separation of the layers, the total strains in both layers are constrained to be equal;

$$\epsilon_c(t) = \epsilon_{Cu}(t) = \epsilon_{Nb}(t) \tag{4.5}$$

therefore σ_{Nb} and σ_{Cu} are also stress dependent, accounting for the transient composite response, despite constant deformation behavior in the copper phase.

At all times, simple force balance for equal volume fractions of layers implies that $\frac{1}{2}\sigma_{Nb}(t) + \frac{1}{2}\sigma_{Cu}(t) = \sigma_a$. Define $t = 0$ to the be time immediately after the application of the applied load σ_a, which is held fixed in time. Since we assume $\epsilon_c = \epsilon_{Nb} = \epsilon_{Cu}$ at all times, the strain for the composite is given by:

$$\epsilon_c(t) = \frac{2\sigma_a - \sigma_{Nb}(t)}{E_{Cu}} + \alpha \left(\frac{2\sigma_a - \sigma_{Nb}(t)}{E_{Cu}} \right)^N \tag{4.6}$$

One can obtain a single equation describing the stress evolution in the copper by differentiating eqns. 4.3 and 4.4 with respect to time and using the results to eliminate $\dot{\epsilon}_c(t)$, then substituting eqn. 4.2 for $\dot{\epsilon}_{cr}$:

$$\left(\frac{E_{Nb} + E_{Cu}}{E_{Nb}} + N\alpha \left(\frac{E_{Cu}}{E_{Nb}} \right)^N \left(\frac{2\sigma_a - \sigma_{Cu}}{E_{Nb}} \right)^{N-1} \right) \frac{\dot{\sigma}_2}{E_{Nb}} + \dot{\epsilon}_o \left(\frac{\sigma_{Nb}}{E_{Nb}} \right)^n = 0 \tag{4.7}$$

Using [51,117,118], one estimates that $90\ GPa < E_{Cu}^{400^\circ C} < 110\ GPa$, and $E_{Nb}^{400^\circ C} \sim E_{Nb}^{RT} = 105 GPa$; here we adopt $E_{Cu} = E_{Nb} = E$. With this simplification and by defining $\Sigma_{Cu} \equiv \sigma_{Cu}/E$ and $\Sigma_a \equiv \sigma_a/E$, the creep governing equation is:

$$\dot{\Sigma}_{Cu} = -\frac{\dot{\epsilon}_o \Sigma_{Cu}^n}{\left(2 + N\alpha \left(2\Sigma_a - \Sigma_{Cu} \right)^{N-1} \right)} \tag{4.8}$$

At time $t = 0$ (i.e. the start of the hold phase) and neglecting any strain hardening during the initial loading phase, the initial condition is given by $\Sigma_{Cu}(0) = \Sigma_a$. Once the stress in the copper layer has been computed, the composite strain can be computed from:

$$\epsilon_c(t) = \left(2\Sigma_a - \Sigma_{Cu}(t) \right) + 2\alpha \left(2\Sigma_a - \Sigma_{Cu}(t) \right)^N \tag{4.9}$$

When the composite strain exceeds that associated with the plateau strength of

niobium, these equations are replaced with their steady-state equivalents. In such cases, we simply have:

$$\dot{\epsilon}_c \;=\; \dot{\epsilon}_o \left(2\Sigma_a - \Sigma_p\right)^n \tag{4.10}$$

Where $\Sigma_p \equiv \sigma_p/E$ is the normalized plateau stress in the composite. Thus, eqns. 4.8, 4.9, and 4.10 provide a complete model for the strain history in the composite resulting from the load phase.

4.4 Comparison of Modeling and Experiments

To generate modeling results, we followed the following procedure. First, the Ramberg-Osgood constants α and N were determined for all layers via least-squares fitting. For simplicity $E_{Cu} = E_{Nb} = E = 100\ GPa$ was adopted for all specimens. Further, $N = 8$ provided a reasonable fit for all layer thicknesses; choosing individual values of N improved the fit in some portions of the curve but not others, with no clear advantage over the $N = 8$ cases. For each layer thickness, the plateau stress σ_p for the niobium was estimated from the composite stress-strain curves in Figure 4.1.

The solution to the creep eqns. 4.8, 4.9, and 4.10 were generated in *Mathematica* [119], using the copper creep constants n and $\dot{\epsilon}_o$ as inputs, for fixed values of the other parameters. The numerical solution was generated up to a composite strain of $\epsilon_c = 0.029$. Comparison with the measures transient strain-time responses at different load levels was used to determine creep properties for copper at each layer thickness.

The determination of a constant set of copper creep parameters $(\dot{\epsilon}_o, n)$ for a

given layer thickness, i.e. fitting multiple transient curves at different stress levels with a single value $(\dot{\epsilon}_o, n)$, is unwarranted given that (i) only a single test was conducted at each load at each layer thickness, and (ii) even at steady-state, creep responses at fixed stress exhibit significant scatter. Instead, the transient creep curves were fit for each loading case to determine values $(\dot{\epsilon}_o, n)$ that provided the best fit for that specified test. As shown by the solid lines in Figure 4.4, for nearly all cases, the predicted strains were in excellent agreement with the measurements. The range of creep parameters obtained for each layer thickness at different stress levels is provided in Table 4.2, along with the average values obtained across all stress levels.

It is noteworthy that the range of creep exponents $(1.25 < n < 1.65)$ obtained from this procedure is quite narrow, both across the relevant range of stresses and across all layer thicknesses. Interestingly, while the scatter in creep coefficient $\dot{\epsilon}_o$ is much larger (as is typical of true steady-state creep tests), the average values are quite close to one another with the exception of the 65 nm layer thickness specimens. The strain-time predictions using average values of $(\dot{\epsilon}_o, n\ )$ - constant for a given layer thickness and hence independent of stress level - are also shown in Figure 4.4 with dashed lines. Naturally, using the average value of $\dot{\epsilon}_o$ leads to larger discrepancies, since the best fit can vary significantly from one test to another. Nevertheless, the agreement for all but the 65 nm layer thickness is reasonable for most of the curves.

The results shown in Figure 4.4 demonstrate that, even when the composite strain surpasses the strain sufficient to reach the plateau stress of niobium, the appearance of constant creep rates (i.e. steady-state) is often difficult to identify. Despite this fact, it is informative to compare the model predictions for minimum creep rate, previously reported in [16]. Figure 4.5 compares measured values of

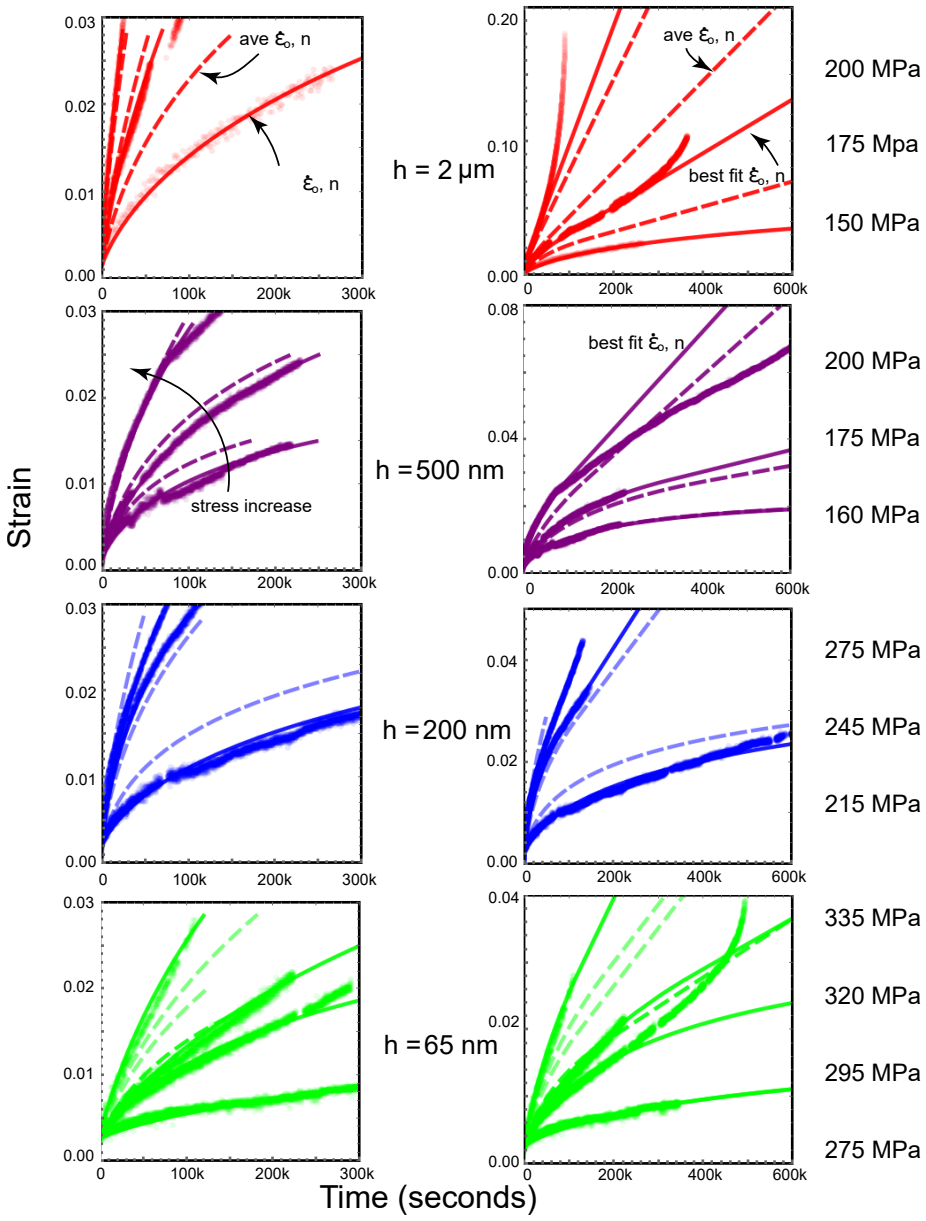


Figure 4.4: Composite strain versus time for four layer thicknesses. (Left) Transient behavior up to the strain at which the composite reaches its plateau stress. (Right) Full response. Solid lines indicate best fits for $(\dot{\epsilon}_0, n$ in the transient model. Dashed lines indicate predictions for each stress using average values.

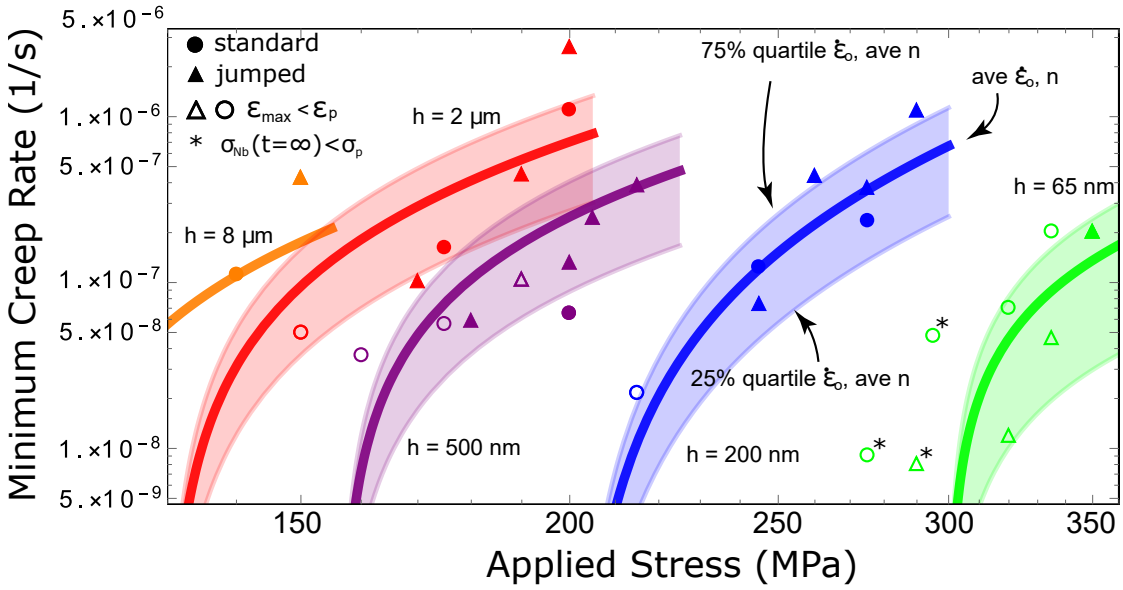


Figure 4.5: Experimental minimum creep rates (symbols) with predicted values from fitting the transient response. Triangles are the results of jump tests, while circles are standard tests. Closed symbols indicate the test reached the composite plateau strain (and hence should be at steady-state) and open symbols indicate the test fell entirely in the transient regime. Solid lines indicate predicted steady-state creep rates given average $\dot{\epsilon}_0$ and n.

the minimum creep rate to predictions obtained from eqn. 4.10. Circles represent minimum creep rates obtained from standard creep tests, with transients used for model fitting. Triangles represent minimum creep rates measured from jump tests. Closed symbols indicate that the composite strain surpassed the strain at composite plateau stress - the threshold for theoretical steady-state. Open symbols did not reach the requirements for theoretical steady-state. The predicted curves indicate the steady-state response dictated by eqn. 4.10 using the average values of creep coefficient $\dot{\epsilon}_o$ and stress exponent n; the shaded region around each curve represents the calculated 25 % and 75 % quartiles of $\dot{\epsilon}_o$ for each layer thickness.

The agreement in Figure 4.5 is very good to excellent, despite the fact that there may be insufficient time to obtain steady-state creep rates before the composite

Layer thickness	Range $\dot{\epsilon}_o$	Range n	Average $\dot{\epsilon}_o$, n
8 μm	1.6 $x10^{-2}$	1.6	1.6 $\times 10^{-2}$, 1.6
2 μm	1.65-4.50 $x10^{-2}$	1.5-1.8	2.83×10^{-2}, 1.65
0.5 μm	0.35-1.80 $x10^{-2}$	1.3-1.6	0.78×10^{-2}, 1.43
0.2 μm	0.25-2.75 $x10^{-2}$	1.5-1.7	1.60×10^{-2}, 1.33
0.065 μm	0.01-0.05 $x10^{-2}$	1.0-1.5	3.35×10^{-3}, 1.25

Table 4.2: Creep properties determined purely from transient response; different values of $\dot{\epsilon}_o$ and n were fit to each load case for a given layer thickness. Both the range and average values of parameters are listed.

experiences tertiary creep. High stress level outliers (primarily jump test data) suggest that composites transitioned to tertiary creep, with higher creep rates, without measurable time at steady-state. Hence, the measured minimum creep rates generally fall above the predicted creep rates associated with the theoretical end of the transient.

4.5 Discussion

4.5.1 Creep Mechanism

As the map in Figure 4.3 shows, experiments were performed at the lower bound of stress conditions necessary for steady-state behavior. Any prediction of composite behavior at lower stresses should consider the transient model, only. Predictions of composite behavior above the conditions tested must consider the transient model and steady-state conditions outlined in this paper. At higher applied stresses, however, one should be apprehensive about the variation in onset of tertiary creep and composite strains to failure.

The present creep descriptions are quantitatively similar to a previous description of composite creep [16]; one must consider that composite creep exponents

are actually an amalgam of creep and strain hardening and therefore the stress exponents are quite different. The present approach is to be favored, as it decouples these behaviors and allows one to identify creep mechanism active in just the copper.

The entire transient response of the composite is due to stress in the copper phase changing as a function of time. Upon loading, the stress in Cu is the same as that of the Nb layers, and is a relatively high stress ($140-320\ MPa$), and therefore higher values of n may fit better at these short times (but produce poor fits at longer times). It is possible that the creep exponent evolves with time; in which case, there may be greater stress-dependence at short times when the stress in the copper is most elevated. However, additional experiments focusing on behaviors at short times are required to say so definitely.

Figure 4.6 shows the experimental minimum creep rates as a function of the theoretical stress in the Cu phase, rather than the initial stress as is shown in Fig. 4.5. Plotting measured minimum creep rates versus the copper stress (at steady-state) highlights that creep rates fall in narrow band regardless of layer thickness, i.e. layer thickness does not appear to impact copper creep mechanism. Despite the low stress dependence ($n \sim 1.5$) , this suggests that the deformation mechanism related to dislocation activity, rather than dominated by diffusion.

Traditionally, a higher stress dependence is found for Cu creep dominated by motion of dislocations. Reasoning for this high stress dependence has been justified by the relationship between dislocation density and stress within the metal ($\rho \propto \sigma_{Cu}^2$). Assumptions of dislocation pile-up geometries with respect to average length scale are not appropriate for the ARB Cu-Nb system. The stress dependence in Cu changes due to the high densities of bi-metal interfaces, grain aspect ratios, and confined nature of grains.

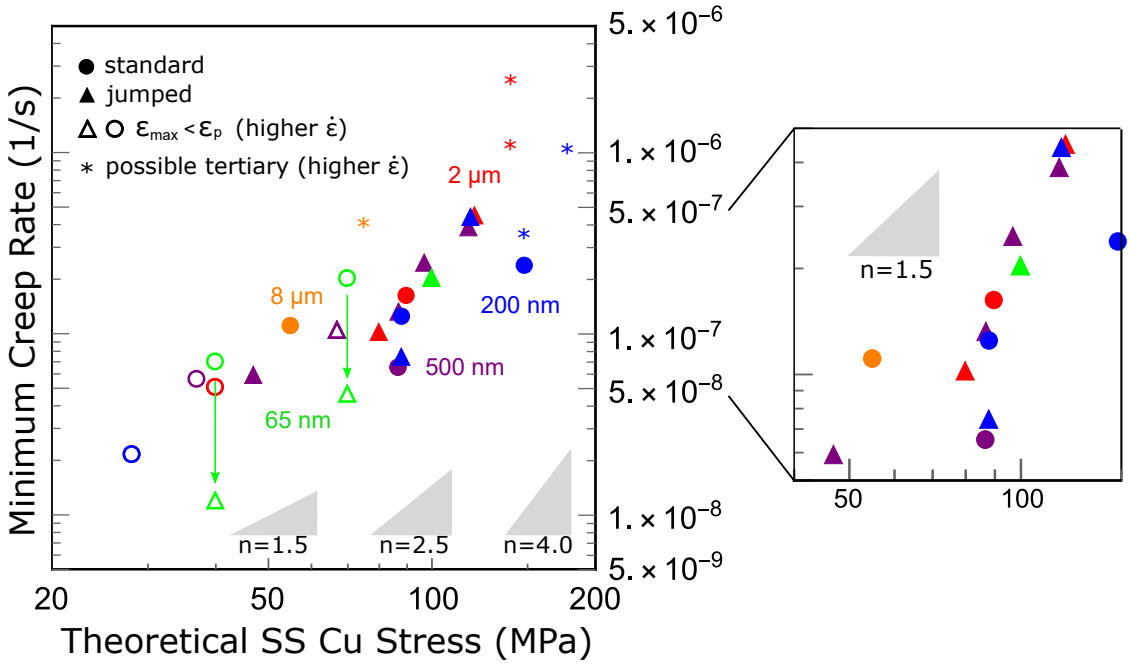


Figure 4.6: Experimental minimum creep rates as a function of theoretical stress in Cu at steady-state (SS): stress values calculated according to Nb plateau stress for each layer thickness. In this narrow stress range, all tests lie within scatter of the stress dependence fit to transient curves ($n \sim 1.5$). Creep rate data includes all length scales tested, only excluding points where stress in the niobium would never reach the plateau stress, and/or the stress in the copper is nearly zero. * Asterisks indicate minimum creep rates which failed after less than 26 hours at load. Open shapes refer to minimum creep rates collected before theoretical steady-state and would be measurably slower given time: see arrows referencing minimum creep rates at the same stress for standard tests (lower strain) compared to jump tests (higher strain). Standard tests (transients) include samples that reach ϵ_p and those which did not. Pop-out includes all data that satisfies steady-state criteria without doubt.

Dislocation motion through Cu at moderate and high stresses, at 400 °C is likely controlled by vacancies and climb: a mechanism that is significantly influenced by stress and the lattice diffusion (D_l^{Cu}) in the Cu as well as temperature (T). Climb velocity (v_c) for a given stress in Cu layers can be calculated by the following equation:

$$v_c = 2\pi \frac{\Omega \tau_{Cu}}{kT} \frac{D_l^{Cu}}{b^2} \frac{b}{ln\left(\frac{R}{r_o}\right)} \tag{4.11}$$

where Ω is atomic volume, k is Boltzmann's constant, and b is Burgers vector. For this calculation, we assume $\tau_{Cu} = \sigma_{Cu}/2$. The average dislocation glide distance, R, here can be taken as half of the layer thickness ($h/2$); and the dislocation core radius, r_o, is taken as $2b$. Knowing the climb velocities for Cu under the stress and temperature conditions of experimental creep tests allows us to calculate the dislocation densities (ρ) necessary to achieve the observed creep rates. Values reported in Table 4.3 were calculated using Orowan's equation:

$$\dot{\gamma} = \rho b v_c \tag{4.12}$$

Climb Velocity	Dislocation Density	Copper Stress	Strain Rate	Layer Thickness
v_c (m/s)	ρ (m^{-2})	σ_{Cu} (MPa)	$\dot{\gamma}$ (s^{-1})	h (nm)
5.1×10^{-14}	5.2×10^{15}	50	6.8×10^{-8}	65
1.5×10^{-13}	1.0×10^{16}	150	4.1×10^{-7}	65
2.8×10^{-14}	9.5×10^{15}	50	6.8×10^{-8}	2000
8.4×10^{-14}	1.9×10^{16}	150	4.1×10^{-7}	2000

Table 4.3: Climb velocities and dislocation densities calculated for 65 nm and 2 μm layer thicknesses at moderate and high stresses in Cu (50 and 150 MPa, respectively). $(\sigma_{Cu}, \dot{\gamma})$ couples were determined by the best fit of data the Fig. 4.6 subset.

These dislocation densities are similar to those reported in as rolled ARB Cu-Nb composites of similar length scales: 0.5×10^{15} and 0.9×10^{15} for 200 nm and 1.2 μm laminates, respectively [58]. Cu can sustain a much higher density of dislocations within this composite system than is traditionally achievable in pure, large grain Cu, which builds a cell structure during creep [120]. This can be justified by the high density of bi-metal interfaces (efficient dislocation sources), and high stresses in Cu during creep.

4.5.2 Impact of Inhomogeneity

While ARB Cu-Nb laminates are $50-50$ composites of continuous single phase layers, they are far from ideal. Factors that might cause experimental results to deviate from the model outlined in this paper include: structure flaws that result from rolling, as well as characteristic events of structural evolution. This model neglects the spatial distribution of stress through a single layer.

The steady-state deformation of Cu-Nb composites occurs after $\sim 2-3$ % composite strain, according to the analysis of 400 °C tensile curves in Fig. 4.1. For 65 nm laminates, which typically fail before 5 % strain [16], it is very likely that void formation and tertiary creep begin during the composite transient response. Creep failure in ARB Cu-Nb multilayers occurs at structural defects which result from the rolling process [16]. Shear bands and poorly bonded interfaces exist prior to testing, and damage accumulation at these defects may begin very early in the creep process.

Figure 4.7 shows the microstructure of a 65 nm laminate which failed at 5 % strain after 87 hours at temperature. Interface voids were observed throughout the structure at Cu-Nb interfaces, and some triple points with Cu-Cu grain boundaries.

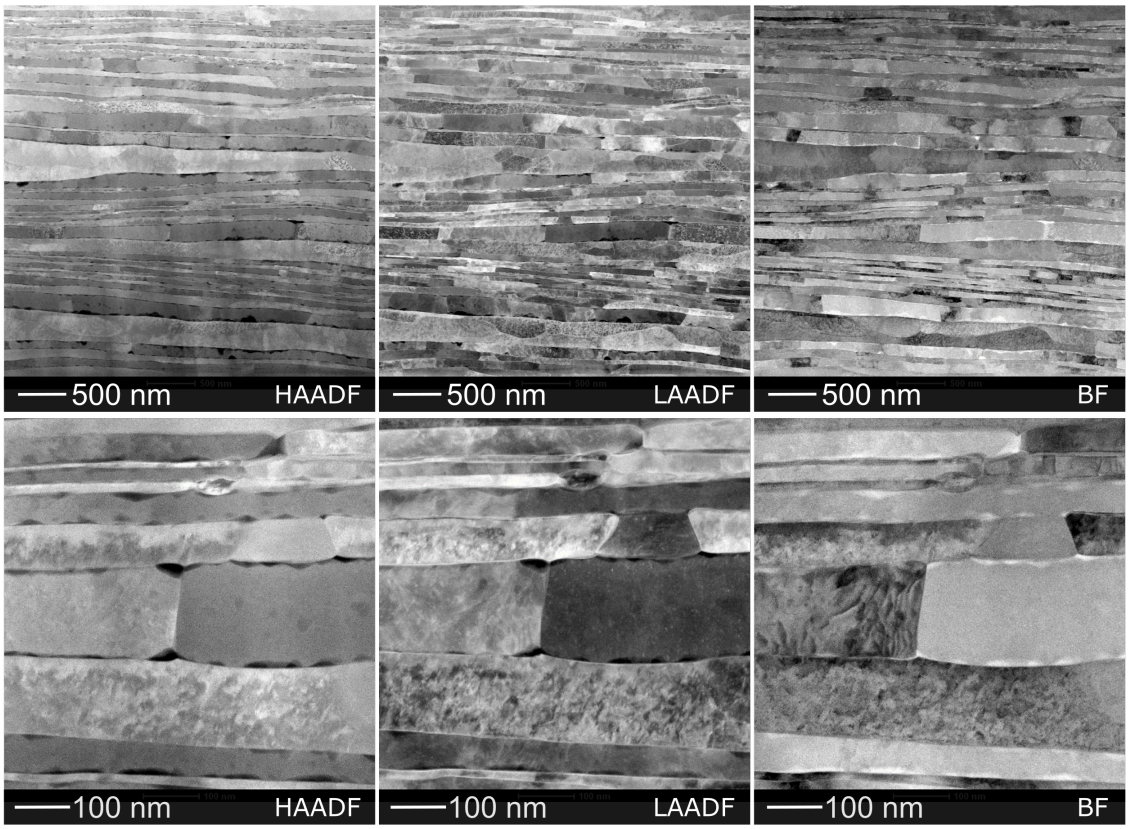


Figure 4.7: (S)TEM micrographs of a 65 nm laminate post-failure. Left to right, image contrast highlights phases (HAADF), defects (LAADF), and voids (BF). (Top) Overview of laminate structure. (Bottom) Close-up view of bi-metal interface voids. Creep load axis and rolling direction is shown left to right. Sample endured 5 % strain, 87 hours at 400 °C, and applied creep stress of 320 MPa jumped to 350 MPa.

Similar distributions of voids were observed in laminates interrupted prior to failure (65 nm at 2.5 % and 200 nm at 5% strain). The assumption of uniform stress throughout each phase during transient and steady-state may be compromised by the presence of these interface voids at low creep strains.

Cu-Nb laminates form voids which grow into the Cu phase after significant time at temperature with no externally applied stress [108]. It is likely that samples tested at low strain rates develop voids at low strains, due to the effect of time at temperature; while high strain rate tests develop voids by a more traditional

tertiary creep procedure, the accumulation and accommodation of strain. In any case, the range of applied stresses is very limited by the composite behavior.

While it has been reported that pure Cu creep curves show that stage I and III are significant fractions of Cu creep life [121–123], these deformation responses have been neglected in this study. At 400 °C stage I copper creep occurs significantly faster than the time scale associated with composite transient creep [124]. Stage III creep is likely delayed by the confined nature of Cu and stress redistribution accommodated by Nb, and it has been assumed that tertiary failure of the composite is dominated by processing defects effecting both phases. For these reasons, it is sensible to assume that Cu deforms according to stage II creep laws for the entirety of transient and steady-state composite behavior.

The as rolled ARB laminate structure contains significant non-uniformity. Texture evolution and shear localization during rolling contribute to the tortuous interface morphologies seen in Figure 4.1 [3]. These factors and the resulting distribution in layer thickness cause local variations in stress. The distribution of layer thickness in the larger length scale laminates (500 nm and above) is Gaussian and therefore modeling an average behavior is likely a reasonable assumption. On the other hand, the smaller layer thicknesses (below 500 nm) have a log normal distribution, and the contribution of large, creeping Cu layers may skew the deformation behavior locally.

The bounds of this model assume that Cu and Nb deform together for the entirety of transient and steady-state regimes. ARB Cu-Nb composites show significant layer pinch-off and even void formation at bi-metal interfaces with sufficient heat treatment [12, 101, 108]. Pinch-off of Nb layers increases connectivity of the creeping Cu phase, decreasing the aspect ratio of Nb, ultimately resulting in spherodized Nb in a Cu matrix [13, 85, 101]. This structure evolution occurs more

quickly and frequently in thin layers and at shear bands. These regions are likely to have stress concentrations which may upset model assumptions.

4.6 Summary and Conclusions

The strong correlation between minimum creep rate and laminate length scale is explained by the increased hardening in the Nb layer with decreasing layer thickness. Despite the fact that only one phase is creeping, the composite creep response can be described in similar regimes: transient, steady-state, and tertiary. The composite transient response is a result of a load transfer from Cu to Nb. Once Nb plateau stress is reached, the stress in each phase is constant, and therefore the time dependent deformation is in steady-state, until tertiary failure.

The semi-analytical model detailed in this study can predict transient and steady-state creep rates within excellent agreement to experiments. The creep parameters fit to composite transient behavior suggest that diffusion dominates stage II creep in the Cu phase, and therefore limits composite deformation in steady-state.

Main conclusions include:

- Modeling Nb strain hardening behavior and Cu stage II creep behavior provides excellent prediction of ARB Cu-Nb composite creep behavior.
- The plateau stress, and the associated strain, defines the transition from transient to steady-state creep.
- There is a narrow stress range in which steady-state behavior is achievable, and it is further limited by total composite strain and structure evolution within the layers.

- The Cu creep mechanism is dominated by vacancy diffusion enabling dislocation climb and is consistent between all length scales of Cu-Nb laminate.

Chapter 5

Structural Evolution

In this chapter, the thermal stability of ARB Cu-Nb is assessed through microstructural analysis of heat treated material of various length scales. Heat treatments were performed at high temperatures for copper (0.50-0.57 T_m), but at which niobium diffusivity is limited (0.25-0.28 T_m). Annealing times range from 30 minutes to 30 days at temperature. Structural evolution and hardness measurements were assessed for laminates with layer thicknesses ranging from 8 μm to 30 nm. After 30 days, 65 nm laminates remain nanostructured with no significant coarsening. Voids at bi-metal interfaces, a phenomena that has not been previously reported in these systems, grow larger and more frequent with time. Analysis of structural evolution mechanisms and system stability will be discussed in relation to microstructure, thermal property mismatch, and the driving force for copper recrystallization.

Important notes about terminology for this Chapter are that: (1) Laminate length scale is synonymous with "nominal layer thickness", and (2) microstructure is framed in the context of grain structure and layer structure, rather than nominal

layer thickness. Structure evolution of this bulk composite system as a combination of mechanisms at several length scales due to the distribution of layer thicknesses and variation in initial microstructure for a given length scale. "Large" laminates have nominal layer thicknesses of 500 nm and above. "Small" laminates have nominal layer thicknesses below 500 nm.

5.1 Background

Nanocrystalline metals perform well structurally, however they are known to coarsen at elevated temperatures. Structure evolution can significantly decreases the mechanical performance of metals, therefore thermal stability is a critical design parameter for materials which have to perform well in high temperature environments. Bi-metal nanolaminates show promising resistance to coarsening at high temperatures due to the confined nature of multilayer structures. Grains can only coarsen to the length scale of the laminate layer thickness. Immiscible systems, such as Cu-Nb, are most advantageous because diffusion paths allowing structural evolution of layer morphologies are limited to grain and interface boundaries.

Layer discontinuity has been predicted in laminates based on boundary grooving kinetics [13, 50, 86, 125]. It is assumed that structure coarsening will occur after the structure pinches off because phases are no longer confined at bi-metal interfaces. For this reason, thermal stability in multilayer systems is associated with the time necessary to groove through a given layer thickness. This definition of stability and degradation mechanism accurately describes metallic multilayer systems which are created via deposition methods because grains are either equiaxed or columnar, and span the entire thickness of a single layer. The ARB multilayers investigated in this study cannot be predicted so reliably. Initial microstructures in ARB material vary

with the nominal length scale of the multilayer, and do not have the same "ideal" structure as PVD materials. The evolution of texture with temperature has been well characterized for the Cu-Nb ARB systems [12, 33], though these studies do not consider the layer structure or grain coarsening.

The structural evolution of ARB laminates is significantly different from PVD laminates due to differing initial grain structures, dislocation densities, and layer morphologies. Additionally, previous authors do not investigate anneals at extended times and moderate temperatures.

5.2 Relevant Experimental Details

Structural evolution of grain and layered structures in ARB Cu-Nb multilayers was characterized using tensile testing, hardness measurements and microscopy. Microscopy analysis techniques included: backscatter secondary electron (BSE), electron backscatter diffraction (EBSD), and scanning transmission electron microscopy (STEM). Annealing was performed at 400 °C and 500 °C in protective environments.

Results of a recovery anneal (30 min at 400 °C will be presented, which corresponded to the heat treatment performed prior to compression testing [68, 74, 80]. Anneals two days in length produced microstructures consistent with those that developed prior to steady-state creep.

Finally, 65 nm laminates were heat treated at increments up to 30 days in order to understand pinch-off and coarsening effects anticipated from theory.

Length Scale (nm)	AR Hardness (HV)	HT Hardness (HV)
1800	122 ± 11	108 ± 1.0
500	160 ± 2.1	134 ± 1.0
245	169 ± 1.2	157 ± 1.6
140	183 ± 1.0	173 ±3.7
65	213 ± 1.0	215 ± 2.0
30	237 ± 3.6	243 ± 3.5

Table 5.1: Comparisons of as rolled (AR) ARB Cu-Nb to multilayers heat treated (HT) for 30 minutes at 400 °C. These values are graphed in Fig.5.1

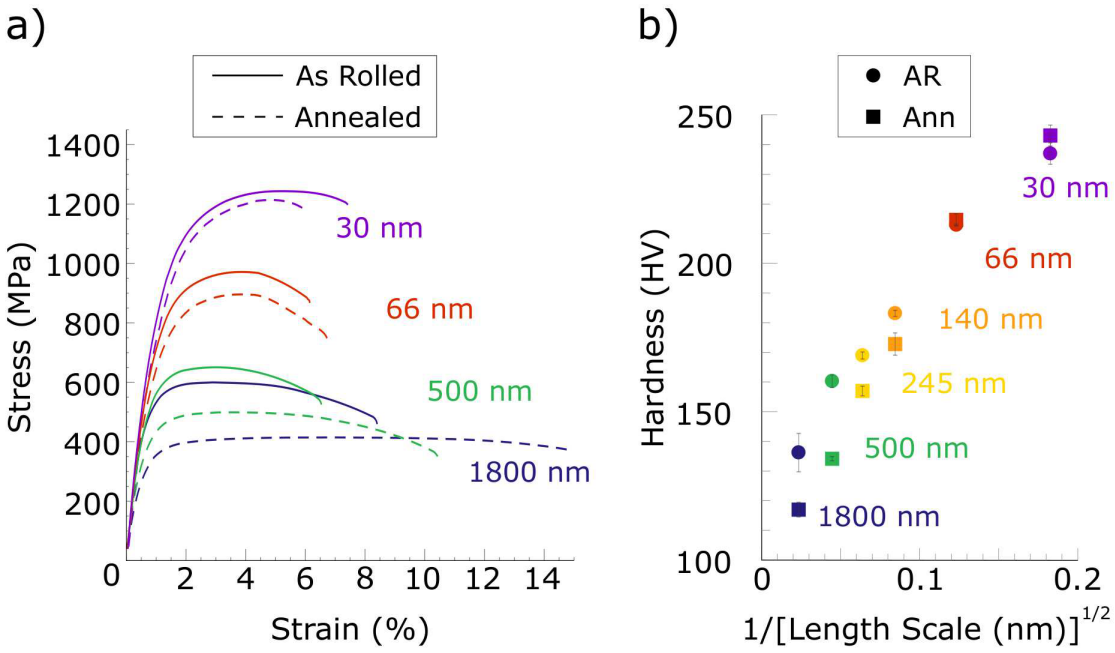


Figure 5.1: Comparisons of as rolled ARB Cu-Nb to multilayers annealed for 30 minutes at 400 °C. (a) Tensile behavior (b) Vicker's hardness measurements plotted against the inverse square root of nominal layer thickness to simplify for the known Hall-Petch relationship observed in Cu-Nb multilayers.

5.2.1 Recovery Anneal

Laminate dislocation density, initially very high, was partially recovered by annealing samples at 400 °C for 30 minutes. The variation in recovery with composite length scale was assessed by comparing tensile and hardness behavior of these re-

covered laminates to the as rolled condition.

Deformation behavior observed during tensile testing is shown in figure 5.1a. Ultimate tensile strength (UTS) of small length scale laminates (30 nm and 66 nm) decreased by less than 6 %. Annealed laminates of these smaller layer thicknesses showed negligible change in ductility. Behavior of the larger length scale laminates changed significantly after annealing. UTS of the 500 nm and 1800 nm laminates decreased over 18 % and 30 %, respectively. Ductility of the annealed larger laminates increased significantly compared to the as rolled condition.

Hardness measurements were performed on laminate samples of the same layer thicknesses as those for the tensile tests, as well as a few intermediate length scales. Figure 5.1b is a Hall-Petch-type plot of Vicker's hardness, showing a linear dependence with inverse square root of length scale for both as rolled and annealed laminates. Hardness measurements show that strength decreased more significantly for larger length scale laminates than smaller length scales, comparably to tensile results. Hardness values are reported in Table 5.1.

5.2.2 2 Day Anneal: Varied Length Scales

Table 5.2 lists samples of various length scales which were annealed for 2 days at 400 °C and 500 °C, and the Vicker's hardness calculated for each. A Hall-Petch type plot, Figure 5.2, was created to show the relationship between hardness and length scale, comparing as rolled strength to that after the annealing conditions. Hardness decreased after all heat treatments. Similar to the recovery anneal results, annealing decreased the strength of laminates with larger length scales more significantly than the smaller layers. Hardness decreased more after annealing at 500 °C as compared to 400 °C.

Length Scale (nm)	Temperature (°C)	Time (hours)	Hardness (HV)
8000	400	48	97.6 ± 1.5
8000	500	54	78.8 ± 1.4
2000	400	48	107.4 ± 2.1
2000	500	54	96.8 ± 2.2
100	400	48	187.3 ± 1.5
100	500	54	172.0 ± 2.0
65	400	48	211.3 ± 2.6
65	500	54	188.6 ± 1.3

Table 5.2: Heat treatments performed on ARB Cu-Nb laminates and corresponding Vicker's Hardness values. 2 Day heat treatments were performed on several length scales.

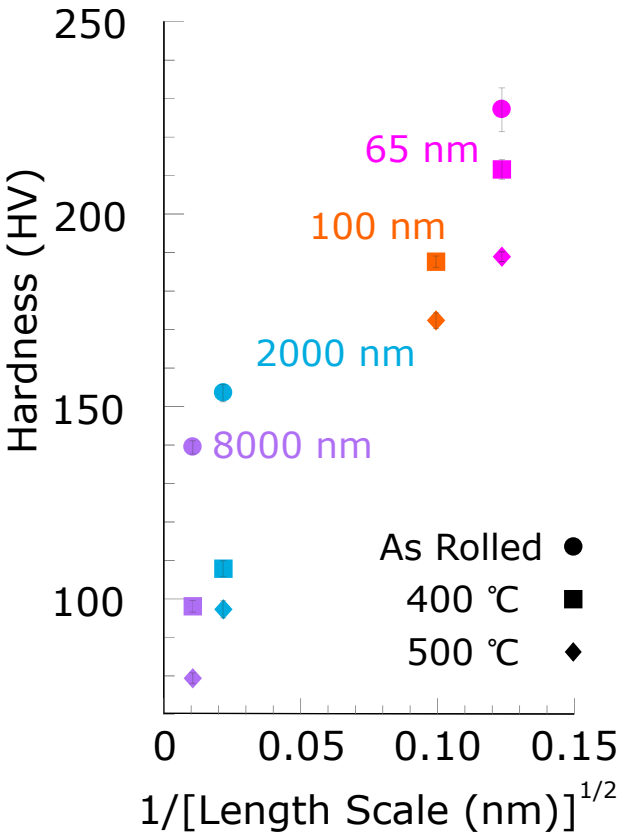


Figure 5.2: Hardness of CuNb laminates of several length scales (from 8000nm down to 65 nm) annealed for 2 days at 400 °C and 500 °C is compared to as rolled material. Data shown in Table 5.2

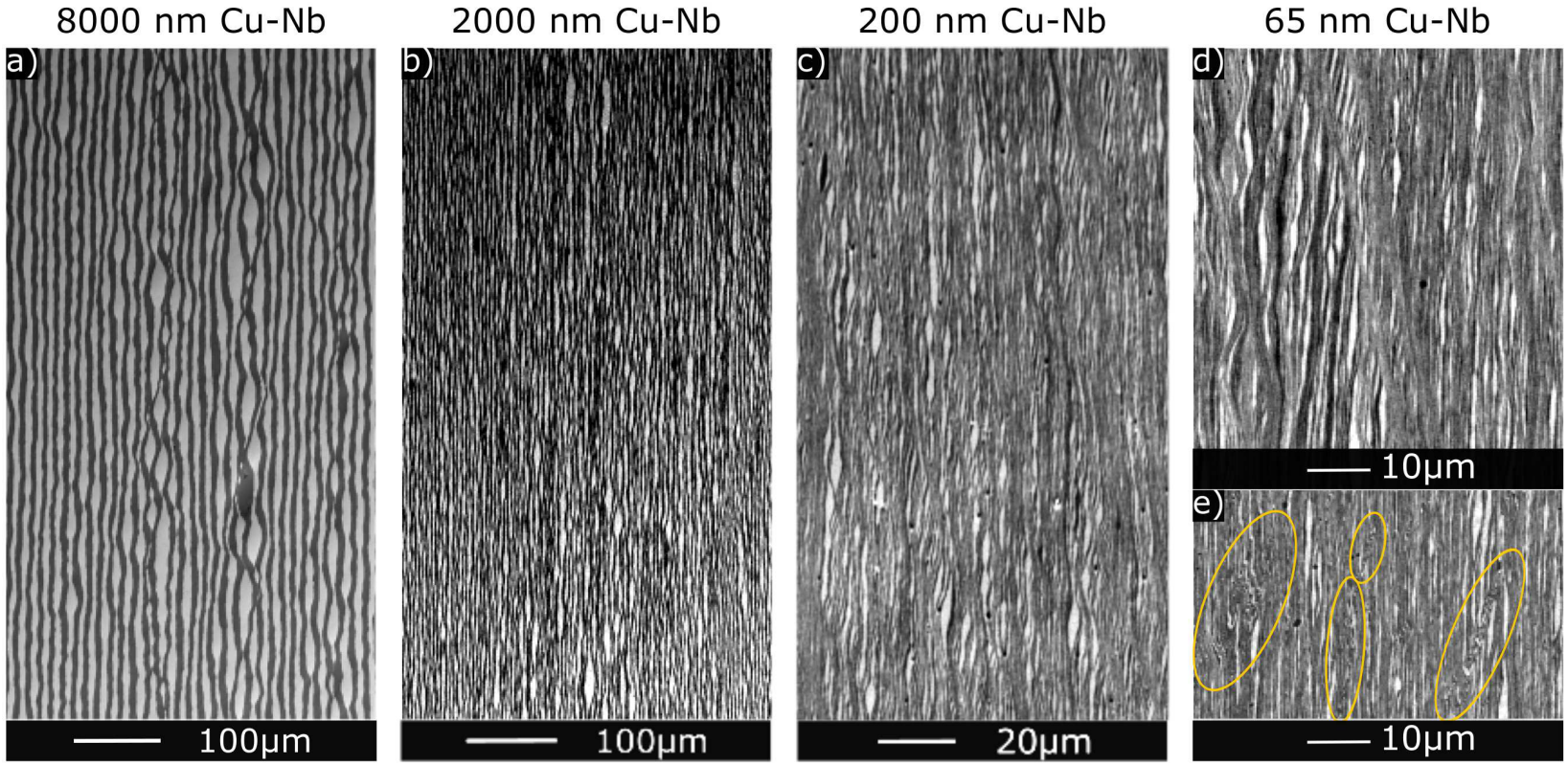


Figure 5.3: Layered structures of material annealed at 500 °C for 54 h. (a) 8000 nm, (b) 2000 nm, (c) 200 nm, (d) 65 nm, and (e) highlights kinked regions of 65 nm laminate.

Layered structures remained largely the same after annealing for 2 days. Figure 5.3 shows a variety of laminate length scales after annealing at 500 °C for 2 days. Comparing these structures to those in Figure 1.10 (Chapter 1), very little difference can be noticed. The most notable differences occur in the 65 nm material, as highlighted in Fig. 5.3e. Regions of this material kinked locally during annealing. Kinking has been reported for ARB Cu-Nb under compressive stresses [44, 68, 74, 80], and has not been observed in as rolled material. Unlike the phenomenon of macroscopic kink band formation, misorientation of the layered structure here is local and does not propagate in a wide band. The traditional $\phi = 2\beta$ geometry was maintained even within these small regions.

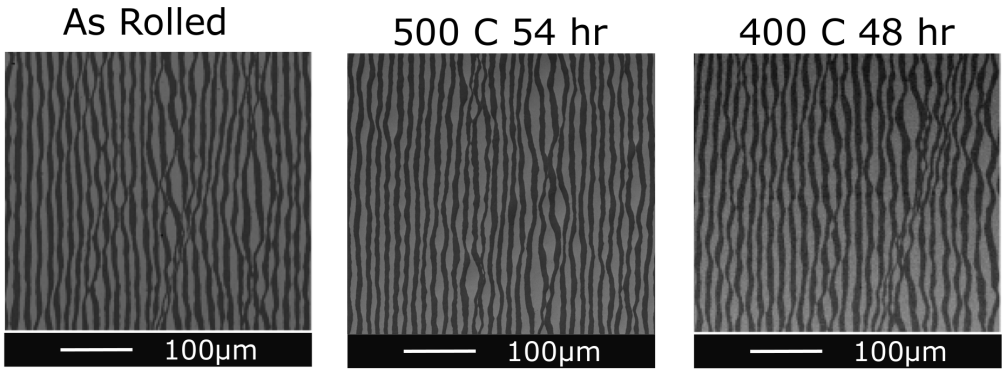


Figure 5.4: Layer structures of 8000 nm laminates shown as rolled (a), after annealing at 400 °C for 48 h (b), and 500 °C for 54 h (c).

Grain boundary grooving was observed at triple points and pinch-off occurred in very thin layers within laminates of all nominal layer thicknesses heat treated. In larger laminates, these regions were solely associated with shear bands present in the as rolled material. Figure 5.4 compares backscatter SEM micrographs of 8000 nm laminates as rolled to those annealed at 400 °C and 500 °C. Boundary grooving was noticeable, but not significant. This larger structure was stable after annealing for 2 days.

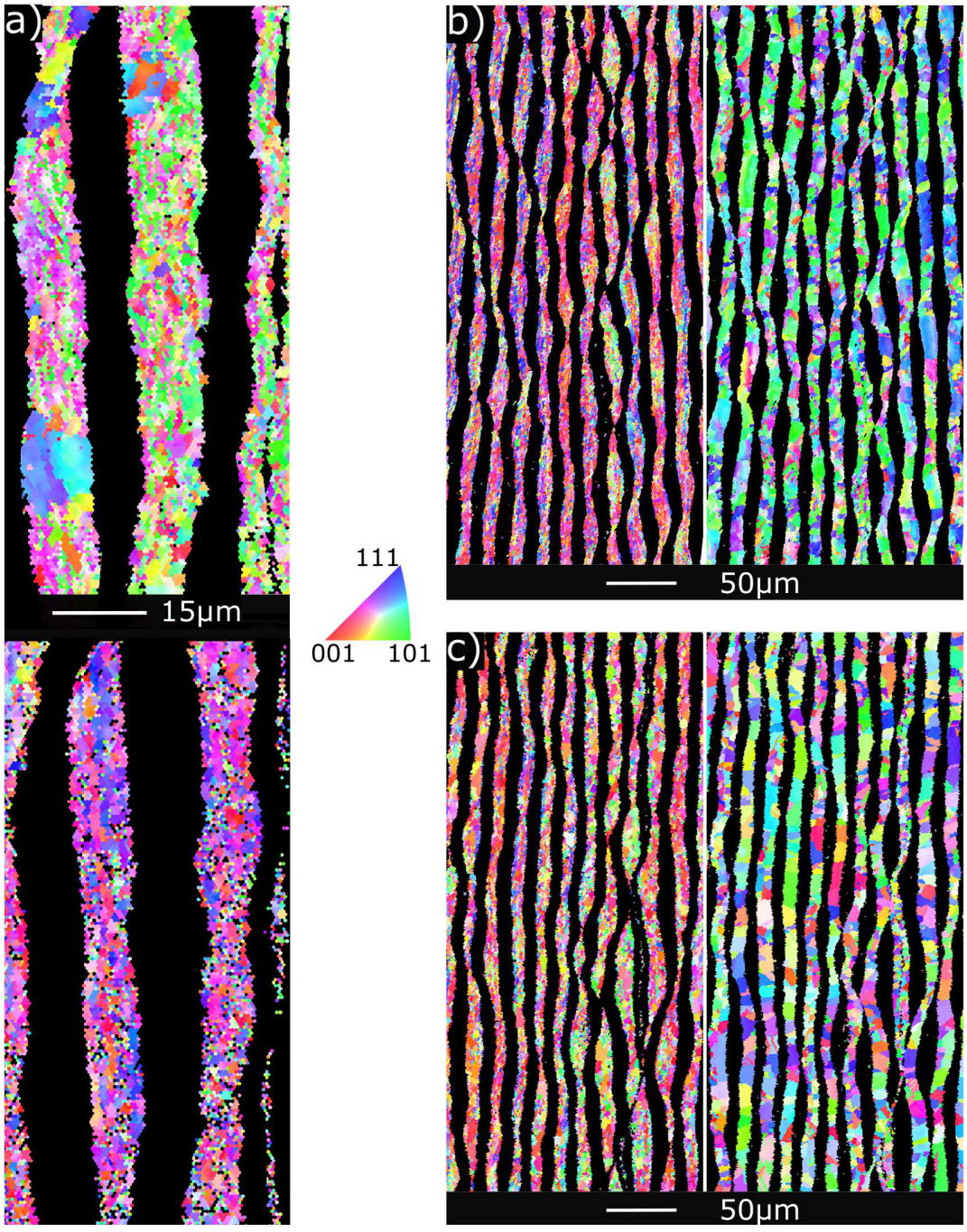


Figure 5.5: Grain structures of 8000 nm laminates shown as rolled (a), after annealing at 400 °C for 48 h (b), and 500 °C for 54 h (c).

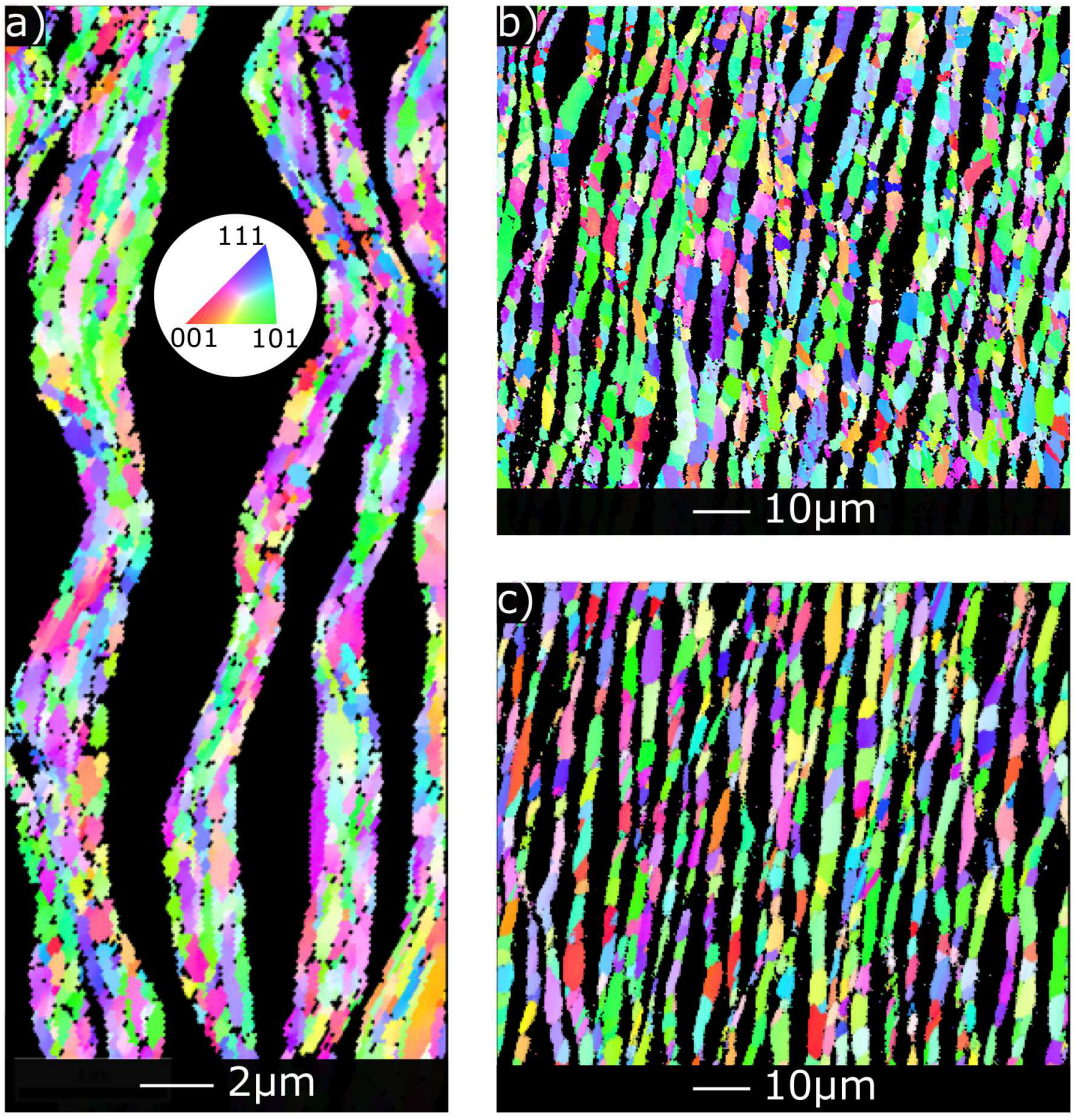


Figure 5.6: Grain structures of Cu in 2000 nm laminates shown as rolled (a), after annealing at 400 °C for 48 h (b), and 500 °C for 54 h (c).

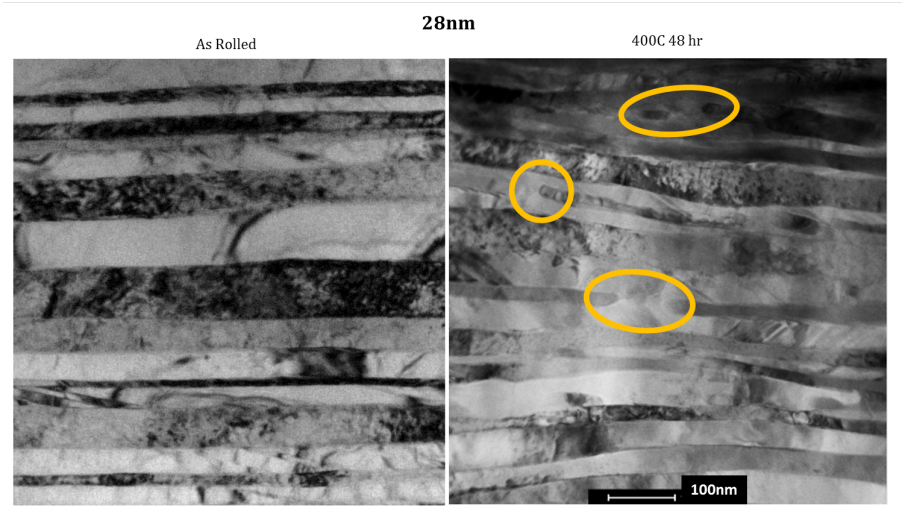


Figure 5.7: The left image is a bright field TEM micrograph showing the AR grain structure of a nominally 28 nm layer thickness ARB Cu-Nb laminate. The right image is a 28 nm laminate after annealing at 400 °C for 48 h. Pinch-off events are circled for emphasis. Note that the scale bar is the same for both images.

The grain structures of larger laminates are shown in Figures 5.5 and 5.6 comparing IPF maps of as rolled material to the structures after 2 days annealed at both 400 °C and 500 °C. Figure 5.5 shows both Cu and Nb. The change in grain structure of Nb was not significant at either temperature. Cu grains grow and, in some regions, recrystallize (note the presence of annealing twins). Unconstrained, grain growth be effectively limitless. Recrystallized grain sizes in this system are limited in one dimension by the layer thickness; boundary energies in this system dictate that even the calculated maximum grain sizes maintain low aspect ratios (between 1 and 1.6) [50, 97, 126]. This significant evolution of Cu grain structure was observed in both 8000 nm and 2000 nm laminates, at both temperatures. Micrographs in Figure 5.7 show grain and layer structure of 28 nm Cu-Nb as rolled and after annealing at 400 °C for 48 hours. Layer discontinuity is observed in thin Nb layers.

Length Scale (nm)	Temperature (°C)	Time (hours)	Hardness (HV)
65	400	120	199.5 ± 2.2
65	500	120	188.3 ± 1.1
65	400	360	197.2 ± 1.0
65	500	360	180.8 ± 2.5
65	400	720	191.4 ± 1.2
65	500	720	175.9 ± 1.2

Table 5.3: Heat treatments performed on ARB Cu-Nb laminates and corresponding Vicker's Hardness values. 65 *nm* laminates were analyzed at increments up to 30 days at temperature.

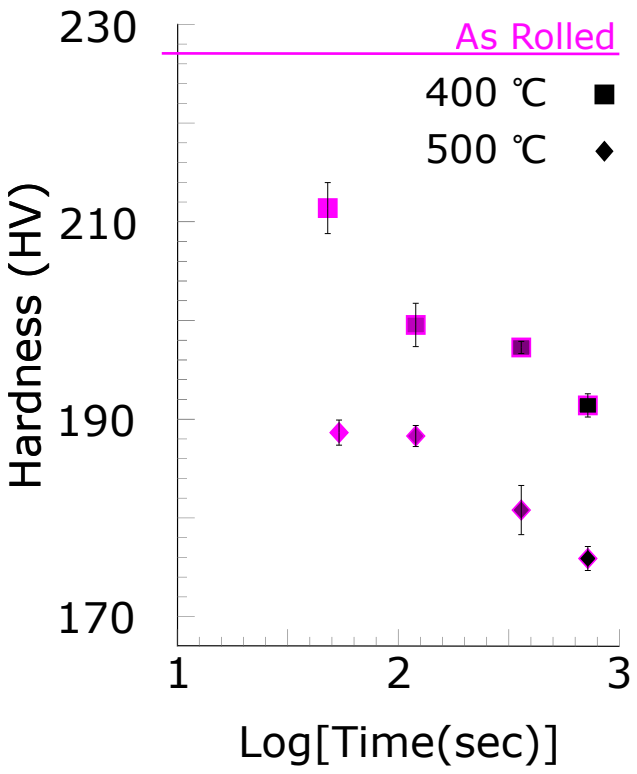


Figure 5.8: Hardness of 65 nm Cu-Nb laminates annealed at 2, 5, 15 and 30 days at both 400 °C and 500 °C is compared to as rolled material. Data shown in Table 5.3 (longer times), 5.2 (2 days), and 5.1 (as rolled).

5.2.3 30 Day Anneal: 65 nm laminates over time

Table 5.3 and Figure 5.8 show the evolution of Cu-Nb multilayers over long times at temperature. Table 5.3 lists Vicker's hardness for 65 nm samples which were annealed for 5, 15, and 30 days at 400 °C and 500 °C. Figure 5.8 plots these, along with the as rolled and 2 day annealed, hardness values over time on a log scale. There is a clear decrease in hardness with increases in both annealing time and temperature as compared to the as rolled 65 nm laminate hardness values.

Micrographs illustrating the structural variation over time at 400 °C are shown in Figure 5.9. All images are at the same scale, and atomic contrast (HAADF) shows the layered structure, while the grain structures of the same regions are shown for comparison (BF and LAADF). The laminate layer structure is maintained well at 400 °C over this period of time. Grain substructures can be identified in initially very high aspect ratio grains. High dislocation densities are notable even after 30 days of structural evolution.

A comparison of the structural degradation at 15 and 30 days is shown for both 400 °C and 500 °C in Figure 5.10. Evolution at 500 °C is clearly more significant than that at 400 °C. In all cases, pinch-off of Nb layers is evident (and even some Cu layers at 500 °C). Similar dislocation content and substructures is observed for all heat treatments shown in this figure. Some locally kinked regions are evident after 15 days at 400 °C, Fig. 5.10a. Bi-metal interface voids exist after 30 days at both temperatures. These voids have grown further into the Cu phase at the higher temperature.

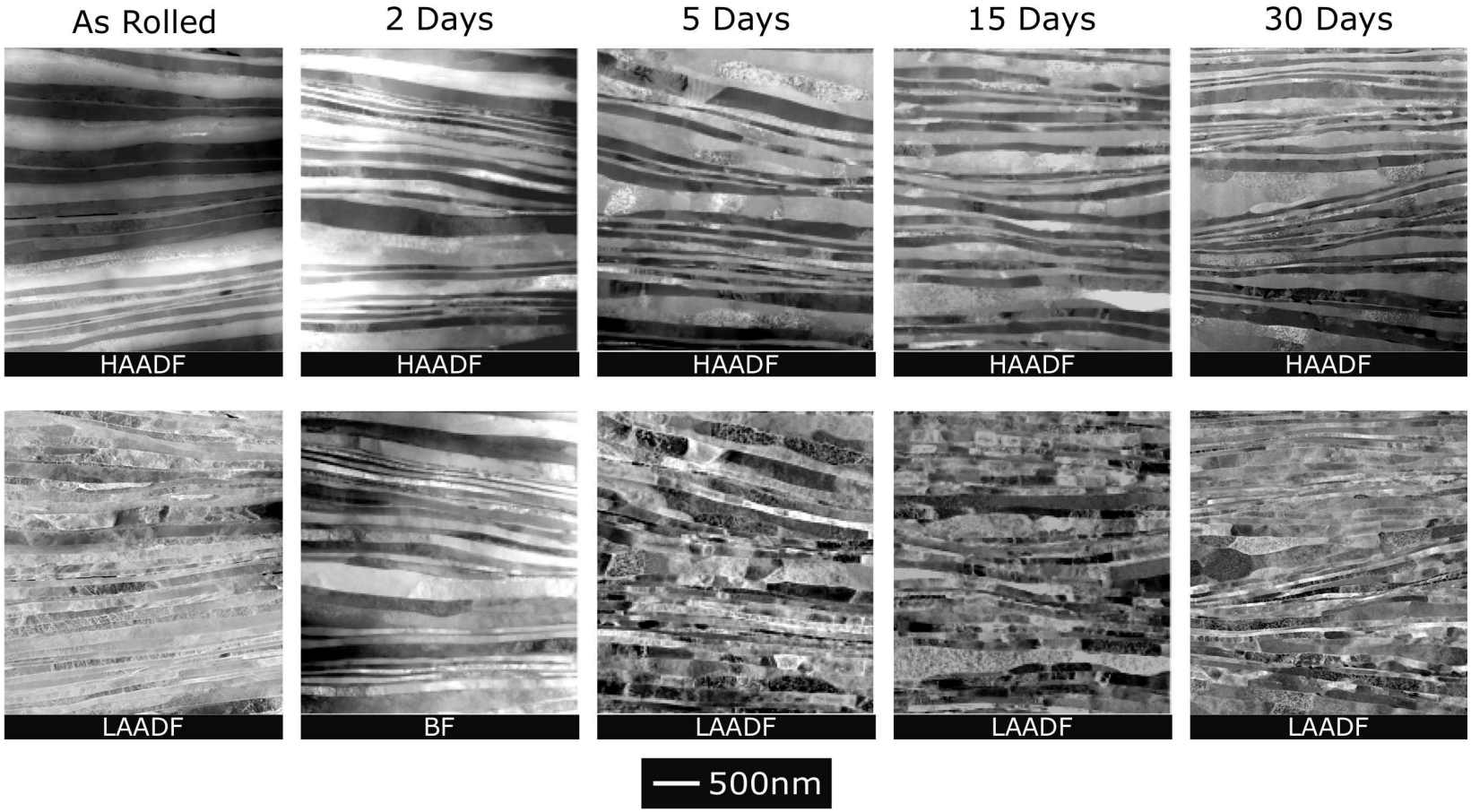


Figure 5.9: 65 nm laminates do not coarsen significantly over 30 days heat treated at 400 °C. Structure shown for various annealing times in atomic contrast (Top) and defect contrast (Bottom).

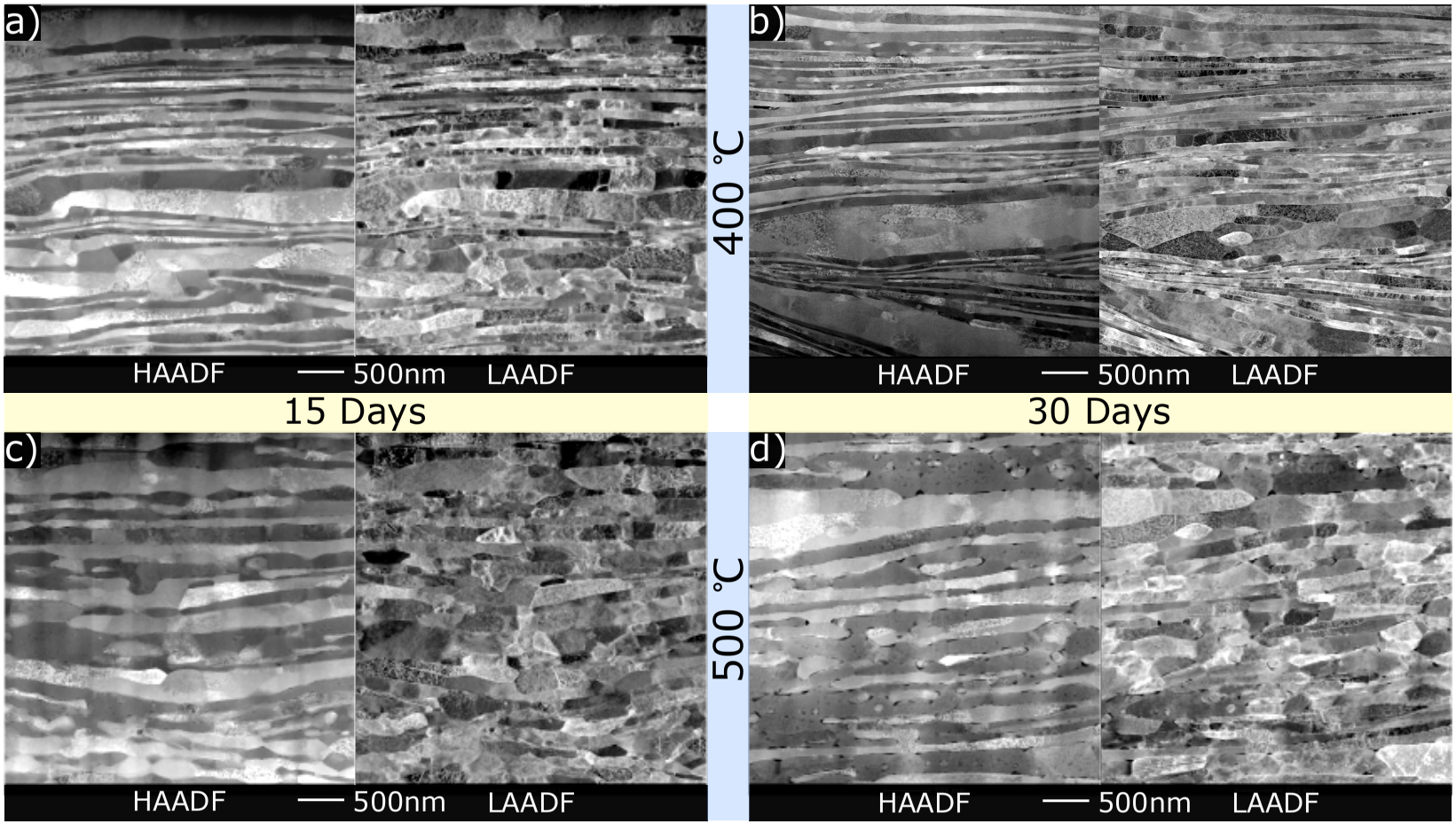


Figure 5.10: 65 *nm* laminate annealed for 15 and 30 Days at 400 °C and 500 °C

Micrographs highlighting the most prominent structure evolution mechanisms are shown in Figures 5.11, 5.12, and 5.13. The features indicating these mechanisms include: grain recrystallization and substructures; pinch-off, grooving and spheroidization; and voids at triple junctions and bi-metal interfaces.

Figure 5.11 outlines copper layers that have evolved grain structures. Within the 65 nm laminates, both substructure formation and recrystallization are observed. Recrystallization (with annealing twins) is most notable in Fig. 5.11d-f. High dislocation density grains which have formed substructures are frequent throughout. Circled regions within Fig. 5.11 indicate pinched off Nb layers.

Figure 5.12a shows a typical region of 65 nm laminate degradation. Bi-metal interface voids are present at a very small volume fraction, but frequent throughout the structure. An initially very thin Nb layer has pinched off at regularly spaced increments, leaving behind a train of Nb spheres in a Cu layer. Fig. 5.12b and c are close-up views of some of these phenomena. Notably, a Cu-Cu-Nb triple junction that has grooved and formed a bi-metal interface void which grew into the Cu grain boundary.

The void fraction at 500 °C is higher than that at 400 °C, as seen in Figure 5.13. Bright field contrast (BF) shows voids in white, while they are black in the other contrasts. These voids occur at both tortuous and flat interface regions, in areas with both substantial and very little evolution.

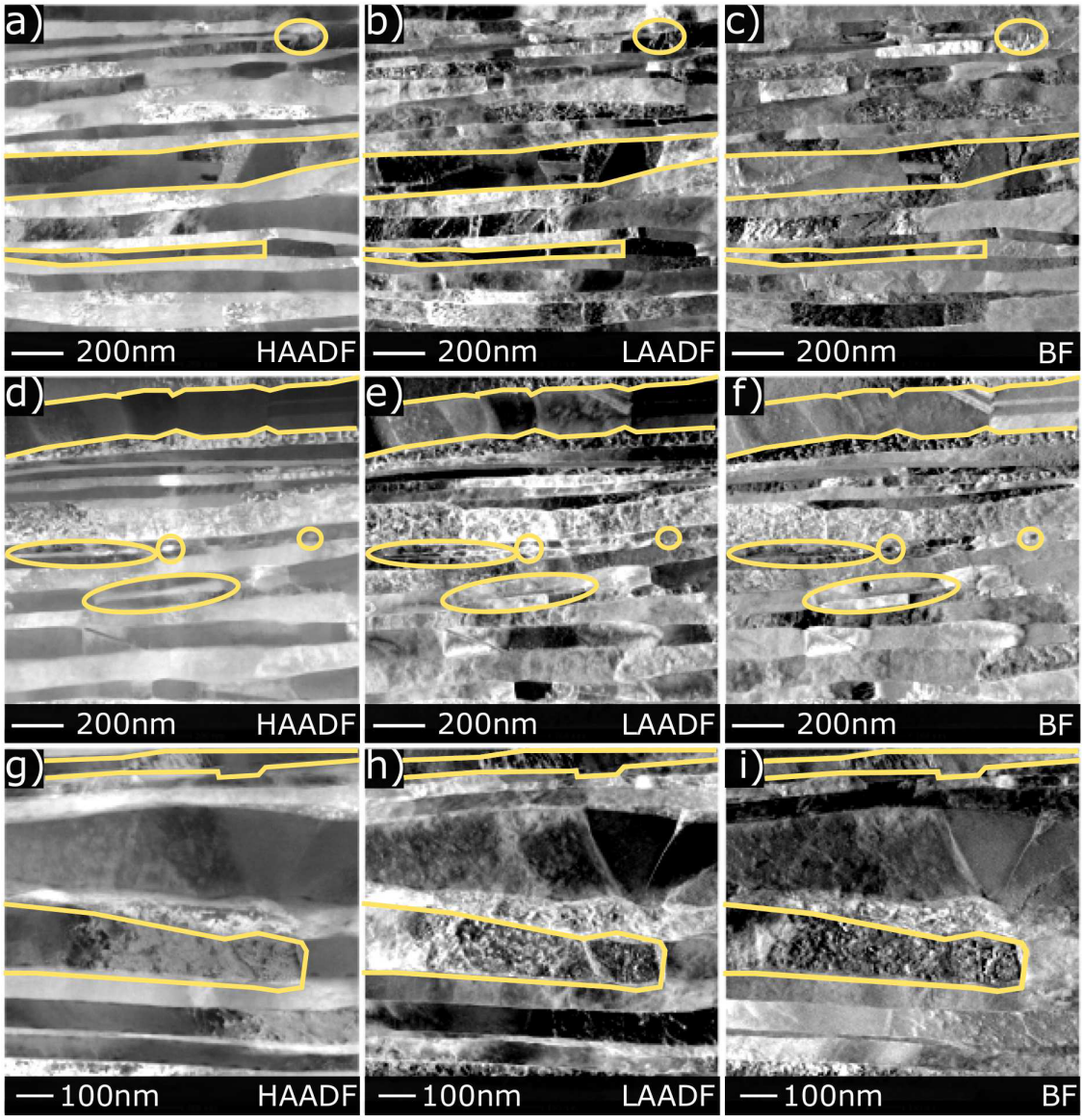


Figure 5.11: 3 regions showing evolution of structure after annealing of a 65 *nm* laminate for 15 Days at 400 °C. Discontinuous Nb layers are circled. (a-c) and (g-i) outline Cu layers with dislocation substructures. (d-f) outlines a larger Cu layer which has substructures and recrystallized grains (note annealing twins). Grooving at RX grain boundaries is notable.

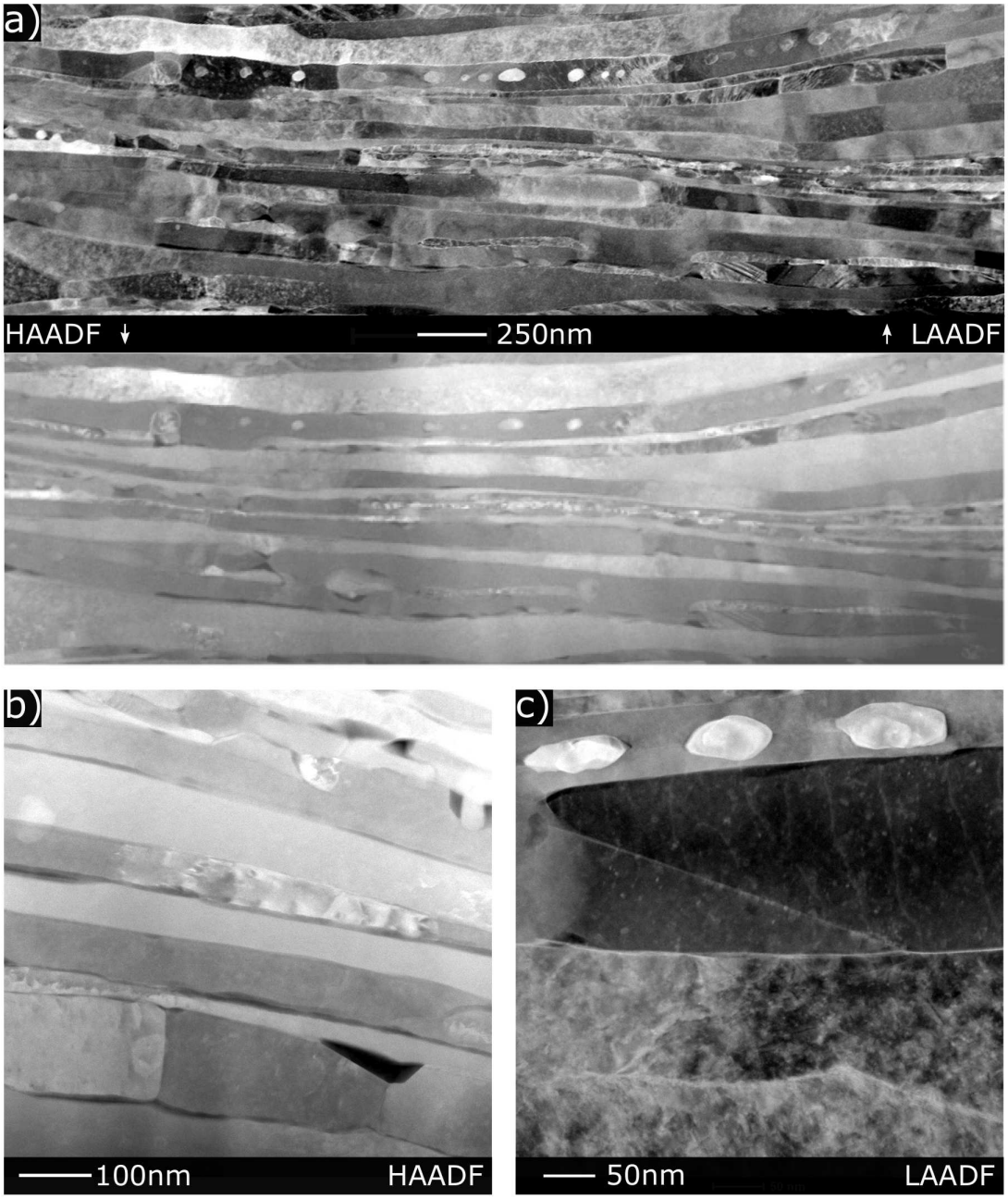


Figure 5.12: A variety of grooving and pinch-off morphologies shown for 65 nm laminate annealed for 30 Days at 400 °C. Nb spheroidization regularly spaced indicates Rayleigh instability driven pinch-off (a,c). Void growth at Cu-Cu-Nb triple point (b). Cu grain coarsening in Nb pinch-off region (a).

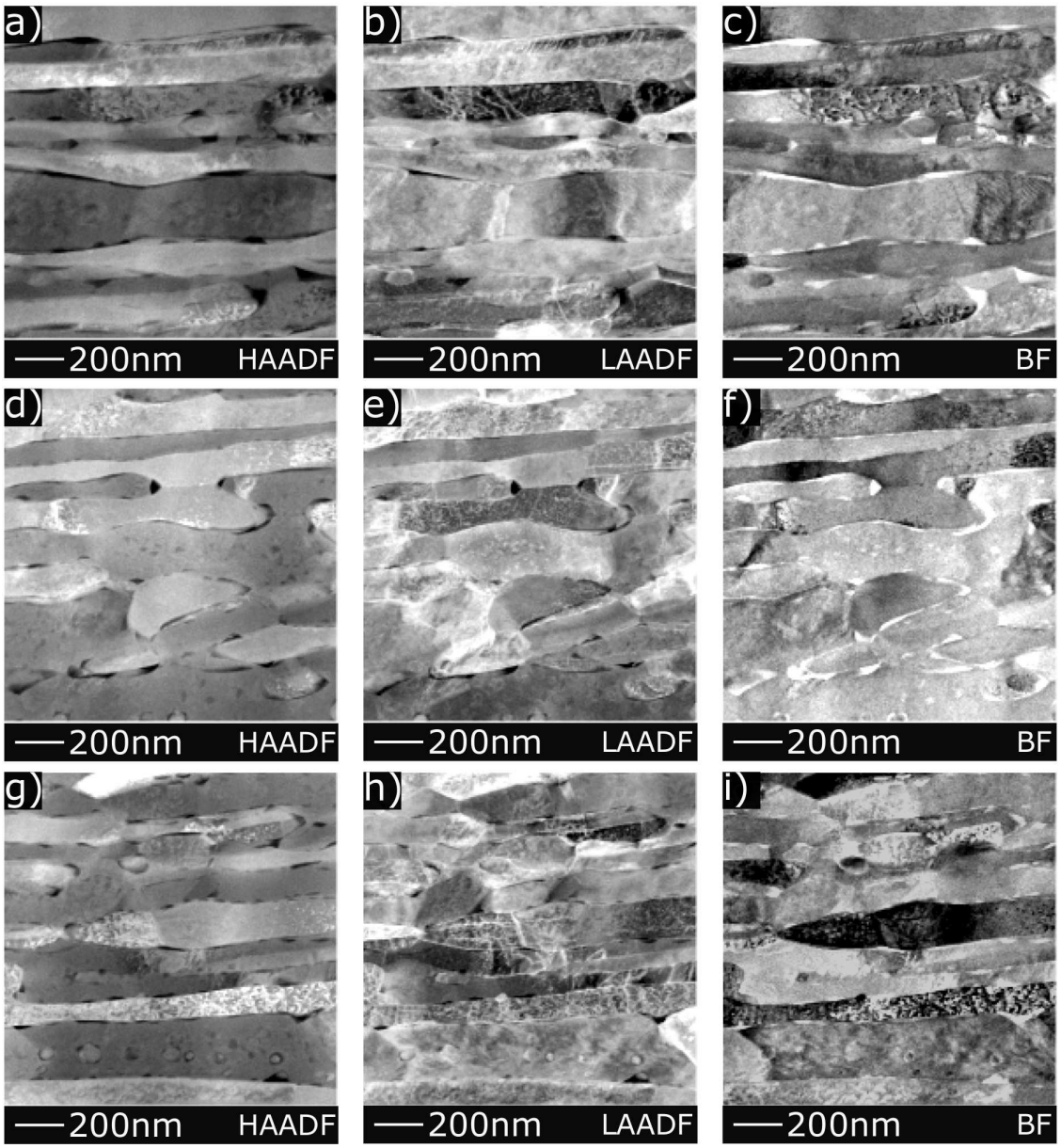


Figure 5.13: 3 representative regions showing high fraction of voids in 65 nm laminate after 30 Days at 500 °C.

5.3 Discussion

Structural evolution in ARB Cu-Nb is dependent on high dislocation densities, variations in boundary energies (and curvatures), and most notably on the initial variation in grain structure. Due to the rolling process, within a single multilayer, layers can contain polycrystalline regions, regions in which every grain is in contact with a Cu-Nb interface (bi-crystals), and effectively single-crystalline regions. The distribution of these types of regions varies with the nominal length scale of the multilayer; through the thickness of a layer, larger length scale multilayers are generally polycrystalline, and smaller length scale multilayers are single-crystalline. The ratio of elastic energy to boundary energy, and therefore the mechanisms of structural evolution, vary between these different types of regions.

Grains within polycrystalline regions are effectively unconfined, and grain growth is a large driver for structure evolution. Grain boundary grooving at bi-metal interfaces is evident, but layer pinch-off is infrequent. The modified Mullin's theory for grooving cannot be directly applied to polycrystalline layers, as grain boundary structures are more complex than a single grain boundary grooving from one bi-metal interface to the other. Single crystalline regions are highly confined and have high aspect ratios. Groove theory predicts times to pinch-off for thin Nb layers, however layer coarsening is not observed, as anticipated due to slow self diffusion of Nb. Even after 30 days at 500 °C coarsening is minimal.

5.3.1 Texture and recrystallization

A detailed study by Carpenter et al. assesses the evolution of texture in ARB Cu-Nb at various temperatures [12]. The frequency of high energy interfaces de-

creases at high temperatures, sharpening the texture peaks associated with low energy interface orientations [12, 90]. This is true for all annealing procedures, however, the sharpness of the texture tends to increase with increasing temperature, Figure 1.20 (Chapter 1) [12]. EBSD inverse pole figure (IPF) maps of as rolled and post-anneal microstructure analysis for 8 μm and 2 μm are shown in Figures 5.5 and 5.6. Clearly, after 48 hours at 400 °C, grain growth in copper is more significant than niobium. This difference is primarily due to a Cu:Nb melting point ratio of about 1:2 and the mobility character associated with this property. Texture data corresponding to these scanned area are too small to be statistically significant on their own, but the qualitative texture agrees strongly with the dominant orientations found in previous studies [12, 33, 62]. The deformation in the as rolled structure (particularly notable in the large color gradient within individual grains in the $2\mu m$ material.

Figure 5.1 shows tensile test data for a range of layer thicknesses of as rolled and annealed material. After a short annealing time, the dislocation content decreases due to dislocation recovery and annihilation. The larger layer thicknesses exhibit a greater decrease in strength as compared to the smaller layer thickness material due to dislocation recovery because the high initial content of dislocations after rolling contributes to hardening by forest dislocation barriers. The distribution of dislocations in smaller laminates is different, geometrically; the dislocation content is not only lower, but a significant portion is at bi-metal interfaces rather than within the grains. The primary source of hardening in smaller layer thicknesses is likely related to interface density, therefore, strength is maintained after annealing so long as layer continuity is maintained.

Additionally, high dislocation densities in ARB Cu-Nb drive continuous recrystallization during rolling [33] and are remain high in as rolled laminates [58]. Clearly,

Cu recrystallization is more significant than that in Nb at large layer thicknesses. Smaller layer thickness laminates are limited in dislocation storage and there is a higher threshold for nucleating grains [58]. Additionally, the area of Cu grain boundaries is small compared to the area of bi-metal interface. Therefore, the number of potential nucleation sites is limited by the grain structure. Texture evolution in Cu of small layer thicknesses may be reflected in substructures that reinforce low energy interface orientation relationships.

5.3.2 Layer morphology

The primary degradation mechanism in polycrystalline layers is boundary grooving. At moderate temperatures, 400 °C - 600 °C copper grains grow significantly, but niobium does not recrystallize. Figure 5.5 clearly illustrates this fact by contrasting the as rolled 8 μm laminate to heat treatments at 400 °C (48 h), 500 °C (54 h). It is difficult to discern whether layers have pinched off or the step size of EBSD may be larger than the smallest layer thickness scanned.

Figure 5.7 confirms pinching off of niobium layers. Both grooving and perturbation growth are interface diffusion controlled mechanisms, therefore have similar time dependence. It is likely that the dominant mechanism behind layer discontinuity will change with initial laminate length scale and grain structure from grooving at large layer thicknesses to perturbation growth at smaller layer thicknesses. Prediction of pinch-off is more complicated in the ARB Cu-Nb system due to the number of grains through thickness of a given layer and the variable angle of grain boundaries which complicates the application of Mullins' groove theory.

Pinch-off is predicted in Nb layers because the average grain boundary energies in Nb are larger than that of Cu ($\gamma_{gb}^{Nb} \sim 1.2\gamma_{gb}^{Cu}$) [13]. The most frequent interfaces in

the ARB system are significantly lower than the average grain boundary energies of both phases: Cu and Nb, $\gamma_{gb}^{Cu} = 650\ mJ/m^2$ and $\gamma_{gb}^{Nb} = 760\ mJ/m^2$, as compared to Kurdjumov-Sacs and Nishiyama-Wasserman, $\gamma_{int}^{KS} = 586\ mJ/m^2$ and $\gamma_{int}^{NW} = 576\ mJ/m^2$ [13, 28]. Significant grooving is most likely to occur at triple points associated with the less common, higher energy interfaces (reported up to 1000 mJ/m^2) [13, 28].

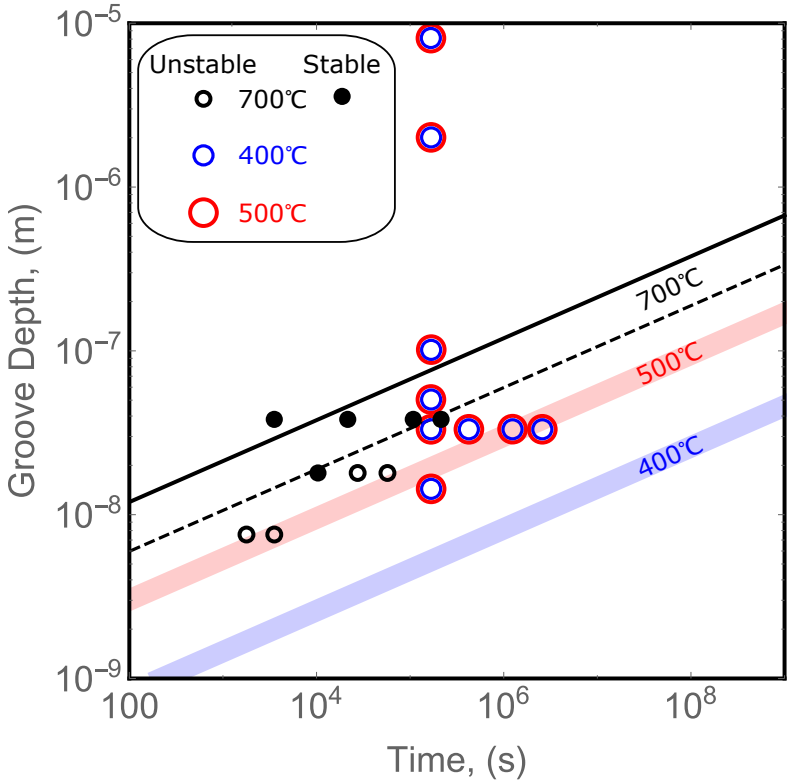


Figure 5.14: Unstable data indicates that pinch off was observed for a given layer thickness after some amount of time. Lines show predictions of groove depth over time based on a modified Mullin's groove theory [82]. Dashed line represents groove depth equal to a full layer thickness, solid line (and shaded lines) represent groove depth of one half the layer thickness. Data at 700 °C was recreated from reference [13].

Annealing for 48 h at 400 °C, as in Fig. 5.7, layers very thin layers (about 7 nm) are predicted to pinch off by grooving according to eqn. 1.12. Figure 5.14

is a recreation of Fig. 1.23 showing groove depth over time for 700 °C and the associated experimental data presented by Misra *et al.* [13]. The original figure predicts pinch-off with groove depth is equal to layer thickness (dotted line). The modified figure notes that layers groove from both triple points associated with a boundary, therefore pinch-off occurs with groove depth is one half of the layer thickness. Significant factors in predicting pinch off include interface and grain boundary energies, as well as annealing temperature (and subsequently boundary diffusion).

All laminate length scales contain very thin Nb layers, whether that be at shear bands in large laminates, or throughout in smaller laminates. As stability is defined here as a continuous structure, none of the annealed laminates here can be considered fully stable. The comparison of this experimental data, and that of the PVD material studied by Misra *et al.* in Fig. 5.14 emphasizes the complex nature of ARB Cu-Nb material.

5.3.3 Temperature effects and thermal stresses

Thermal stresses at 400 °C and 500 °C are significant in the Cu-Nb system due to the large mismatch in thermal expansion coefficients: $16.5 \times 10^6\ K^{-1}$ for Cu and $7.3 \times 10^6\ K^{-1}$ for Nb. Table 5.4 shows calculated thermal stress values for Cu and Nb with no external load, and assumptions of negligible residual rolling stresses, and co-deformation ($\epsilon_{Cu} = \epsilon_{Nb}$). Copper is in compression and niobium is in tension, significantly during heat treatment. Cu likely creeps in compression at this high stress. Ultimately, 0.3 % strain will accrue due to copper creeps, relieving this stress.

Void formation at Cu-Nb interfaces suggest that Cu creeps in compression.

Temperature °C **T (°C)**	**Cu thermal Stress** $\sigma_{th}^{Cu}\ (MPa)$	**Nb thermal Stress** $\sigma_{th}^{Nb}\ (MPa)$
300	-142	142
400	-193	193
500	-245	245
600	-296	296
700	-348	348
800	-399	399

Table 5.4: Thermal stresses in Cu and Nb are significant due to large coefficient of thermal expansion mismatch. Cu is in compression and Nb is in tension at elevated temperature.

The bi-metal boundaries are imperfect sources of vacancies, and readily initiate, terminate, and store dislocations [1, 26–28]. The tortuous nature of layers in this laminate combined with the large thermal stresses at elevated temperatures can cause significant shear stress along Cu-Nb interfaces, increasing dislocation mobility and diffusion long the boundary [127]. Stress gradients at a boundary, in a system which has active boundary diffusion, is a primary driving force for void formation in creep [78]. The large dislocation density in these laminates (particularly those stored at Cu-Nb interfaces) further drive vacancies toward the interface allowing for void formation. In addition to serving as sinks for vacancies created by climb, diffusion is enhanced by "imperfect boundary" character [128]. Nabarro-Herring and Coble creep activity combined with high dislocation densities and high mobility augment creep damage [121, 128].

The 65 nm laminates experienced local kinking. This phenomena occurs in compression and is associated with highly anisotropic deformation behavior and composite structures with significant local misorientation [68, 74]. The mismatch in thermal expansion coefficients for Cu and Nb put Cu in compression. A likely explanation for this local kinking is that highly tortuous regions of locally single

crystalline material influencing surrounding Nb layers.

5.4 Summary and Conclusions

The variables in annealing experiments were length scale, temperature, and hold time. Large layer thickness distributions within laminates cause all laminates to experience a combination of structural evolution mechanisms. Layers of larger thickness are polycrystalline, while smaller layers are single crystalline. The main conclusions from all heat treatments include:

Grain Structure

1. Recrystallization and grain growth is much more significant in copper than niobium due to higher Cu diffusivity at 400 °C and 500 °C.

2. Grains within polycrystalline layers coarsen during annealing. The majority of Cu grains span the entire layer thickness after annealing at 400 °C after 2 days even in 8 μm laminates.

3. Single crystalline layers, of grains with initially very high aspect ratios, form dislocation substructures during annealing. Nucleation sites are limited, and driving forces for nucleation of new grains are too high due to nanoscale confinement.

Layer structure

4. Predictions of grooving and pinch-off, which assume uniformity in layer thickness, cannot accurately describe degradation of ARB Cu-Nb. Fine layers

pinch off frequently in small laminates and at major shear localizations in large laminates.

5. Despite the development of layer discontinuities, the 65nm layer thickness laminates remain nanostructured after 30 days at 400 °C and 500 °C.

6. Interface void formation and growth into Cu layers is observed. This phenomenon is likely associated with thermal mismatch, local stress concentrations, high dislocation content at interfaces, and dislocation climb in Cu.

Mechanical Properties

7. Heat treatments which allow recovery without recrystallization cause significant decreases in strength for larger length scale composites, and little influence on small length scale laminates.

8. There is a clear decrease in hardness after heat treatment which corresponds to an increase in Cu grain size for larger laminates and layer discontinuity in smaller laminates.

9. Structural degradation of the layers within small length scale laminates systems outweighs any strengthening that may occur due to in-plane grain refinement. Hardnesses decrease steadily over time for 65nm laminates at both 400 °C and 500 °C.

Chapter 6

Conclusions and Outstanding Questions

6.1 Summary and Conclusions

The unique, length scale dependent microstructures of ARB Cu-Nb multilayers experience a complex combination of deformation and structural evolution mechanisms. The objective of this research was to determine the high temperature deformation behavior and concurrent microstructural evolution of ARB Cu-Nb multilayers with various laminate length scales.

Creep behavior was determined for laminates with nominal length scales ranging from 8 μm to 65 nm at 400 °C in a high stress range ($140-350\ MPa$). All tests were performed using a specialized creep set-up which provided an inert environment and optical strain tracking. Microscopy (the same techniques as described above) was used to analyze deformation, failure, and evolution of structure in creep.

Composite behavior was quantified using *Matlab* and *Stan* to predict stress and

length scale dependence of the system overall. Finally, a model was developed, using *Mathematica*, to describe the mechanism of deformation based on stage II creep in Cu and plasticity with strain hardening in Nb.

Evolution of grain and layer structures was investigated via heat treatment of laminates: with nominal layer thicknesses varying from 8 μm to 30 nm, at 400 °C and 500 °C, and for times of 30 minutes to 30 days. Grain structures were analyzed via electron backscatter diffraction techniques and scanning transmission electron microscopy. Layer structures were analyzed using the atomic contrast techniques backscatter of secondary electrons and high angle annular dark field.

The main findings from these investigations are summarized below, with outstanding questions and recommendations for future work outlined in Section 6.2.

6.1.1 Creep

Composite behavior

A traditional Muhkerjee-Bird-Dorn creep analysis of the ARB Cu-Nb system can be used to predict composite strain rates at 400 °C at high stresses for multilayers with layer thicknesses which range two orders of magnitude. Quantification of the experimental composite minimum creep rates yields stress and length scale exponents of $n = 7.2$ and $p = -1.8$. These parameters do not describe the creep behavior of either individual phase, rather a combination of the Cu creep mechanism and the Nb plastic deformation behavior.

1. Cu-Nb multilayers exhibit typical three stage creep behavior at all stresses and length scales investigated, despite the difference in homologous temperatures at 400 °C (0.50 T_m^{Cu} and 0.25 T_m^{Nb}).

2. Creep behavior improves with *decreasing* length scale, with the most creep resistant material possessing layers that are nominally 65 nm thick. Ultimately, this is associated with increased strain-hardening in Nb with decreasing layer thickness.

Deformation mechanisms

A comprehensive analytical model, defining the stresses within each phase at a given time, was based on reasonable assumptions gleaned from the analysis of composite behavior. Comparing this model to experimental data allowed for the definition of a Cu creep mechanism and justified the composite creep response with respect to Nb strain-hardening. Considering the tensile behavior of Cu-Nb at 400 °C and assuming Cu stage II creep ($\dot{\epsilon} = A''_{cr}\sigma^{n}_{Cu}$) provides excellent prediction of transient and steady-state ARB Cu-Nb composite creep behavior.

1. The entire composite transient response is a result of load shedding from Cu to Nb. The Nb plateau stress, and the associated strain, defines the transition from transient to steady-state creep.

2. Steady-state creep deformation is controlled by dislocation climb and glide within the Cu phase, where the stress within Cu is determined by Nb plateau stress. This is possible because low energy bi-metallic interfaces act as continuous dislocation sources to maintain extremely high dislocation densities.

3. The Cu creep mechanism is dominated by vacancy diffusion enabling dislocation climb and is consistent between all length scales of Cu-Nb laminate. Other diffusional mechanisms are likely active and contributing to structural evolution.

Failure and experimental limitations

Advancements in ARB processing procedures could greatly increase Cu-Nb laminate life times. Failure strains at 400 °C are highest in 500 nm laminates for both creep and quasi-static loading, with maximum failure strain at 22 %. The defects which ultimately cause failure exist in the as rolled material, therefore asserting bulk composite behavior from experiments can be controversial.

1. There is a narrow stress range in which steady-state creep behavior is achievable for Cu-Nb laminates due to the potential for infinite load shed at low applied stresses. Experimental minimum creep rates are further limited by total composite strain and structure evolution within the layers.

2. Tertiary creep and failure ultimately occurs due to void formation and coalescence along processing flaws. Shear bands and poorly bonded Cu-Cu interfaces account for a majority of post-failure void locations. These defects can grow at small strains, due to diffusion (given time at temperature), and composites may never experience steady-state behavior.

6.1.2 Structural evolution

Composite behavior scales predictably with nominal length scale (i.e. Hall-Petch relation, analytical creep model); however, behavior cannot be fully described by a single length scale dependent mechanism. Large layer thickness distributions within laminates cause all laminates to experience a combination of deformation and structural evolution mechanisms. Layers of larger thickness are polycrystalline, while smaller layers are effectively single crystalline. The variables of annealing, for assessment of structure evolution, were length scale, temperature, and hold time.

The main conclusions from all heat treatments include:

Layer structure

Discontinuity of the layers in Cu-Nb laminates occurs at all length scales. Despite the "nominal" layer thickness of a laminate, there is a distribution of layer thicknesses in every multilayer composite. Above 500 nm this distribution is Gaussian, and below it is log-normal [3, 24]. Layer morphologies are tortuous; this significantly influences structural evolution at temperature, and the mobility of dislocations along interfaces.

1. Predictions of grooving and pinch-off, which assume uniformity in layer thickness, cannot accurately describe degradation of ARB Cu-Nb. Fine layers pinch off frequently in small laminates and at major shear localizations in large laminates.

2. Despite the development of layer discontinuities, the 65nm layer thickness laminates remain nanostructured after 30 days at 400 °C and 500 °C.

3. Interface void formation and growth into Cu layers is observed. This phenomenon is likely associated with thermal mismatch, local stress concentrations, high dislocation content at interfaces, and dislocation climb in Cu.

Grain Structure

Initial microstructures contain microscale layers with polycrystalline grain structure, and nanoscale layers with nearly single crystalline grains through thickness [17]. Grain aspect ratios (ND:RD) in polycrystalline regions are significantly different than those in single crystalline regions, $(1 : 3 - 5)$ and $(1 : 20 - 80)$, re-

spectively [3,101]. For this reason, structure evolution was assessed with respect to initial grain structure, rather than solely on nominal layer thickness.

1. Cu experienced significant recrystallization and grain growth when compared to Nb. Evolution of Cu grains was achieved through diffusion (high mobilities at $0.50 - 0.57\ T_m$) and driven by high dislocation content.

2. Grains within polycrystalline layers coarsen during annealing. The majority of Cu grains span the entire layer thickness after annealing at 400 °C after 2 days even in 8 μm laminates.

3. Single crystalline layers, of grains with initially very high aspect ratios, form dislocation substructures during annealing. Nucleation sites are limited, and driving forces for nucleation of new grains are too high due to nanoscale confinement.

Impact on Mechanical Properties

Structure evolution changes the deformation of ARB Cu-Nb in a few different ways. Recrystallization and recovery of dislocations alter strengthening mechanisms. Similarly, grain growth can change the effective length scales associated with such mechanisms. Finally, discontinuity of the layer structure influences the composite response due to a change in structure confinement and redistribution of the reinforcing (Nb) phase.

1. Heat treatments which allow recovery without recrystallization cause significant decreases in strength for larger length scale composites due to decreased forest dislocation content. Small length scale laminates primarily store dislocations at interfaces, therefore hardening behavior is unchanged.

2. There is a clear decrease in hardness after heat treatment which corresponds to an increases in Cu grain size for larger laminates and layer discontinuity in smaller laminates.

3. Structural degradation of the layers within small length scale laminates systems outweighs any strengthening that may occur due to in-plane "grain refinement" from substructure formation. Hardnesses decrease steadily over time for 65nm laminates at both 400 °C and 500 °C.

6.2 Outstanding Questions

6.2.1 Structure Evolution

Full characterization of structure evolution in ARB Cu-Nb is difficult due to the combinations of mechanisms occurring simultaneously within a single laminate. Statistical significance of any given mechanism is difficult to assert definitively. Some aspects of structure evolution, however, could be explored with respect to specific mechanisms

Pinch-off is not as predictable as theory suggests due to the variation layer thicknesses. Additionally, variation in boundary energies (associated with the less frequent texture components and high energy interfaces) and curvatures which drive for layer degradation are highly variable throughout ARB multilayer structures. Large aspect ratio grains not experience pinch off due to boundary grooving, however they are more susceptible to Rayleigh instabilities. Understanding the influence of texture and grain shape on pinch off mechanism could help design more thermally stable multilayers.

The phenomenon of bi-metal interface void formation is a very recent discovery

in metallic multilayer systems. These occur after very long annealing times, and at shorter times under creep stress - yet the mechanism of formation is not very clear. Thermal stresses ($> 200\ MPa$) may be enough to cause dislocation motion at interfaces and thus void formation. However, dislocation dynamics modeling is needed to fully understand the conditions necessary for this to occur, as it is likely a combination of diffusion, dislocation activity and complex local stress which is not captured in simple models. Additionally, better understanding of the interface void phenomena could be found through 3D characterization of the void structures by tomography.

6.2.2 Creep

Dislocation climb in Cu, assisted by a high generation of dislocations from bi-metal interfaces is the deformation rate limiting mechanism for Cu-Nb creep at the temperatures discussed in this document. Future work includes dislocation dynamic modeling to understand the influence of stress-driven interfacial diffusion and resulting boundary motion on deformation in this composite system. Using a discrete dislocation dynamics model that explicitly considers interfacial diffusion, in collaboration with Shishvan and Desphande, this work is in progress. [129, 130]

As mentioned, thermal stresses are significant in the Cu-Nb system. The creep model discussed in Chapter 5 neglects these stresses on because the strains associated are far smaller than those in transient creep. The thermal stresses, however, may influence compression creep in the Cu phase, as well is initial stresses in Nb. Further exploration of the influence of thermal stress on the initial stages of Cu-Nb creep could be helpful in further detailing a model for the system behavior. As thermal stress increases with temperature, these may also be more significant when

creeping Cu-Nb at higher temperatures.

6.2.3 Pre-existing Conditions

There are a number of defects present in the initial structure which are critically important to the deformation and failure of ARB Cu-Nb composites, particularly at high temperatures. All analysis of structures in this system were performed as-rolled or post deformation, therefore the evolution of initial defects is a black box. Structures of concern include: immeasurably high dislocation densities, shear localization (bands), poorly bonded regions of a laminate, and variation in microstructures at a given "nominal" layer thickness.

6.2.4 Dislocations

Experimentally, it is nearly impossible to quantify the dislocation density of ARB Cu-Nb multilayers, particularly the very small layer thickness laminates. The high dislocation densities observed in this ARB multilayers are largely qualitative because it is not possible to discern 10^{14} m^3 from 10^{16} m^3 with the characterization techniques described in this thesis.

Thermal stresses cause concern about the dislocations observed post anneal and creep. Assuming that initial thermal stresses relax over time (with long annealing and creep times), cooling of Cu-Nb specimen can induce large thermal stresses. The concern is that thermal stresses may be high enough to generate and move around dislocations within the layers because of the nature of bi-metal interfaces. An in-situ heating study could provide new insights on these CTE mismatch-driven plasticity processes, as one could observe dislocations during expansion.

Experimental Procedures: Appendix

2.A FIB Daily Procedure

Set-up

1. Load Sample

• Lamella direction perpendicular to Ion beam path

2. Turn on Beams

• Wake-up Ion Source

• E-Beam : 5kV, 0.17nA

• I-Beam: 30kV, 28pA

3. Focus e-Beam/Set WD

• UCSB: WD 4mm .

o Focus and find location – Link Z

o Set to 4.5mm

o Tilt to 5 degrees and accommodate for image movement with Z

o Tilt back to 0 and focus – Link Z

o Tilt to 52 degrees and adjust Z

o Back to 0 and focus – Link Z

4. Shift I-Beam

• Image Shift: X (clockwise = right), Y (clockwise = up)

• Low mag (same for E and I beams) to find location in ion image

• Mag to 10,000x – Ion Image snapshot

Trenching

5. Deposit Pt

• In Pattern: Warm Pt

• Insert Pt Needle

• Electron Beam dep: make Rectangle in e image, “e pt dep”.

o Y(1.8-2um), X(20-22um), Z(0.85um)

o 5kV, 5.5nA – auto dwell time = 1.4ms change to 1us

o should take 13 minutes

o (back to 0.17nA for viewing)

• Retract Pt Needle

• Tilt to 52 degrees

• Insert Pt Needle

• Ion Beam dep: make rectangle in I-beam image “pt dep”

o Y(1.8-2um), X(20-22um), Z(0.75um)

o 30kV, 0.28nA (Correct beam shift when changing ion current, snapshot!)

o Should take 4 min

• Retract Pt Needle

6. Trench

• In Pattern: Reg X-section (Bott to Top) – place thick end at edge of Pt

o Y(6.5-7.5um), X(20-22um), Z(2.0um) (choose Si)

o 30kV, 9.3 nA (Correct beam shift when changing ion current, snapshot!)

o I-beam Scan Rotate 180 (beam control) Again for other side of Lamella

• Fix tapered edges: Cleaning X-section

o Y(0.5um), X(20-22um), Z(2.0um) (choose Si)

o 30kV, 6.5 nA (Correct beam shift when changing ion current, snapshot!)

o I-beam Scan Rotate 180 (beam control) Again for other side of Lamella

• Goal Lamella width 800nm

o UNDERCUT 1.3 degrees from on edge - 53.3 (180) and 51.7 (0)

o 30kV, 2.8 nA (Correct beam shift when changing ion current, snapshot!)

7. U-cut

• Tilt to 7 degrees

• (180 Rotated in I-beam) : Short cut on left side, full cut on right)

o 30kV, (0.46 nA or 900pA is ok for less redep)

o Correct beam shift when changing ion current, snapshot!

o Rectangle Patterns Verticals : X(0.65um) – Horizontal: Y(0.75um)

o Both Z(2um), but really until cut is finished

• Change from Serial to Parallel Milling – watch to see cut

• Tilt to 52 – clean up w/ rectangles

• ((Tilt to 7 to check that clean-up did not fill holes – re-mill if necessary))

Lift-out

8. Insert Probe to Eucentric High

9. Insert Pt Needle

10. Lower Probe

• E-beam: Sample in focus, not probe

• I-beam: measure height between sample and needle

o Distance:Speed - 50um:5um/s - 20um:2um/s

• **CLEAN PROBE**

o 30kV, 0.28nA or 0.46nA is ok for thicker probe

o Correct beam shift when changing ion current, snapshot!

• Fully Lower Probe over fully cut side

11. Attach Probe to sample

• Rectangle Pattern – 1/3 Probe, 2/3 Sample

o Y(1.5um), X(1.5um), Z(0.3um) (Pt Dep)

o 30kV, 28pA

o Correct beam shift when changing ion current, snapshot!

• Pt Source Cool

• Wait for chamber pressure to go back to normal before cutting

• Rectangle Pattern – get rid of bridge

o 30kV, 2.8nA

o Correct beam shift when changing ion current, snapshot!

• ((Tap table to check that sample is no longer attached))

12. Retract Probe

• Manually lift probe/sample out to safe distance from bulk

• Eucentric High – Probe Retract - Pt Needle

• Park – Probe Retract – Probe

Attach to Grid

13. Insert/Find Grid

14. Focus on Grid

15. Trench Grid

• 30kV 21nA : Si Rectangle

• Angle slightly to avoid shadowing (10 degrees)

• Change current back before moving on.

16. Insert Probe Eucentric High

17. Insert Pt Needle

• Warm Source

• Insert

18. Lower sample to Grid

• E-beam: Grid in focus, not probe/sample

• I-beam: measure height between sample and needle

o Distance:Speed - 50um:5um/s - 20um:2um/s

19. Deposit Pt

o Y(3.0 um), X(1.0um), Z(0.3um) (Pt Dep)

o 30kV, 48pA

o Correct beam shift when changing ion current, snapshot!

20. Cut off Probe

• Wait for chamber pressure to return to normal

o Y(3.0 um), X(0.8um), Z(2.0um or more if needed) (Si Rectangle)

o 30kV, 0.28nA

o Correct beam shift when changing ion current, snapshot!

21. Retract Probe

• Eucentric High – Probe Retract - Pt Needle

• Park – Probe Retract - Probe

22. Deposit Pt

• Rotate 180 degrees

• Insert - Pt Needle

o Y(3.0 um), X(1.0um), Z(0.3um) (Pt Dep)

o 30kV, 48pA

o Correct beam shift when changing ion current, snapshot!

23. Retract Needle

• Cool Source

• Retract – Pt Needle

Cleaning

24. Tilt to 52 (or on edge) + 1.3 degrees

25. 30kV 93pA (Scan rotation 0 degrees)

• NOTE: if 0 scan rotation, mill from bottom e-beam image will show progress

o Correct beam shift when changing ion current, snapshot!

o Cleaning X-section

o Y(14 um), X(200nm), Z(um) (Si) for 20-40 seconds at a time

• GOAL: wedge 60nm-120nm

• Tilt to 0 Rotate 180 Tilt to 52+1.3 → Mill further!

26. Lower kV

• 16kV 47pA

• 5kV 47pA

o (to improve image, increase dwell time, if needed)

In General : SEM

- Check Astigmatism
- Zero Beam Shift for e-beam
- Save images as .tif

2.B TITAN Daily Alignment

1. Plasma clean
    - Turn on (switch in back) Plasma Cleaner
    - Take out placeholder – insert sample – Vacuum ON
    - When down to 2-3 bars, set Time (3 minutes) – plasma ON
    - Vacuum OFF – sample out – placeholder in – vacuum ON
    - Turn off (switch in back (when vacuum is good)
2. Refill LN every 3-4 hours
3. Insert sample
4. Begin Alignment
    - Super User alignment file upload: select all "Apply" (DO NOT SAVE)
5. Condenser aperture (C2)
    - 50um for STEM (100um for Regular TEM and Ronchigram)
    - Beam settings free control C3 off
    - Focus beam to a point, track ball center

- Expand clockwise, MF to fix beam open & close intensity to sure it does
- Turn TEM mode back on in free control & out of free control (2 buttons!)

6. Gun alignment
   - All 5 steps in Align gun tab
   - Quick check: if you focus the beam to a spot, you should see a bright center inside a halo

   o Gun tilt: check dose rate – 265-300 maximize! (use small screen)

   o Pivot point: use binoculars – central spot with stationary wings

   o Gun shift: center spot (size 9 @ 9000x, 3 @61000x)

   o Gun crossover focus:

   1: use R2 to fix stig with MF knobs, R2 to get out of stig

   2: focus beam w/o changing stigs

   3: focus on crossover make central spot as sharp as possible

   o Spotsize dependent gunshift

   Give beam time to stabilize between spot size changes

   ** you can spread beam out to check alignment

   If beam is stigmated – R2 to fix

7. STEM mode
   - STEM Tab STEM mode (should be yellow)
   - Insert detector
   - Check image beam shift X & Y is ZERO in system status (use MF knobs to get back to 0 if not)
   - Keep MF knobs as diff shift XY

- Move central beam to center of annular detector
- (Spot 10 for HRSTEM) – Spot 6
- Camera length – Atomic contrast (48 or 60) – diffraction contrast (480, 600, or 980)

  o Misalignment can cause diff shift between cameral lengths, save alignment file for different conditions.

8. Sample to Object plane

9. Ronchigram (Condenser Stig)
   - C2 aperture – change to 100um for stig adjustment
   - Look with spot 9 then decrease to size used for imaging.
   - C2 – back to 50um aperture

10. Collecting Images
    - ** Save images immediately! TIA is finicky
    - Right click images, export data – PC Tiff w/ scale marker (full res)

11. Shutting Down
    - Remove EDX & HAADF detectors
    - Out of STEM mode
    - Low Mag
    - Reset holder
    - Close column valves

Fix for (objective) Rotation Center alignment

⇒ Move beam to vacuum after fixing diffraction shift

• Remove detector, get out of diffraction

• 500,000X

• (can fix beam shift in direct alignments)

• Check beam tilt X and Y pivot points (wings should be symmetrical)

• Fix: Use focus step knob to change wobble intensity (turn all the way down)

o Insert beam blanker – track ball to get beam on tip of beam blanker

o Go slightly out of focus & use multifunction knobs to get disc to open up concentrically on itself

• Go back to diffraction

o Insert detector, search, point on Pt.

o Use diff shift to re-center Ronchigram change condenser to 100um & adjust to re-center aperture

2.C Creep Procedure Code

2.C.1 AutoHotKey Image capture with DigiCamControl

; WinWaitActive("Procedure - pas de 45 autour de 0.mx2 - Teaching, remote operation")

Local $i = 0

Do

;Image at 0 deg

WinActivate (”digiCamControl”)

MouseClick($MOUSE_CLICK_LEFT, 29, 58)

sleep(60000)

$i=$i+1

Until $i = 600

Local $i = 0

Do

;Image at 0 deg

WinActivate (”digiCamControl”)

MouseClick($MOUSE_CLICK_LEFT, 29, 58)

sleep(90000)

$i=$i+1

Until $i = 12000

2.C.2 Image J Processing

Macro.ijm

setBatchMode(true);

for (i=1;i¡10;i=i+1)...

for (i=10;i¡100;i=i+1)...

for (i=100;i¡1000;i=i+1)...

for (i=1000;i¡2000;i=i+1)

run(”DCRaw Reader...”, ”open=G://TEST//SAMPLE_STRESS_00”+i+”.NEF

use_temporary_directory white_balance=[Camera white balance]

output_colorspace=raw read_as=16-bit

```
interpolation=[High-speed, low-quality bilinear]");
makeRectangle(1550, 1520, 530, 4000);
run("Crop");
run("Gaussian Blur...", "sigma=4");
run("Enhance Contrast", "saturated=0.35");
run("Find Edges");
run("Enhance Contrast", "saturated=0.35");
run("RGB Color");
run("16-bit");
saveAs("Tiff","G://TEST//edge//SAMPLE_STRESS_edge_00"+i+".tif");
close();
setBatchMode(false);
```

2.C.3 Matlab Strain Tracking

```
    Disk= 'C:';
Folder = 'Folder';
Subfolder = 'Subfolder';
SubSubfolder = 'Desktop';
Testfolder = 'TEST';
Edgefolder = 'Edges';
CreepInfo = zeros(3000,12);
FileEx = 'SAMPLE_Exp_edge_';
FileEl = 'SAMPLE_Ela_edge_';
FileSTRESS1 = 'SAMPLE_STRESS1_edge_'; ...
FileSTRESSN = 'SAMPLE_STRESSN_edge_';
```

%% Ex ...

%% El ...

%% STRESS 1...

%% STRESS N

for n = 1:1:1678; **% manually note number of images at each stress**

nSTRESSN=n+nexp;**% manually note number of images at each stress**

% Column 1 Time (sec)

CreepInfo(nSTRESSN,1) = VarName1(nSTRESSN);

% Column 2 Time (hours)

CreepInfo(nSTRESSN,2) = VarName3(nSTRESSN);

% Column 3 Stress

CreepInfo(nSTRESSN,3) = STRESS;

filename = strcat(FileSTRESSN,num2str(sprintf('%06d',n)),'.tif');

Image =

imread(fullfile(Disk,Folder,Subfolder,SubSubfolder,Testfolder,Edgefolder,filename));

Intensity= zeros(length(Image),2);

%(Intensity, Y distance) : (i,a) where a is a Y distance 1-6000 pixels

% Intensity is the sum of pix150 values in a row i = sum(y,:)

for a = 1:1:length(Image);

i=sum(Image(a,:));

Intensity(a,1) = i;

Intensity(a,2) = a;

end

% Find peaks of Intensity v. Y distance % Output [Peak Intensity,

Y distance, Peak Width at HM] : [p,y,w] in descending intensity

% Sort highest 4 peaks by Y distance (descending)

% Peak location measurement error half peak width (sP)

[p,y,w] = findpeaks(Intensity(:,1),Intensity(:,2), 'SortStr','descend');

Peaks = [p,y,w];

toppeaks = [Peaks(1,:);Peaks(2,:);Peaks(3,:);Peaks(4,:)];

TopPeaks = sortrows(toppeaks,-2);

sP = TopPeaks(:,3)/2;

% Find Gauge Lengths (G) and errors (sG) % G = ytop - ybot

G1 = TopPeaks(1,2)-TopPeaks(3,2);

G2 = TopPeaks(2,2)-TopPeaks(4,2);

sG1 = sP(1)+sP(3);

sG2 = sP(2)+sP(4);

% Mean Gauge Length (GM) and error (sGM)

GM = (G1+G2)/2;

sGM = $((\frac{sG1}{2})^2 + (\frac{sG2}{2})^2)^(.5)$;

% Fill in CreepInfo for gauge length (pixels)

CreepInfo(nSTRESSN,4) = nSTRESSN;

CreepInfo(nSTRESSN,5) = GM;

CreepInfo(nSTRESSN,6) = sGM;

CreepInfo(nSTRESSN,7) = TopPeaks(1,2);

CreepInfo(nSTRESSN,8) = TopPeaks(2,2);

CreepInfo(nSTRESSN,9) = TopPeaks(3,2);

```
CreepInfo(nSTRESSN,10) = TopPeaks(4,2);

    % Calculate strain and error
e = (GM - CreepInfo(1,5))/CreepInfo(1,5);
se =(((CreepInfo(1,5)*CreepInfo(1,6))^2+(GM*sGM)^2)^(.5))/(CreepInfo(1,5))^2;

    % Fill in CreepInfo for strain and error
CreepInfo(nSTRESSN,11) = e;
CreepInfo(nSTRESSN,12) = se;

    end

    %% Plot
%% STRAIN RATE (seconds)
figure;
plot(CreepInfo(:,1),CreepInfo(:,11));
title('Creep Rate','FontSize',12,'FontWeight','bold','Color','k');
ylabel('Strain','FontSize',12,'FontWeight','bold','Color','k');
xlabel('Time (sec)','FontSize',12,'FontWeight','bold','Color','k');
grid on
grid minor
```

2.C.4 Matlab Creep Spline Fitting

This code was adapted from code written by Luke Rettberg for Cu-Nb analysis of primary and steady-state creep rates

%% Define SAMPLE(s) to be analyzed. Individual loops will plot Jump tests together.

```
Stress = [STRESS];
Creepdata = ;
Creepdata = creep_SAMPLE_STRESS1, creep_SAMPLE_STRESS2,
..., creep_SAMPLE_STRESSn;
figure;
for i = 1:1:n;
k=i+10;
runtime = Creepdatai(:,1);
creepstrain = Creepdatai(:,2);
rawcreeprate = [runtime(2:end) diff(creepstrain)];

    ignoredinitialpoints = 1;
iipruntime = runtime(ignoredinitialpoints:end);
iipcreepstrain = creepstrain(ignoredinitialpoints:end);

    CreepStrain = max(Creepdatai(:,2));
RunTime = max(Creepdatai(:,1));
```

% Separate Variable SP defines different smoothing parameters for each stress level potentially

smoothingparameter1 = SP(i,1);

smoothingparameter2 = SP(i,2);

%Use a cubic smoothing spline to fit the data

%smoothingspline1 = csaps(runtime, creepstrain, smoothingparameter1, [], [zeros(1, 200) , ones(1, length(runtime)-200)]);

smoothingspline1 = csaps(iipruntime, iipcreepstrain, smoothingparameter1, [], [1 , ones(1, length(iipruntime)-1)]);

smoothingspline2 = csaps(iipruntime, iipcreepstrain, smoothingparameter2, [], [1 , ones(1, length(iipruntime)-1)]);

%First derivative (creep rate) of the cubic smoothing spline

%creepratesmoothingspline1 = fnder(smoothingspline1, 1);

creepratesmoothingspline1 = fnder(smoothingspline1, 1);

creepratesmoothingspline2 = fnder(smoothingspline2, 1);

%Assigning the generated creep rate data points, primary creep rate, and minimum creep rate

SmoothCreepData1 = fnplt(smoothingspline1);

SmoothCreepData2 = fnplt(smoothingspline2);

CreepRate1 = fnplt(creepratesmoothingspline1);

CreepRate2 = fnplt(creepratesmoothingspline2);

PrimaryCreepRate = max(CreepRate1(2,1:round(max(size(CreepRate1(2,:)))/3)));

MinimumCreepRate = min(CreepRate2(2,:));

%Determining the primary creep strain

%Generating a linear function with a slope equal to the minimum creep rate at the corresponding run time

```
    [row1,col1] = find(CreepRate2 == MinimumCreepRate);
    [row2,col2] = find(CreepRate1 == PrimaryCreepRate);
b1 = -MinimumCreepRate*SmoothCreepData2(1,col1)+SmoothCreepData2(2,col1);
b2 = -PrimaryCreepRate*SmoothCreepData1(1,col2)+SmoothCreepData1(2,col2);

    xintersect = (b2-b1)/(MinimumCreepRate-PrimaryCreepRate);
yintersect = MinimumCreepRate*xintersect + b1;

    PrimaryCreepStrain = yintersect;
```

%Plotting the data

```
spr = 2;
spc = 2;

    subplot(spr,spc,1);
plot(Creepdatai(:,1),Creepdatai(:,2),'k'), hold on
fnplt(smoothingspline1,2), hold off
title('Creep Rate Spline 1','FontSize',12,'FontWeight','bold','Color','k');
ylabel('Strain','FontSize',12,'FontWeight','bold','Color','k');
xlabel('Time (sec)','FontSize',12,'FontWeight','bold','Color','k');
legend('Raw STRESS','Primary STRESS', 'Location', 'NorthWest' )
hold on

    subplot(spr,spc,3)
```

```
fnplt(smoothingspline1,2), line([SmoothCreepData1(1,col2) xintersect],
    SmoothCreepData1(2,col2) yintersect

,'Color','k'), line([SmoothCreepData1(1,col1) xintersect],
    SmoothCreepData1(2,col1) yintersect

,'Color','k'),

title('Primary Creep Strain (Spline 1)','FontSize',12,'FontWeight','bold','Color','k');

ylabel('Strain','FontSize',12,'FontWeight','bold','Color','k');

xlabel('Time (sec)','FontSize',12,'FontWeight','bold','Color','k');

legend('Primary STRESS','Intersection', 'Location', 'NorthWest' )

hold on


    subplot(spr,spc,2);

plot(Creepdatai(:,1),Creepdatai(:,2),'k'), hold on

fnplt(smoothingspline2,2), hold off

title('Creep Rate Spline 2','FontSize',12,'FontWeight','bold','Color','k');

ylabel('Strain','FontSize',12,'FontWeight','bold','Color','k');

xlabel('Time (sec)','FontSize',12,'FontWeight','bold','Color','k');

legend('Raw STRESS','SS STRESS', 'Location', 'NorthWest' )

hold on


    subplot(spr,spc,4);

fnplt(creepratesmoothingspline1,2,'k'), hold on

fnplt(creepratesmoothingspline2,2), hold off

title('Creep Rate','FontSize',12,'FontWeight','bold','Color','k');

ylabel('Strain Rate (1/s)','FontSize',12,'FontWeight','bold','Color','k');

xlabel('Time (sec)','FontSize',12,'FontWeight','bold','Color','k');

legend('Primary STRESS','SS STRESS', 'Location', 'NorthEast' )
```

```
hold on

    SmoothedCurvesSAMPLE(i,1) = Stress(i);%Stress
SmoothedCurvesSAMPLE(i,2) = MinimumCreepRate;%SS Creep Rate
SmoothedCurvesSAMPLE(i,3) = CreepStrain;%Strain at Jump or failure
SmoothedCurvesSAMPLE(i,4) = PrimaryCreepRate;%Primary Creep Rate
SmoothedCurvesSAMPLE(i,5) = PrimaryCreepStrain;%Primary Creep Strain
SmoothedCurvesSAMPLE(i,6) = smoothingparameter1;
SmoothedCurvesSAMPLE(i,7) = smoothingparameter2;


    end
```

Cu-Nb Creep: Appendix

Sample No.	**Scale (nm)**	**Temp (°C)**	**Type**
1	8000	400	Jump
1	2000	400	Standard
2	2000	400	Standard
3	2000	400	Jump
1	2000	500	Jump
1	500	400	Standard
2	500	400	Jump
3	500	400	Jump
1	200	400	Standard
2	200	400	Jump
3	200	400	Jump
1	200	500	Jump
1	65	400	Standard
2	65	400	Standard
3	65	400	Jump
4	65	400	Jump
5	65	400	Failed
6	65	500	Failed
1	65	400	HT Jump
2	65	400	HT Jump
1	28	400	Failed

Table 3.i: Number of samples and testing conditions for all creep tests performed.

3.A As Rolled Cu-Nb creep

Sample	Scale (nm)	Temp (°C)	Type	Stress (MPa)	Strain (%)
8A	8000	400	Jump	140, 150	5.2 [a]
2D	2000	400	Standard	175	14.2
2A	2000	400	Standard	200	19.2
2B	2000	400	Jump	150, 170, 190, 200	11.9
500C	500	400	Standard	200	14.5 [b]
500B	500	400	Jump	160, 180, 200, 215	14.6
500A	500	400	Jump	175, 190, 205	17.2
200B	200	400	Standard	275	– [c]
200D	200	400	Jump	215, 230, 260	17.3
200A	200	400	Jump	245, 275, 290	7.5
65H	65	400	Standard	295	5.2
65G	65	400	Standard	335	3.7
65C	65	400	Jump	320, 350	5.0
65D	65	400	Jump	275, 290, 320, 335	– [c]
65F	65	400	Failed	335	×
65A	65	400	Failed	140+	*d*
28A	28	400	Failed	415	×

Table 3.A.i: All as rolled Creep Tests at 400 °C. a) Limited strain due to poorly bonded interfaces. This length scale was not tested again. b) Failed in less than 26 h. Tertiary was significant a portion of lifetime. c) Interrupted because of power outage. d) Power outage disabled load frame and furnace, sample saw unknown loads. [–] interrupted, [×] Immediate failure along shear band during loading.

3.A.1 Micrographs of 65 nm Cu-Nb Interrupted Creep

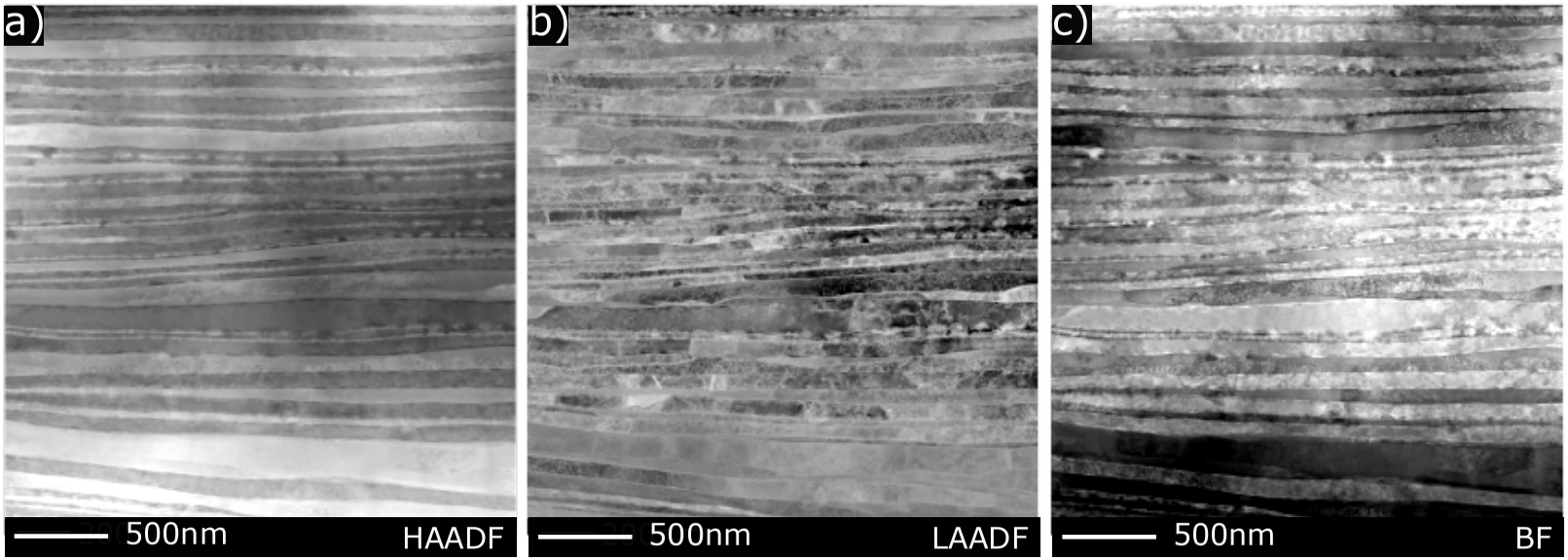


Figure 3.A.1.i: Overview of sample 65D interrupted in creep. Layers have some discontinuity and some interface voids. (*Sample was prepared by PIPS and redeposition is notable.*)

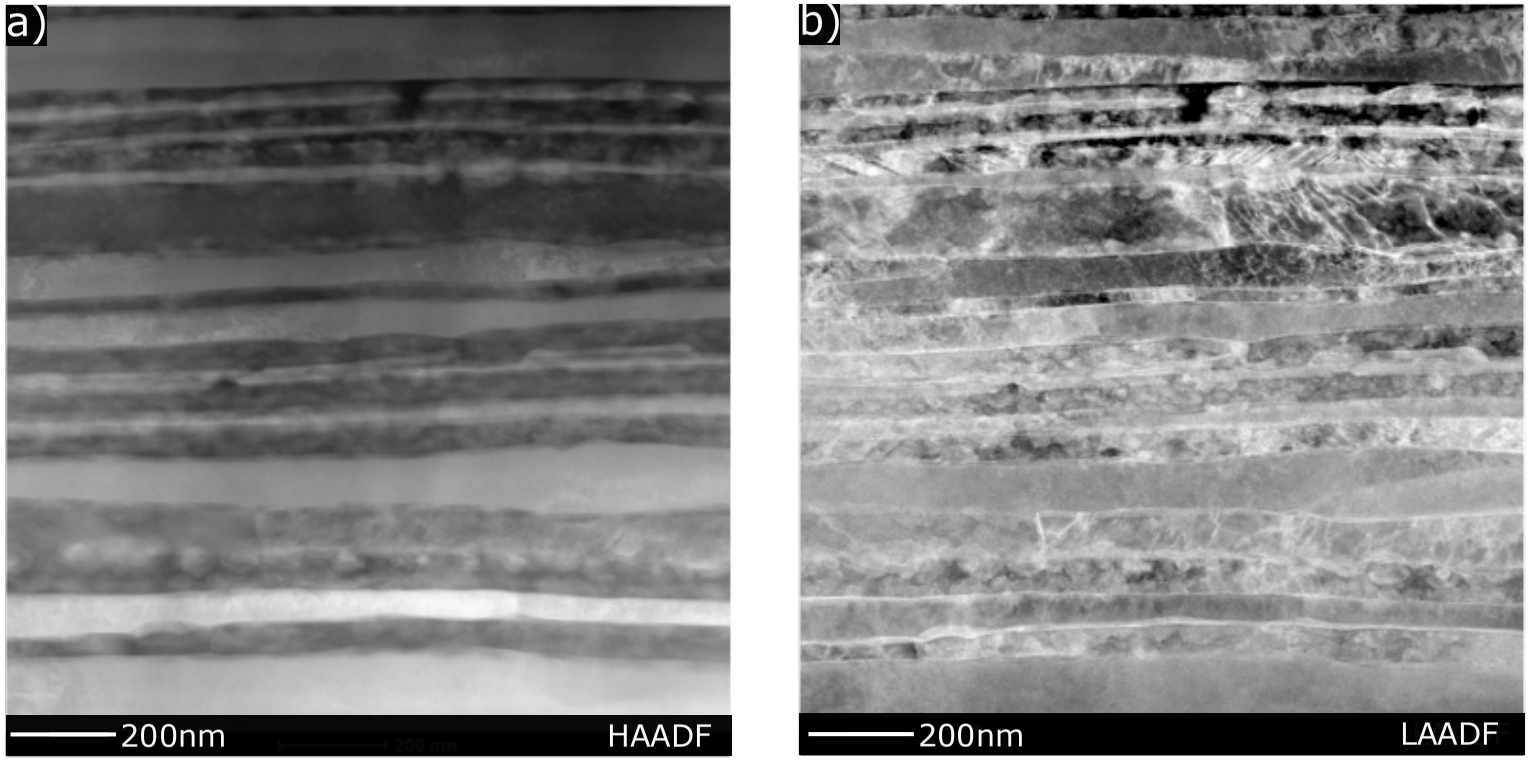


Figure 3.A.1.ii: Large area of sample 65D interrupted in creep. Layers have some discontinuity and some interface voids. (*Sample was prepared by PIPS and redeposition is notable.*)

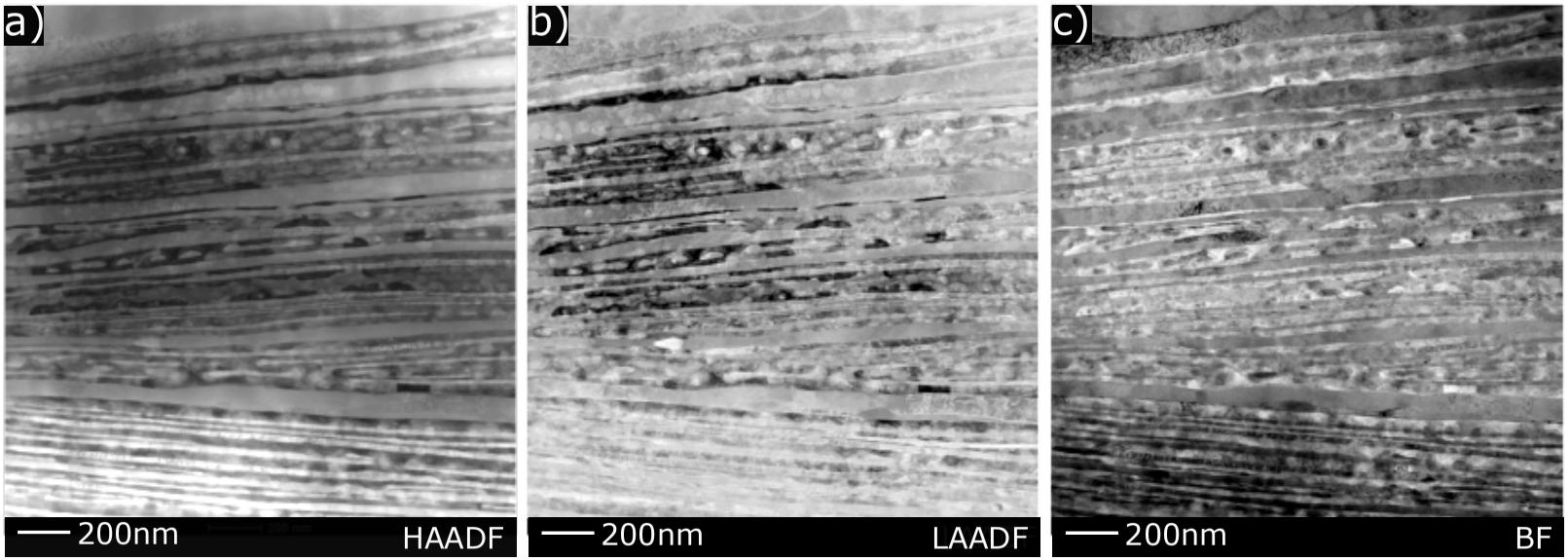


Figure 3.A.1.iii: Large area of sample 65D interrupted in creep. Layers have some discontinuity and some interface voids. (*Sample was prepared by PIPS and redeposition is notable.*)

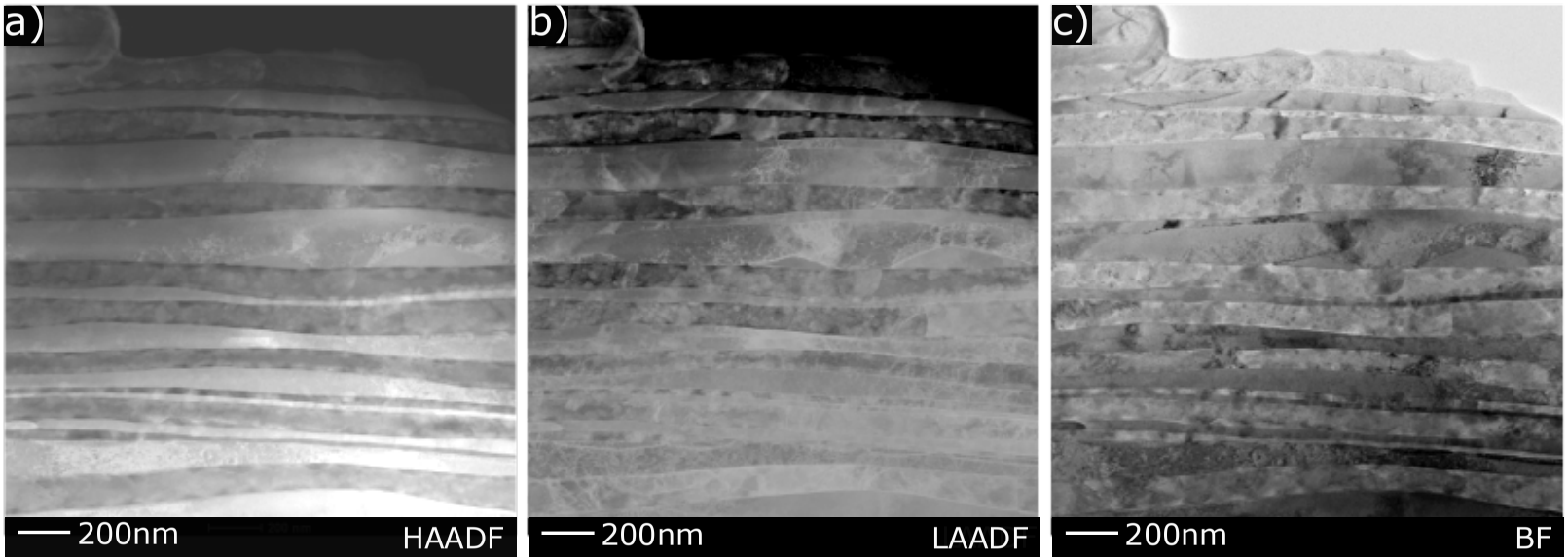


Figure 3.A.1.iv: Large area of sample 65D interrupted in creep. Layers have some discontinuity and some interface voids. (*Sample was prepared by PIPS and redeposition is notable.*)

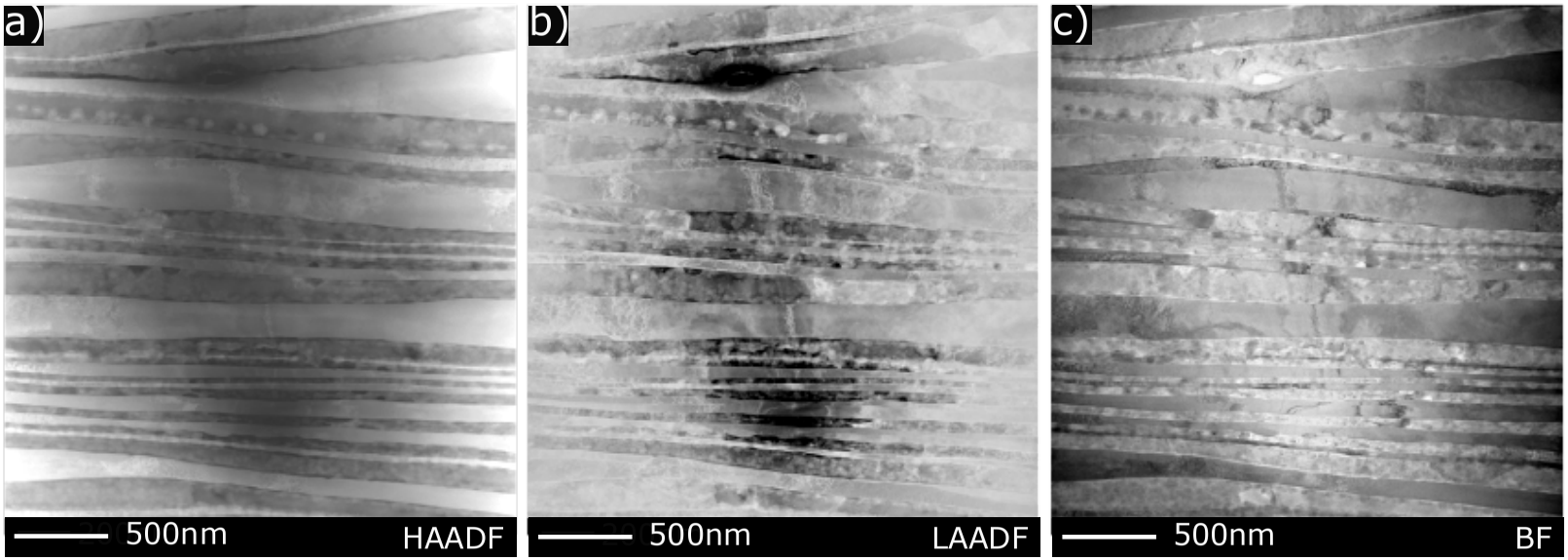


Figure 3.A.1.v: Large area of sample 65D interrupted in creep. Layers have some discontinuity and some interface voids. (*Sample was prepared by PIPS and redeposition is notable.*)

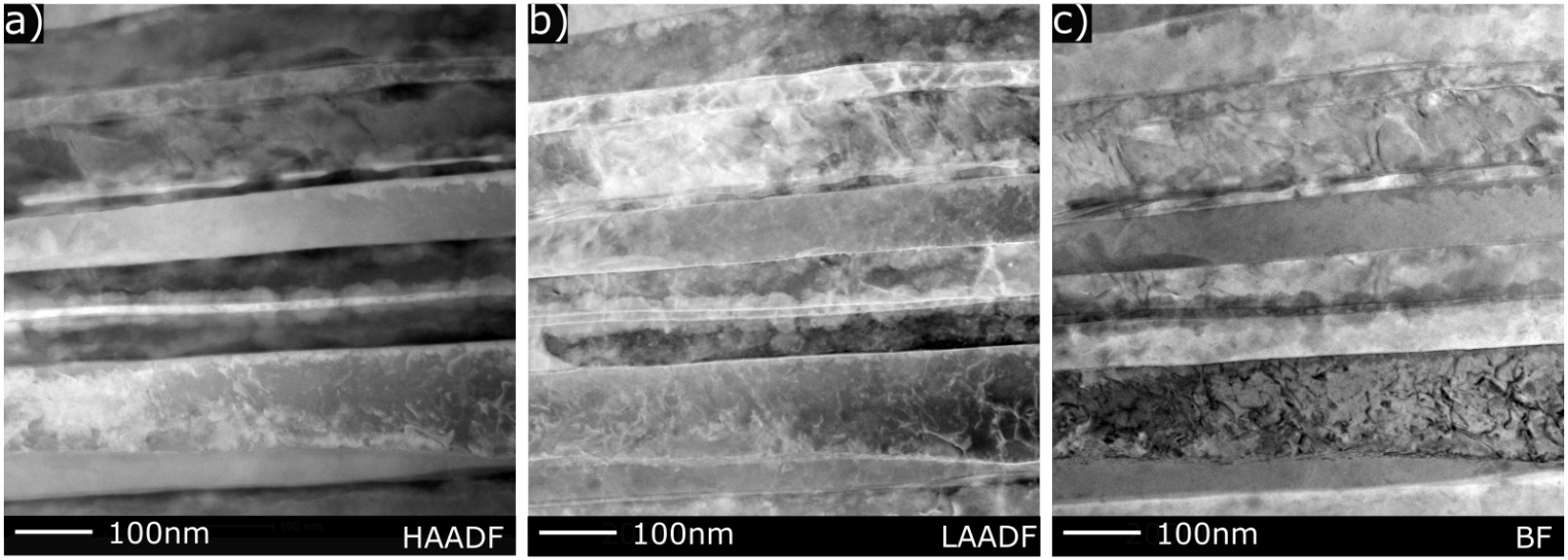


Figure 3.A.1.vi: Close-up view of sample 65D interrupted in creep. Layers have some discontinuity and some interface voids. (*Sample was prepared by PIPS and redeposition is notable.*)

3.A.2 Post-failure Micrographs of 65 nm Cu-Nb

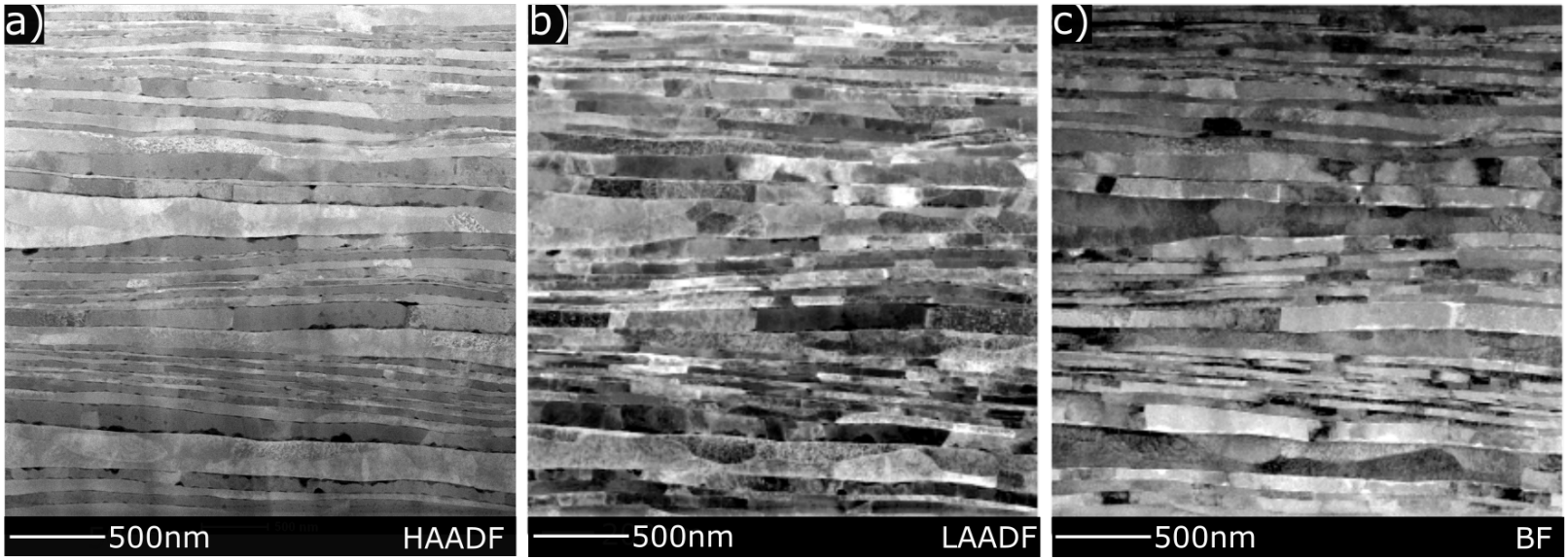


Figure 3.A.2.i: Large area of sample 65C post creep failure. Layers have some discontinuity and some interface voids. Contrasts Labeled.

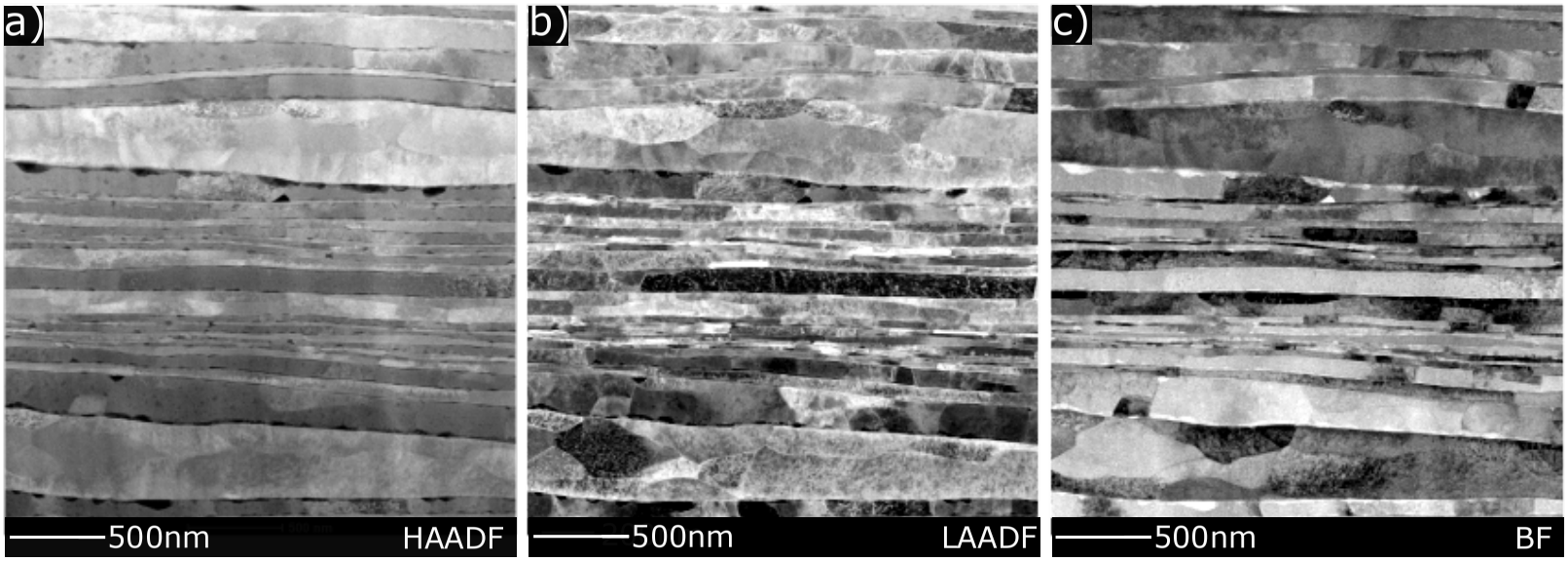


Figure 3.A.2.ii: Large area of sample 65C post creep failure. Layers have some discontinuity and some interface voids. Contrasts Labeled.

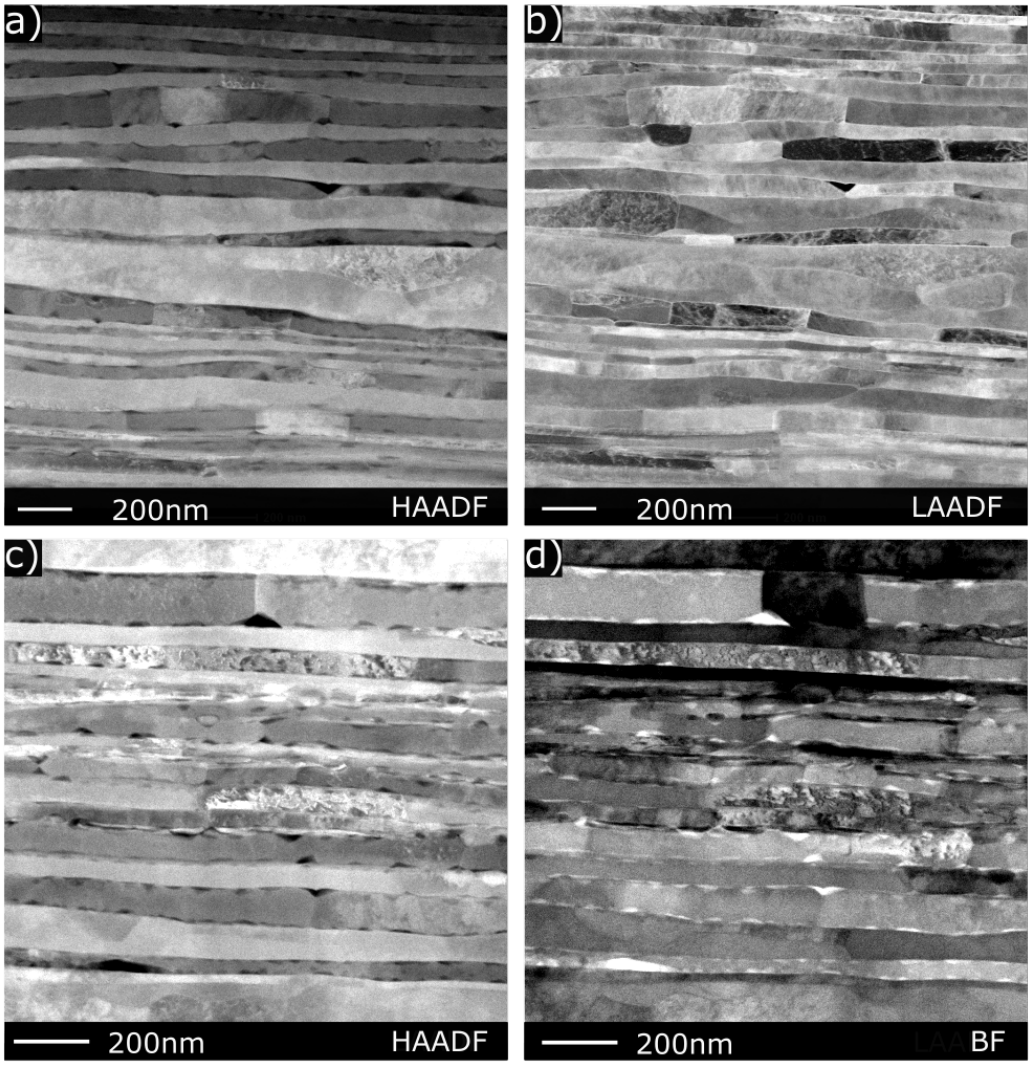


Figure 3.A.2.iii: Large areas of sample 65C post creep failure. a) and b) show one area, which largely resembles as rolled structures. c) and d) show another area with notable grooving and interface voids. Contrasts Labeled.

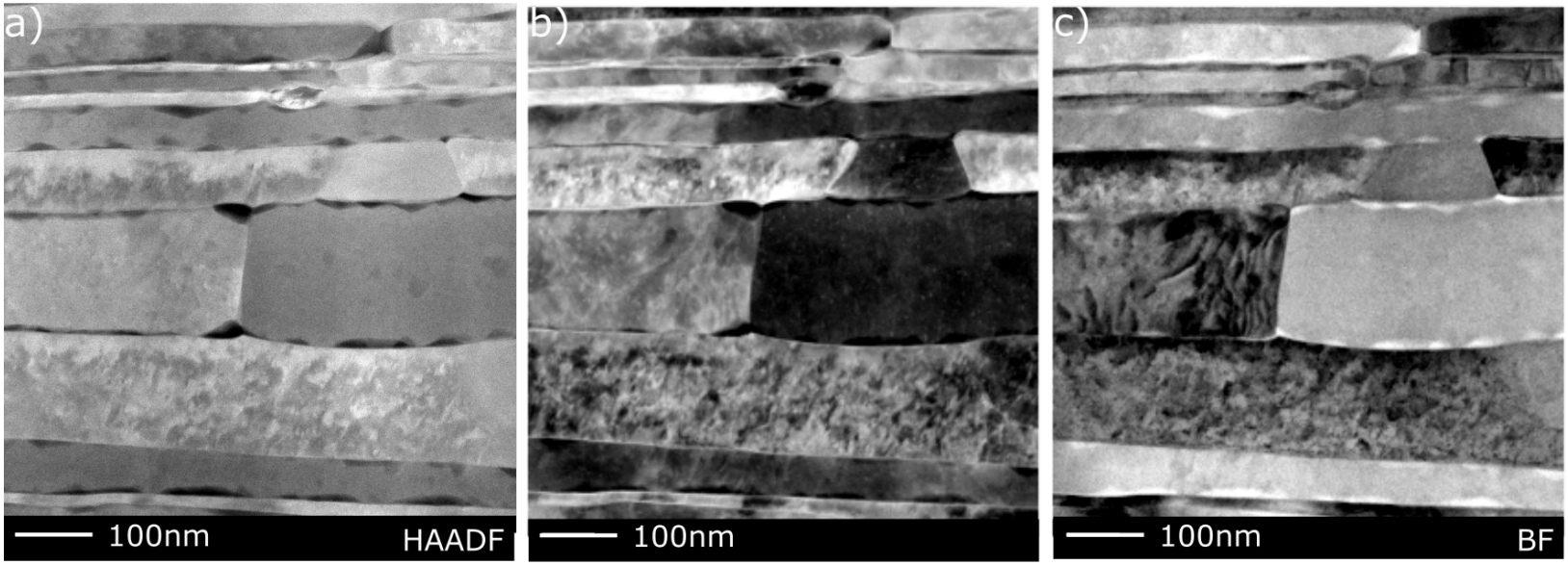


Figure 3.A.2.iv: Close-up view of sample 65C (65 nm Cu-Nb) post failure. Grooving and interface voids are notable. Contrast is labeled.

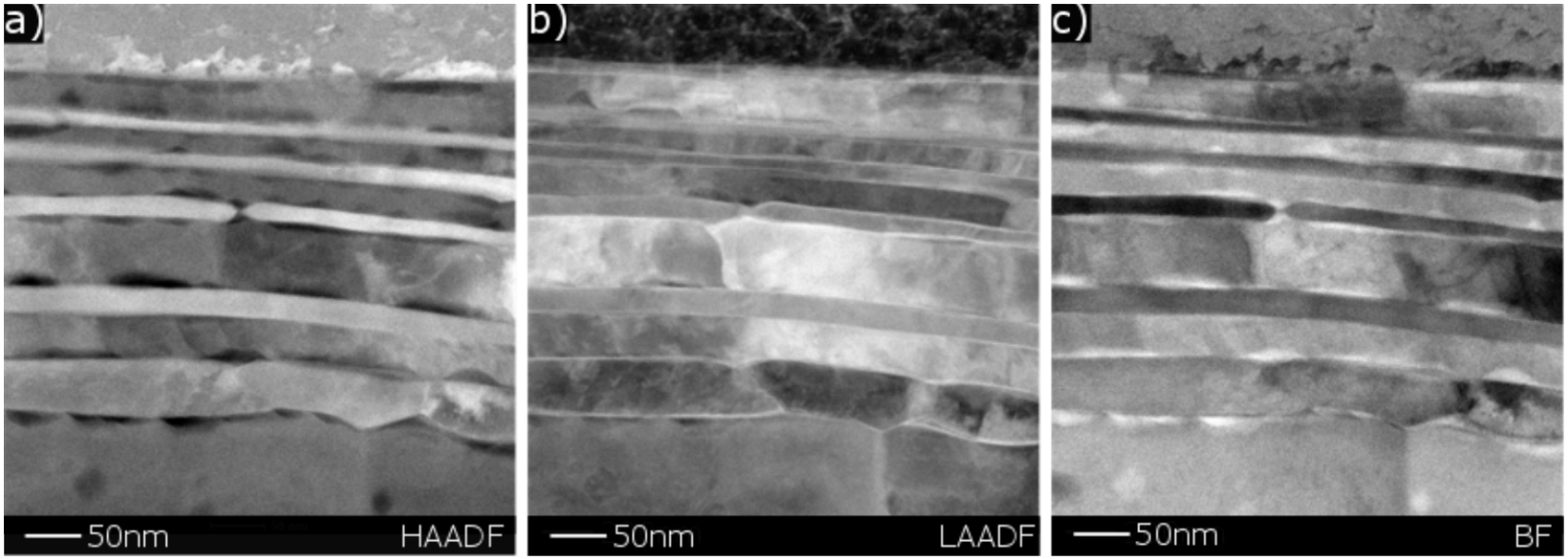


Figure 3.A.2.v: Close-up view of sample 65C (65 nm Cu-Nb) post failure. Grooving and pinch off are notable. Cu-Nb interface voids occur throughout and grow into Cu. Contrast is labeled.

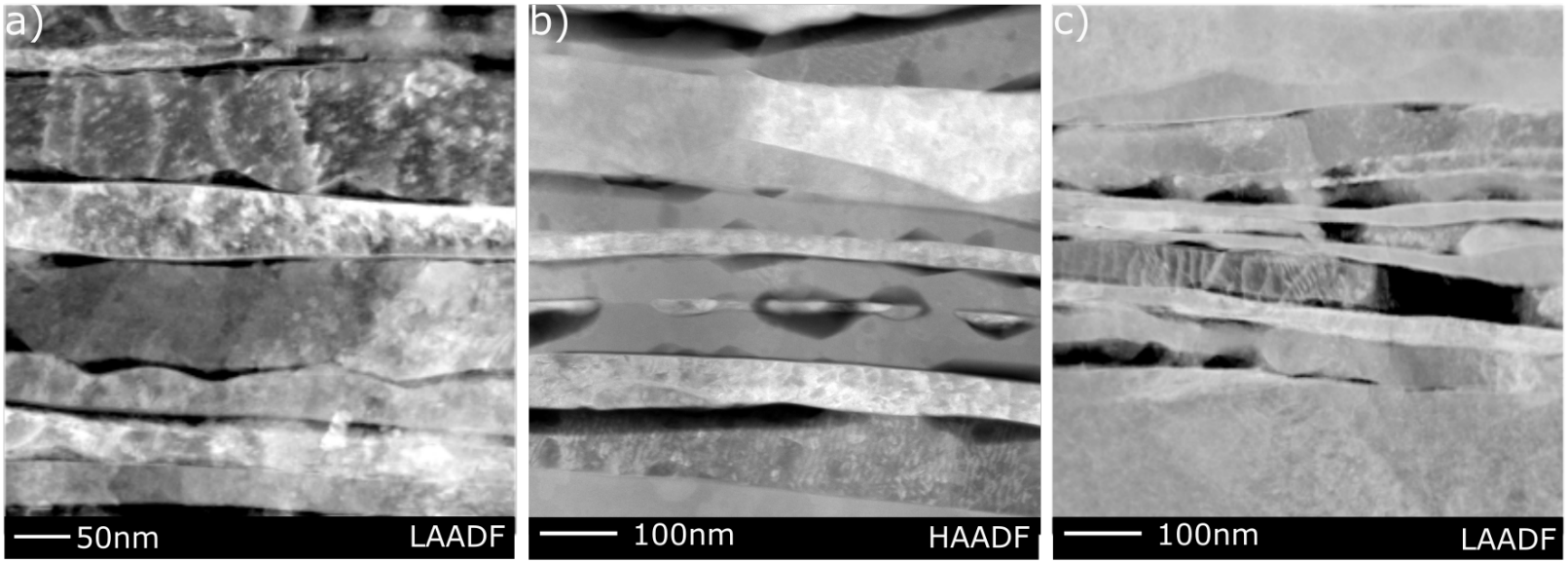


Figure 3.A.2.vi: Close-up STEM of 65C (65 nm) shows Cu-Nb interface voids.

3.A.3 Micrographs of 200 nm Cu-Nb Interrupted Creep

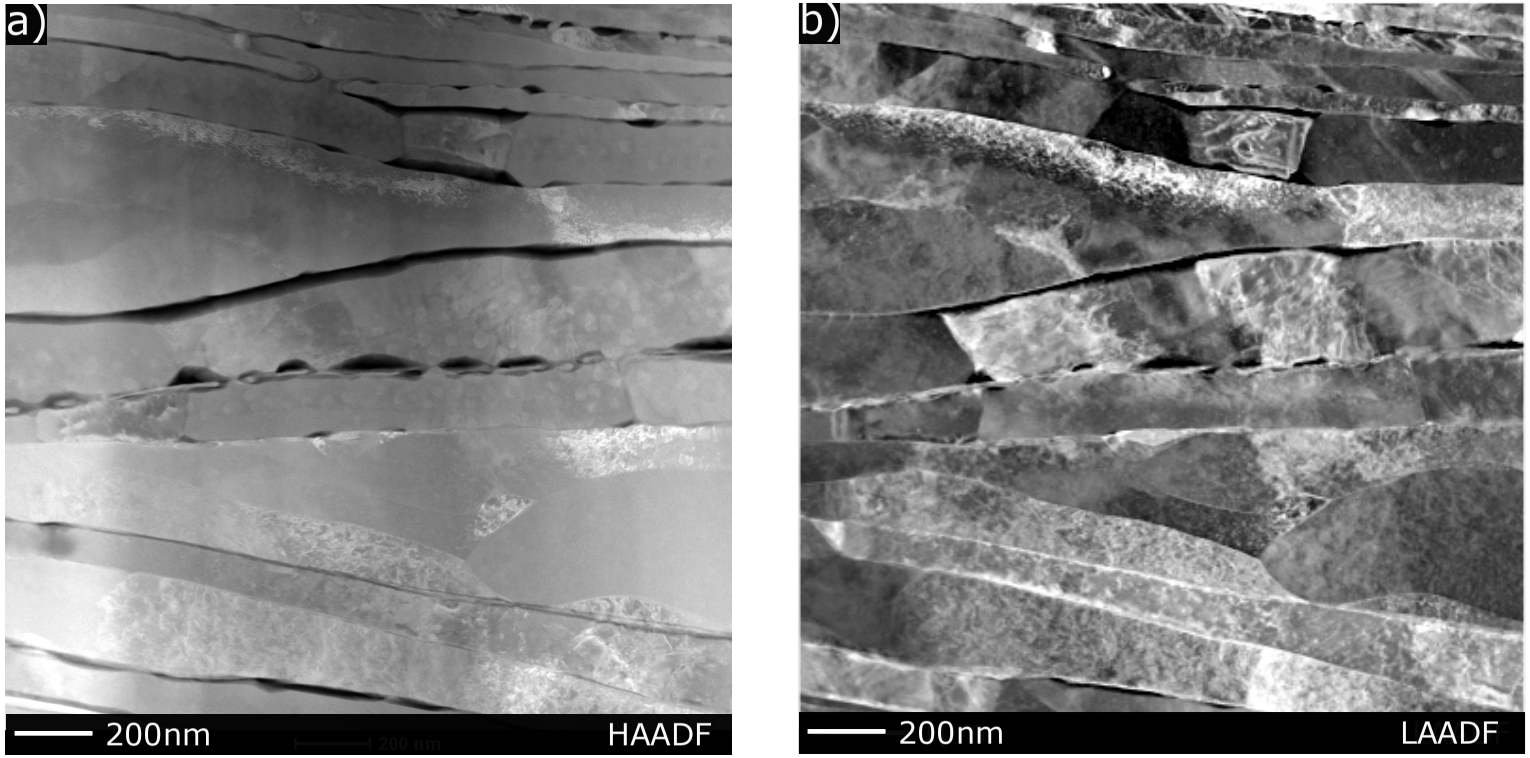


Figure 3.A.3.i: STEM of sample 200B (200 nm Cu-Nb) interrupted in creep. Cu-Nb interface voids occur throughout and grow into Cu. Contrasts labeled.

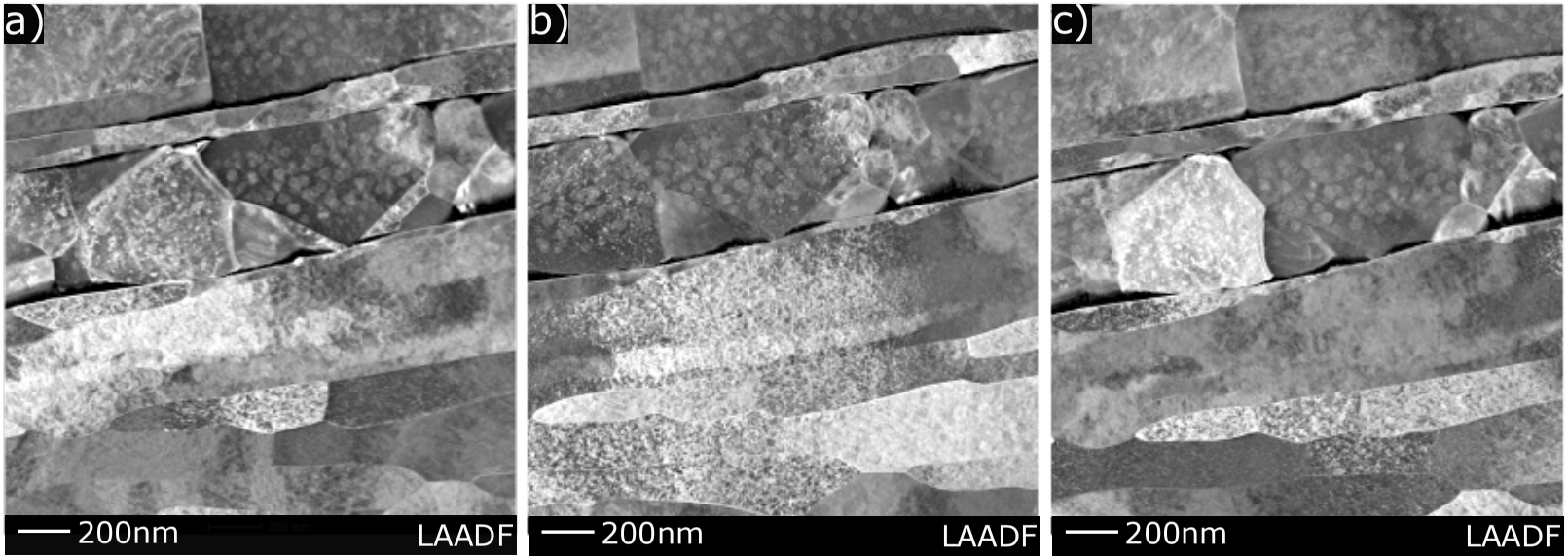


Figure 3.A.3.ii: STEM image overview of sample 200B (200 nm Cu-Nb) interrupted in creep. Series shows varying dislocation and grain contrast with varied tilt angle.

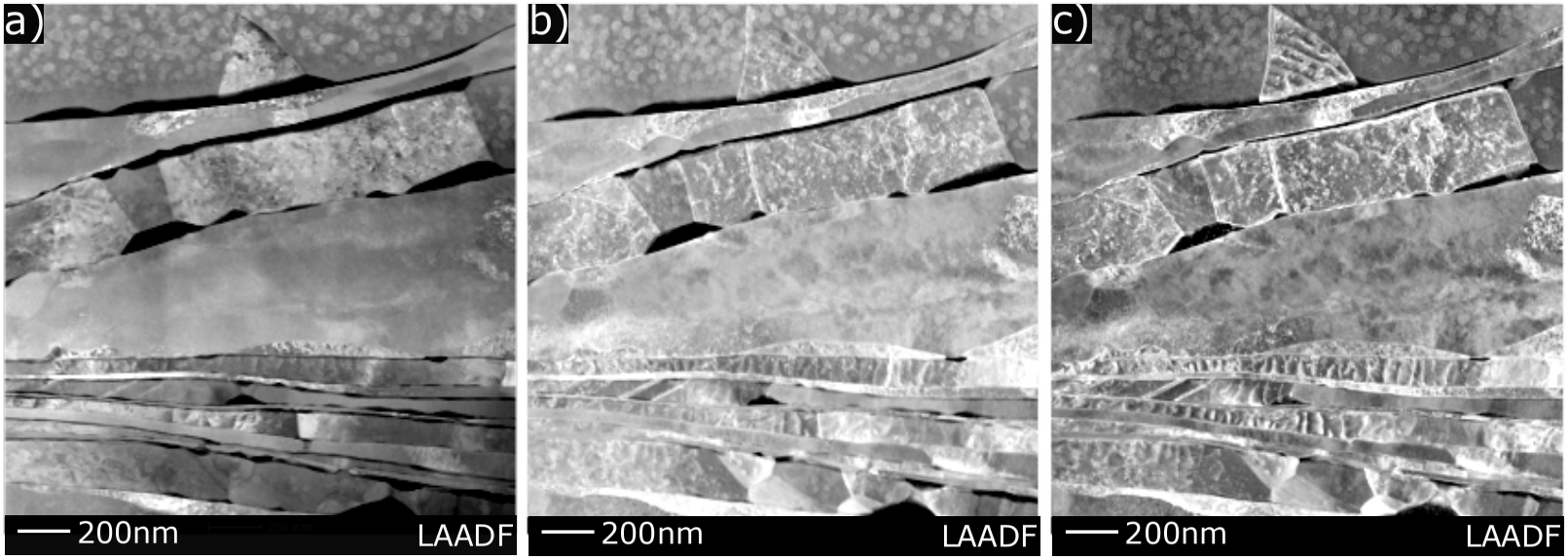


Figure 3.A.3.iii: STEM image overview of sample 200B (200 nm Cu-Nb) interrupted in creep. Series shows varying dislocation and grain contrast with varied tilt angle.

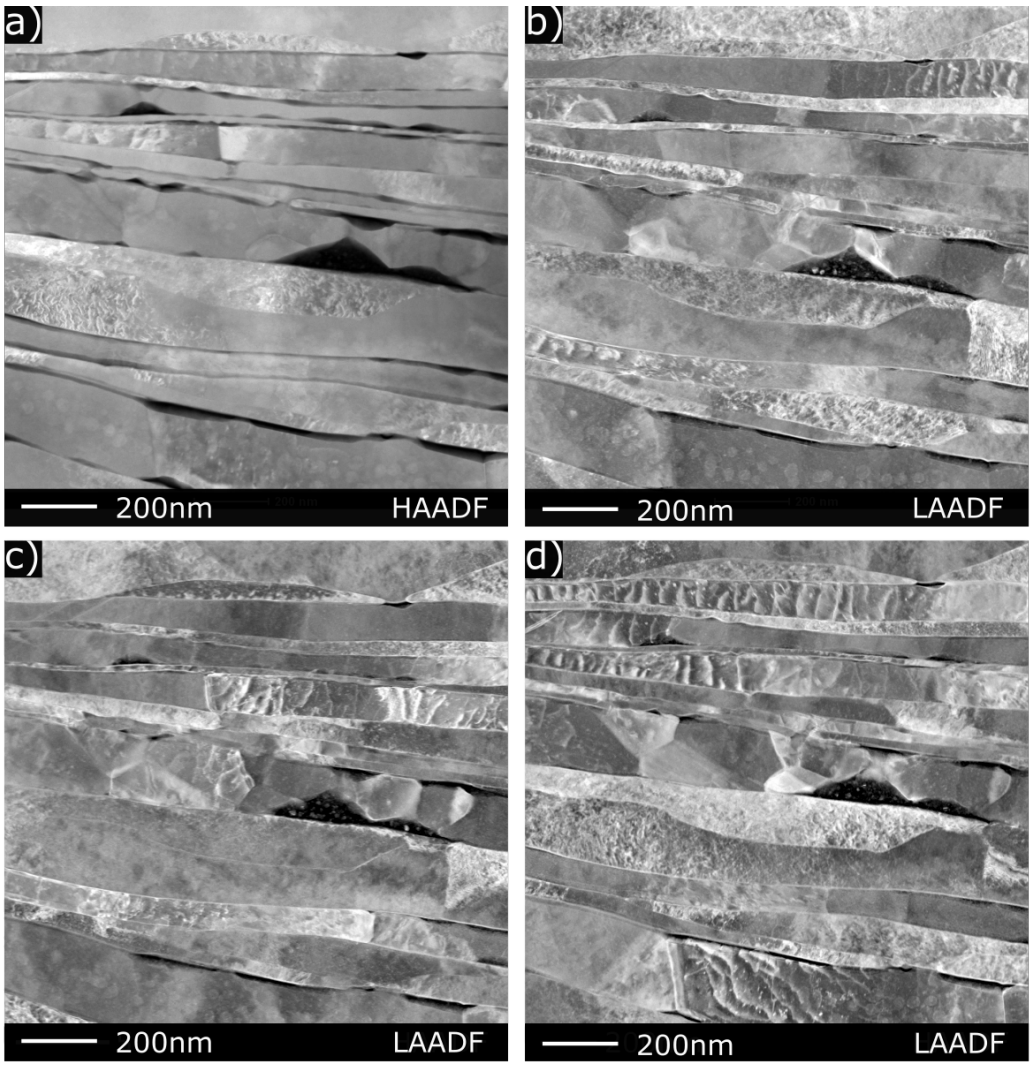


Figure 3.A.3.iv: STEM image overview of sample 200B (200 nm Cu-Nb) interrupted in creep. a) is HAADF contrast, showing Cu and Nb (lighter phase). b)-d) shows varying dislocation and grain contrast with varied tilt angle.

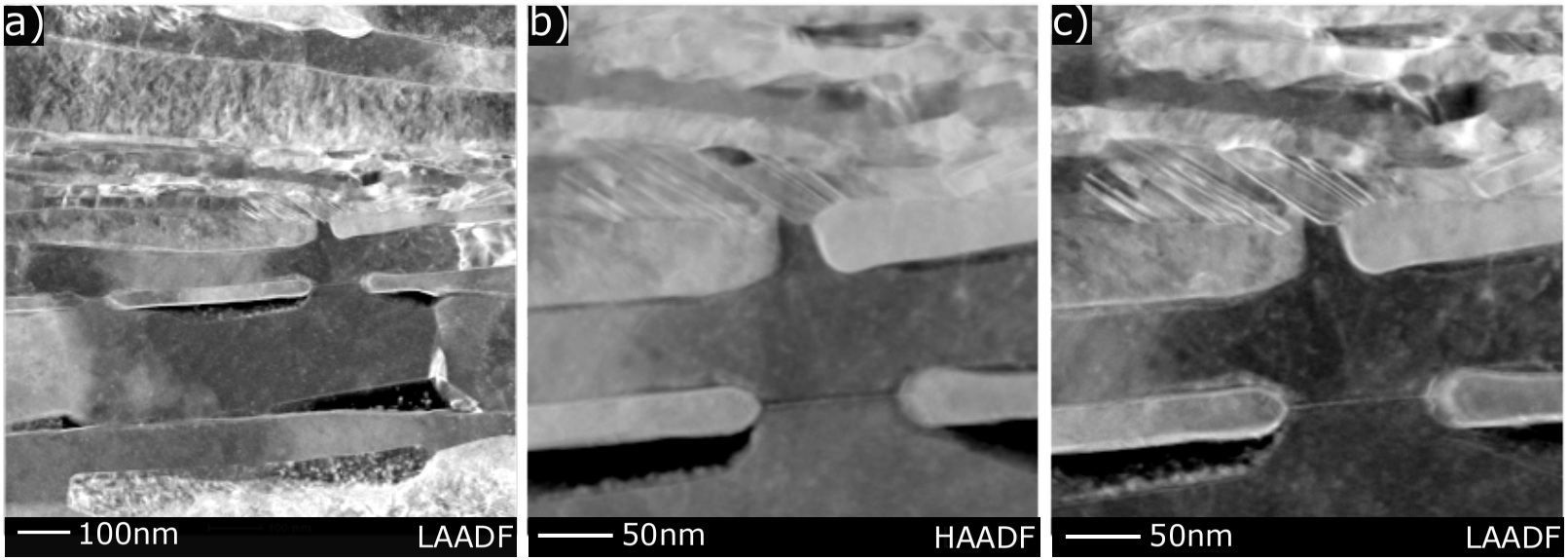


Figure 3.A.3.v: STEM of sample 200B (200 nm Cu-Nb) interrupted in creep. a) shows a larger area view of a pinch off site. b) and c) show a close up of a pinched off Nb layer in HAADF and LAADF contrast.

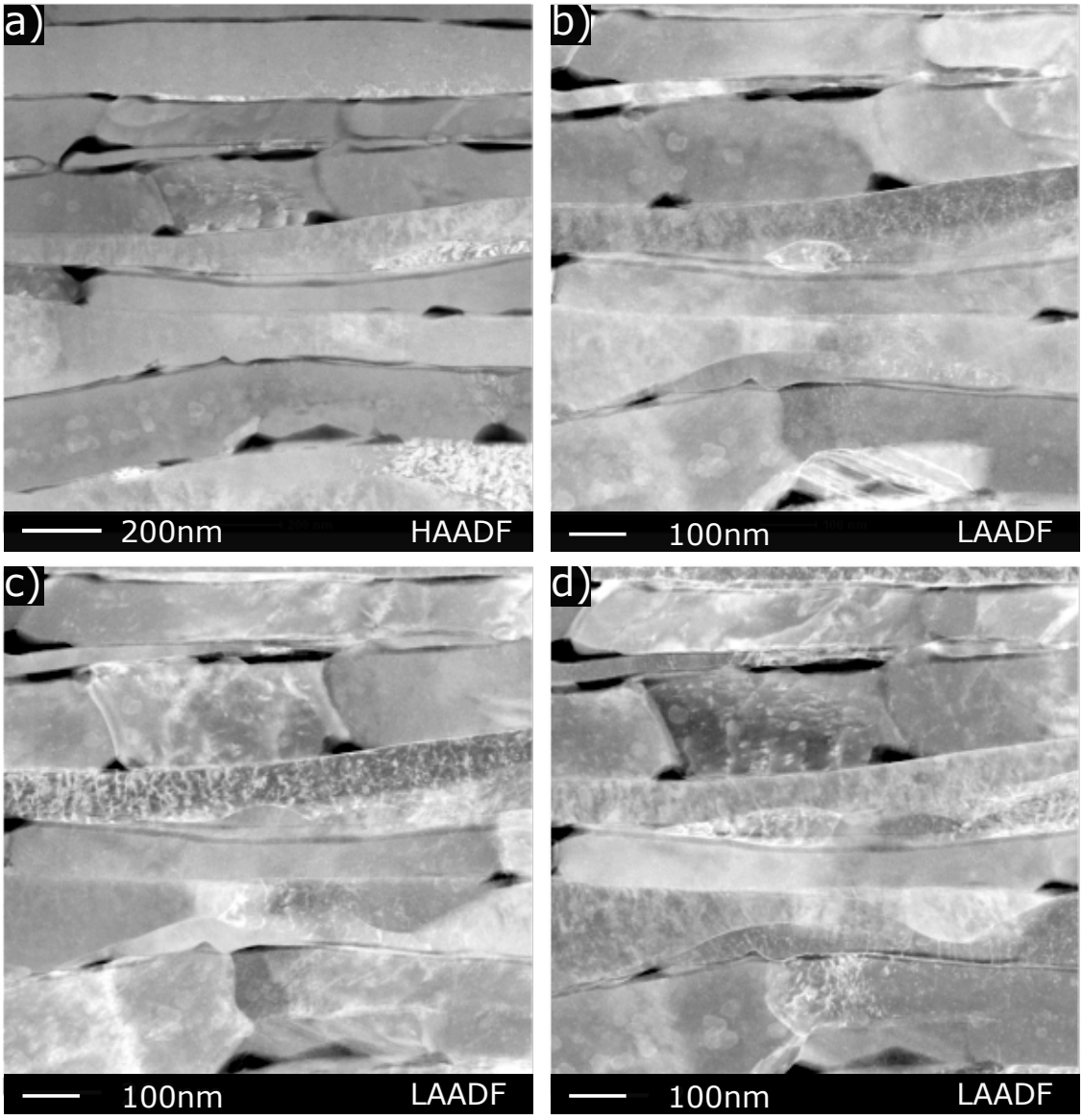


Figure 3.A.3.vi: STEM of sample 200B (200 nm Cu-Nb) interrupted in creep. Cu-Nb interface voids grow into Cu significantly. a) HAADF, b)-d) LAADF contrast at varying tilt angles.

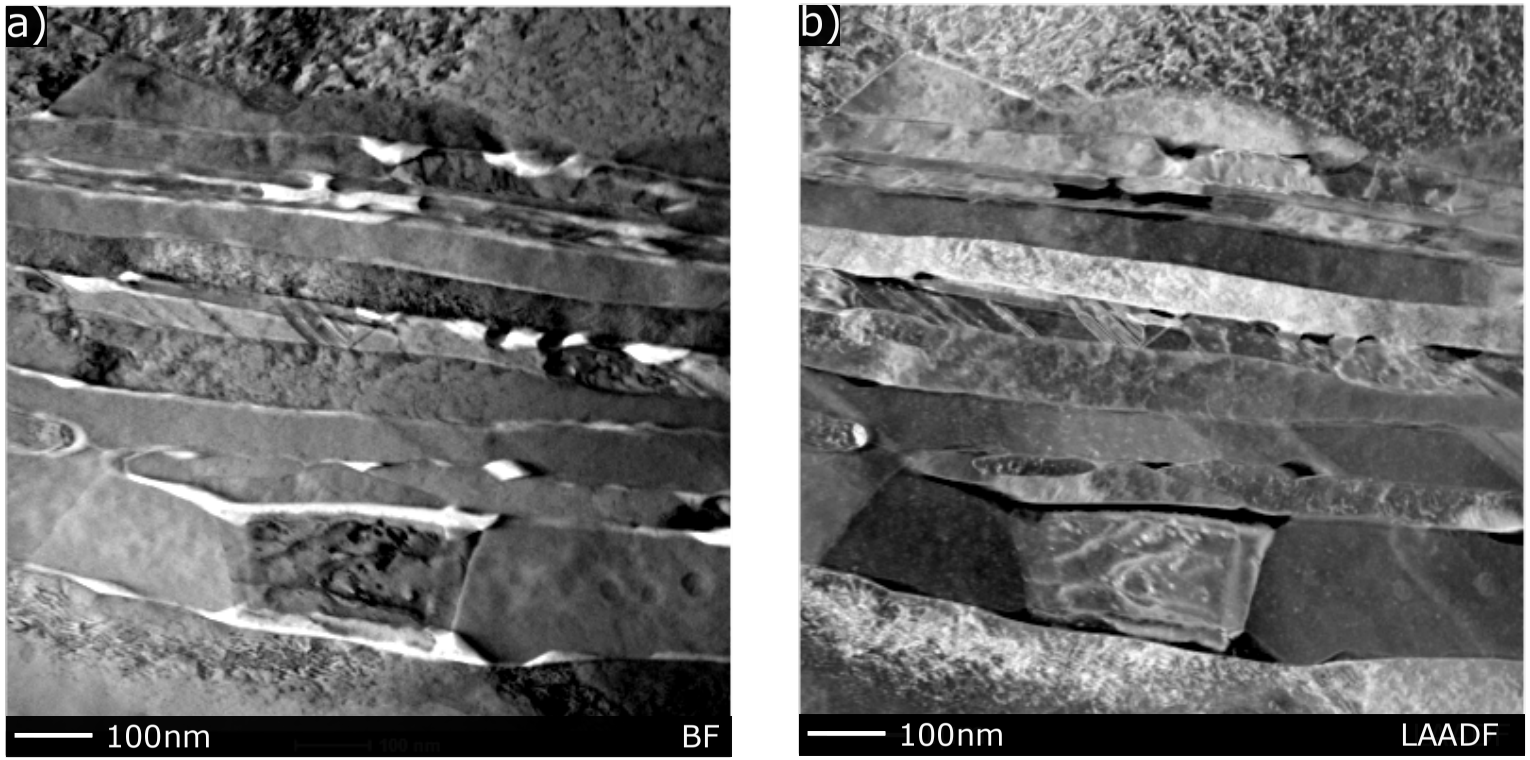


Figure 3.A.3.vii: Close-up view of sample 200B (200 nm Cu-Nb) interrupted in creep. Cu-Nb interface voids grow into Cu significantly. Contrasts labeled.

3.A.4 Post-failure Micrographs of 200 nm Cu-Nb

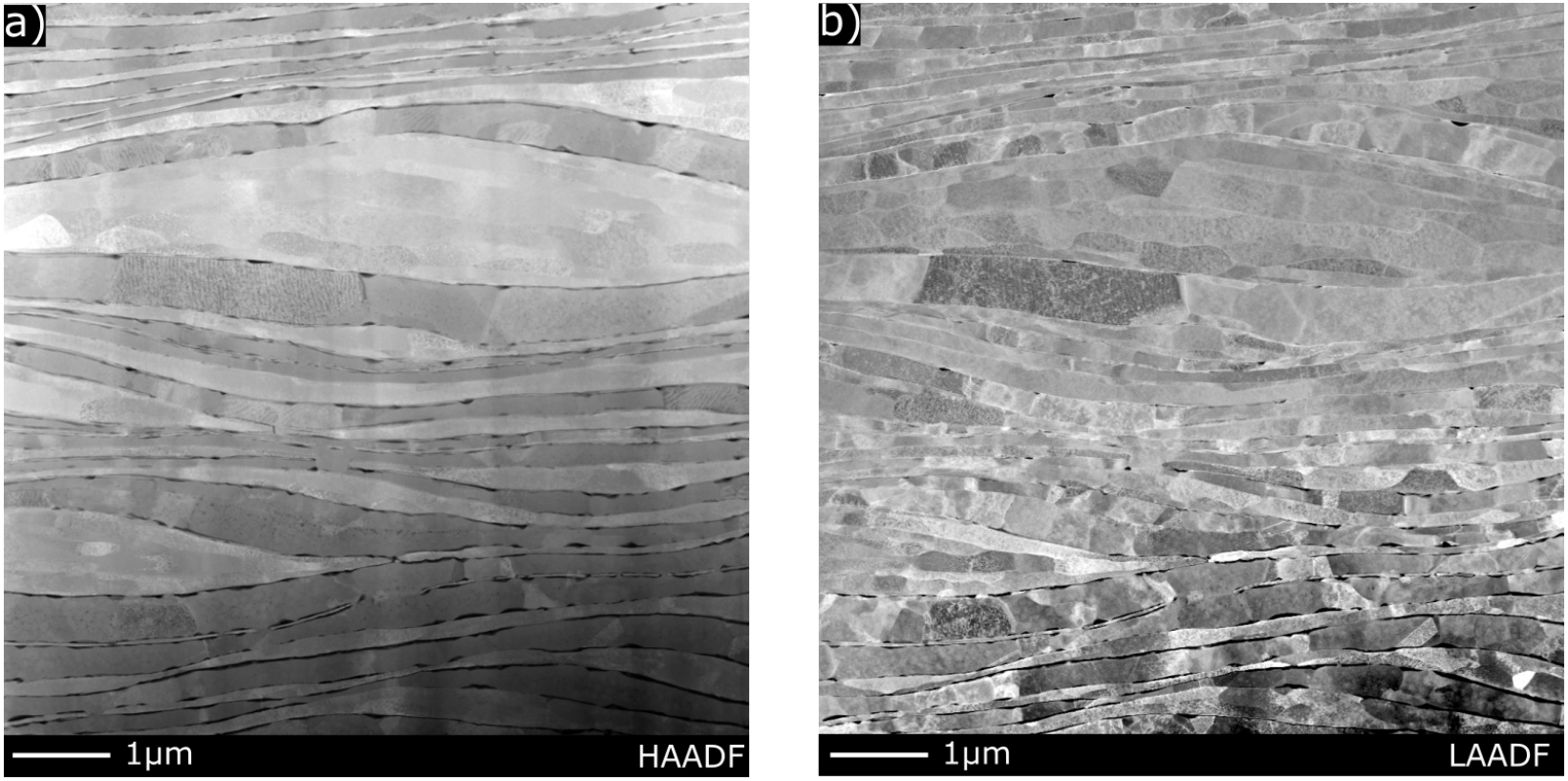


Figure 3.A.4.i: STEM image overview of sample 200A (200 nm Cu-Nb) post failure. Contrasts labeled.

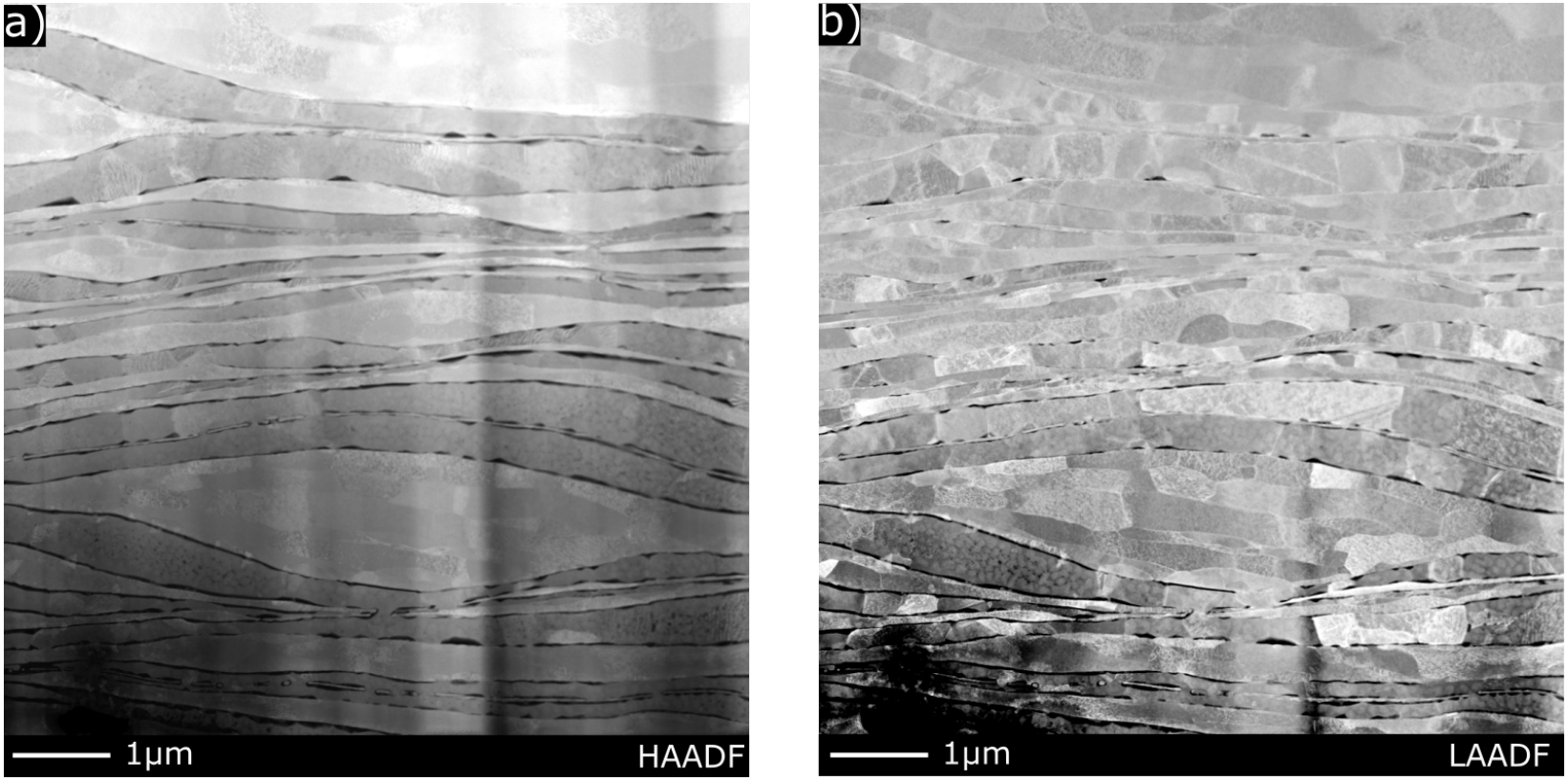


Figure 3.A.4.ii: STEM image overview of sample 200A (200 nm Cu-Nb) post failure. Contrasts labeled.

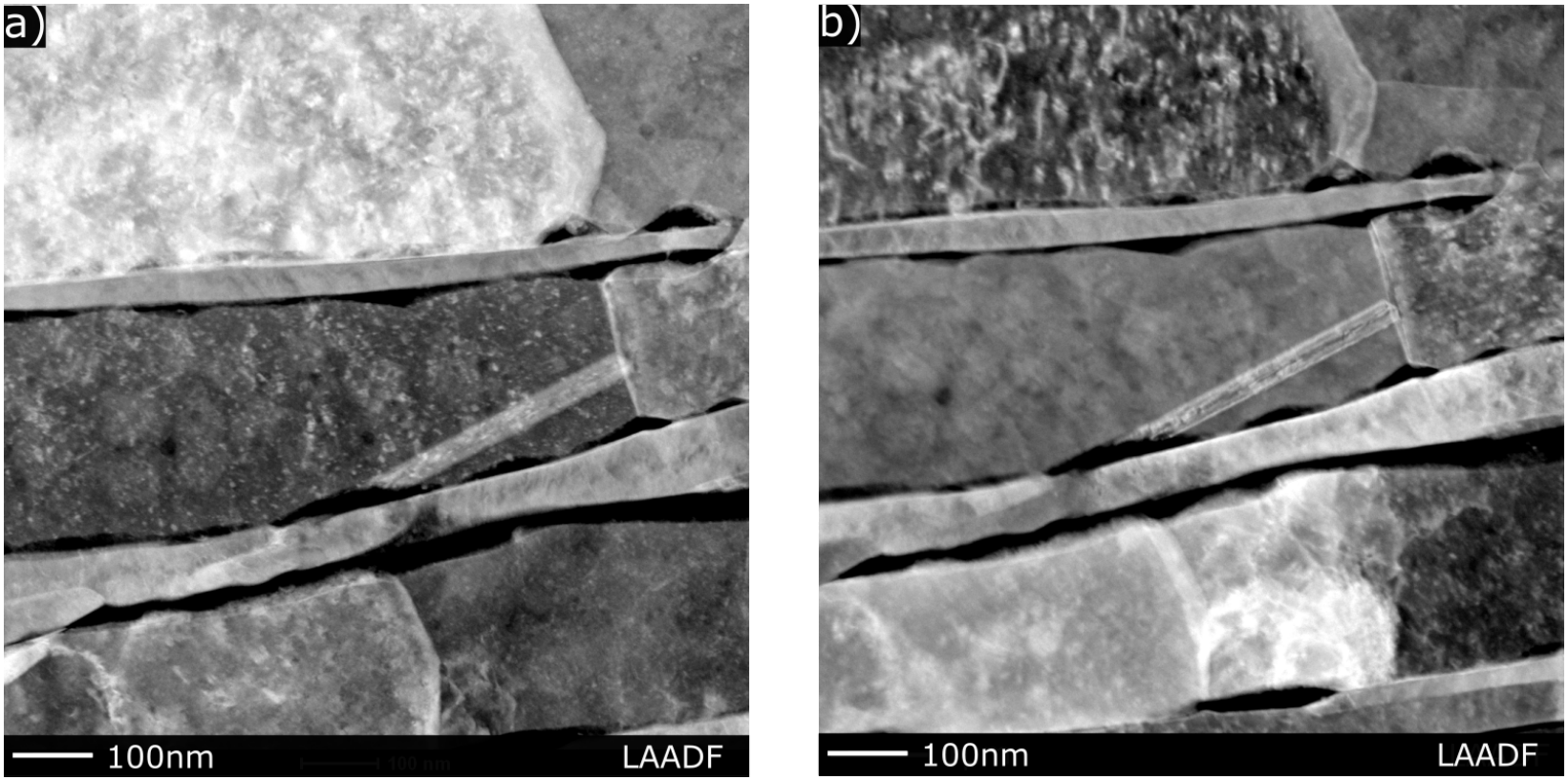


Figure 3.A.4.iii: LAADF STEM of sample 200A (200 nm Cu-Nb) post failure. Series shows varying dislocation and grain contras with varied tilt angle.

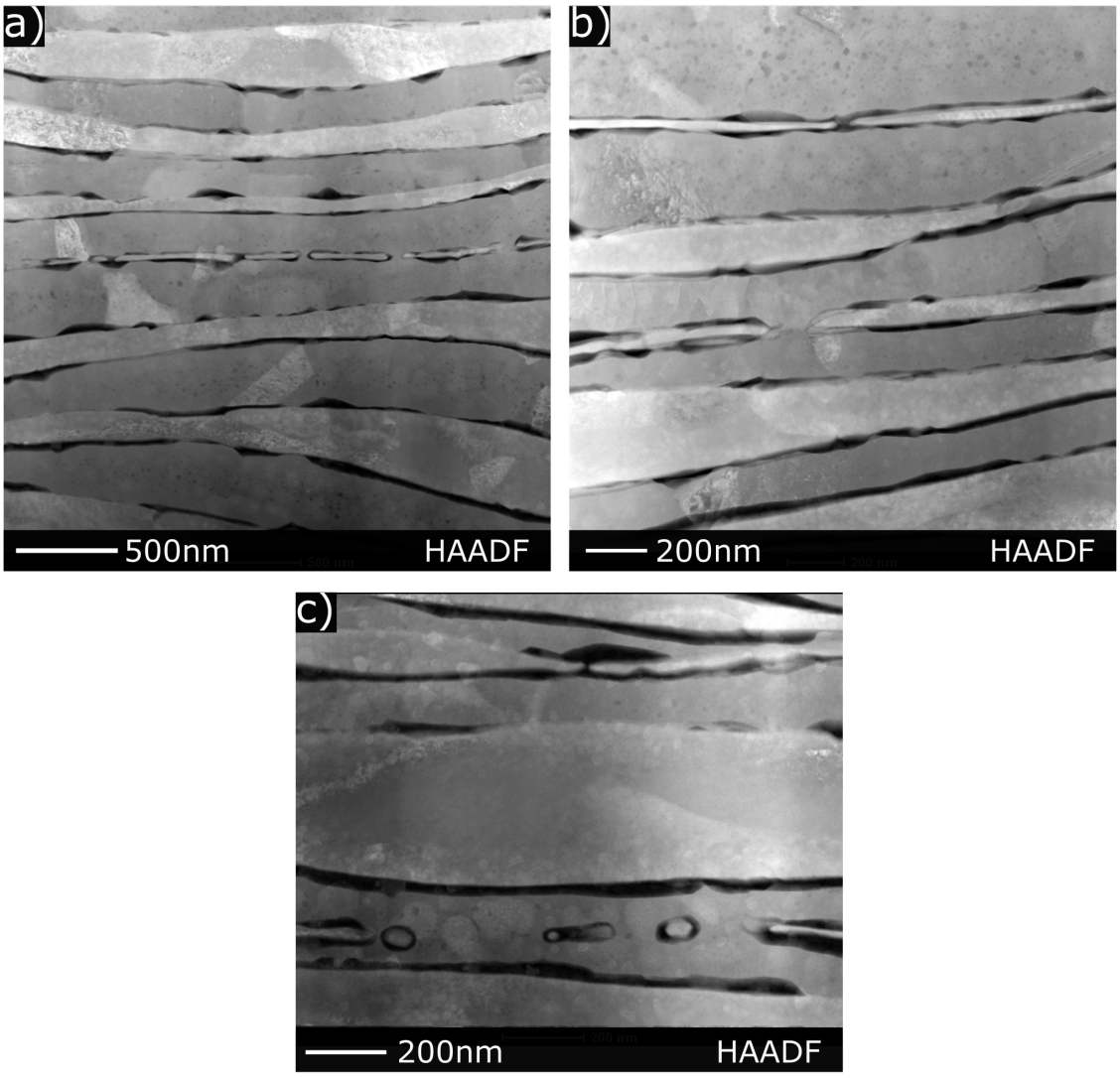


Figure 3.A.4.iv: HAADF STEM of sample 200A (200 nm Cu-Nb) post failure. Cu-Nb interface voids occur throughout and grow into Cu.

3.B "Heat treated" Cu-Nb creep at 400 °C

Sample	Scale (nm)	Temp (°C)	Type	Stress (MPa)	Strain (%)
65B	65	400	HT [a] Jump	140, 150, 160, 200, 230, 240, 260, 290, 320, 350, 370	2.5
65HT	65	400	HT [b] Jump	320, 350	2.5

Table 3.B.i: a) This sample is considered heat treated because loads were too low for measurable strain accumulation for 20 days. Frame error resulted in unloading of the sample, new surface preparation, and restarting of creep test after a week at temperature without any strain. Total time at temperature was over 30 days at failure. b) This sample was heat treated for 30 days at 400 °C prior to testing.

3.B.1 Post-failure Micrographs of 65HT

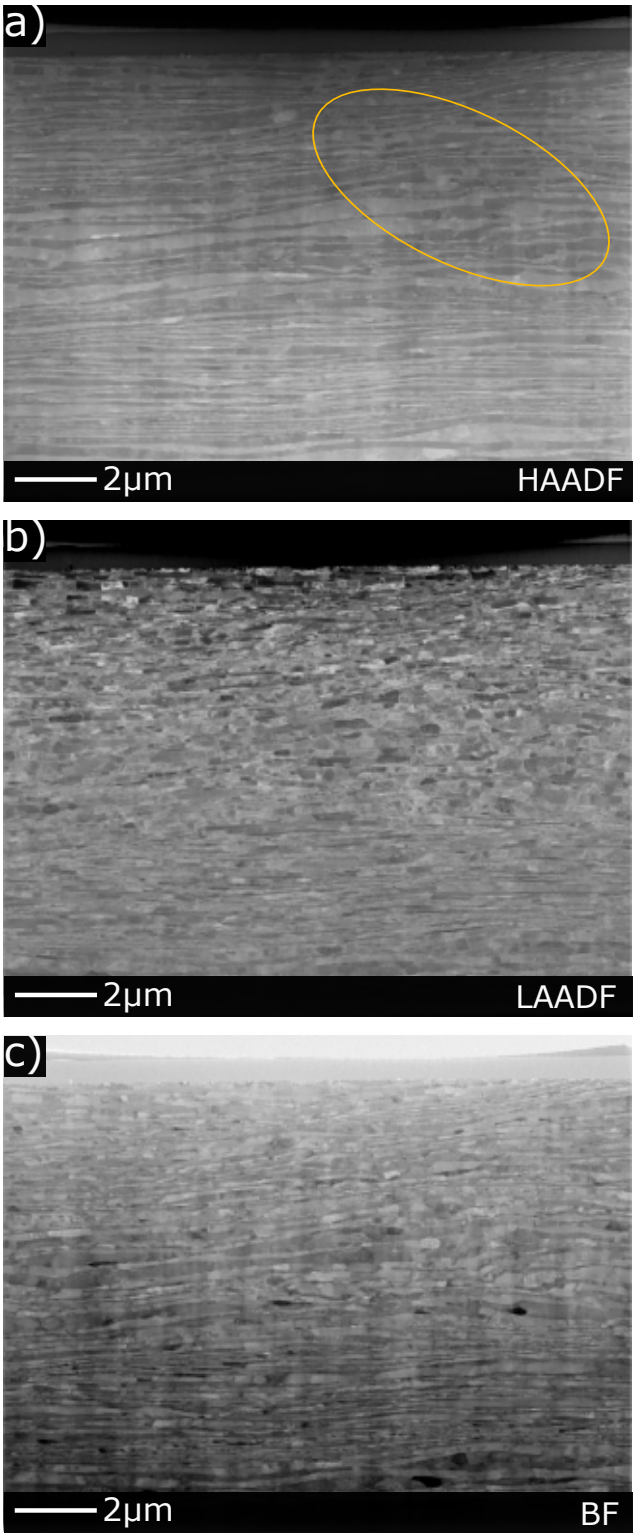


Figure 3.B.1.i: Overview of sample 65HT post creep failure. Note locally kinked region, circled. Contrasts Labeled.

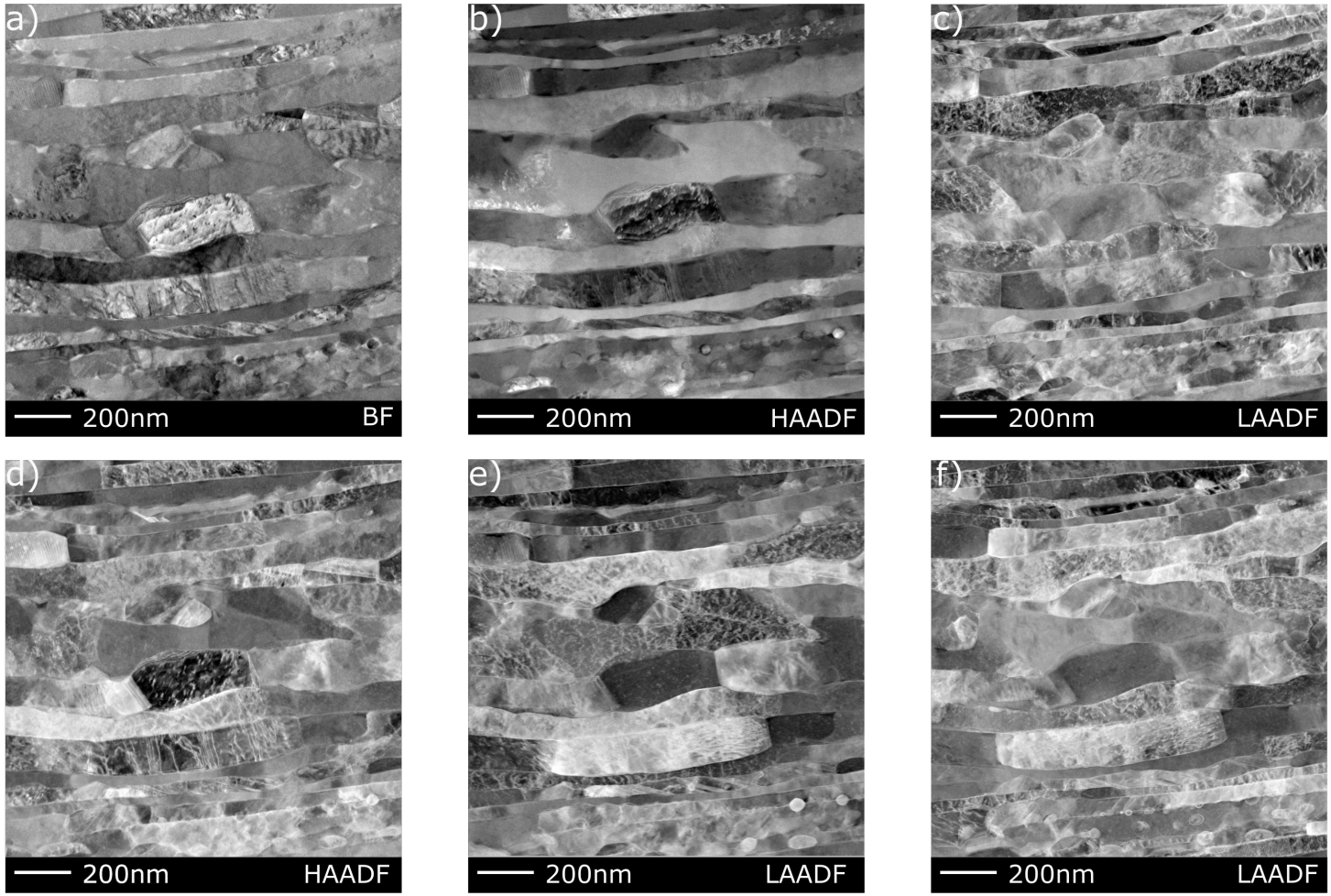


Figure 3.B.1.ii: Large areas of sample 65HT post creep failure. Grain structure within local kink shows subgrains at varying tilt angles. Contrasts Labeled.

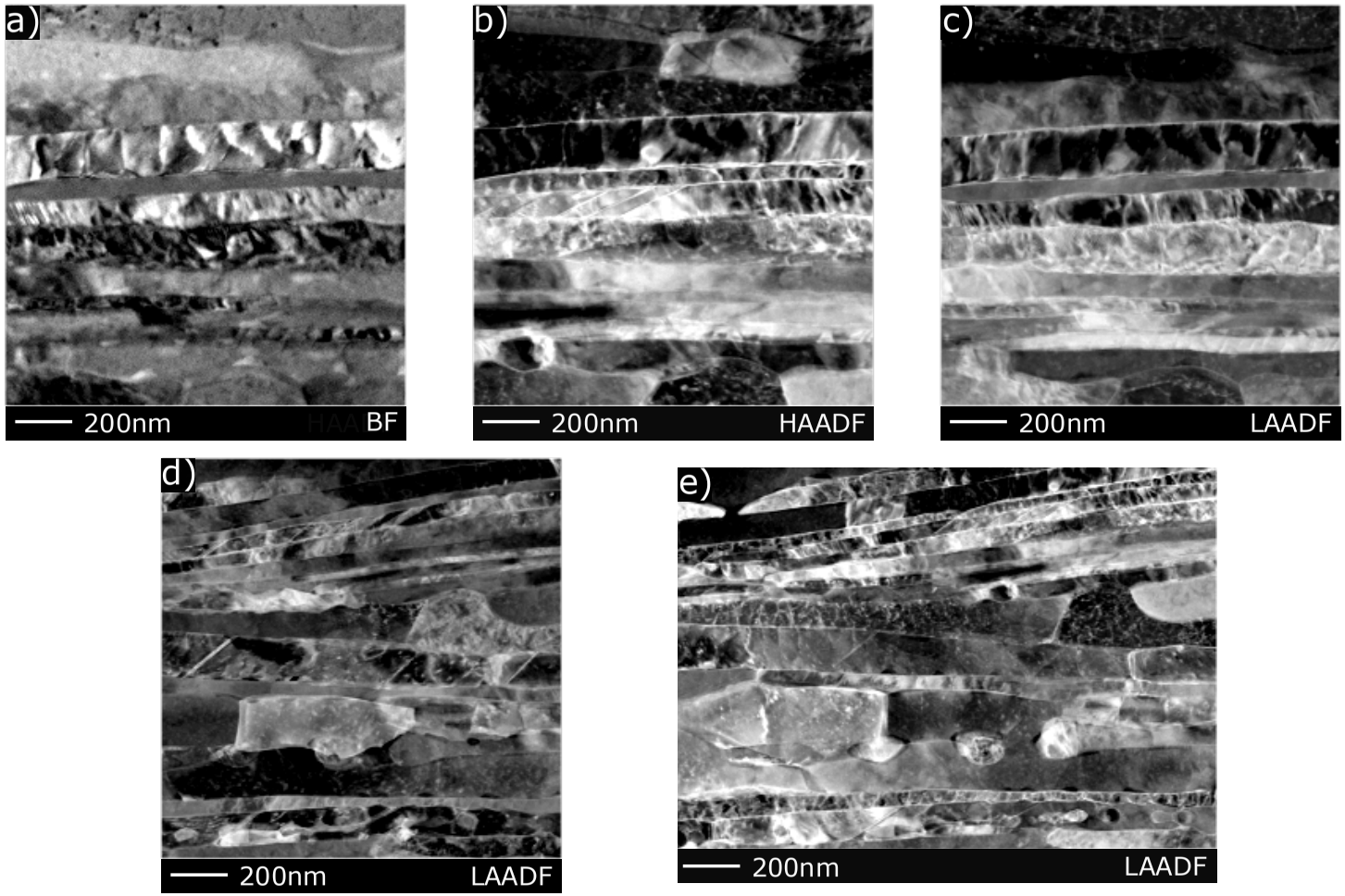


Figure 3.B.1.iii: LAADF STEM of sample 65HT (65 nm Cu-Nb) post failure. Series shows varying dislocation and grain contras with varied tilt angle.

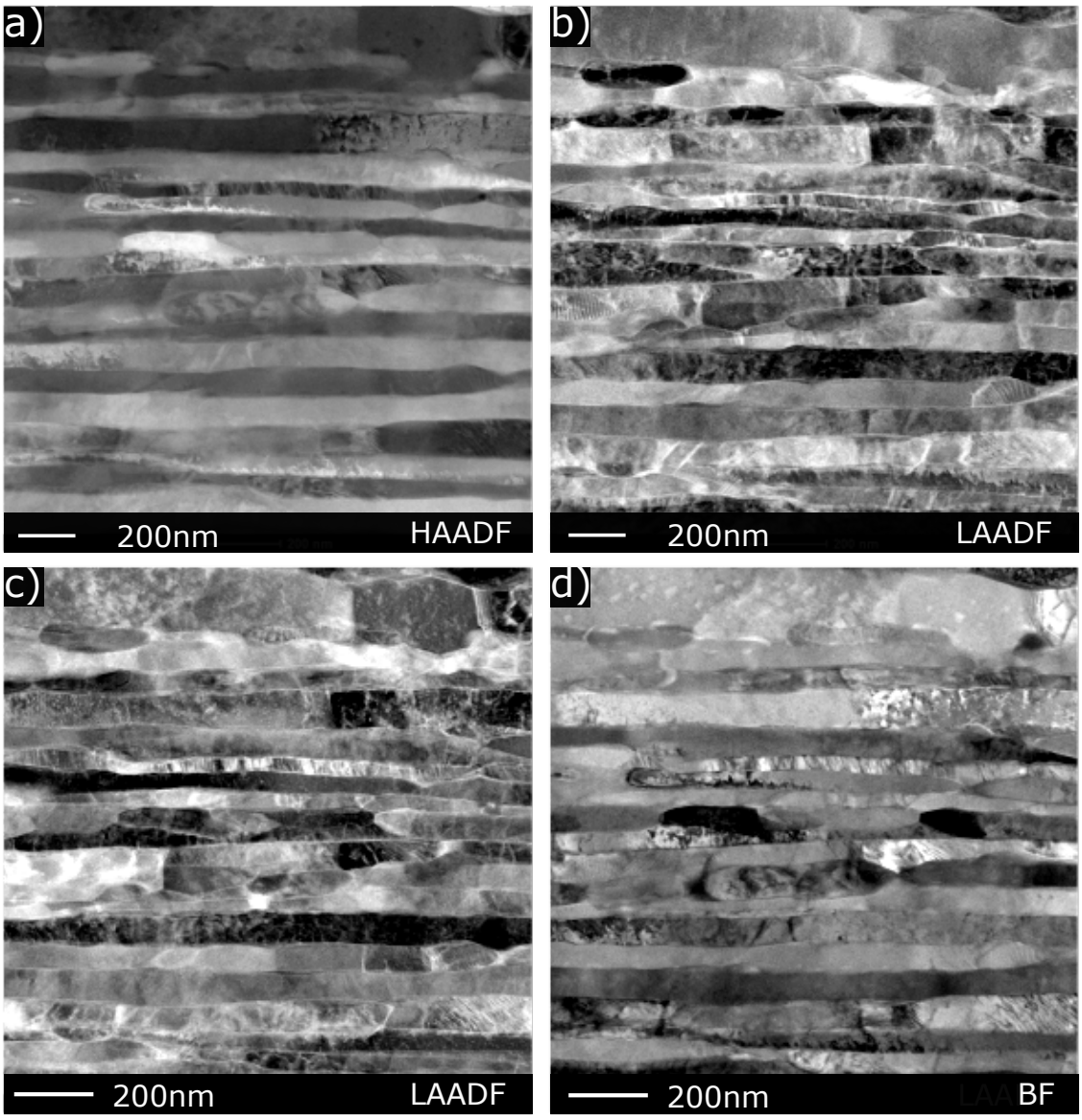


Figure 3.B.1.iv: STEM of sample 65HT (65 nm Cu-Nb) post failure. b) and c) show varying dislocation and grain contras with varied tilt angle. a) and d) show HAADF and BF contrast of the same region, respectively.

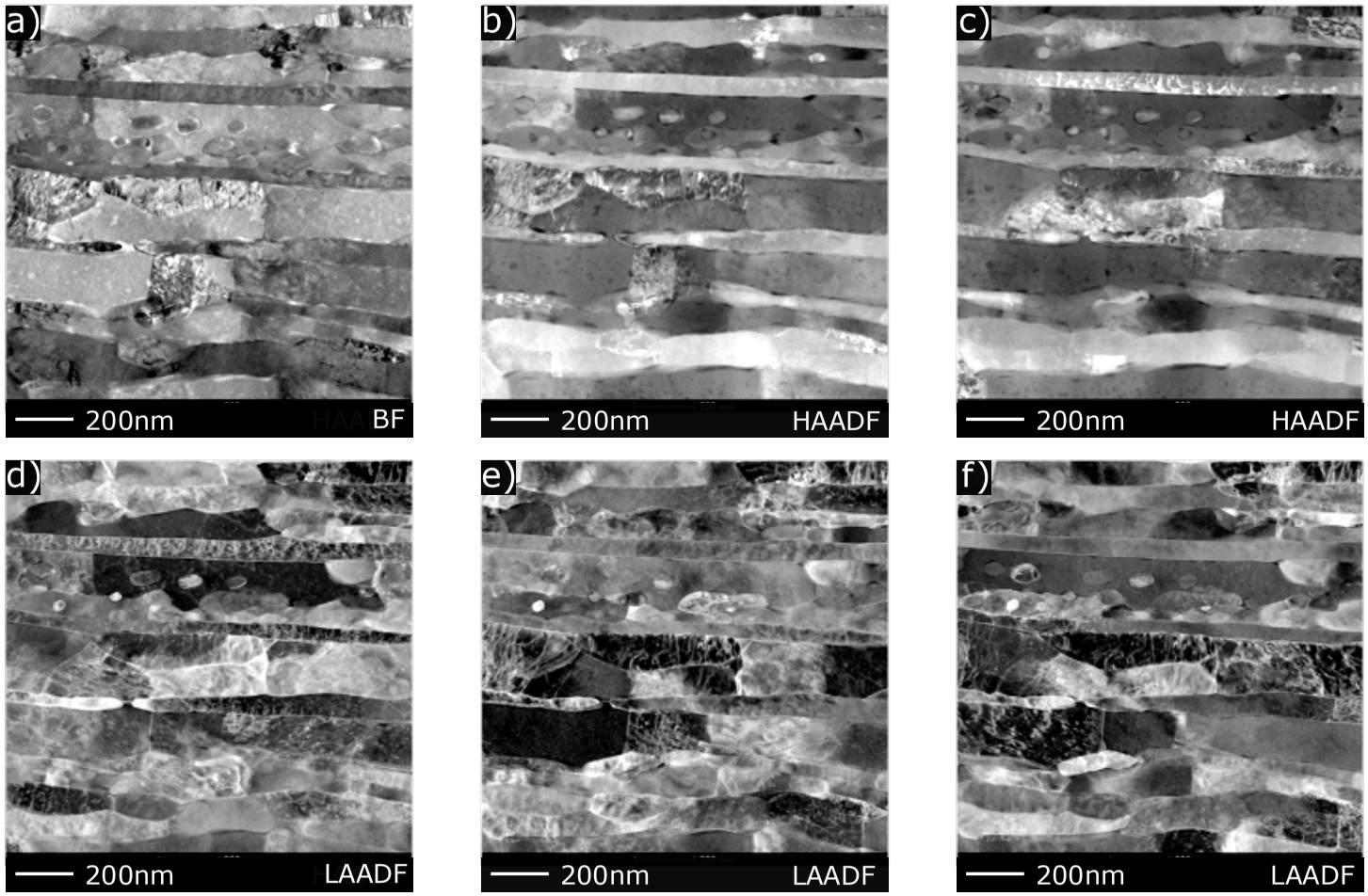


Figure 3.B.1.v: STEM of sample 65HT (65 nm Cu-Nb) post failure. a) is Bright field contrast, highlighting voids. b) and c) are HAADF images at different tile angles. Large defect concentrations inhibit atomic contrast in select regions. d)-f) show varying dislocation and grain contras with varied tilt angle.

3.B.2 Creep Curves

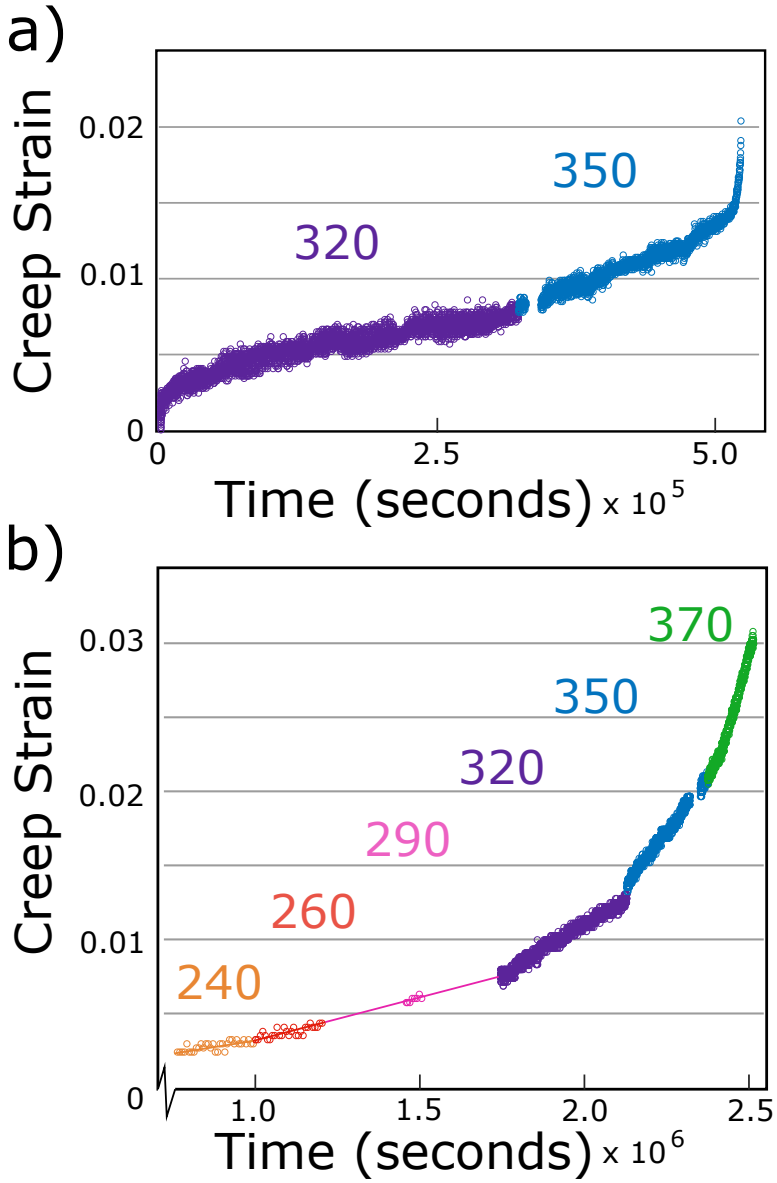


Figure 3.B.2.i: Jumped creep response of (a) 65HT and (b) 65B. Stresses are labeled in MPa. *Note: lower stresses of 65B are not shown, as they had negligible creep for over a week of testing.*

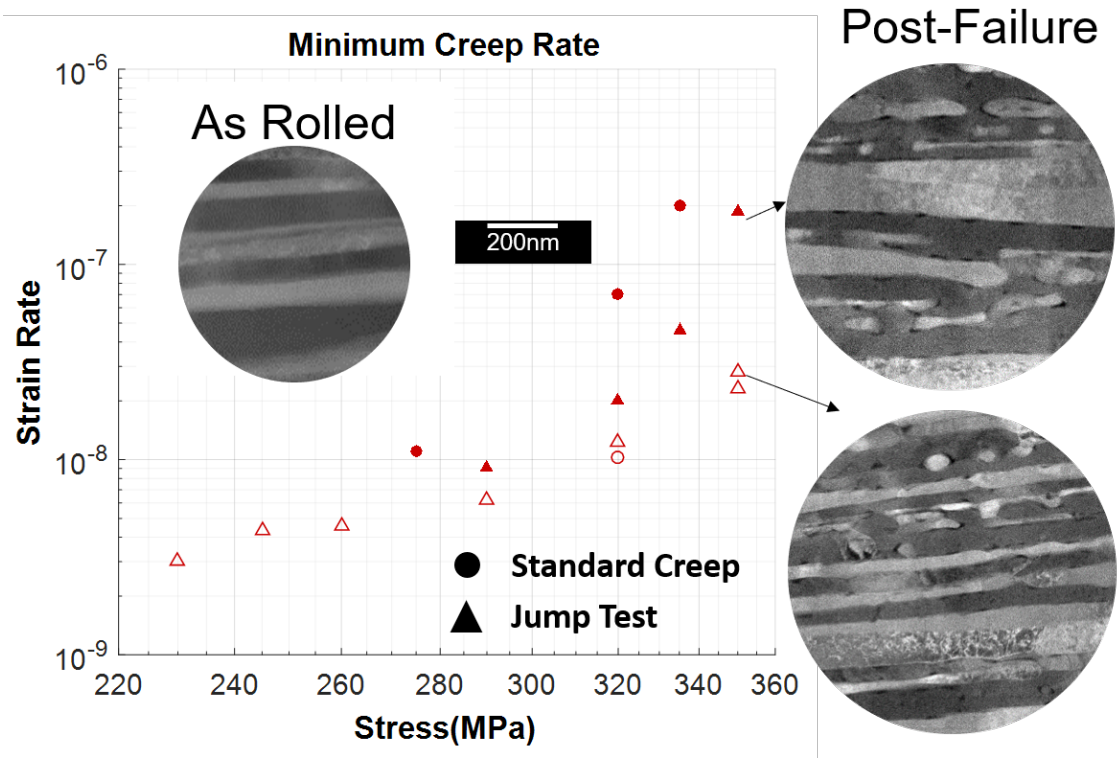


Figure 3.B.2.ii: Minimum creep rates (1/s) for 65 nm Cu-Nb. Closed shapes are as rolled, open shapes are heat treated.

3.C "As rolled" Cu-Nb creep at 500 °C

Sample	Scale (nm)	Temp (°C)	Type	Stress (MPa)	Strain (%)
2C	2000	500	Jump	75, 90, 105, 120	5.5
200C	200	500	Standard	150	1.5
65E	65	500	Failed	275	×

Table 3.C.i: [–] interrupted, [×] Immediate failure along shear band during loading.

3.C.1 Post-failure Micrographs of 200 nm Cu-Nb

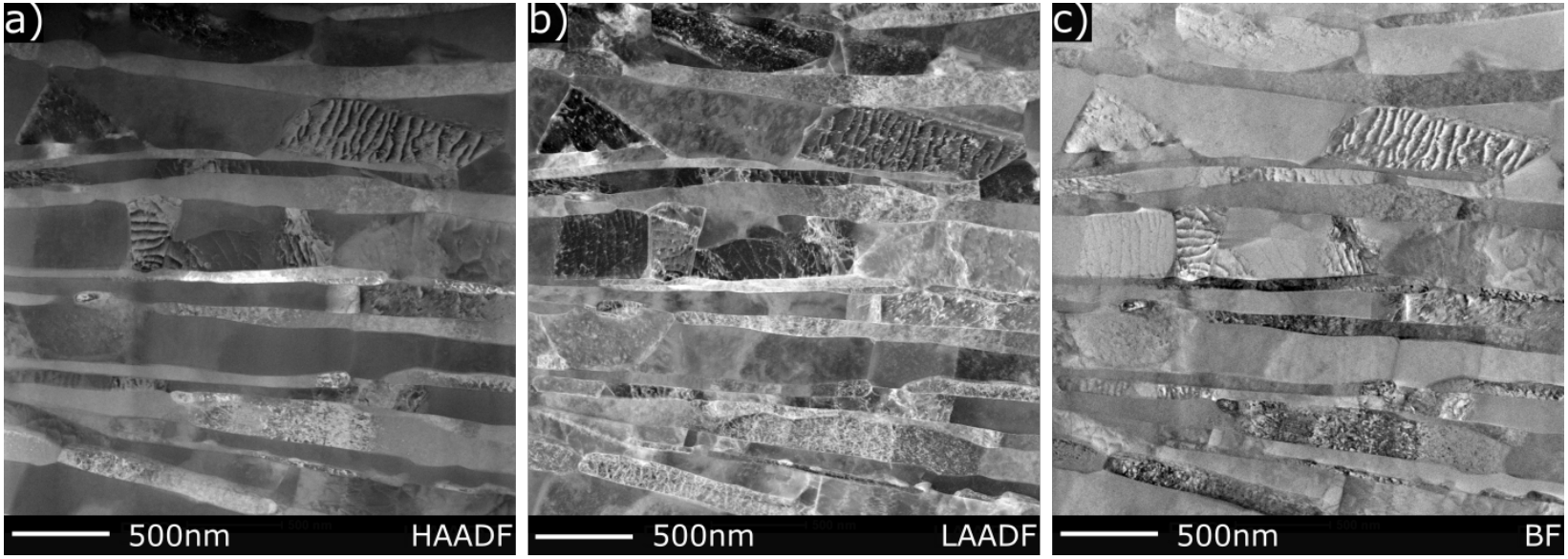


Figure 3.C.1.i: Large are of sample 200C (200 nm Cu-Nb) post failure. Contrasts labeled.

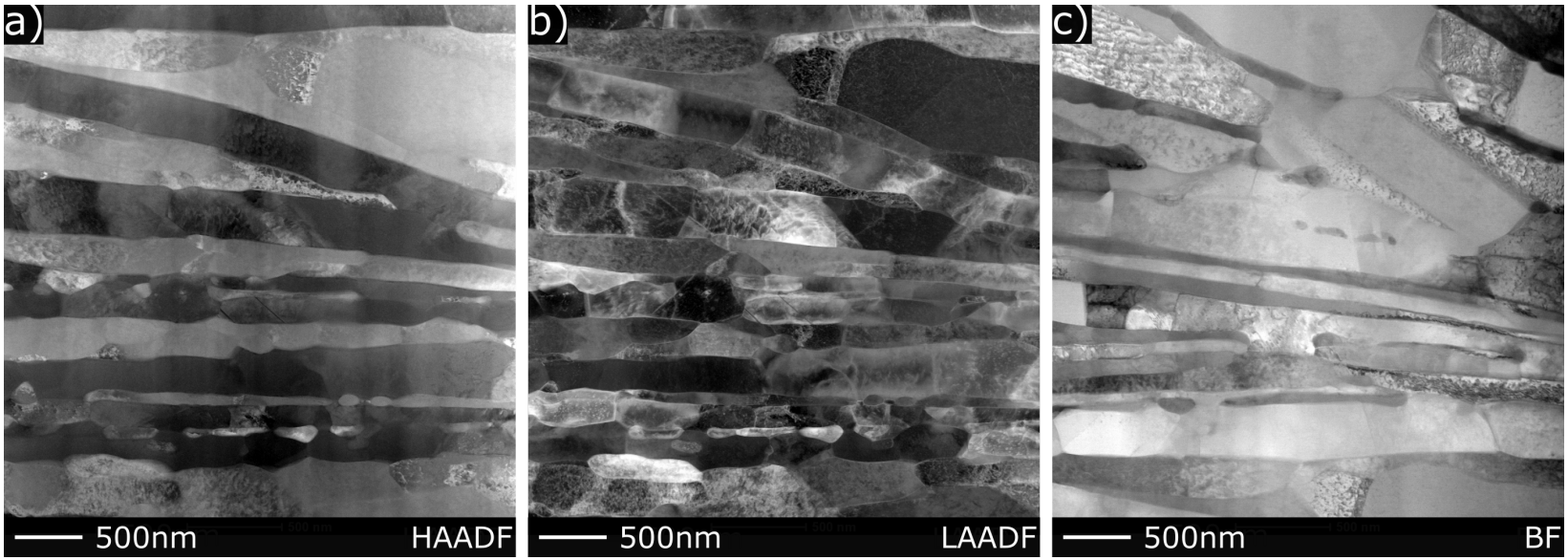


Figure 3.C.1.ii: Large are of sample 200C (200 nm Cu-Nb) post failure. Contrasts labeled.

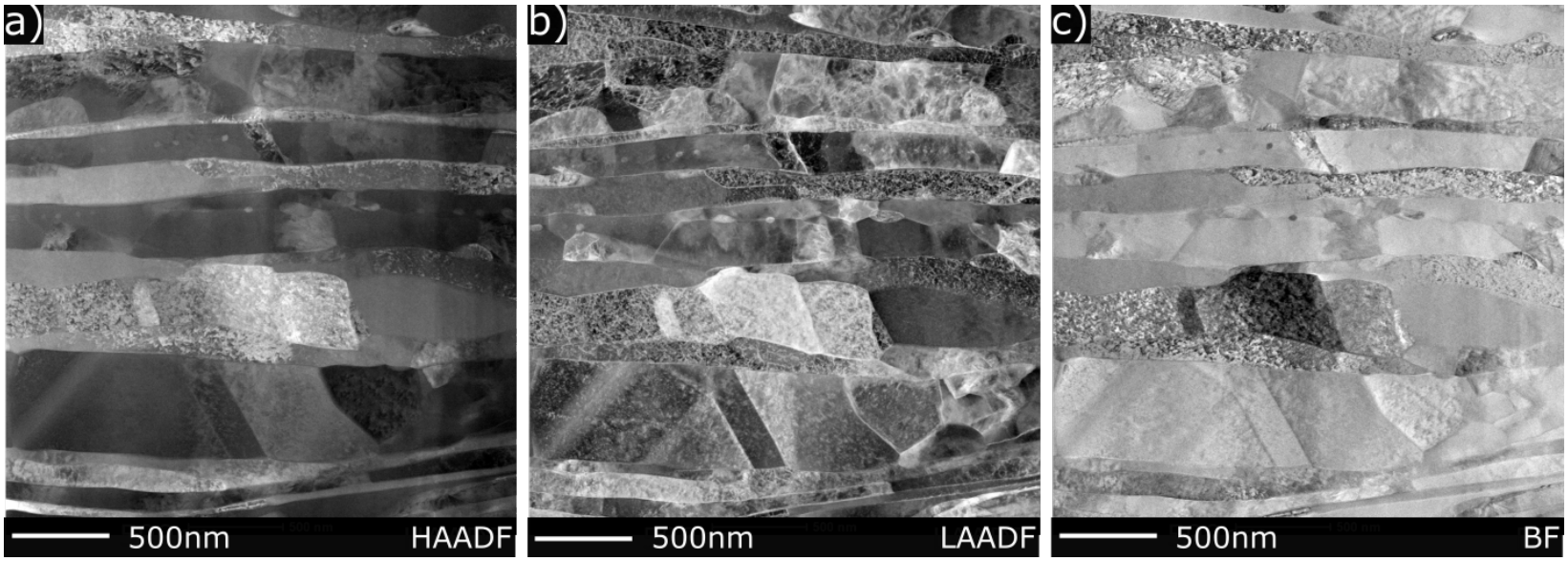


Figure 3.C.1.iii: Large are of sample 200C (200 nm Cu-Nb) post failure. Contrasts labeled.

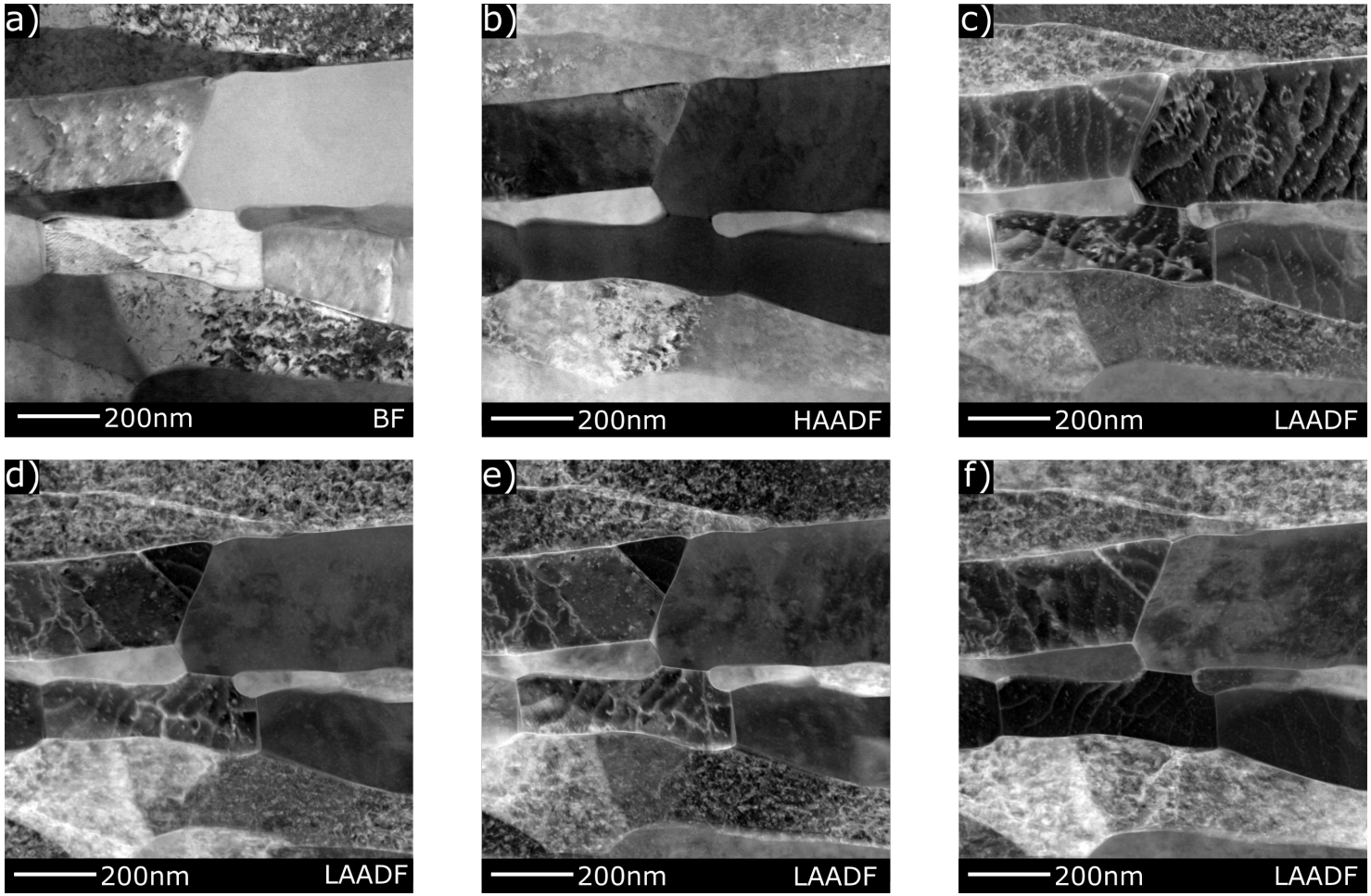


Figure 3.C.1.iv: STEM of sample 200C (200 nm Cu-Nb) post failure. This area is a close view of a pinched off Nb layer in a) BF contrast, b) HAADF contrast, and c)-f) a LAADF contrast series shows varying dislocation and grain contras with varied tilt angle.

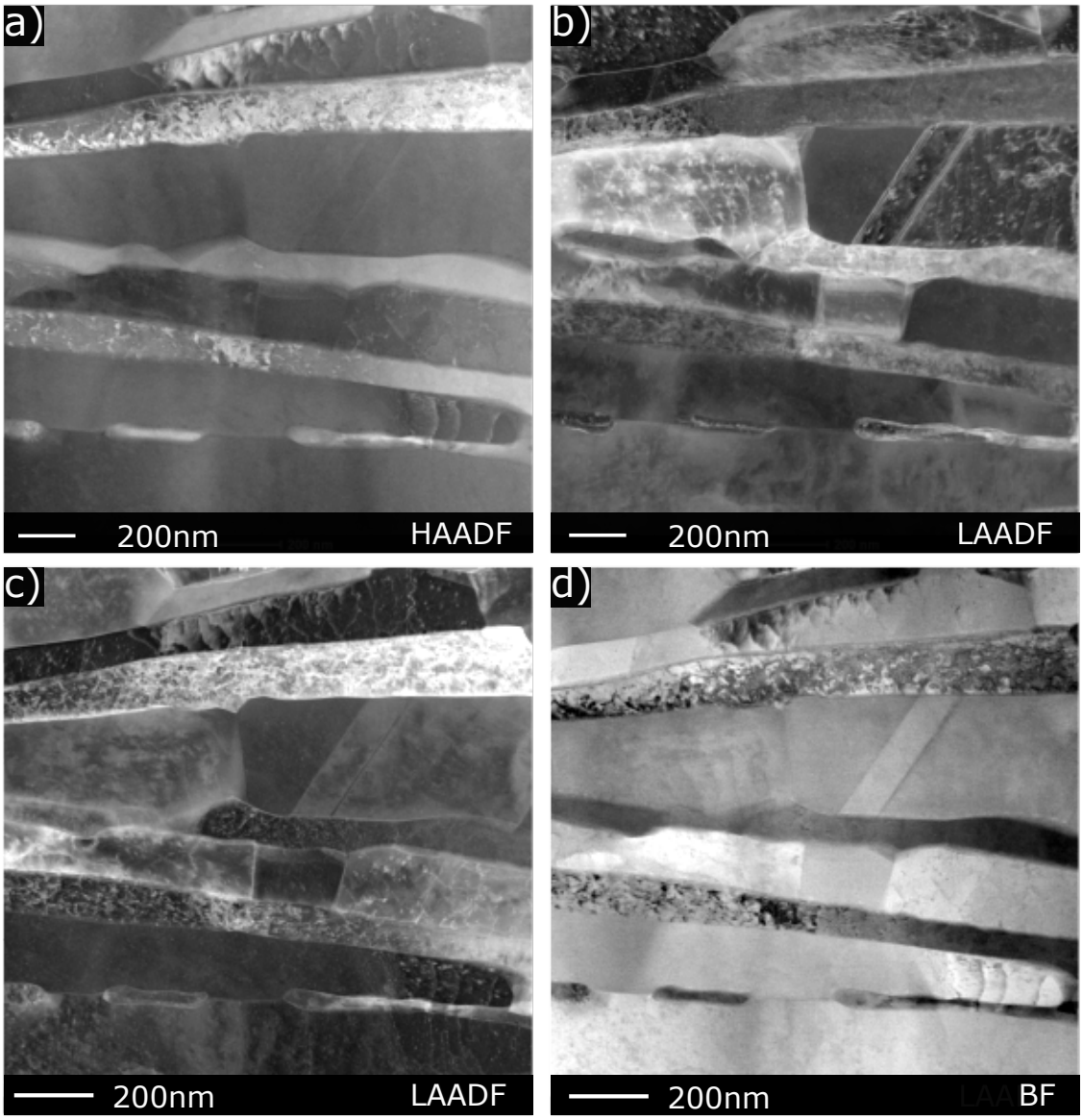


Figure 3.C.1.v: STEM of sample 200C (200 nm Cu-Nb) post failure. This area includes pinched off Nb layers, grooving, and annealing twins in d) BF contrast, a) HAADF contrast, and b)-c) LAADF contrast.

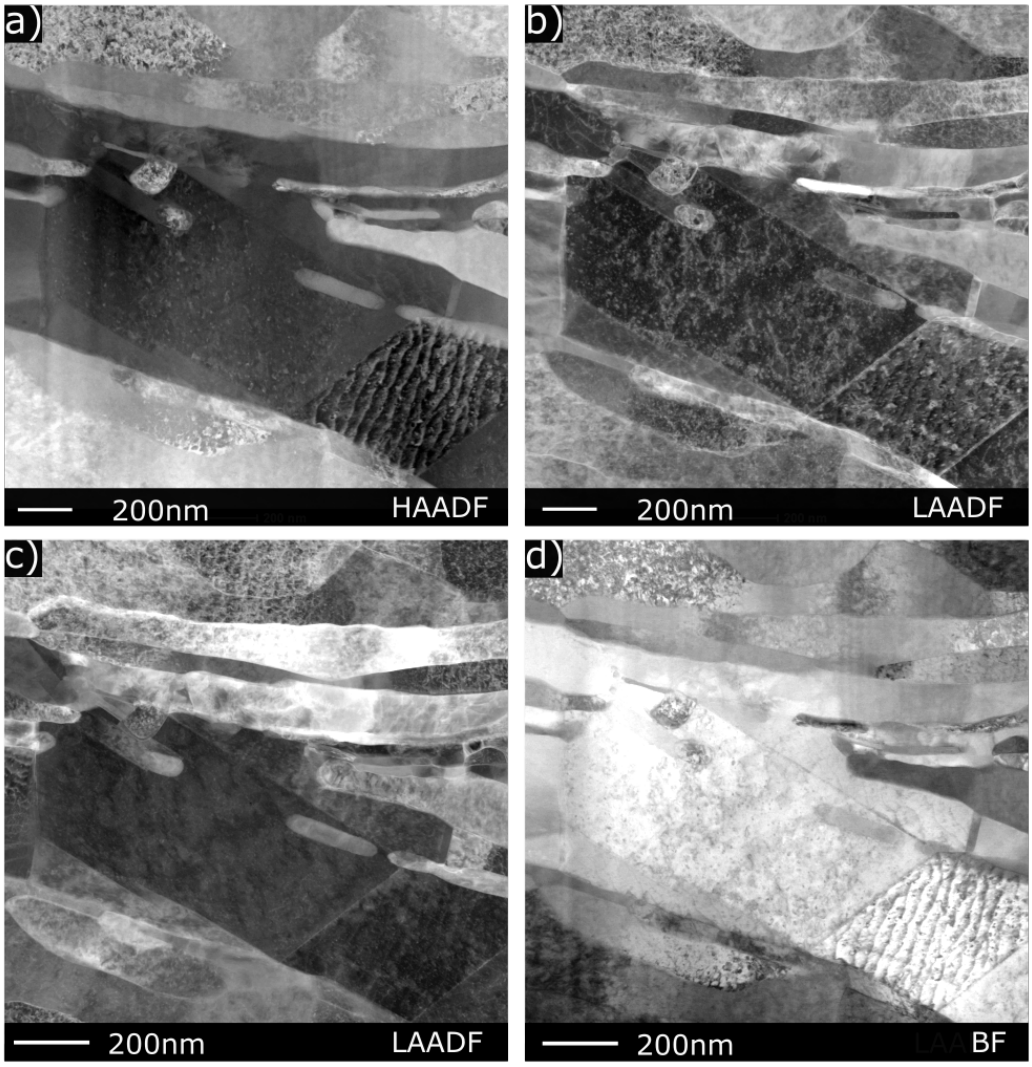


Figure 3.C.1.vi: STEM of sample 200C (200 nm Cu-Nb) post failure. This area is a close view of a pinched off Nb layers at a shear band and Cu recrystallization at the pinched off area. d) BF contrast, a) HAADF contrast, and b)-c) a LAADF contrast series shows varying dislocation and grain contras with varied tilt angle.

3.C.2 Creep Curves

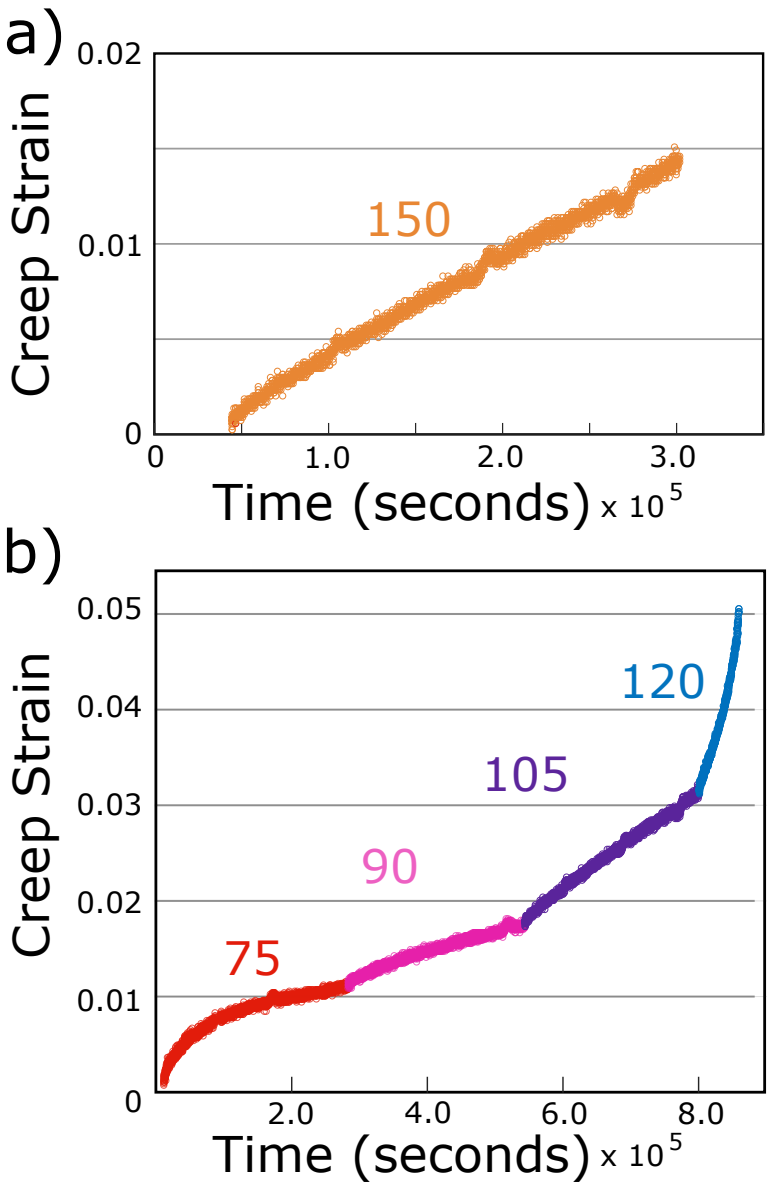


Figure 3.C.2.i: Creep response of (a) 200C and (b) 2C. 200C failed abruptly at a shear band. Stresses are labeled in MPa.

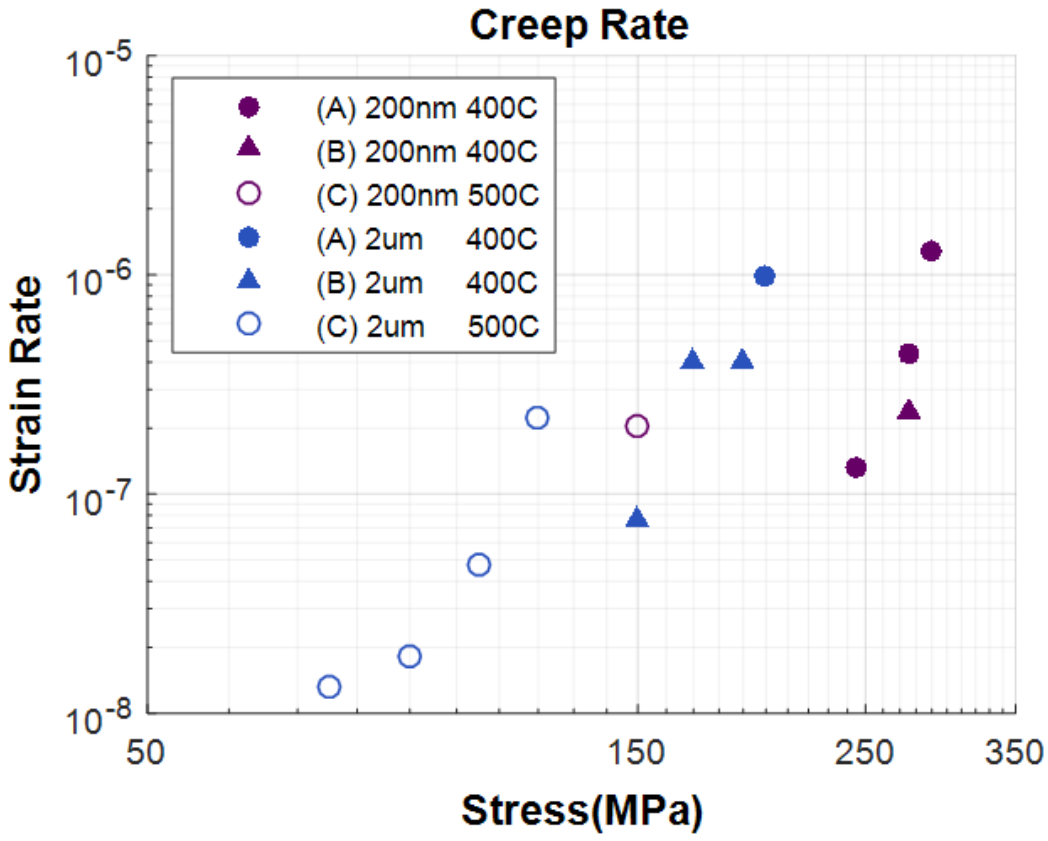


Figure 3.C.2.ii: Minimum creep rates (1/s) for Cu-Nb tested at 500 °C compared to the 400 °C response. Open shapes are 500 °C tests. Closed shapes are 400 °C tests showing differentiation between jump (triangle) and standard (circle).

Structural Evolution: Appendix

5.A 65 nm Anneal Micrographs

5.A.1 2 Days at 400 °C

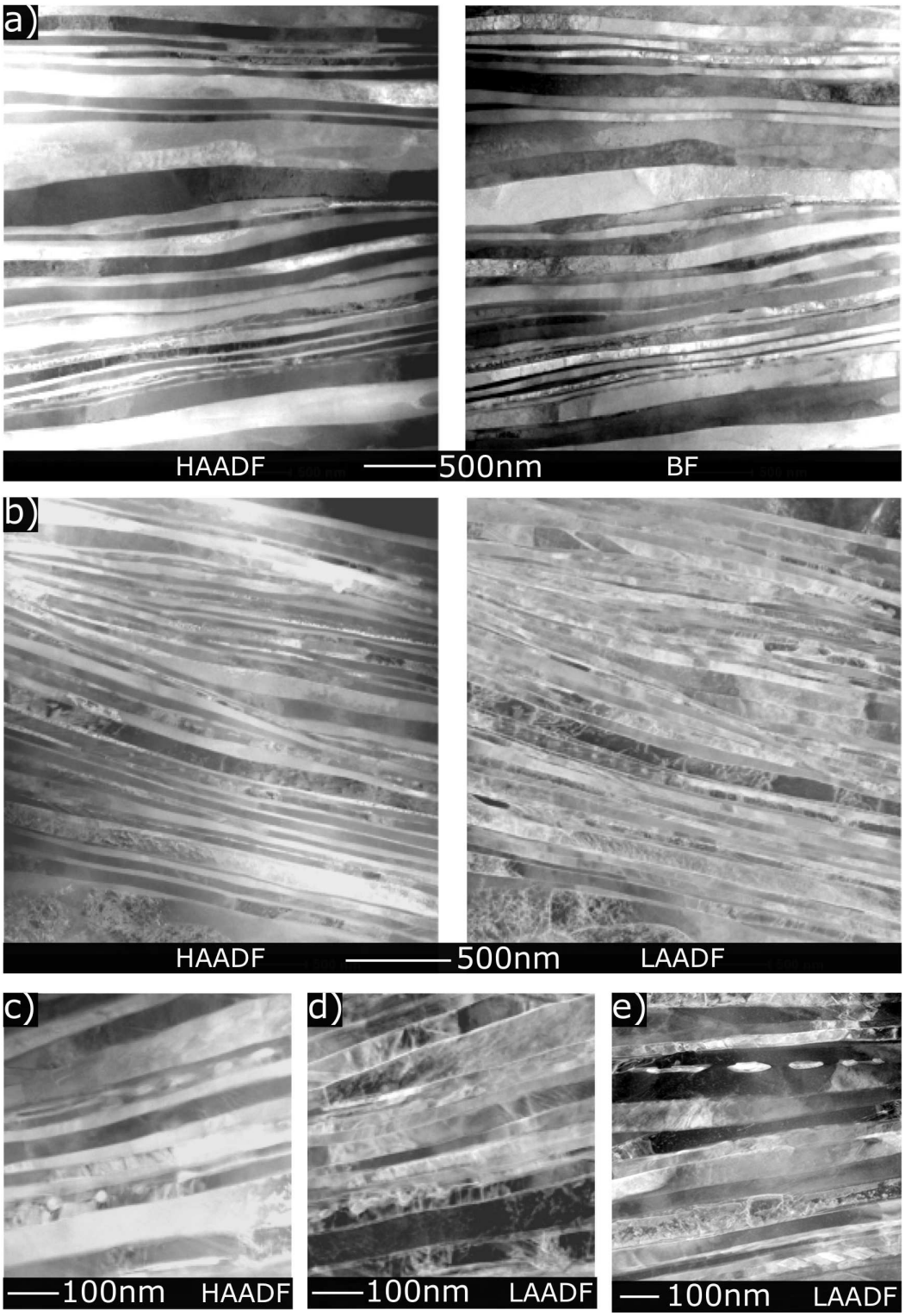


Figure 5.A.1.i: 65 *nm* Annealed 2 days at 400 °C

5.A.2 5 Days at 400 °C

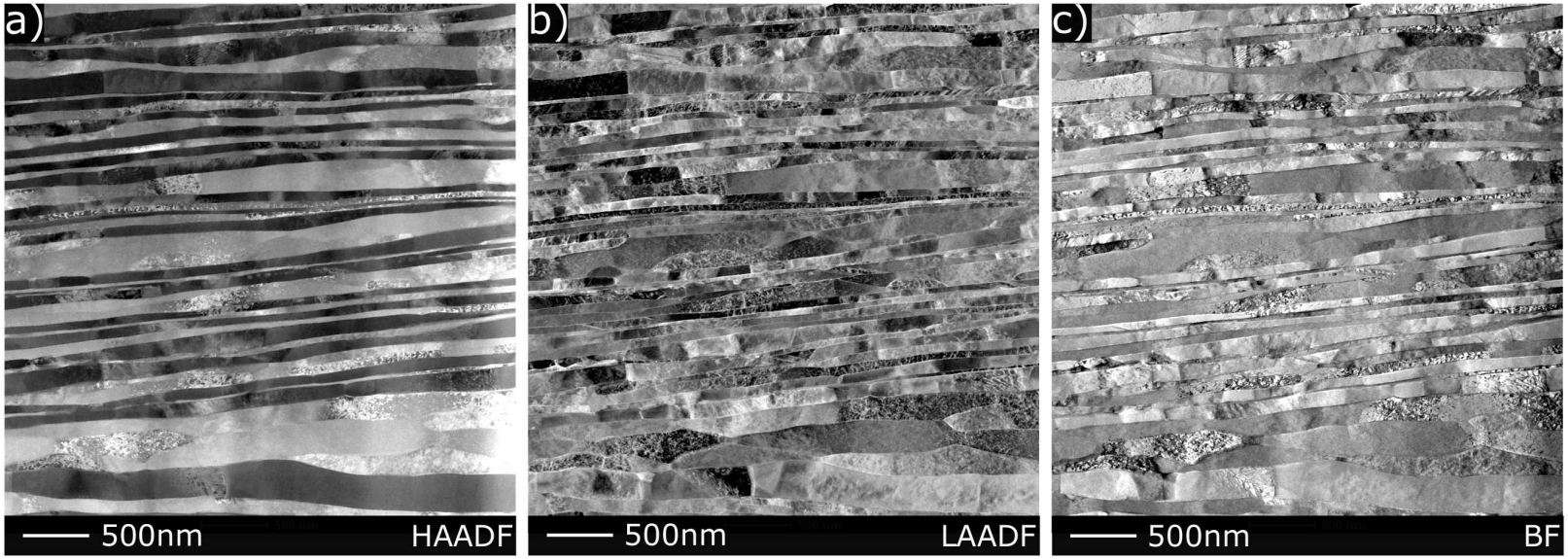


Figure 5.A.2.i: Large Area 1: 65 nm Annealed 5 days at 400 °C

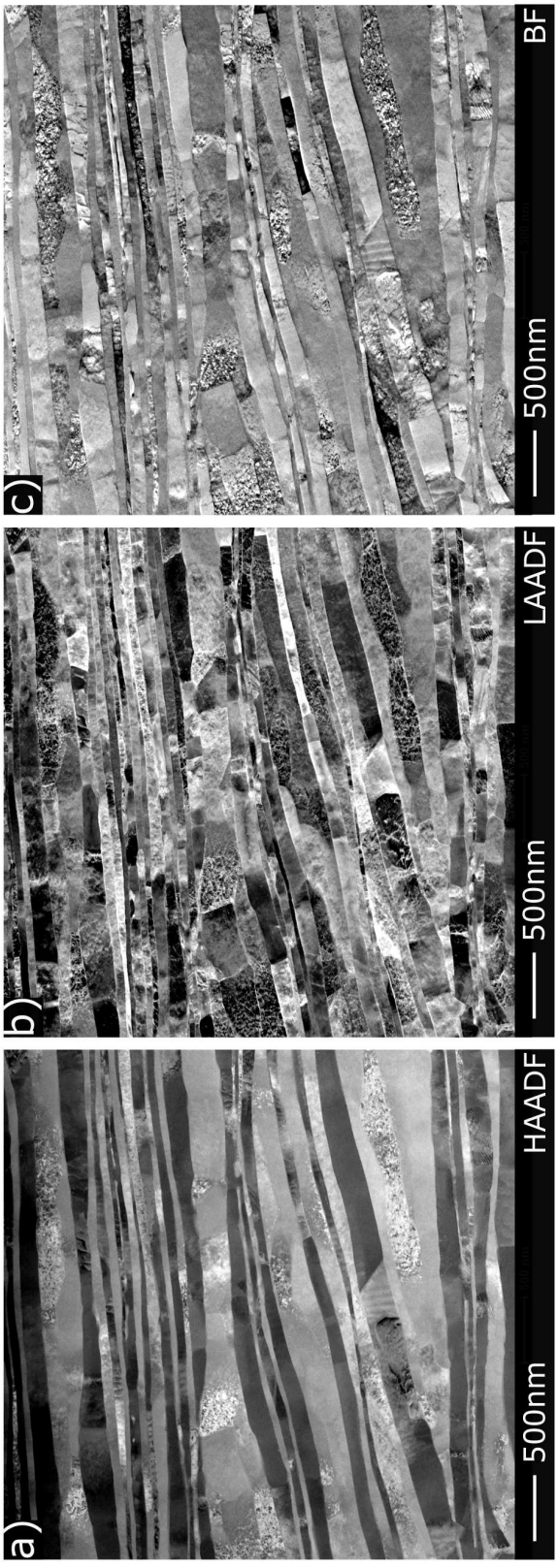


Figure 5.A.2.ii: Large Area 2: 65 *nm* Annealed 5 days at 400 °C

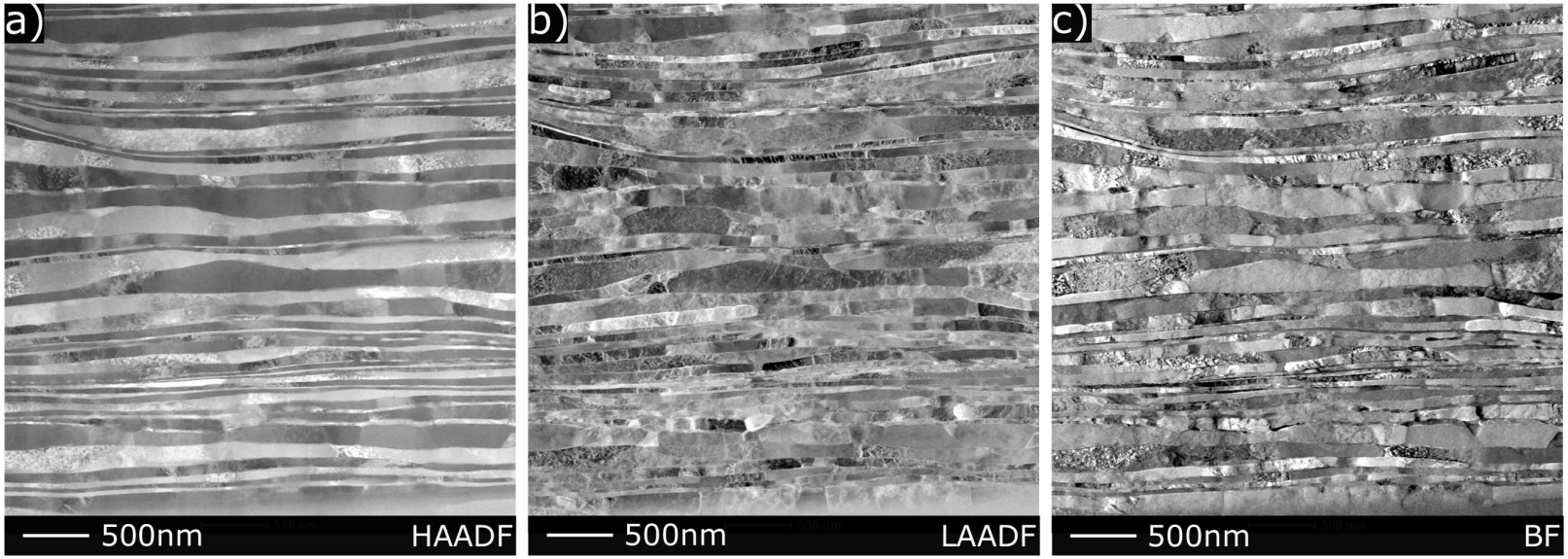


Figure 5.A.2.iii: Large Area 3: 65 nm Annealed 5 days at 400 °C

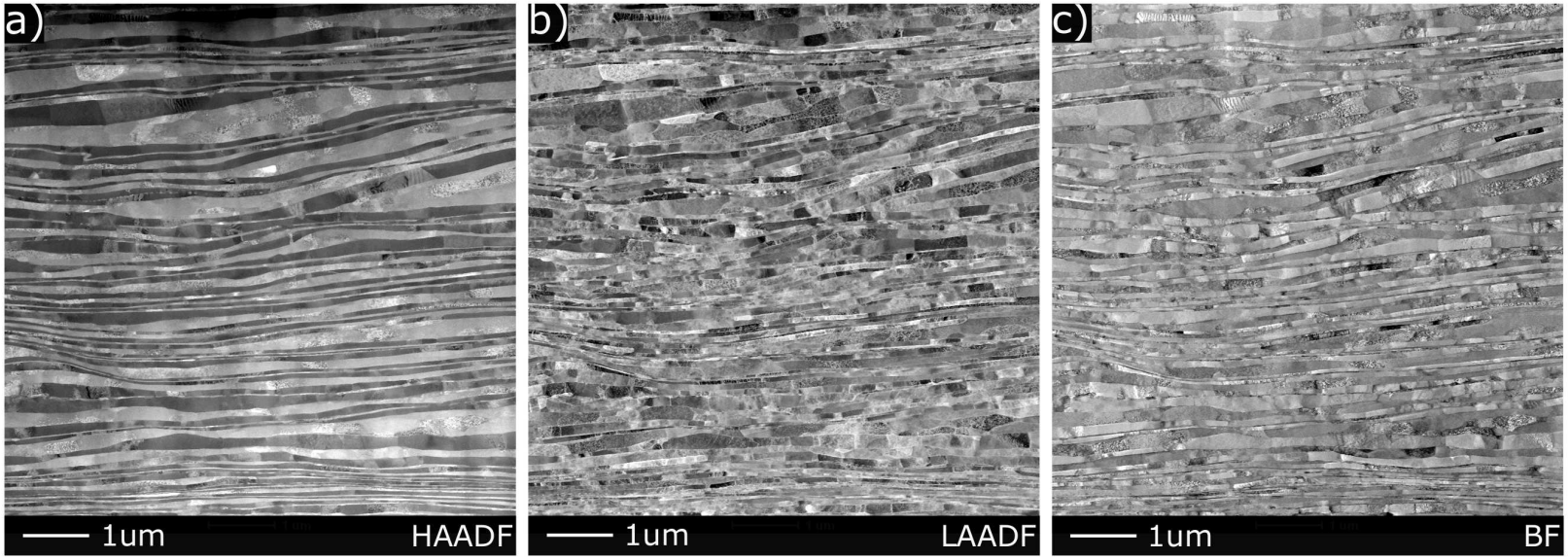


Figure 5.A.2.iv: Overview of 65 *nm* Annealed 5 days at 400 °C

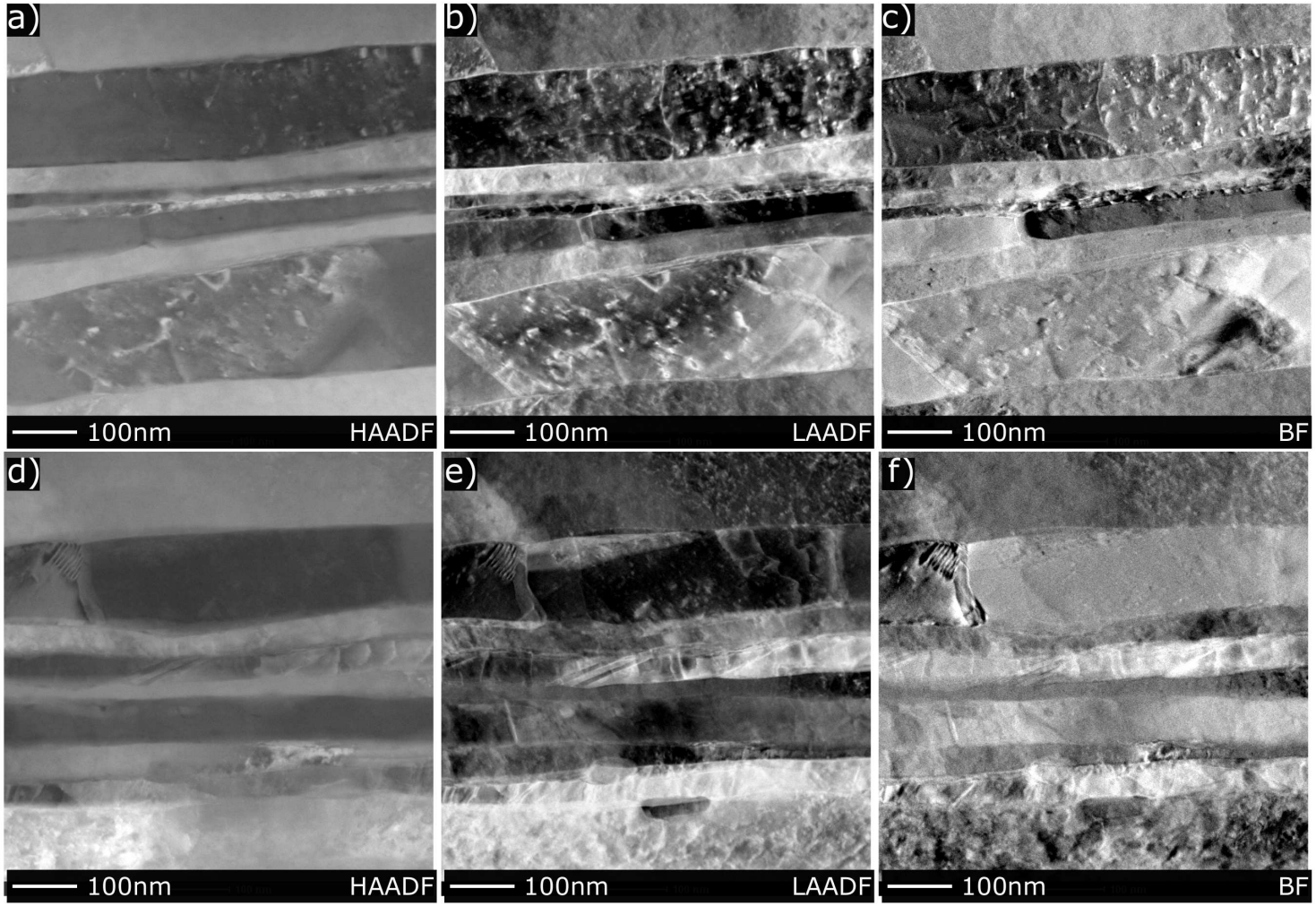


Figure 5.A.2.v: Close-up of 65 *nm* Annealed 5 days at 400 °C

5.A.3 15 Days at 400 °C

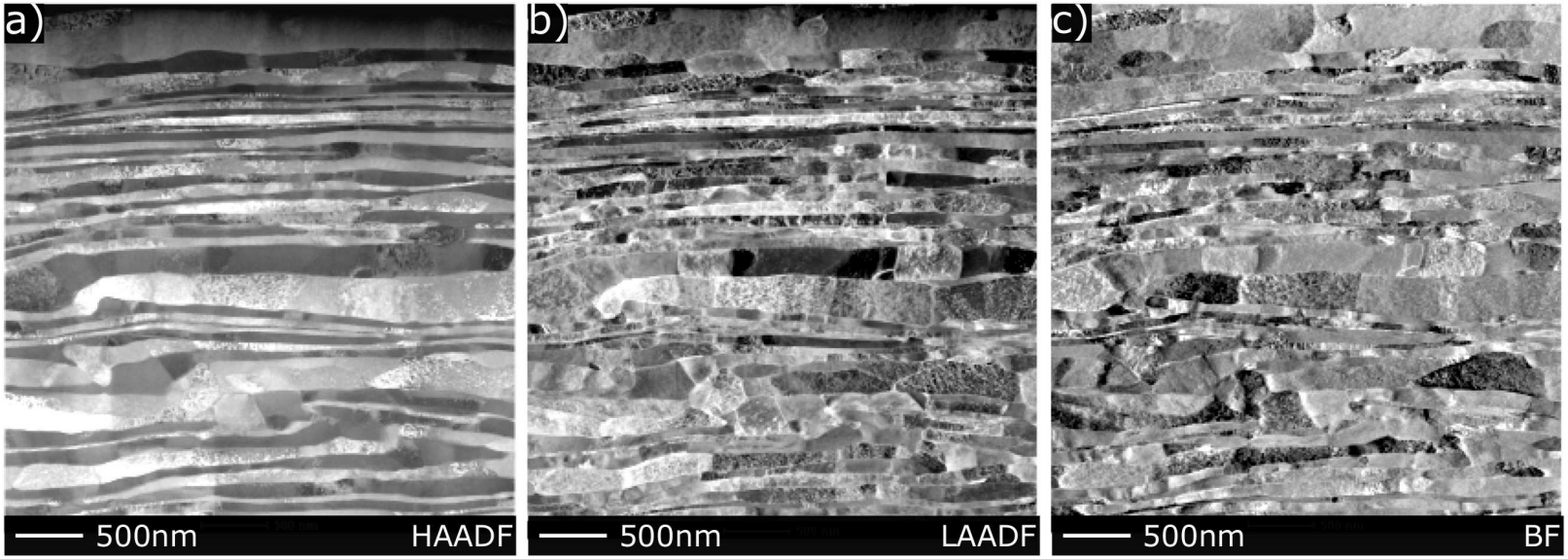


Figure 5.A.3.i: Large Area 1: 65 nm Annealed 15 days at 400 °C

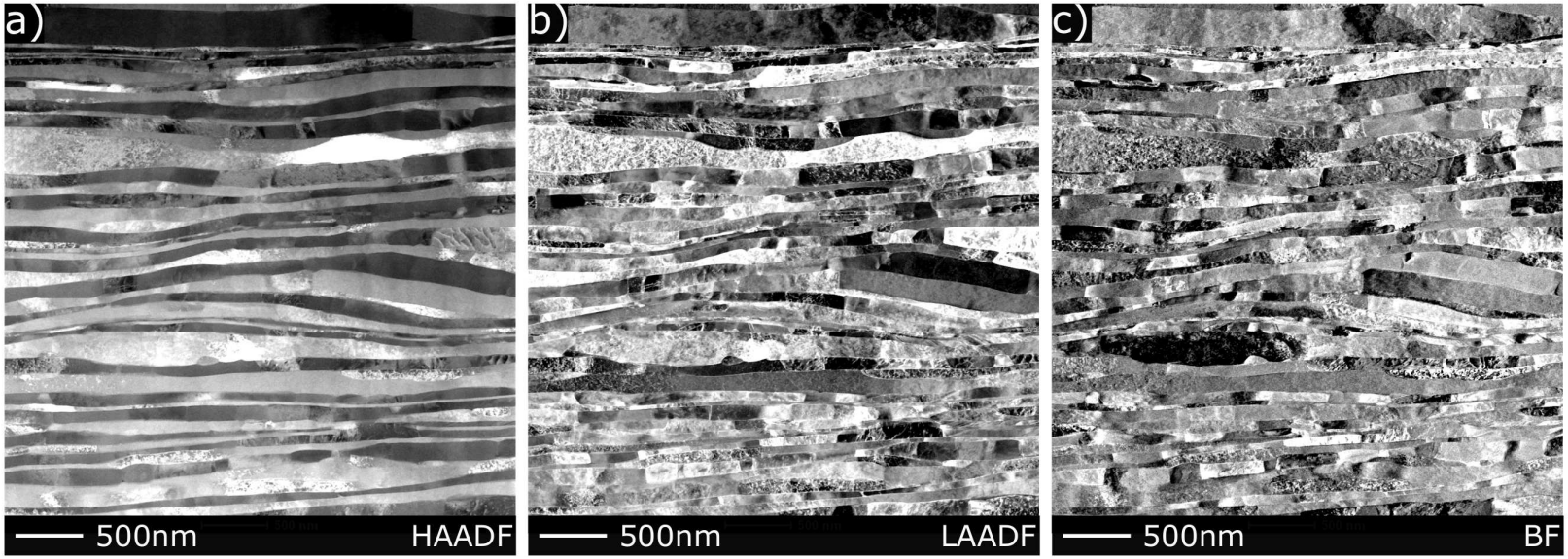


Figure 5.A.3.ii: Large Area 2: 65 nm Annealed 15 days at 400 °C

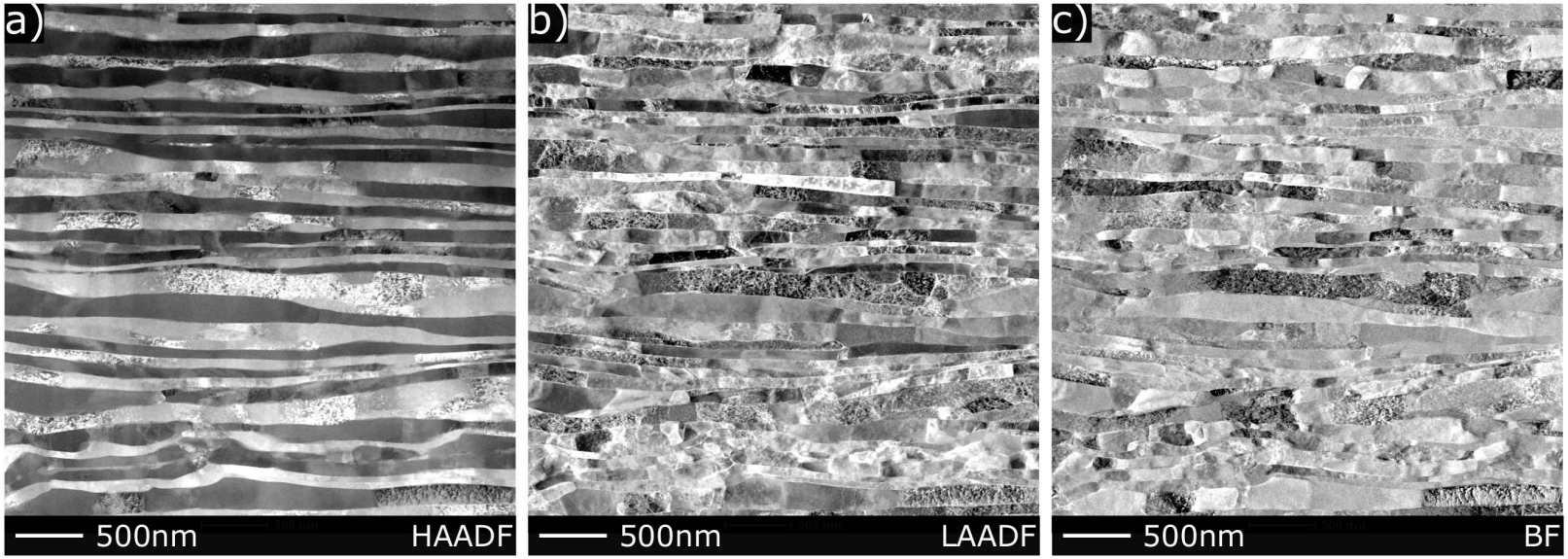


Figure 5.A.3.iii: Large Area 3: 65 nm Annealed 15 days at 400 °C

5.A.4 15 Days at 500 °C

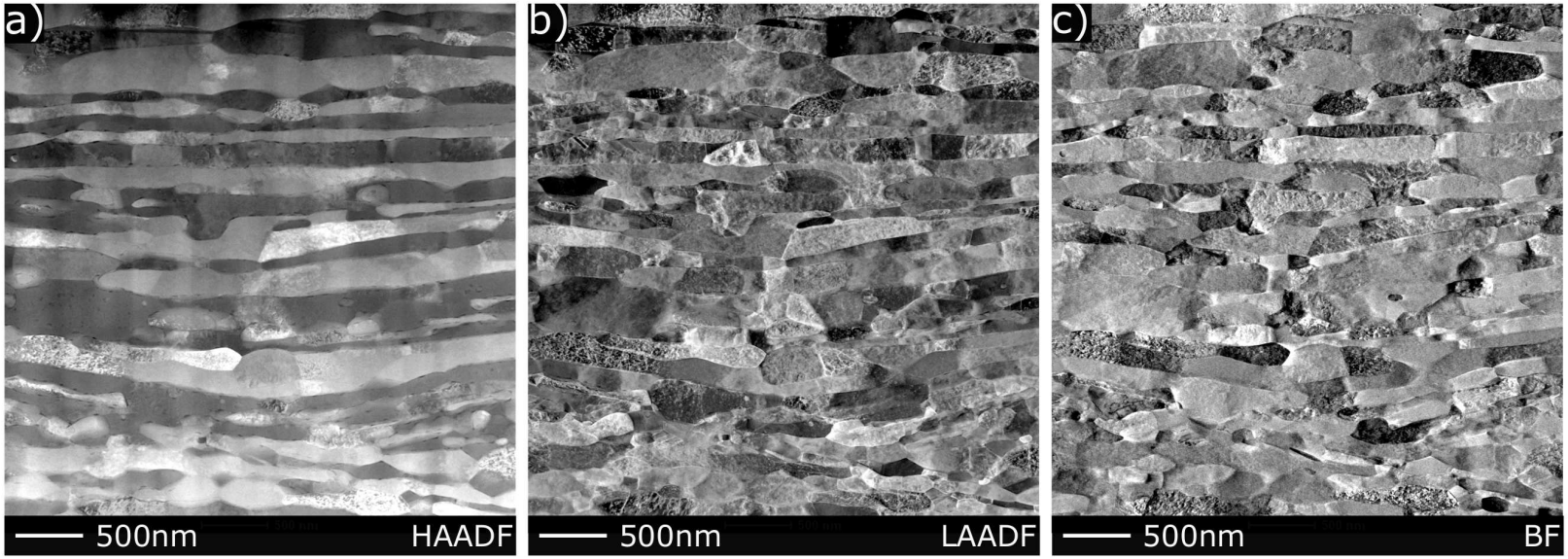


Figure 5.A.4.i: Large Area 1: 65 nm Annealed 15 days at 500 °C

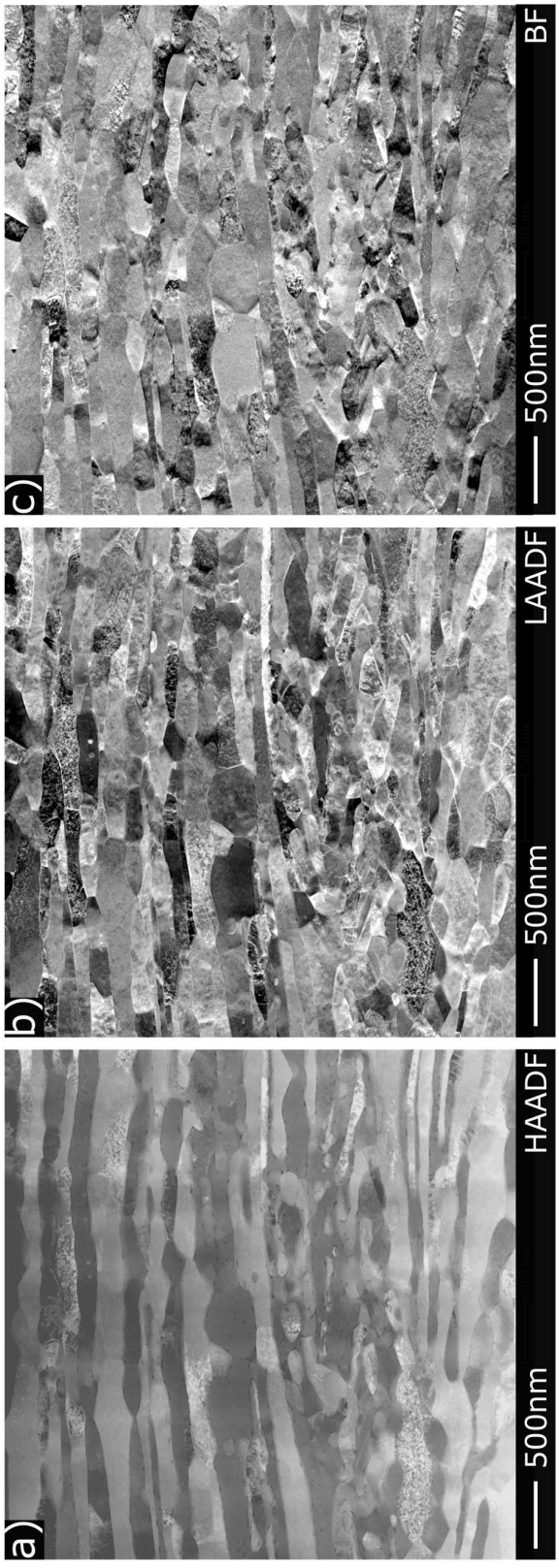


Figure 5.A.4.ii: Large Area 2: 65 *nm* Annealed 15 days at 500 °C]

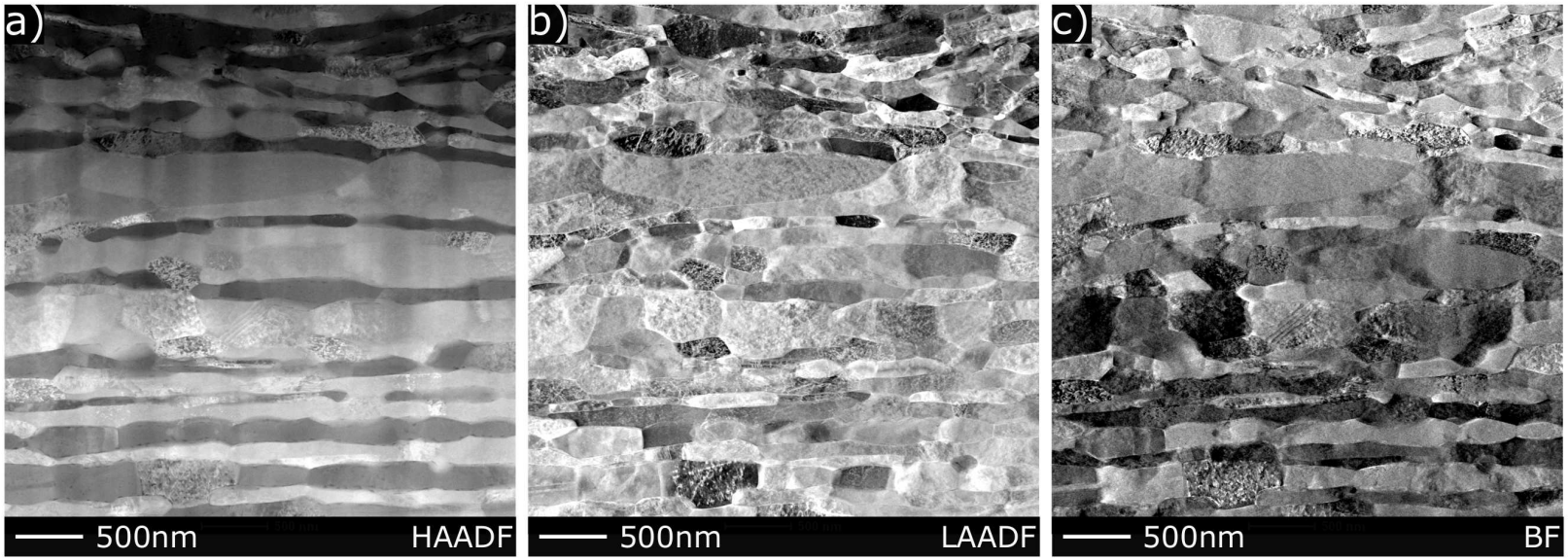


Figure 5.A.4.iii: Large Area 3: 65 nm Annealed 15 days at 500 °C]

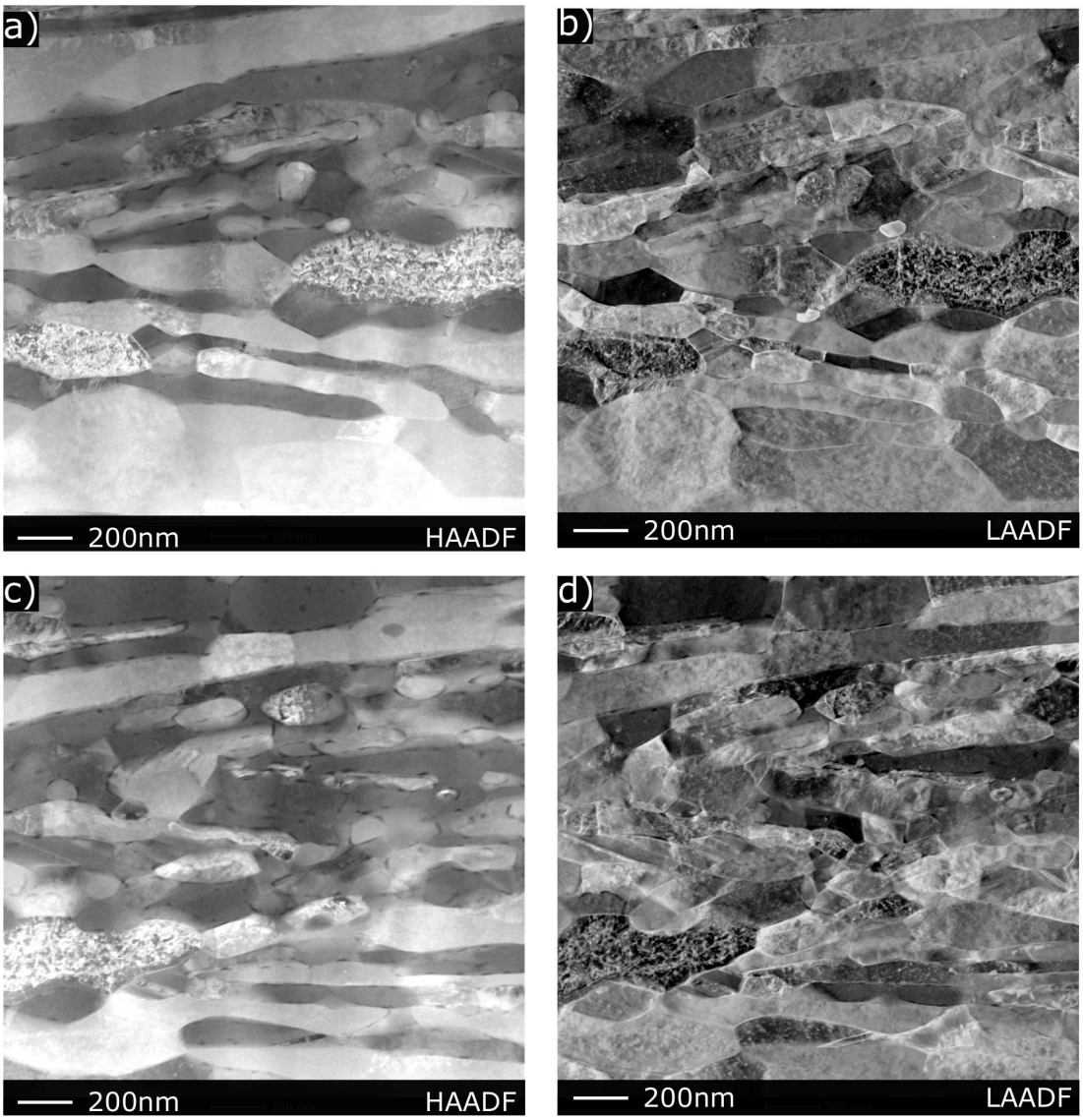


Figure 5.A.4.iv: Instabilities in 65 nm Annealed 15 days at 500 °C]

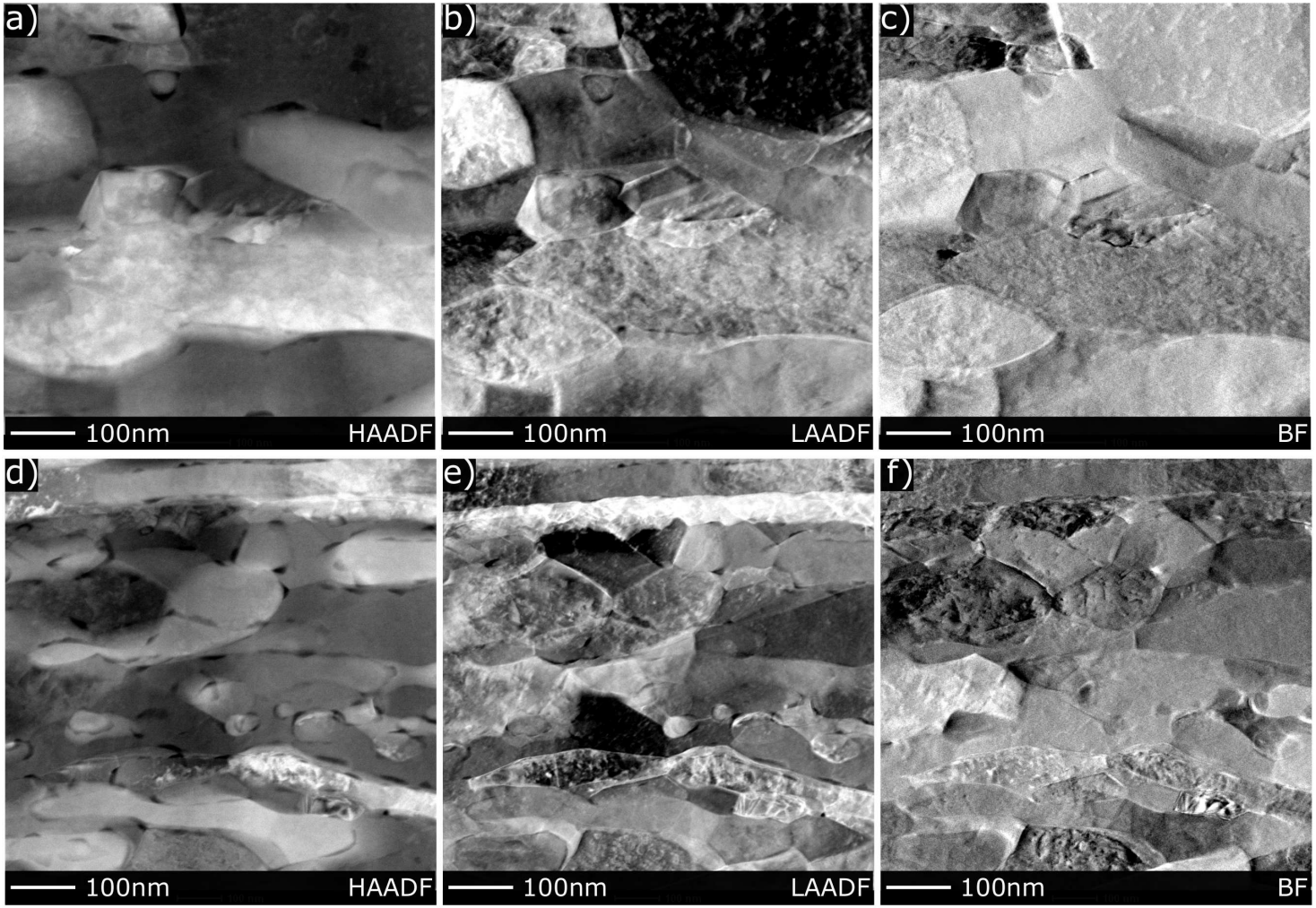


Figure 5.A.4.v: Close-up of 65 *nm* Annealed 15 days at 500 °C

5.A.5 30 Days at 400 °C

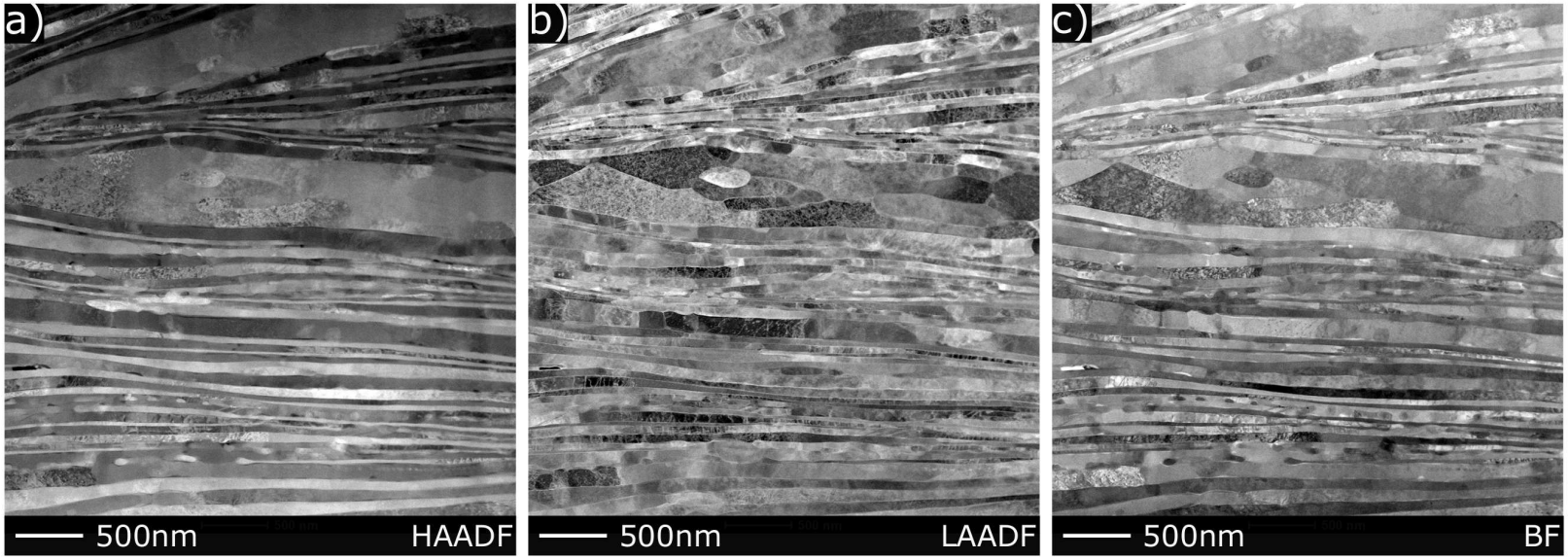


Figure 5.A.5.i: Large Area 1: 65 nm Annealed 30 days at 400 °C

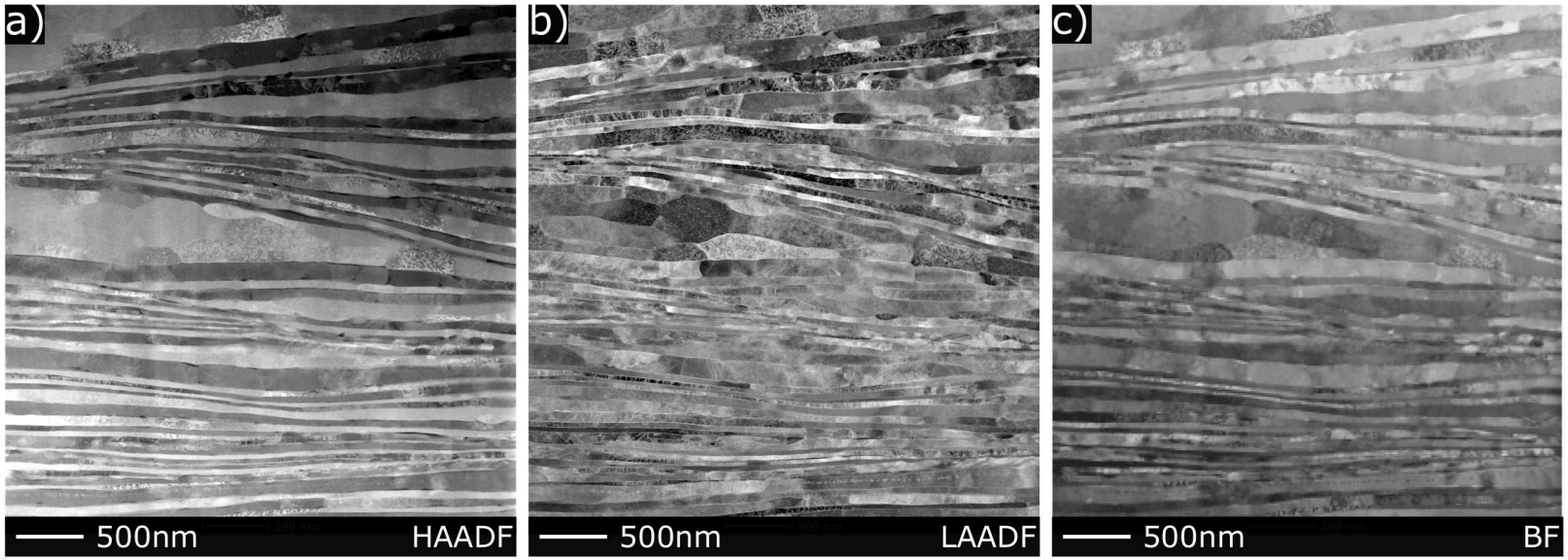


Figure 5.A.5.ii: Large Area 2: 65 nm Annealed 30 days at 400 °C

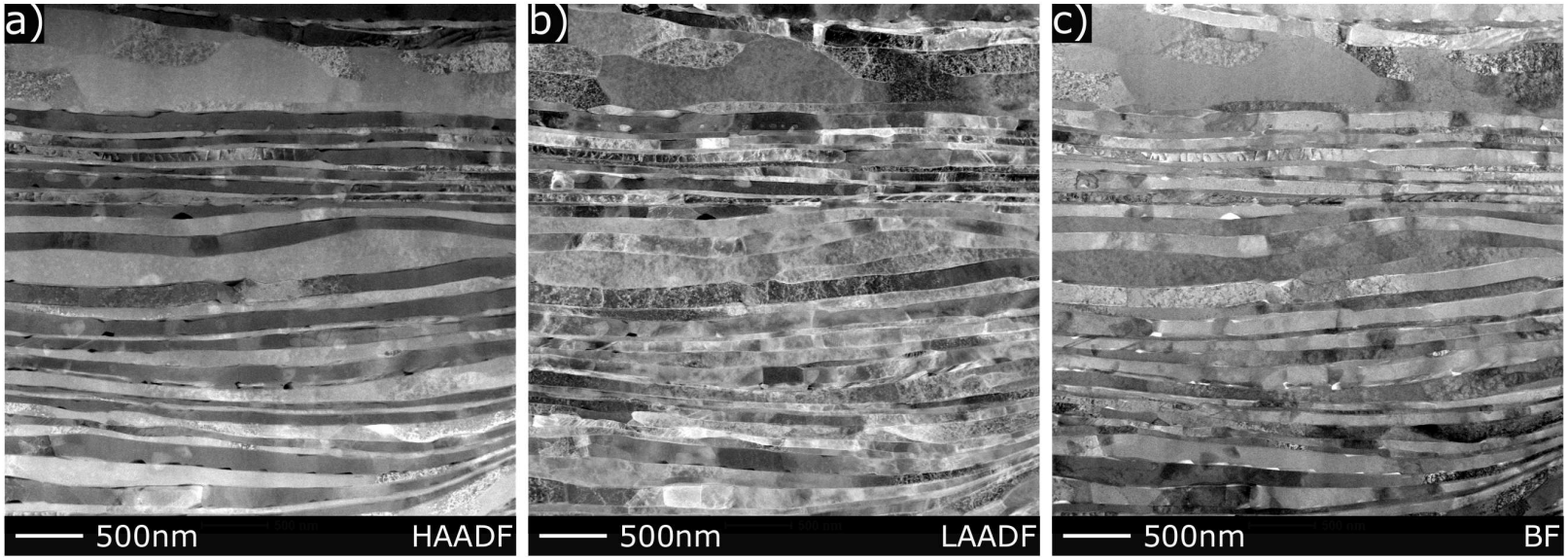


Figure 5.A.5.iii: Large Area 3: 65 nm Annealed 30 days at 400 °C

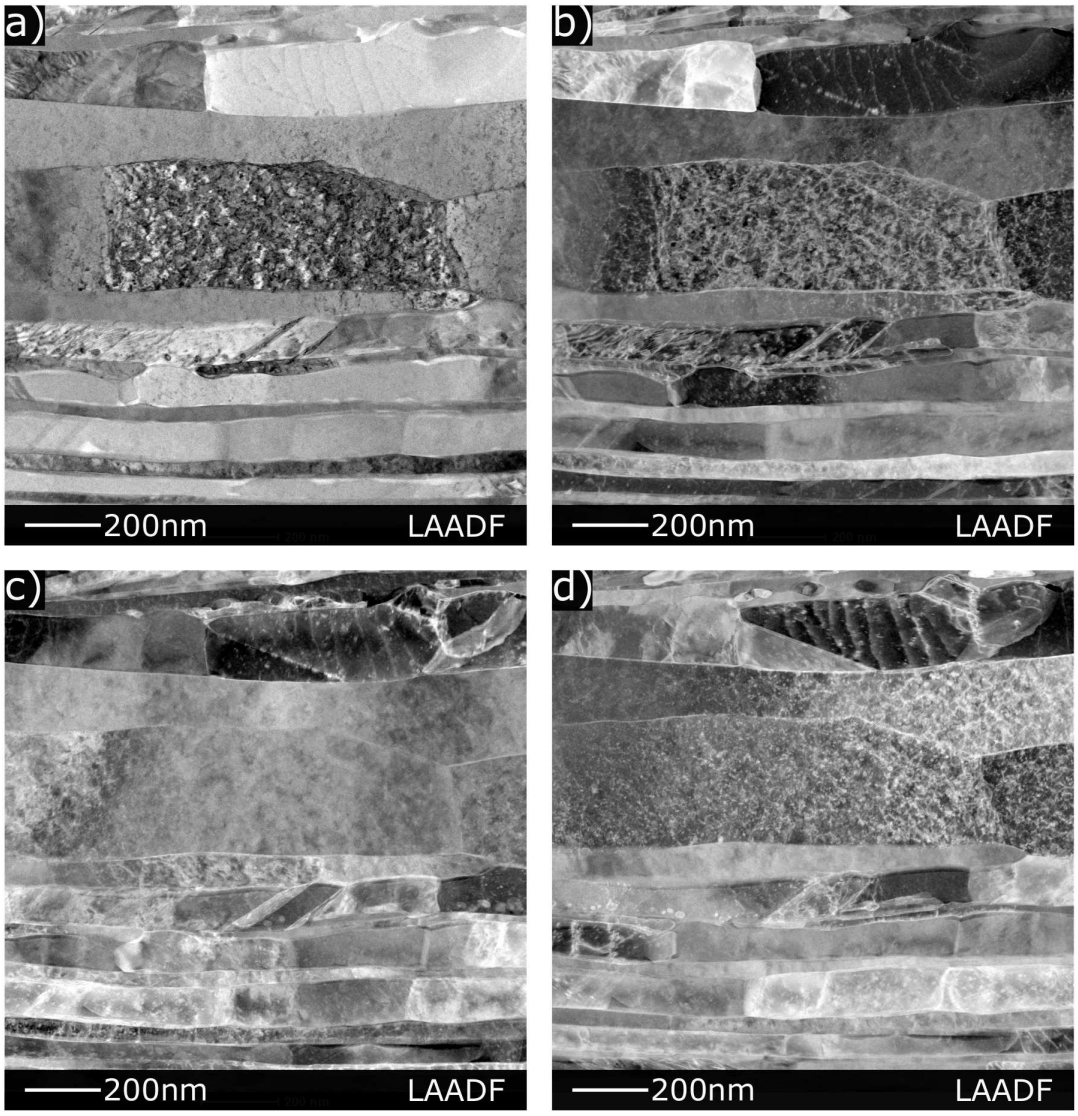


Figure 5.A.5.iv: Tilt series 1: 65 *nm* Annealed 30 days at 400 °C

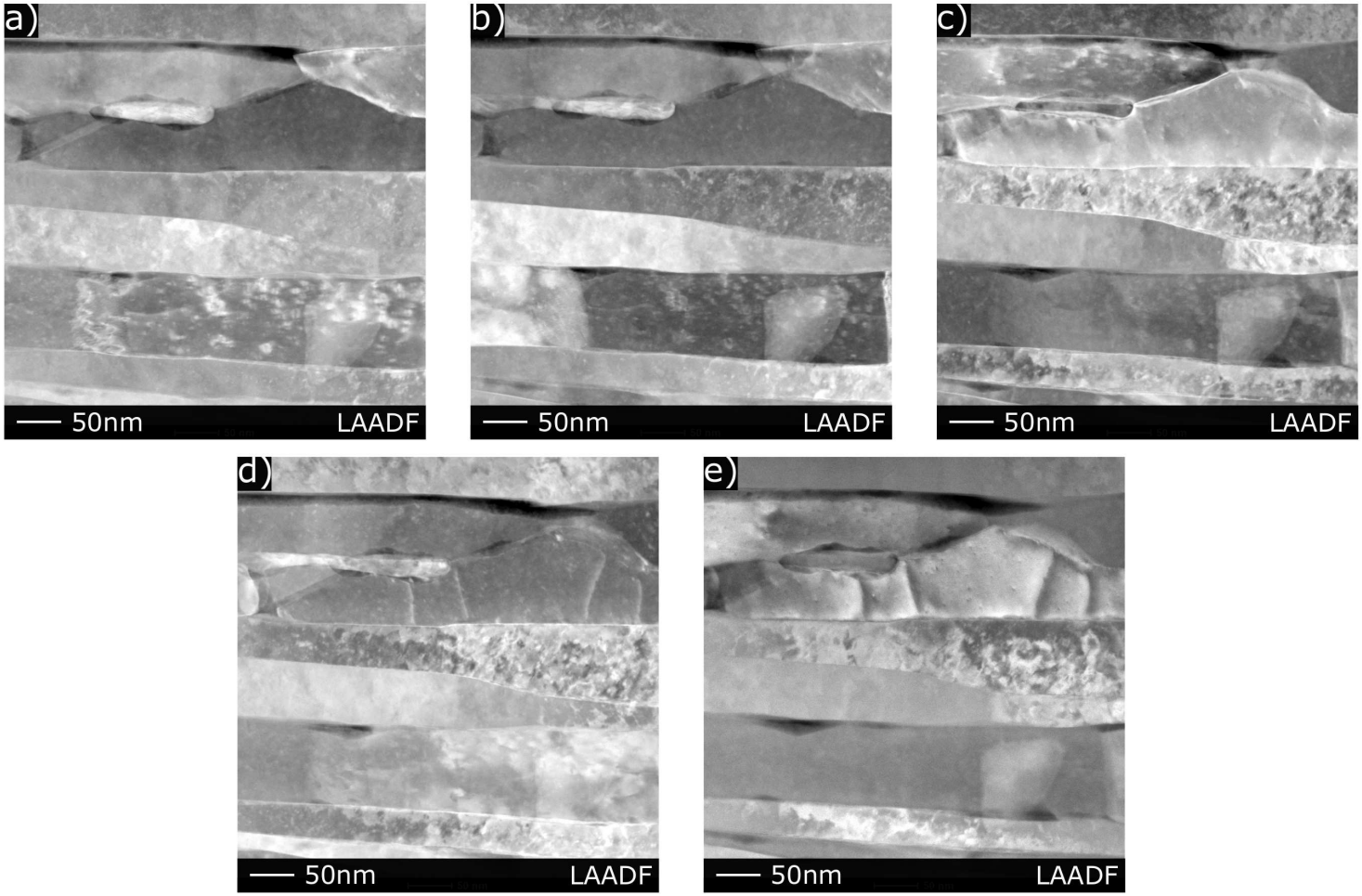


Figure 5.A.5.v: Tilt series 2: 65 nm Annealed 30 days at 400 °C

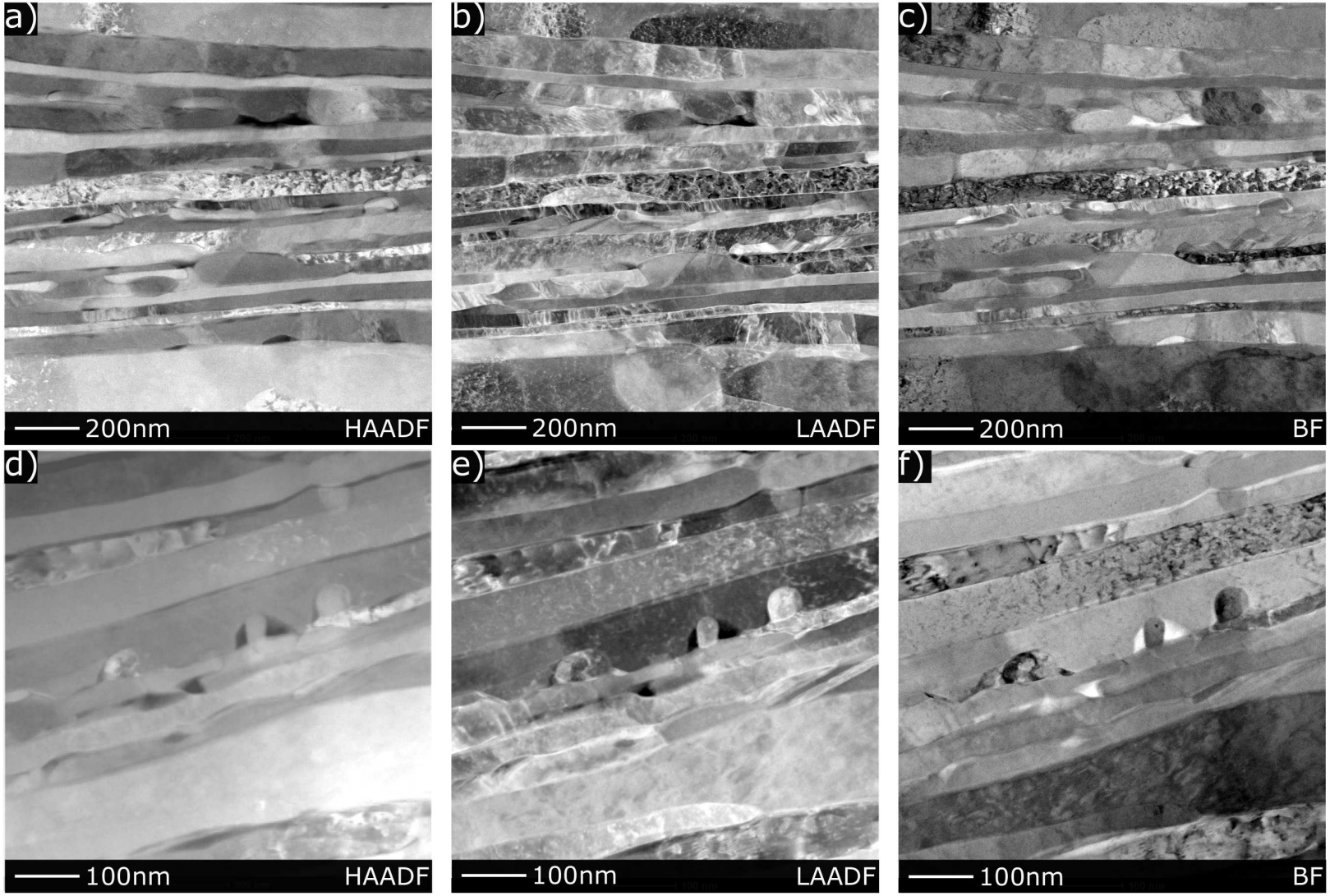


Figure 5.A.5.vi: Close-up of 65 *nm* Annealed 30 days at 400 °C

5.A.6 30 Days at 500 °C

5.B Single Crystal Anneal: 2 h at 800 °C

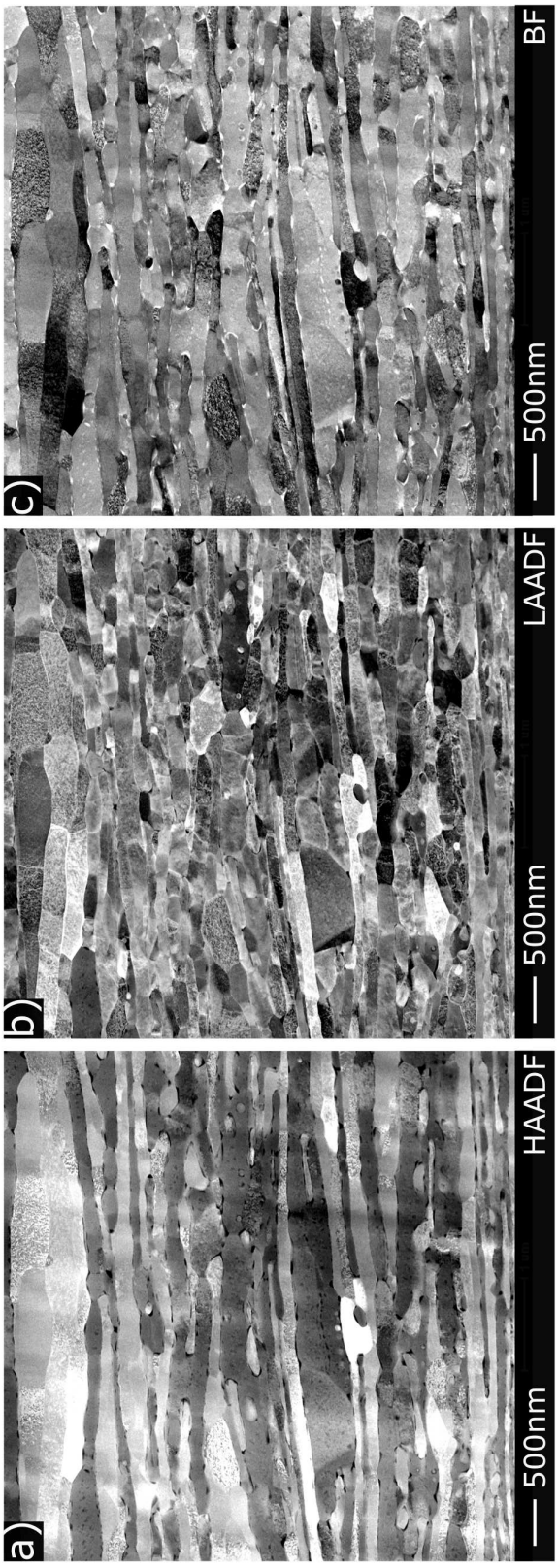


Figure 5.A.6.i: Overview of 65 *nm* Annealed 30 days at 500 °C

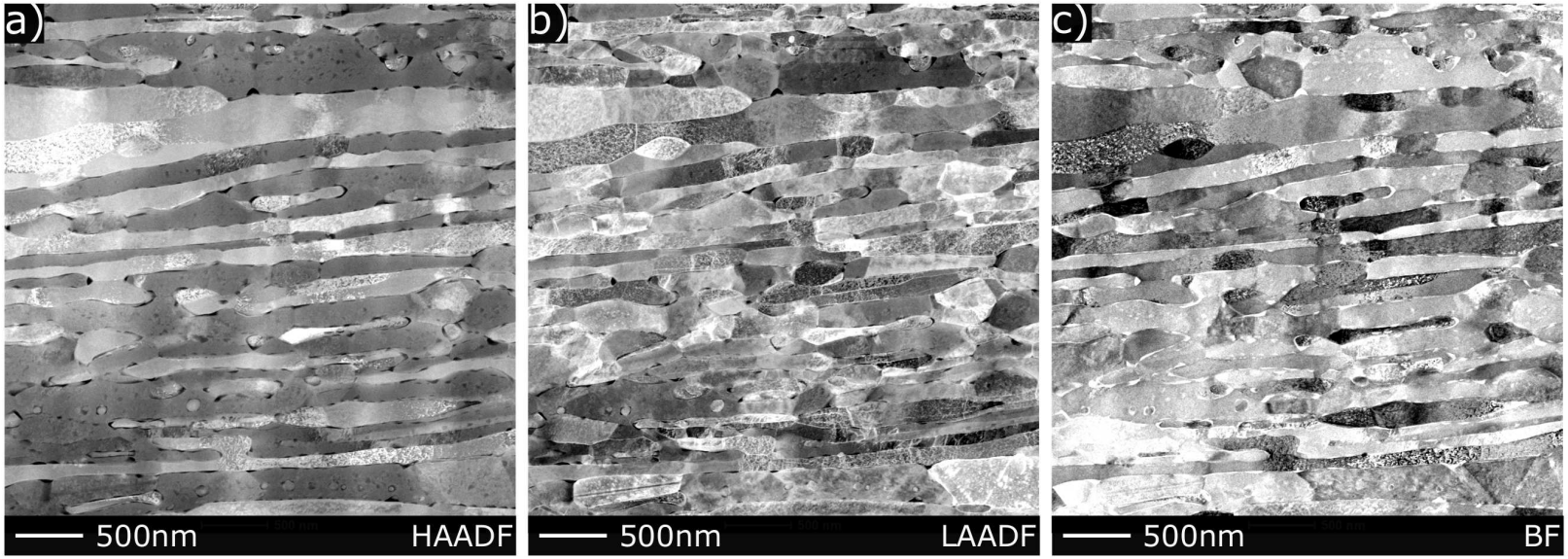


Figure 5.A.6.ii: Large Area 1: 65 nm Annealed 30 days at 500 °C

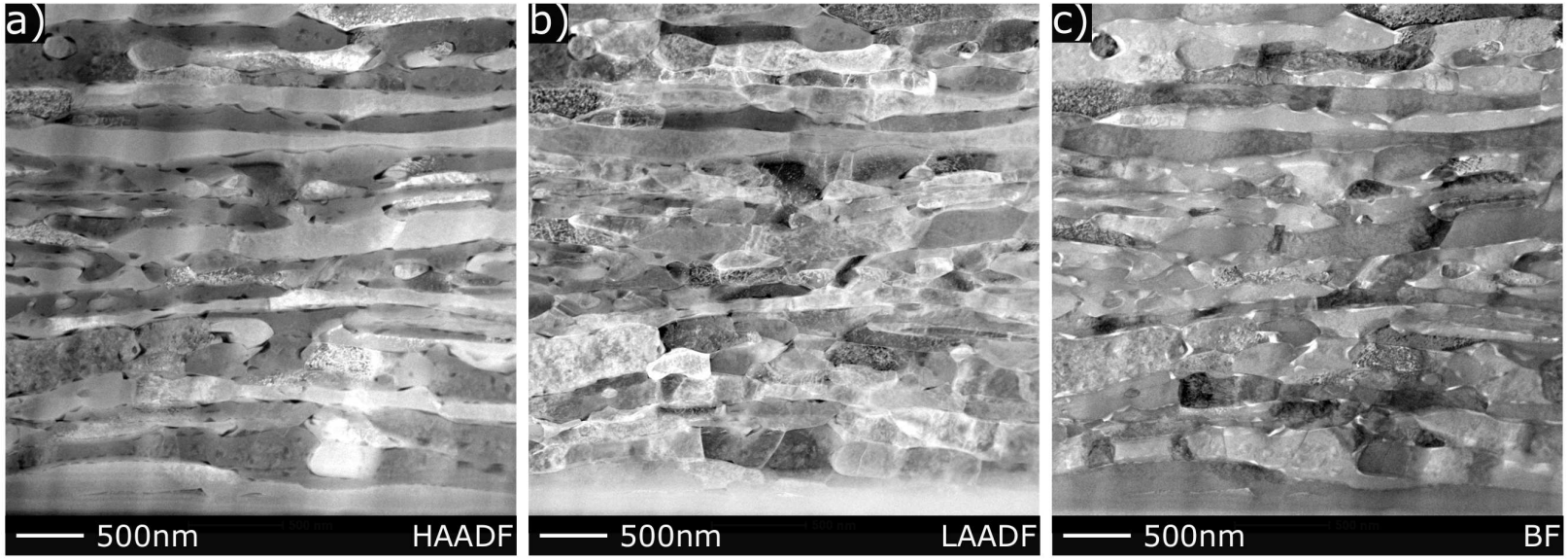


Figure 5.A.6.iii: Large Area 2: 65 nm Annealed 30 days at 500 °C

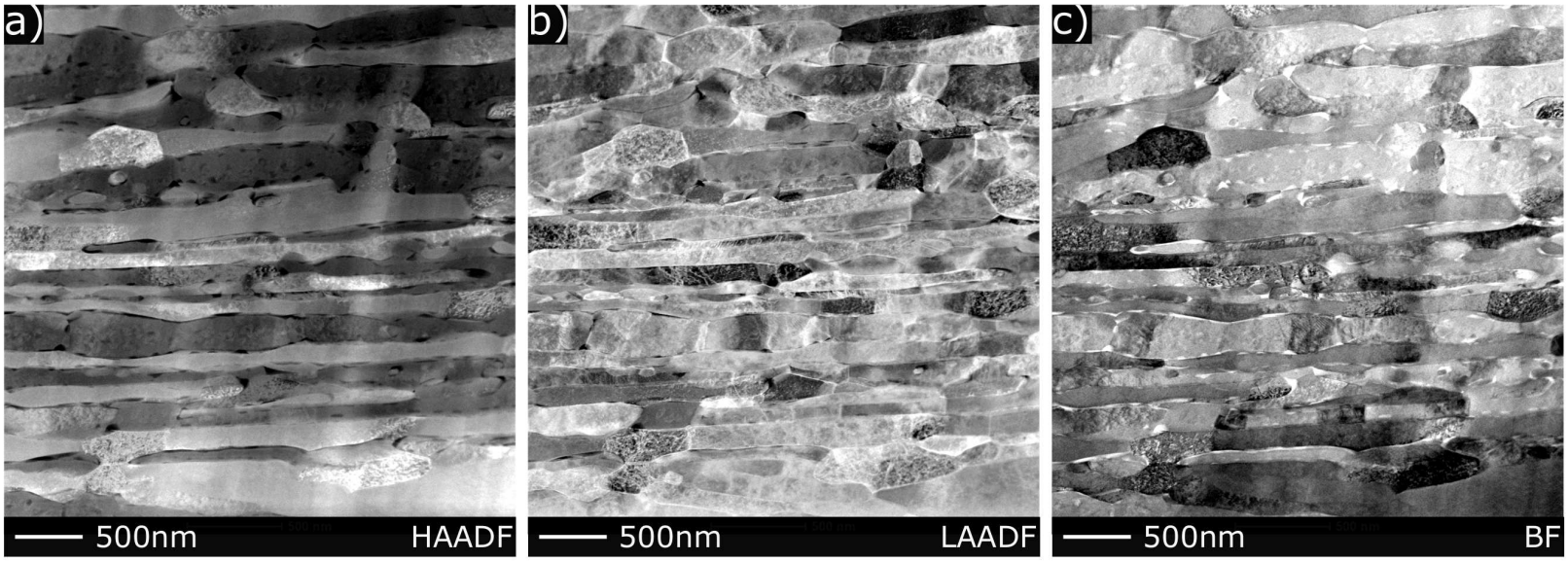


Figure 5.A.6.iv: Large Area 3: 65 *nm* Annealed 30 days at 500 °C

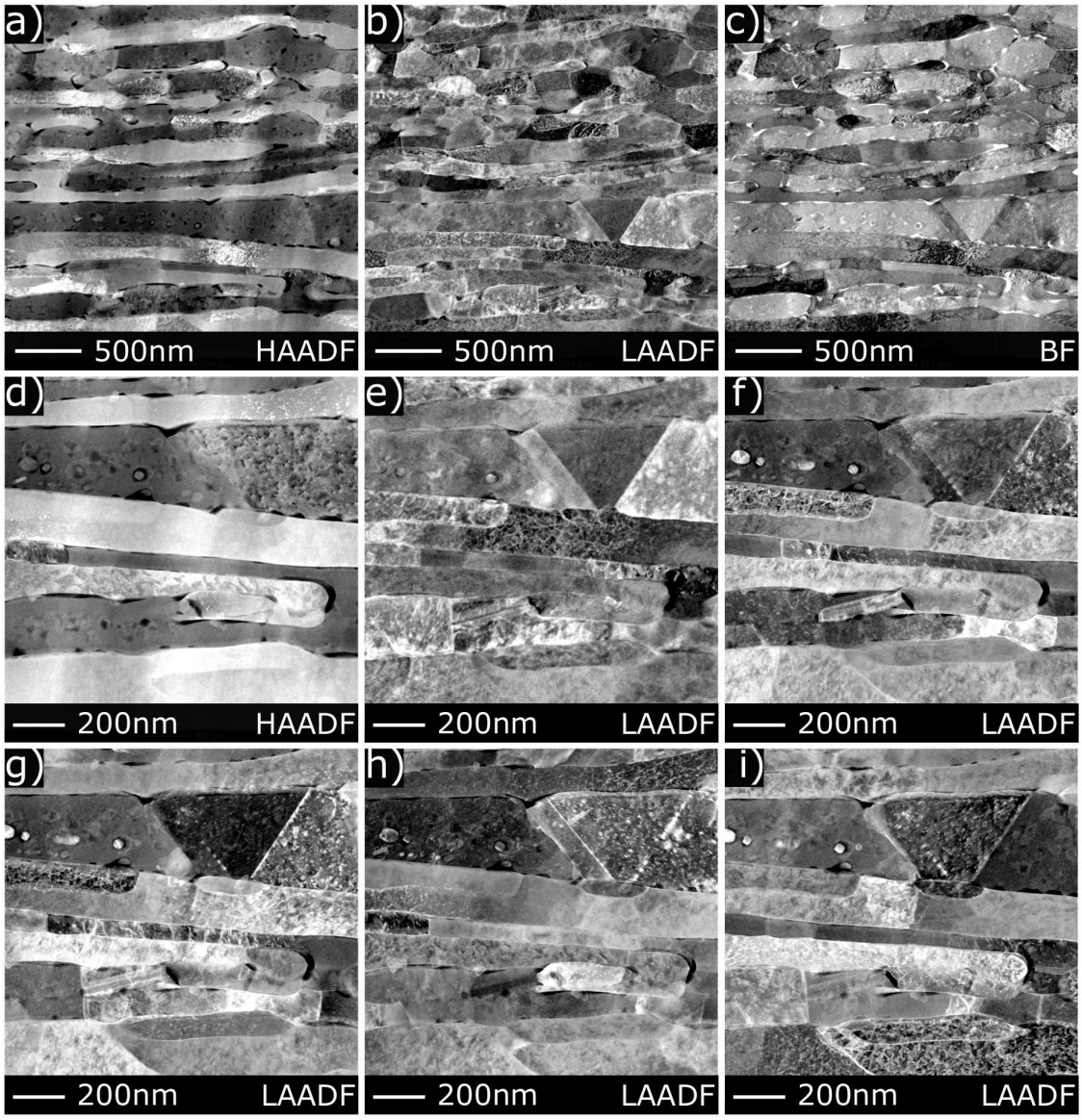


Figure 5.A.6.v: Tilt series 1: 65 nm Annealed 30 days at 500 °C

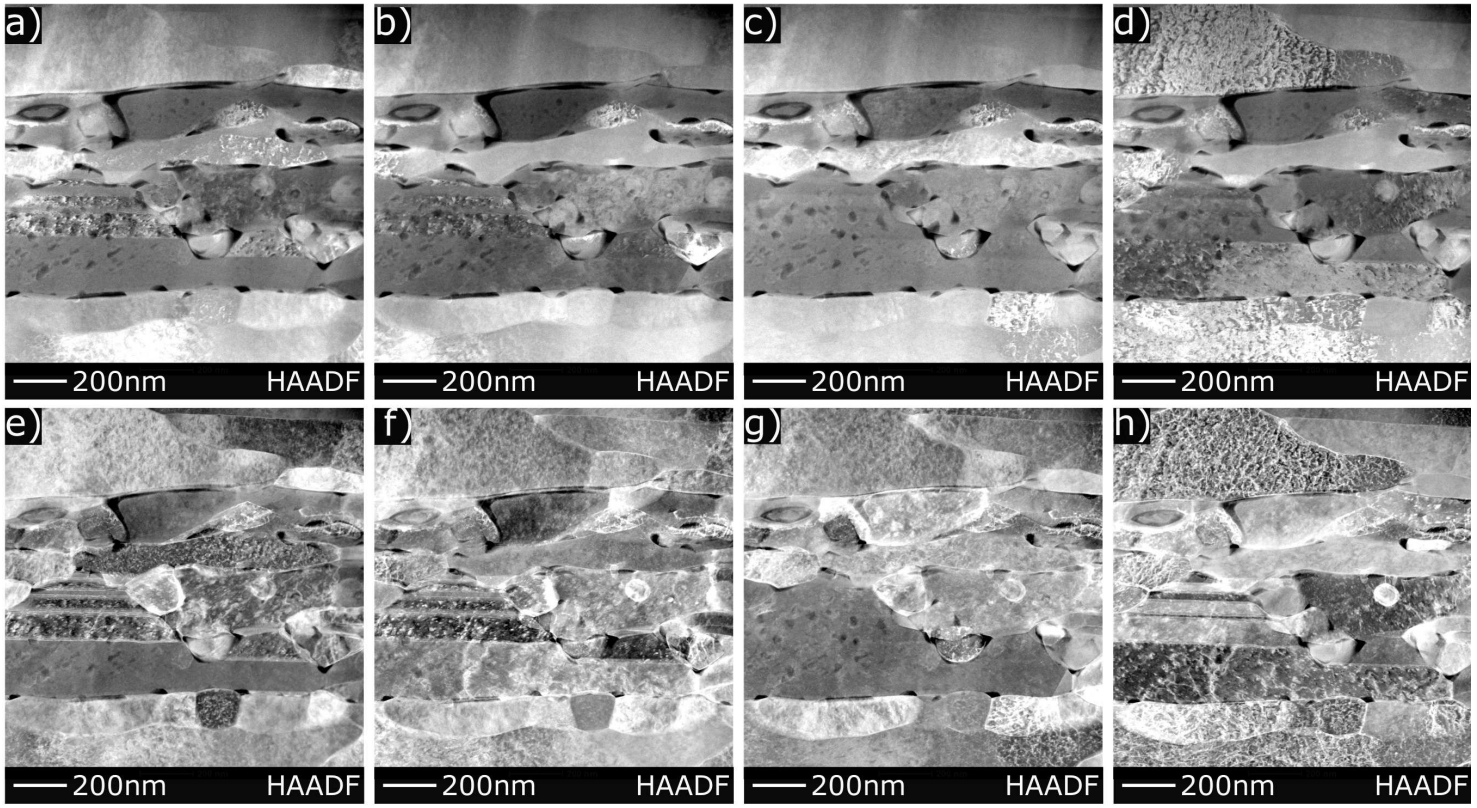


Figure 5.A.6.vi: Tilt series 2: 65 nm Annealed 30 days at 500 °C

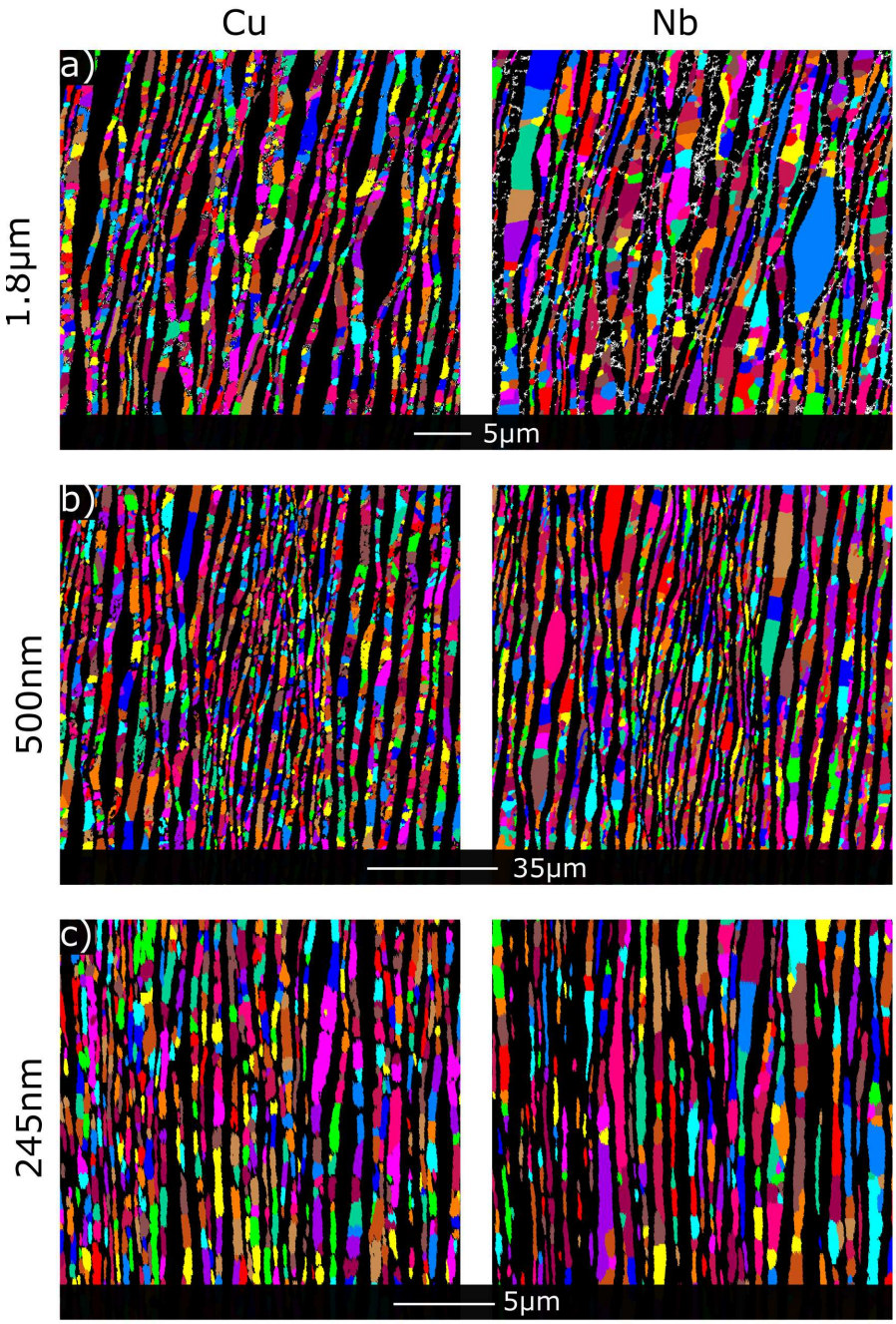


Figure 5.B.i: Large length scale laminates, initially polycrystalline, were heat treated to produce microlaminates with single crystalline layers. Anneal was performed at LANL using vacuum set-up for 30 m at 600 °C, then 2 h at 800 °C. Unique grain maps are shown with Cu and Nb layers separated for distinction. Layer thicknesses annealed are labeled in the figure.

5.C 8 μm EBSD

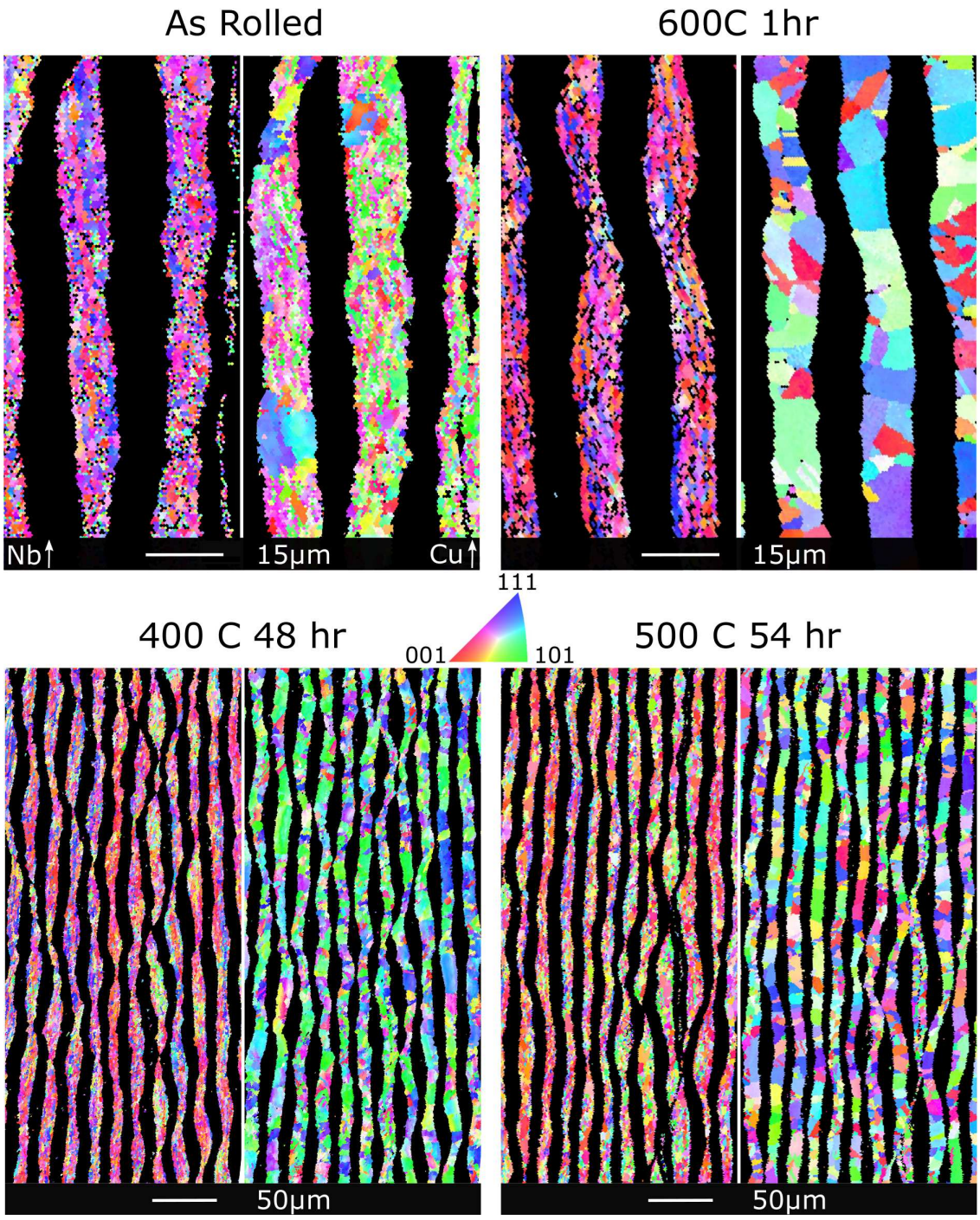


Figure 5.C.i: As rolled grain structure is compared to anneal after: 1 h at 600 °C, 54 h at 500 °C, and 48 h at 400 °C

5.D 28 nm Anneal: 2 Days at 400 °C

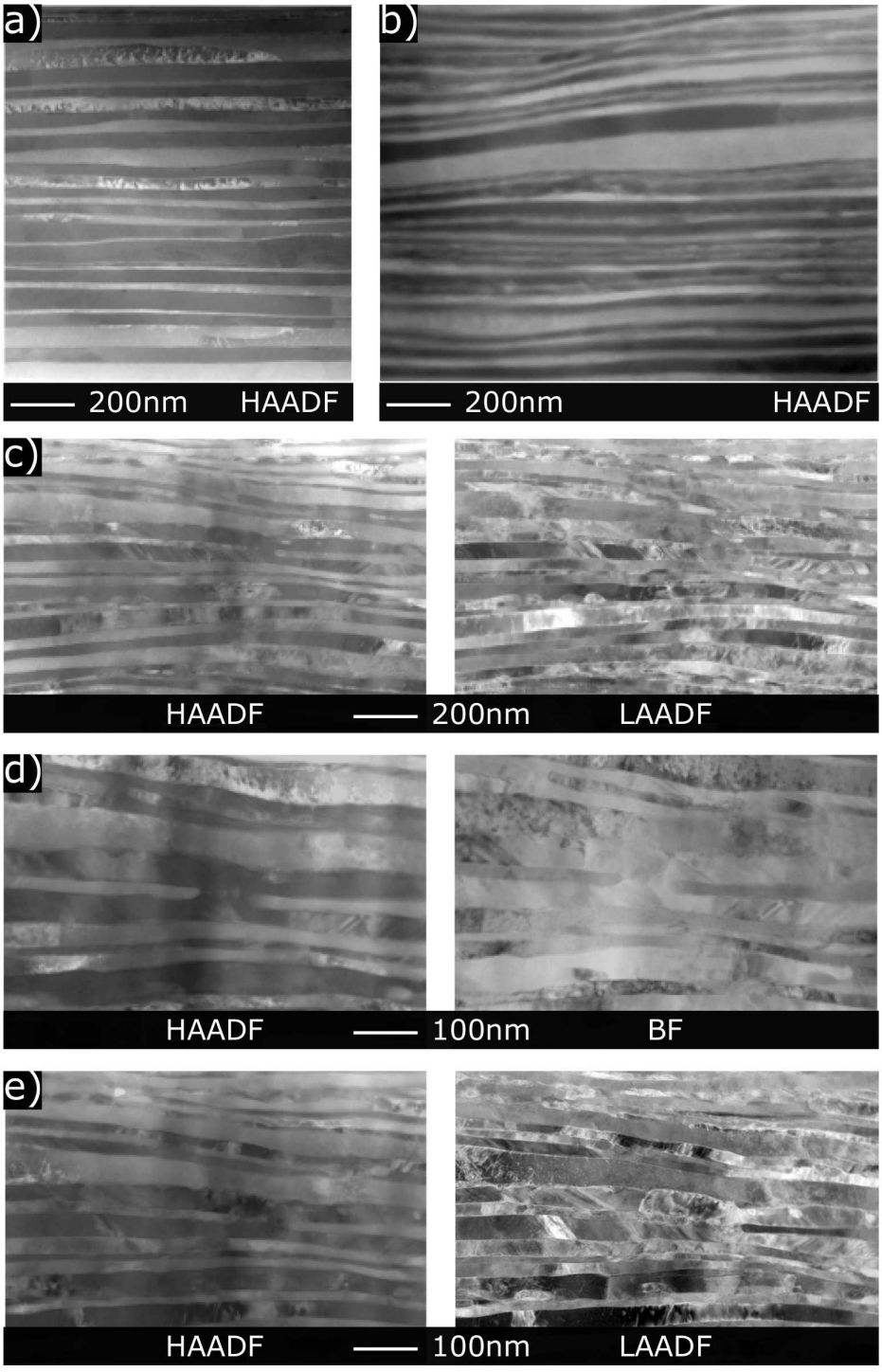


Figure 5.D.i: 28 nm Annealed 2 days at 400 °C

Bibliography

[1] J. Wang and A. Misra. An overview of interface-dominated deformation mechanisms in metallic multilayers. *Current Opinion in Solid State and Materials Science*, 15(1):20–28, Feb 2011.

[2] J. Wang, R.F. Zhang, C.Z. Zhou, I.J. Beyerlein, and a. Misra. Interface dislocation patterns and dislocation nucleation in face-centered-cubic and body-centered-cubic bicrystal interfaces. *International Journal of Plasticity*, 53:40–55, Feb 2014.

[3] C. A. Bronkhorst, J. R. Mayeur, I. J. Beyerlein, H. M. Mourad, B. L. Hansen, N. a. Mara, J. S. Carpenter, R. J. McCabe, and S. D. Sintay. Meso-Scale Modeling the Orientation and Interface Stability of Cu/Nb-Layered Composites by Rolling. *Journal of Materials*, 65(3):431–442, Jan 2013.

[4] R F Zhang, I J Beyerlein, S J Zheng, S H Zhang, A Stukowski, and T C Germann. Manipulating dislocation nucleation and shear resistance of bimetal interfaces by atomic steps. *Acta Materialia*, 113:194–205, 2016.

[5] A Misra, M J Demkowicz, X Zhang, and R G Hoagland. The Radiation Damage Tolerance of Ultra-High Strength Nanolayered Composites. *Journal of Materials*, (September):3–6, 2007.

[6] K. Hattar, M. J. Demkowicz, A. Misra, I. M. Robertson, and R. G. Hoagland. Arrest of He bubble growth in Cu–Nb multilayer nanocomposites. *Scripta Materialia*, 58(7):541–544, Apr 2008.

[7] M J Demkowicz, R G Hoagland, and J P Hirth. Interface Structure and Radiation Damage Resistance in Cu-Nb Multilayer Nanocomposites. *Physical Review Letters*, 100(13):2–5, Apr 2008.

[8] Y. Chen, E. Fu, K. Yu, M. Song, Y. Liu, Y. Wang, H. Wang, and X. Zhang. Enhanced radiation tolerance in immiscible Cu/Fe multilayers with coherent and incoherent layer interfaces. *Journal of Materials Research*, pages 1–10, Feb 2015.

[9] Jaime Ortún-palacios, Antonio Mario Locci, Sarah Fadda, Francesco Delogu, and Santiago Cuesta-lópez. Role of Interface in Multilayered Composites under Irradiation : A Mathematical Investigation. 2017, 2017.

[10] W Z Han, A Misra, N A Mara, T C Germann, J K Baldwin, and S N Luo. Role of interfaces in shock-induced plasticity in Cu / Nb nanolaminates. *Philosophical Magazine*, 91(32):4172–4185, 2011.

[11] R.F. Zhang, T.C. Germann, X.-Y. Liu, J. Wang, and I.J. Beyerlein. Layer size effect on the shock compression behavior of fcc–bcc nanolaminates. *Acta Materialia*, 79:74–83, Oct 2014.

[12] J S Carpenter, S J Zheng, R F Zhang, S C Vogel, I J Beyerlein, and N A Mara. Thermal stability of Cu – Nb nanolamellar composites fabricated via accumulative roll bonding. *Philosophical Magazine*, 93(7):718–735, 2013.

[13] A Misra and R G Hoagland. Effects of elevated temperature annealing on the structure and hardness of copper/niobium nanolayered films. *Journal of Materials Research*, 20(8):2046–2054, Apr 2005.

[14] Nathan A. Mara and Irene J. Beyerlein. Interface-dominant multilayers fabricated by severe plastic deformation: Stability under extreme conditions. *Current Opinion in Solid State and Materials Science*, pages 1–12, Apr 2015.

[15] L. F. Zeng, R. Gao, Q. F. Fang, X. P. Wang, Z. M. Xie, S. Miao, T. Hao, and T. Zhang. High strength and thermal stability of bulk Cu/Ta nanolamellar multilayers fabricated by cross accumulative roll bonding. *Acta Materialia*, 110:341–351, 2016.

[16] J. T. Avallone, T. J. Nizolek, B. B. Bales, and T. M. Pollock. Creep Resistance of Bulk Copper-Niobium Composites: an Inverse Effect of Multilayer Length Scale. *Acta Materialia*, 2018.

[17] T.J. Nizolek, I.J. Beyerlein, N.A. Mara, J.T. Avallone, and T.M. Pollock. Tensile behavior and flow stress anisotropy of accumulative roll bonded Cu-Nb nanolaminates. *Applied Physics Letters*, 051903(108), 2016.

[18] S. Subedi, I.J. Beyerlein, R. LeSar, and A.D. Rollett. Strength of nanoscale metallic multilayers. *Scripta Materialia*, 145:132–136, 2018.

[19] A. Misra, R. G. Hoagland, and H. Kung. Thermal stability of self-supported nanolayered Cu/Nb films. *Philosophical Magazine*, 84(10):1021–1028, Apr 2004.

[20] W.Z. Han, A. Misra, N.A. Mara, T.C. Germann, J.K. Baldwin, T. Shimada, and S.N. Luo. Role of interfaces in shock-induced plasticity in Cu/Nb nanolaminates. *Philosophical Magazine*, 91(32):4172–4185, Nov 2011.

[21] R. Odette. 289J: Irradiative Damage Lecture, 2012.

[22] N.A. Mara and I.J. Beyerlein. Review: effect of bimetal interface structure on the mechanical behavior of Cu–Nb fcc–bcc nanolayered composites. *Journal of Materials Science*, 49(19):6497–6516, Jul 2014.

[23] S. Shao, A. Misra, H. Huang, and J. Wang. Micro-scale modeling of interface-dominated mechanical behavior. *J. Mater. Sci.*, 2017.

[24] I. J. Beyerlein, N. A. Mara, J. S. Carpenter, T. Nizolek, W. M. Mook, T. A. Wynn, R. J. McCabe, J. R. Mayeur, K. Kang, S. J. Zheng, J. Wang, and T. M. Pollock. Interface-driven microstructure development and ultra high strength of bulk nanostructured Cu/Nb multilayers fabricated by severe plastic deformation. *Journal of Materials Research*, 28(13), 2013.

[25] M. J. Demkowicz, R. G. Hoagland, B. P. Uberuaga, and A. Misra. Influence of interface sink strength on the reduction of radiation-induced defect concentrations and fluxes in materials with large interface area per unit volume. *Phiscal Review B*, 84, 2011.

[26] A Misra, J P Hirth, and R G Hoagland. Length-scale-dependent deformation mechanisms in incoherent metallic multilayered composites. *Acta Materialia*, 53(18):4817–4824, Oct 2005.

[27] R F Zhang, J Wang, I J Beyerlein, A Misra, and T C Germann. Atomic-scale study of nucleation of dislocations from fcc–bcc interfaces. *Acta Materialia*, 60(6-7):2855–2865, Apr 2012.

[28] I J Beyerlein, M J Demkowicz, A. Misra, and B P Uberuaga. Defect-Interface Interactions. *Progress in Materials Science*, (January), Feb 2015.

[29] S. Zheng, J. S. Carpenter, R. J. McCabe, I. J. Beyerlein, and N. A. Mara. Engineering Interface Structures and Thermal Stabilities via SPD Processing in Bulk Nanostructured Metals. *Scientific Reports*, 4:4226, Jan 2014.

[30] F. C. Nix and D. MacNair. The thermal expansion of pure metals: Copper, gold, aluminum, nickel, and iron. *Physical Review*, 60(8):597–605, 1941.

[31] R. K. Bollinger, B. D. White, J. J. Neumeier, H. R.Z. Sandim, Y. Suzuki, C. A.M. Dos Santos, R. Avci, A. Migliori, and J. B. Betts. Observation of a martensitic structural distortion in V, Nb, and Ta. *Physical Review Letters*, 107(7):1–4, 2011.

[32] D. J. Chakrabarti and D. E. Laughlin. The Cu-Nb (Copper-Niobium) system. *Journal of Phase Equilibria*, 2(4):455–460, 1982.

[33] R.J. McCabe, J.S. Carpenter, S. Vogel, N.A. Mara, and I.J. Beyerlein. Recrystallization and Grain Growth in Accumulative Roll-Bonded Metal Composites. *Journal of Materials*, 67(12):2810–2819, 2015.

[34] R. F. Zhang, J. Wang, I. J. Beyerlein, and T. C. Germann. Dislocation nucleation mechanisms from fcc/bcc incoherent interfaces. *Scripta Materialia*, 65(11):1022–1025, Dec 2011.

[35] J. Wang, A. Misra, R. G. Hoagland, and J. P. Hirth. Slip transmission across fcc/bcc interfaces with varying interface shear strengths. *Acta Materialia*, 60(4):1503–1513, Feb 2012.

[36] W. Z. Han, J. S. Carpenter, J. Wang, I. J. Beyerlein, and N. a. Mara. Atomic-level study of twin nucleation from face-centered-cubic/body-centered-cubic interfaces in nanolamellar composites. *Applied Physics Letters*, 100(1):011911, 2012.

[37] Nan Li, Jian Wang, Amit Misra, and Jian Yu Huang. Direct Observations of Confined Layer Slip in Cu / Nb Multilayers. 18:1155–1162, 2012.

[38] J. Wang and a. Misra. Strain hardening in nanolayered thin films. *Current Opinion in Solid State and Materials Science*, 18(1):19–28, Feb 2014.

[39] Sixie Huang, Irene J Beyerlein, and Caizhi Zhou. Nanograin size effects on the strength of biphase nanolayered composites. 2017.

[40] W. Han, M.J. Demkowicz, N.A. Mara, E. Fu, S. Sinha, A.D. Rollett, Y. Wang, J.S. Carpenter, I.J. Beyerlein, and A. Misra. Design of radiation tolerant materials via interface engineering. *Advanced materials (Deerfield Beach, Fla.)*, 25(48):6975–9, Dec 2013.

[41] M. J. Demkowicz and L. Thilly. Structure, shear resistance and interaction with point defects of interfaces in Cu–Nb nanocomposites synthesized by severe plastic deformation. *Acta Materialia*, 59(20):7744–7756, Dec 2011.

[42] R. F. Zhang, T. C. Germann, J. Wang, X. Liu, and I. J. Beyerlein. Role of interface structure on the plastic response of Cu / Nb nanolaminates under shock compression : Non-equilibrium molecular dynamics simulations. *Scripta Materialia*, 68(2):114–117, 2013.

[43] I. J. Beyerlein, N. a. Mara, J. Wang, J. S. Carpenter, S. J. Zheng, W. Z. Han, R. F. Zhang, K. Kang, T. Nizolek, and T. M. Pollock. Structure–Property–Functionality of Bimetal Interfaces. *Jom*, 64(10):1192–1207, Sep 2012.

[44] T. Nizolek, N.A. Mara, I.J. Beyerlein, J.T. Avallone, J.E. Scott, and T.M. Pollock. Processing and Deformation Behavior of Bulk Cu–Nb Nanolaminates. *Metallography, Microstructure, and Analysis*, 3(6), 2014.

[45] J. Steigman, W. Shockley, and F. C. Nix. The Self-Diffusion of Copper. *Physical Review*, 56, 1939.

[46] D. Ablitzee. Diffusion of niobium, iron, cobalt, nickel and copper in niobium. *Philosophical Magazine*, 35(5):1239–1256, 1977.

[47] H.J. Frost and M. F. Ashby. *Deformation mechanism maps: the plasticity and creep of metals and ceramics*. Pergamon Press, Oxford, UK, 1982.

[48] A.C. Lewis, D. Van Heerden, C. Eberl, K.J. Hemker, and T.P. Weihs. Creep deformation mechanisms in fine-grained niobium. *Acta Materialia*, 56(13):3044–3052, Aug 2008.

[49] J. Horvath, R. Birringer, and H. Gleiter. Diffusion in nanocrystalline material. *Solid State Communications*, 62(5):319–322, 1987.

[50] H. Ludtke Knoedler, G. E. Lucas, and C. G. Levi. Morphological stability of copper-silver multilayer thin films at elevated temperatures. *Metallurgical and Materials Transactions A*, 34(5):1043–1054, May 2003.

[51] M. Meyers and K. Chawla. *Mechanical Behavior of Materials*. 2009.

[52] L. Li, K. Nagai, and F. Yin. Progress in cold roll bonding of metals. *Science and Technology of Advanced Materials*, 9(2):023001, Apr 2008.

[53] T. Nizolek, N. A. Mara, I. J. Beyerlein, J. T. Avallone, J. E. Scott, and T. M. Pollock. Processing and Deformation Behavior of Bulk Cu-Nb Nanolaminates. *Metallography, Microstructure, and Analysis*, 3(6):470–476, 2014.

[54] J Y Zhang, J Li, X Q Liang, G Liu, and J Sun. Achieving optimum mechanical performance in metallic nanolayered Cu/X (X = Zr, Cr) micropillars. *Scientific reports*, 4:4205, 2014.

[55] N. A. Mara, A. Misra, R. G. Hoagland, A. V. Sergueeva, T. Tamayo, P. Dickerson, and A. K. Mukherjee. High-temperature mechanical behavior/microstructure correlation of Cu/Nb nanoscale multilayers. *Materials Science and Engineering: A*, 493(1-2):274–282, Oct 2008.

[56] N. A. Mara, T. Tamayo, A. V. Sergueeva, X. Zhang, A. Misra, and A. K. Mukherjee. The effects of decreasing layer thickness on the high temperature mechanical behavior of Cu/Nb nanoscale multilayers. *Thin Solid Films*, 515(6):3241–3245, Feb 2007.

[57] T. J. Nizolek. *Plastic Anisotropy and Kink Band Formation in Fine Grained Copper-Niobium Multilayers Produced by Accumulative Roll Bonding*. Phd, University of California, Santa Barbara, 2016.

[58] S. C. V. Lim and A. D. Rollett. Length scale effects on recrystallization and texture evolution in Cu layers of a roll-bonded Cu–Nb composite. *Materials Science and Engineering: A*, 520(1-2):189–196, Sep 2009.

[59] J S Carpenter, R J McCabe, I J Beyerlein, T a. Wynn, and N a. Mara. A wedge-mounting technique for nanoscale electron backscatter diffraction. *Journal of Applied Physics*, 113(9):94304, 2013.

[60] S.-B. Lee, J. E. LeDonne, S. C. V. Lim, I. J. Beyerlein, and A. D. Rollett. The heterophase interface character distribution of physical vapor-deposited and accumulative roll-bonded Cu–Nb multilayer composites. *Acta Materialia*, 60(4):1747–1761, Feb 2012.

[61] U. F. Kocks, C. N. Tome, and H. R. Wenk. *Texture and anisotropy: preferred orientations in polycrystals and their effect on materials properties*. 2000.

[62] J.S. Carpenter, R.J. McCabe, S.J. Zheng, T.A. Wynn, N.A. Mara, and I.J. Beyerlein. Processing parameter influence on texture and microstructural evolution in cu-nb multilayer composites fabricated via accumulative roll bonding. *Metallurgical and Materials Transactions A*, 45(4):2192–2208, 2014.

[63] Zheng, I J Beyerlein, J Wang, J S Carpenter, W S Han, and N A Mara. Deformation twinning mechanisms from bimetal interfaces as revealed by in situ straining in the TEM. *Acta Materialia- Incomplete Article, in Review...*, 60(16):5858–5866, 2012.

[64] N. A. Mara, D. Bhattacharyya, J. P. Hirth, P. Dickerson, and A. Misra. Mechanism for shear banding in nanolayered composites. *Applied Physics Letters*, 97(2):021909, 2010.

[65] J S Carpenter, S C Vogel, J E LeDonne, D Hammon, I J Beyerlein, and N A Mara. Bulk texture evolution of Cu–Nb nanolamellar composites during accumulative roll bonding. *Acta Materialia*, 60:1576–1586, 2012.

[66] A.C. Lewis, D. Josell, and T.P. Weihs. Stability in thin film multilayers and microlaminates: the role of free energy, structure, and orientation at interfaces and grain boundaries. *Scripta Materialia*, 48(8):1079–1085, Apr 2003.

[67] I. J. Beyerlein, J. Wang, K. Kang, S. J. Zheng, and N. A. Mara. Twinnability of bimetal interfaces in nanostructured composites. *Materials Research Letters*, 1(2):89–95, 2013.

[68] T. J. Nizolek, M. R. Begley, R. J. McCabe, J. T. Avallone, N. A. Mara, I. J. Beyerlein, and T. M. Pollock. Strain fields induced by kink band propagation in Cu-Nb nanolaminate composites. *Acta Materialia*, 133:303–315, 2017.

[69] A. Misra and H. Kung. Deformation Behavior of Nanostructured Metallic Multilayers **. *Advanced Engineering Materials*, 3(4):217–222, 2001.

[70] S. Zheng, I.J. Beyerlein, J.S. Carpenter, K. Kang, J. Wang, W. Han, and N.A. Mara. High-strength and thermally stable bulk nanolayered composites due to twin-induced interfaces. *Nature communications*, 4:1696, Jan 2013.

[71] M A. Monclus, S J Zheng, J R Mayeur, I J Beyerlein, N A. Mara, T Polcar, J Llorca, and J M Molina-Aldareguia. Optimum high temperature strength of two-dimensional nanocomposites. *APL Materials*, 1(5):52103, 2013.

[72] Hull and Bacon. Introduction to Dislocations.

[73] N. A. Mara, A. Sergueeva, A. Misra, and A.K. Mukherjee. Structure and high-temperature mechanical behavior relationship in nano-scaled multilayered materials. *Scripta Materialia*, 50(6):803–806, Mar 2004.

[74] T.J. Nizolek, N.A. Mara, I.J. Beyerlein, J.T. Avallone, J. Scott, and T. M. Pollock. High Strength Bulk Metallic Nanolaminates. *Advanced Materials and Processes*, 173(2):18–21, 2015.

[75] D. Amram, L. Klinger, N. Gazit, H. Gluska, and E. Rabkin. Grain boundary grooving in thin films revisited: The role of interface diffusion. *Acta Materialia*, 69:386–396, 2014.

[76] S. Kumar, X. Li, A. Haque, and H. Gao. Is stress concentration relevant for nanocrystalline metals? *Nano Letters*, 11(6):2510–2516, 2011.

[77] E. Ho and G.C. Weatherly. Interface diffusion in the Al-CuAl2 Eutectic. *Acta Metallurgica*, 23(December):1451–1460, 1975.

[78] B. Fedelich and J. Owen. Creep damage by multiple cavity growth controlled by grain boundary diffusion. *International conference on fracture*, pages 1–10, 2009.

[79] P. H. Dederichs and K. Schroeder. Anisotropic diffusion in stress fields. *Physical Review B*, 17(6):2524–2536, 1978.

[80] T. Nizolek, N.A. Mara, I.J. Beyerlein, J.T. Avallone, and T.M. Pollock. Enhanced plasticity via kinking in cubic metallic nanolaminates. *Advanced Engineering Materials*, 17(6), 2015.

[81] D. Josell and F. Spaepen. Determination of the interfacial tension by zero creep experiments on multilayers- I. Theory. *Acta Materialia*, 41(10):3007–3015, 1993.

[82] D Josell and F Spaepen. Surfaces, Interface, and Chancing Shapes in Multlayered Films. *MRS Bulletin*, February, 1999.

[83] J. Malzahn Kampe, T. Courtney, and Y. Leng. Shape instabilities of platelike structures – I. Experimental observations in heavily cold worked in situ composites. *Acta Metallurgica*, 37(7):1735–1745, 1989.

[84] S. A. Barnett and Anita Madan. Hardness and stability of metal–nitride nanoscale multilayers. *Scripta Materialia*, 50(6):739–744, Mar 2004.

[85] P. M. Anderson, Jue Wang, and Sridhar Narayanaswamy. Thermal Grooving in Single versus Multilayer Thin Films. *Mater. Res. Soc. Symp. Proc.*, 854:2–7, 2005.

[86] Jue Wang and P. M. Anderson. Pinch-off maps for the design of morphologically stable multilayer thin films with immiscible phases. *Acta Materialia*, 53(19):5089–5099, Nov 2005.

[87] H.-J. Lee, K.-W. Kwon, C. Ryu, and R. Sinclair. Thermal stability of a Cu/Ta multilayer: an intriguing interfacial reaction. *Acta Materialia*, 47(15-16):3965–3975, Nov 1999.

[88] D. J. Srolovitz, S. M. Yalisove, and J. C. Bilello. Design of Multiscalar Metallic Multilayer Composites for High Strength , High Toughness , and Low CTE Mismatch. *Metallurgical and Materials Transactions A*, 26(July):1805–1813, 1995.

[89] P Troche, J Hoffman, C Herweg, C Lang, H Freyhardt, and D Rudoph. Thermally driven shape instability of multilayer structures. *Mater. Res. Soc. Symp. Proc.*, 581:635–640, 2000.

[90] D Van Heerden, A J Gavens, P R Subramanian, T Foecke, and T P Weihs. The Stability of Nb / Nb 5 Si 3 Microlaminates at High Temperatures. *Metallurgical and Materials Transactions A*, 32(September):2363–2371, 2001.

[91] A Mozaffari, M Hosseini, and H D Manesh. Al/Ni metal intermetallic composite produced by accumulative roll bonding and reaction annealing. *Journal of Alloys and Compounds*, 509(41):9938–9945, Oct 2011.

[92] P. Troche, J. Hoffmann, K. Heinemann, F. Hartung, G. Schmitz, H. C. Freyhardt, D. Rudolph, J. Thieme, and P. Guttmann. Thermally driven shape instabilities of Nb/Cu multilayer structures: instability of Nb/Cu multilayers. *Thin Solid Films*, 353(1-2):33–39, Sep 1999.

[93] A. C. Lewis, D. Van Heerden, D. Josell, and T. P. Weihs. Creep Deformation in Multilayered and Microlaminate Materials. *Journal of Materials*, (January), 2003.

[94] W. W. Mullins. Theory of thermal grooving. *Journal of Applied Physics*, pages 333–339, 1957.

[95] P.G. Shewmon. Chapter 6 High Diffusivity Paths. In *Diffusion in solids*. McGraw-Hill, New York, 1963.

[96] R. T. DeHoff. *Thermodynamics in Materials Science*. CRC Press, 2006.

[97] W W Mullins. The effect of thermal grooving on grain boundary motion. *Acta Metallurgica*, 6(6):414–427, 1958.

[98] W W Mullins and P G Shewmons. The Kinetics of Grain Boundary Grooving in Copper. *Acta Metallurgica*, 7(March):163–170, 1959.

[99] T H Courtney and J. Malzahn Kampe. Shape instabilities of Plat-like Structyres: II. Analysis. *Acta Metallurgica*, 31(I):1747–1758, 1989.

[100] S. Ig Hong and M.A. Hill. Microstructural stability of Cu–Nb microcomposite wires fabricated by the bundling and drawing process. *Materials Science and Engineering: A*, 281(1-2):189–197, Apr 2000.

[101] S. Zheng, J.S. Carpenter, J. Wang, N. A. Mara, and I. J. Beyerlein. An interface facet driven Rayleigh instability in high-aspect-ratio bimetallic nanolayered composites. *Applied Physics Letters*, 105(111901):1–5, Sep 2014.

[102] T. Chakrabarti, N. Verma, and S. Manna. Grain Boundary Driven Plateau-Rayleigh Instability in Multilayer Nanocrystalline Thin Film: A Phase-field Study. *Materials & Design*, 119(5):425–436, 2017.

[103] D. Josell and F. Spaepen. Determination of the interfacial tension by zero creep experiments on multilayers- II. Experiment. *Acta Materialia*, 41(10):3017–3027, 1993.

[104] P. Feltham and J. D. Meakin. Creep in face-centered cubic metals with special reference to copper. *Acta Metallurgica*, 7(September):614–627, 1959.

[105] R. Resnick and L. S. Castleman. The self-diffusion of columbium. *Trans. Met. Soc. AIME*, 218, 1960.

[106] Stan Development Team. PyStan: the Python interfaces to Stan, Version 2.9.0, 2016.

[107] R. Carpenter, A. Gelman, M. Hoffman, D. Lee, B. Goodrich, M. Betancourt, M.A. Brubaker, J. Guo, P. Li, and A. Riddell. Stan: A probabilistic programming language. *Journal of Statistical Software*, 2016.

[108] J.T. Avallone, X. Liu, T. J. Nizolek, N.A. Mara, I.J. Beyerlein, and T.M. Pollock. Thermal Stability and Structural Evolution of Cu-Nb Multilayers made via Accumulative Roll-Bonding. *In preparation for Metallurgical and Materials Transactions A*, 2018.

[109] R. Resnick and L. S. Castleman. The Self-diffusion of columbium. *Transactions of the Metallurgical Society of AIME*, 218, 1960.

[110] J.T. Avallone, T.J. Nizolek, M.R. Begley, and T.M. Pollock. Prediction of Transient and Steady-State Creep Behavior in Copper-Niobium Multilayer Composites. *In preparation.*, 2018.

[111] S B Biner and W A Spitzig. Creep characteristics of wire-drawn Cu-20 % Nb. *Materials Science and Engineering A*, 150:213–220, 1992.

[112] R Raj and M F Ashby. On Grain Boundary Sliding and Diffusional Creep. *Metallurgical Transactions*, 2(April), 1971.

[113] G Bao, W Hutchinson, and R M McMeeking. Plastic reinforcement of ductile materials against plastic flow and creep. *Acta Metall. Mater*, 39(8):1871–1882, 1991.

[114] A Misra, X Zhang, D Hammon, and R G Hoagland. Work hardening in rolled nanolayered metallic composites. *Acta Materialia*, 53(1):221–226, Jan 2005.

[115] N. A. Mara, D. Bhattacharyya, P. Dickerson, R. G. Hoagland, and A. Misra. Deformability of ultrahigh strength 5 nm CuNb nanolayered composites. *Applied Physics Letters*, 92(23):231901, 2008.

[116] N. A. Mara, D. Bhattacharyya, R. G. Hoagland, and A. Misra. Tensile behavior of 40nm Cu/Nb nanoscale multilayers. *Scripta Materialia*, 58(10):874–877, May 2008.

[117] H.M. Ledbetter and E.R. Naimon. Elastic Properties of Metals and Alloys. II. Copper. *Journal of Physical and Chemical Reference Data*, 3(897), 1974.

[118] S. Nemat-nasser and W. Guo. Flow stress of commercially pure niobium over a broad range of temperatures and strain rates. *Materials Science and Engineering A*, 284:202–210, 2000.

[119] Wolfram Research Inc. Mathematica, 2016.

[120] S. Takeuchi and A. S. Argon. Review Steady-state creep of single-phase crystalline matter at high temperature. *Journal od Materials Science*, 11:1542–1566, 1976.

[121] B Cai, Q.P Kong, L Lu, and K Lu. Low temperature creep of nanocrystalline pure copper. *Materials Science and Engineering: A*, 286(1):188–192, 2000.

[122] H. D. Chandler. Work hardening during primary creep of copper. *Materials Science and Engineering A*, 510-511(C):417–419, 2009.

[123] Rolf Sandström. Basic model for primary and secondary creep in copper. *Acta Materialia*, 60(1):314–322, 2012.

[124] C R Barrett, J L Lytton, and O.D. Sherby. Effect of Grain Size and Annealing Treatment on Steady State Creep of Copper. Technical Report 65-22, Stanford University, 1965.

[125] Josell, Carter, and Bonevich. Stability of multilayer structures: capillary effects. *NanoStructures Materials*, 12(99):387–390, 1999.

[126] a. Gangulee. Structure of electroplated and vapor-deposited copper films. III. Recrystallization and grain growth. *Journal of Applied Physics*, 45(9):3749, 1974.

[127] J. Wang, R. G. Hoagland, X.Y. Liu, and A. Misra. The influence of interface shear strength on the glide dislocation–interface interactions. *Acta Materialia*, 59(8):3164–3173, May 2011.

[128] E. Arzt, M. F. Ashby, and R. A. Verrall. Interface controlled diffusional creep. *Acta Metallurgica*, 31(12):1977–1989, 1983.

[129] S. S. Shishvan, T. M. Pollock, R. M. McMeeking, and V. S. Deshpande. Interfacial diffusion in high-temperature deformation of composites: A discrete dislocation plasticity investigation. *Journal of the Mechanics and Physics of Solids*, 98:330–349, 2017.

[130] S.S. Shishvan, R. M. McMeeking, T. M. Pollock, and V. S. Deshpande. Discrete dislocation plasticity analysis of the effect of interfacial diffusion on the creep response of Ni single-crystal superalloys. *Acta Materialia*, 135:188–200, 2017.